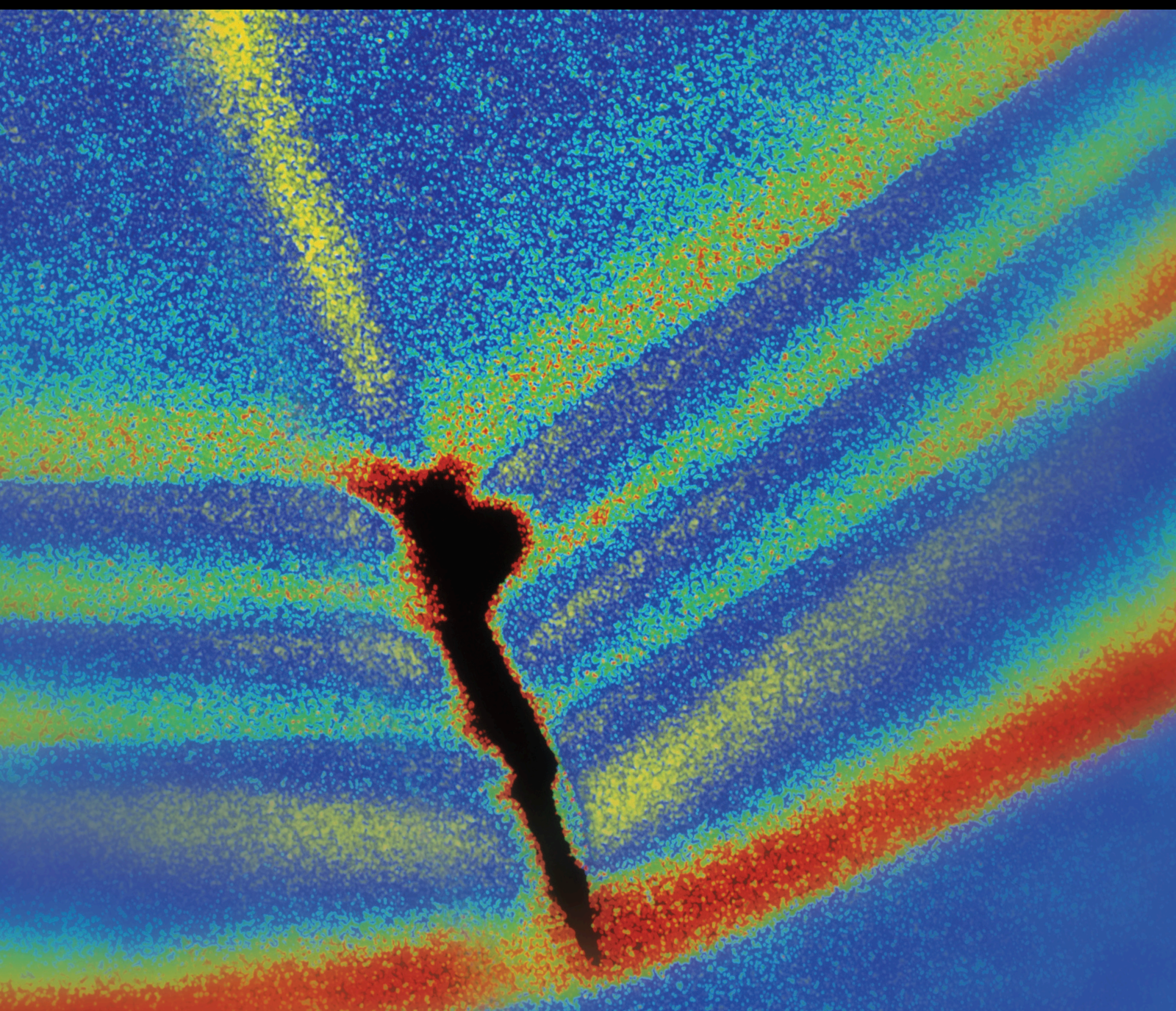


Shock and Vibration

Nonlinear Vibration of Continuous Systems 2020

Lead Guest Editor: Francesco Pellicano

Guest Editors: Matteo Strozzi, Konstantin V. Avramov, and Sinniah Ilanko





Nonlinear Vibration of Continuous Systems
2020

Shock and Vibration

Nonlinear Vibration of Continuous Systems 2020

Lead Guest Editor: Francesco Pellicano

Guest Editors: Matteo Strozzi, Konstantin V. Avramov, and Sinniah Ilanko



Copyright © 2023 Hindawi Limited. All rights reserved.

This is a special issue published in “Shock and Vibration.” All articles are open access articles distributed under the Creative Commons Attribution License, which permits unrestricted use, distribution, and reproduction in any medium, provided the original work is properly cited.












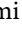









Chief Editor

Huu-Tai Thai , Australia

Associate Editors

Ivo Calì, Italy
Nawawi Chouw , New Zealand
Longjun Dong , China
Farzad Ebrahimi , Iran
Mickaël Lallart , France
Vadim V. Silberschmidt , United Kingdom
Mario Terzo , Italy
Angelo Marcelo Tusset , Brazil

Academic Editors

Omid A. Yamini , Iran
Maher Abdelghani, Tunisia
Mohamed A. A. Abdelkareem , Egypt
Haim Abramovich , Israel
Desmond Adair , Kazakhstan
Manuel Aenlle Lopez , Spain
Brij N. Agrawal, USA
Ehsan Ahmadi, United Kingdom
Felix Albu , Romania
Marco Alfano, Italy
Sara Amoroso, Italy
Huaming An, China
P. Antonaci , Italy
José V. Araújo dos Santos , Portugal
Jorge P. Arenas , Chile
Lutz Auersch , Germany
Matteo Aureli , USA
Azwan I. Azmi , Malaysia
Yi Bao, USA
Antonio Batista, Brazil
Mattia Battarra, Italy
Mahmoud Bayat , USA
Marco Belloli, Italy
Francisco Beltran-Carbajal , Mexico
Denis Benasciutti, Italy
Marta Berardengo , Italy
Sébastien Besset, France
Giosuè Boscato , Italy
Fabio Botta , Italy
Francesco Braghin , Italy
Giuseppe Brandonisio , Italy
Francesco Bucchi , Italy
Rafał Burdzik , Poland

Salvatore Caddemi, Italy
Wahyu Caesarendra, Brunei Darussalam
Baoping Cai, China
Sandro Carbonari , Italy
Cristina Castejón , Spain
Nicola Caterino , Italy
Gabriele Cazzulani , Italy
Athanasios Chasalevris , Greece
Guoda Chen , China
Zengshun Chen, China
Xavier Chimentin , France
Simone Cinquemani , Italy
Marco Civera, Italy
Marco Cocconcelli , Italy
Alvaro Cunha , Portugal
Giorgio Dalpiaz , Italy
Thanh-Phong Dao , Vietnam
Arka Jyoti Das, India
Raj Das, Australia
Silvio L.T. De Souza, Brazil
Xiaowei Deng , Hong Kong
Dario Di Maio , The Netherlands
Raffaella Di Sante, Italy
Luigi Di Sarno, Italy
Enrique Lopez Droguett , Chile
Mădălina Dumitriu, Romania
Sami El-Borgi , Qatar
Mohammad Elahinia , USA
Said Elias , Iceland
Selçuk Erkaya, Turkey
Cheng Fang, China
Gaoliang Fang, Canada
Fiorenzo A. Fazzolari , United Kingdom
Chengwei Fei , China
Luis A. Felipe-Sese , Spain
Matteo Filippi, Italy
Piotr Fołęga , Poland
Paola Forte , Italy
Francesco Franco , Italy
Juan C. G. Prada , Spain
Roman Gabl , United Kingdom
Pedro Galvín , Spain
Jinqiang Gan , China
Shan Gao , China
Arturo García García-Perez, Mexico

Gianluca Gatti , Italy
Rozaimi Ghazali , Malaysia
Marco Gherlone , Italy
Anindya Ghoshal , USA
Gilbert R. Gillich , Romania
Antonio Giuffrida , Italy
Annalisa Greco, Italy
Jiajie Guo, China
Amal Hajjaj , United Kingdom
Mohammad A. Hariri-Ardebili , USA
Seyed M. Hashemi , Canada
Xue-qiu He, China
Agustin Herrera-May , Mexico
M.I. Herreros , Spain
Kazuhiko Hiramoto , Japan
Duc-Duy Ho , Vietnam
Hamid Hosano , Japan
Jin Huang , China
Ahmed Ibrahim , USA
Bernard W. Ikuu, Kenya
Xingxing Jiang , China
Jiang Jin , China
Xiaohang Jin, China
MOUSTAFA KASSEM , Malaysia
Sakdirat Kaewunruen , United Kingdom
Shao-Bo Kang , China
Yuri S. Karinski , Israel
Andrzej Katunin , Poland
Manoj Khandelwal, Australia
Denise-Penelope Kontoni , Greece
Mohammadreza Koopialipoor, Iran
Georges Kouroussis , Belgium
Genadijus Kulvietis, Lithuania
Pradeep Kundu, USA
Simon Laflamme, USA
Luca Landi , Italy
Moon G. Lee , Republic of Korea
Trupti Ranjan Lenka, India
Arcanjo Lenzi, Brazil
Marco Lepidi , Italy
Jinhua Li , China
Shuang Li , China
Yuxing Li , China
Zhixiong Li , China
Xihui Liang , Canada

Tzu-Kang Lin , Taiwan
Jinxin Liu , China
Ruonan Liu, China
Xiang Liu, China
Xiuquan Liu, China
Siliang Lu, China
Yixiang Lu , China
Zeqi Lu , China
R. Luo , China
Tianshou Ma , China
Nuno M. Maia , Portugal
Abdollah Malekjafarian , Ireland
Stefano Manzoni , Italy
Giuseppe Carlo Marano , Italy
Stefano Marchesiello , Italy
Francesco S. Marulo, Italy
Traian Mazilu, Romania
Nur Izzi Md Yusoff , Malaysia
Vittorio Memmolo , Italy
Jean-Mathieu Mencik , France
Laurent Mevel , France
Letícia Fleck Fadel Miguel , Brazil
FuRen Ming , China
Fabio Minghini , Italy
Marco Miniaci, USA
Mahdi Mohammadpour , United Kingdom
Rui Moreira , Portugal
Emiliano Mucchi , Italy
Sara Muggiasca , Italy
Tony Murmu , United Kingdom
Peter Múčka , Slovakia
Fehmi Najar, Tunisia
Roberto Nascimbene , Italy
M. Z. Naser, USA
Amr A. Nassr, Egypt
Sundararajan Natarajan , India
Toshiaki Natsuki, Japan
Miguel Neves , Portugal
Tuan Ngo, Australia
Sy Dzung Nguyen , Republic of Korea
Trung Nguyen-Thoi , Vietnam
Hung Nguyen-Xuan , Vietnam
Baoyu Ni , China
Gianni Niccolini, Italy
Rodrigo Nicoletti , Brazil

Nicola Nisticò, Italy
Bin Niu, China
Leilei Niu, China
Yan Niu , China
Lucio Olivares, Italy
Erkan Oterkus, United Kingdom
Roberto Palma , Spain
Junhong Park , Republic of Korea
Annamaria Pau , Italy
Francesco Pellicano , Italy
Paolo Pennacchi , Italy
Giuseppe Petrone , Italy
Evgeny Petrov, United Kingdom
Antonina Pirrotta , Italy
Franck Poisson , France
Luca Pugi , Italy
Yi Qin , China
Zhaoye Qin, China
Virginio Quaglini , Italy
Mohammad Rafiee , Canada
Carlo Rainieri , Italy
Vasudevan Rajamohan , India
Ricardo A. Ramirez-Mendoza , Mexico
José J. Rangel-Magdaleno , Mexico
Didier Rémond , France
Dario Richiedi , Italy
Francesco Ripamonti , Italy
Fabio Rizzo, Italy
Nibaldo Rodríguez , Chile
Carlo Rosso , Italy
Riccardo Rubini , Italy
Salvatore Russo , Italy
Giuseppe Ruta , Italy
Edoardo Sabbioni, Italy
N. A. Saeed , Egypt
Pouyan Roodgar Saffari , Thailand
Filippo Santucci de Magistris , Italy
Fabrizio Scozzese , Italy
Abdullah Seçgin, Turkey
Roger Serra , France
S. Mahdi Seyed-Kolbadi, Iran
Changqing Shen , China
Yujie Shen, China
Bao-Jun Shi , China
Chengzhi Shi , USA

Gerardo Silva-Navarro , Mexico
Marcos Silveira, Brazil
Kumar V. Singh , USA
Jean-Jacques Sinou , France
Isabelle Sochet , France
Alba Sofi , Italy
Jussi Sopanen , Finland
Stefano Sorace , Italy
Andrea Spaggiari , Italy
Lei Su, China
Shuaishuai Sun , Australia
Fidelis Tawiah Suorineni , Kazakhstan
Cecilia Surace , Italy
Tomasz Szolc, Poland
Iacopo Tamellini , Italy
Zhuhua Tan, China
Gang Tang , China
Chao Tao, China
Tianyou Tao, China
Marco Tarabini , Italy
Gloria Terenzi , Italy
Hamid Toopchi-Nezhad , Iran
Carlo Trigona, Italy
Federica Tubino , Italy
Nerio Tullini , Italy
Filippo Ubertini , Italy
Nicolò Vaiana , Italy
Marcello Vanali , Italy
Christian Vanhille , Spain
F. Viadero, Spain
M. Ahmer Wadee , United Kingdom
C. M. Wang , Australia
Gaoxin Wang , China
Huiqi Wang , China
Pengfei Wang , China
Weiqiang Wang, Australia
Xian-Bo Wang, China
YuRen Wang , China
Wai-on Wong , Hong Kong
Bangbiao Wu , China
Yuanping XU , China
Tang-Bin Xia , China
Biao Xiang, China
Qilong Xue , China
Xin Xue , China


Diansen Yang , China
Jie Yang , Australia
Chang-Ping Yi, Sweden
Junyan Yi , China
Nicolo Zampieri , Italy
Chao-Ping Zang , China
Enrico Zappino , Italy
Guo-Qing Zhang , China
Hong Zhang , China
Shaojian Zhang , China
W. Zhang , China
Yongfang Zhang , China
Yaobing Zhao , China
Zhipeng Zhao, Japan
Changjie Zheng , China
Chuanbo Zhou , China
Hongwei Zhou, China
Hongyuan Zhou , China
Jiaxi Zhou , China
Yunlai Zhou, China
Radoslaw Zimroz , Poland

Contents



Nonlinear Vibration of Continuous Systems 2020

Francesco Pellicano , Matteo Strozzi , Konstantin V. Avramov , and Sinniah Ilanko 
Editorial (2 pages), Article ID 9823640, Volume 2023 (2023)


Detecting and Evaluating Defects in Beams by Correlation Coefficients

Thanh Q. Nguyen  and Hoang B. Nguyen
Research Article (22 pages), Article ID 6536249, Volume 2021 (2021)



Vibrations of Plates with Complex Shape: Experimental Modal Analysis, Finite Element Method, and R-Functions Method

Antonio Zippo , Giovanni Iarriccio , Francesco Pellicano , and Tetyana Shmatko 
Research Article (23 pages), Article ID 8882867, Volume 2020 (2020)

Probabilistic Assessment of Damage from Same Shock Response Spectra due to Variations in Damping

Arup Maji 
Research Article (11 pages), Article ID 8832815, Volume 2020 (2020)


Numerical Study on Acoustic Resonance Excitation in Closed Side Branch Pipeline Conveying Natural Gas

Liuyi Jiang , Hong Zhang, Qingquan Duan, and Yulong Zhang 
Research Article (19 pages), Article ID 8857838, Volume 2020 (2020)


Steady-State Dynamical Response of a Strongly Nonlinear System with Impact and Coulomb Friction Subjected to Gaussian White Noise Excitation

Guidong Yang , Dongmei Huang, Wei Li, and Meng Su
Research Article (11 pages), Article ID 8837638, Volume 2020 (2020)

A Time-Discontinuous Galerkin Finite Element Method for the Solution of Impact Problem of Gas-Saturated Coal

Jingfei Zhang, Deyong Guo, Wenhua Wu, and Pan Guo 
Research Article (10 pages), Article ID 8845056, Volume 2020 (2020)

Aeroelastic Flutter and Sliding Mode Control of Wind Turbine Blade

Lin Chang, Yingjie Yu , and Tingrui Liu
Research Article (8 pages), Article ID 8846529, Volume 2020 (2020)

A Novel Aerodynamic Force and Flutter of the High-Aspect-Ratio Cantilever Plate in Subsonic Flow

Li Ma, Minghui Yao , Wei Zhang , Kai Lou, Dongxing Cao , and Yan Niu 
Research Article (17 pages), Article ID 8841590, Volume 2020 (2020)

Editorial

Nonlinear Vibration of Continuous Systems 2020

Francesco Pellicano ¹, **Matteo Strozzi** ¹, **Konstantin V. Avramov** ²,
and Sinniah Ilanko ³

¹University of Modena and Reggio Emilia, Modena, Italy

²Anatolii Pidhorneyi Institute of Mechanical Engineering Problems of the National Academy of Sciences of Ukraine, Kharkiv, Ukraine

³The University of Waikato, Hamilton, New Zealand

Correspondence should be addressed to Francesco Pellicano; francesco.pellicano@unimore.it

Received 27 February 2023; Accepted 27 February 2023; Published 13 April 2023

Copyright © 2023 Francesco Pellicano et al. This is an open access article distributed under the Creative Commons Attribution License, which permits unrestricted use, distribution, and reproduction in any medium, provided the original work is properly cited.

Scientific research in continuous systems, such as beams, membranes, plates, and shells, has continued to remain strong over several decades due to their role of fundamental structural elements of complex mechanical components in several engineering fields, e.g., aerospace, aeronautical, and automotive. In particular, since these continuous systems are typically designed for high-speed mechanical applications, it is important to investigate their nonlinear vibrations.

The present Special Issue collects eight original research contributions that focus on recent advances and developments in experimental techniques, numerical simulations, and theoretical models related to nonlinear dynamics of continuous systems. Specifically, these papers address the following areas of nonlinear vibration analysis: fault detection, diagnosis and prognosis, impact problems, damping and Coulomb friction, aerodynamic force and aeroelastic flutter, acoustic resonance, and complex shapes. From this collection of contributions dealing with different methods of nonlinear vibration analysis, it clearly shows both relevance and opportunity for the exchange of ideas between the Researchers of these areas. This was the main goal of the Guest Editors in proposing this Special Issue.

It should be underlined that the eight contributions received come from all over the world: Australia, China, Italy, Ukraine, USA, and Vietnam—this shows the generalized interest on the proposed topics. In the following, a short description of the content of the present Special Issue

organized by grouping the contributions in different methods of nonlinear vibration analysis is reported.

1. Experimental Techniques

T. Q. Nguyen and H. B. Nguyen in the paper entitled “Detecting and Evaluating Defects in Beams by Correlation Coefficients” propose a new correlation coefficient for detecting and evaluating defects in beams. This parameter, which is defined starting from Pearson correlation coefficient, is proven, by means of experimental tests, to be more accurate and efficient than other classic parameters, such as natural frequency and damping coefficient, thanks to its high sensitivity to the structural changes. In particular, this new parameter is able to correctly detect increasing levels of defects and is sensitive to the position of the measurement channel, which is a very relevant factor for evaluating and locating defects in structural components, respectively.

The paper entitled “Probabilistic Assessment of Damage from Same Shock Response Spectra due to Variations in Damping” by A. Maji deals with the interpretation of field data from experimental shock tests and the subsequent assessment of product safety margins via laboratory testing based on shock response spectra (SRS). In particular, this work proposes a simple method of capturing damping from shock waves that can allow the original waveform to be more accurately reconstructed from the SRS. The decay rate associated with various shock wave frequencies is varied,

leading to a variation in the acceleration vs. time history, which is correlated to a new parameter, referred to as “Damage Index,” able to capture the fatigue damage imparted to the object under shock until failure.

2. Numerical Simulations

L. Ma et al. in the paper entitled “A Novel Aerodynamic Force and Flutter of the High-Aspect-Ratio Cantilever Plate in Subsonic Flow” derive a new analytic expression of the quasi-steady aerodynamic force related to velocity and deformation for a high-aspect-ratio cantilever plate under subsonic flow by adopting subsonic thin airfoil theory and Kutta–Joukowski theory. This theoretical aerodynamic force distribution is validated by means of comparisons with numerical simulations carried out via Ansys Fluent finite element software. The effect of aspect ratio, thickness, and air damping on the critical flutter velocity of the plate is investigated. Moreover, it is observed that, when the inflow velocity reaches its critical value, the limit cycle oscillation occurs.

The paper entitled “A Time-Discontinuous Galerkin Finite Element Method for the Solution of Impact Problem of Gas-Saturated Coal” by J. Zhang et al. presents a modified time-discontinuous Galerkin FEM based on the general Biot theory of the saturated porous media to simulate structural dynamics and wave propagation problems of gas-saturated coal in the presence of impact loading. Numerical results for 1D and 2D stress wave propagation problems show that this method gives more accurate solutions than standard time-discontinuous Galerkin FEM and Newmark method for the impact problems, as it can effectively capture wave discontinuities and filter out the effects of the spurious numerical oscillations induced by high-frequency impulsive load.

L. Chang et al. in the paper entitled “Aeroelastic Flutter and Sliding Mode Control of Wind Turbine Blade” propose a new aeroelastic flutter model of a pretwisted wind turbine blade based on damping analysis, considering the aeroelastic vibration instability and adopting the parameter fitting method. A numerical system for the sliding mode control is built by Simulink in order to simulate the flap and lead-lag directions of aeroelastic flutter. From these numerical simulations, it is obtained that the proposed sliding mode control algorithm significantly reduces the vibration frequency and therefore is able to suppress flutter-type blade aeroelastic failure under high wind speed and angle of attack.

The paper entitled “Numerical Study on Acoustic Resonance Excitation in Closed Side Branch Pipeline Conveying Natural Gas” by L. Jiang et al. describes an innovative delayed detached eddy simulation model developed to numerically simulate the flow-induced acoustic resonance problem arising in the closed side branch of a natural gas pipeline. This numerical study, which is performed by adopting the commercial CFD code (Fluent), investigates the coupling effect between flow and sound fields that causes acoustic vortex convection along the branch. The proposed model is shown to accurately capture

acoustic resonance phenomenon and self-excited vibration characteristics of the considered pipeline with low computational effort.

3. Theoretical Models

The paper entitled “Steady-State Dynamical Response of a Strongly Nonlinear System with Impact and Coulomb Friction Subjected to Gaussian White Noise Excitation” by G. Yang et al. is devoted to the study of the steady-state dynamic behaviour of a strongly nonlinear system with impact and Coulomb friction under Gaussian white noise excitation. Zhuravlev nonsmooth transformation, Dirac delta function, and stochastic averaging method of energy envelope are adopted to obtain the steady-state probability density functions of the system. It is shown that different intensities of Gaussian white noise excitation can affect the peak value of the probability density functions, whereas the variations of restitution coefficients and friction amplitudes can induce stochastic bifurcations.

In the paper entitled “Vibrations of Plates with Complex Shape: Experimental Modal Analysis, Finite Element Method, and R -Functions Method” by A. Zippo et al., the dynamic behaviour of 3D-printed composite plates with different shapes and boundary conditions is studied. Specifically, natural frequencies and mode shapes of the plates are determined by means of the analytical R -functions method, numerical finite element simulations via NASTRAN software, and experimental tests. From the comparisons, by taking the experimental results as reference, it is found that, in the case of plates presenting rectangular cuts with clamped and free edges, the R -functions method provides better convergence with respect to FEM analyses.

At the end, the Editors hope that the content of the present Special Issue will be interesting and useful to the community of Engineers and Researchers working on nonlinear mechanical vibrations.

Conflicts of Interest

The Editors declare that they have no conflicts of interest regarding the publication of this Special Issue.


Acknowledgments

The Editors would like to express their gratitude to all the Authors for their interest to this Special Issue. The Editors also wish to thank the anonymous Reviewers for their deep analysis of the manuscripts, valuable comments, and suggestions. Finally, the Editors thank the Publisher and in particular the Assistant Editors for their fundamental support to the editorial process.

*Francesco Pellicano
Matteo Strozzi
Konstantin V. Avramov
Sinniah Ilanko*

Research Article

Detecting and Evaluating Defects in Beams by Correlation Coefficients

Thanh Q. Nguyen ^{1,2} and Hoang B. Nguyen²

¹Science, Research and Development Department, Ho Chi Minh City University of Transport, Ho Chi Minh City, Vietnam

²Ho Chi Minh City University of Transport, Ho Chi Minh City, Vietnam

Correspondence should be addressed to Thanh Q. Nguyen; nqthanh@hcmut.edu.vn

Received 13 February 2020; Revised 27 January 2021; Accepted 10 February 2021; Published 19 February 2021

Academic Editor: Sinniah Ilanko

Copyright © 2021 Thanh Q. Nguyen and Hoang B. Nguyen. This is an open access article distributed under the Creative Commons Attribution License, which permits unrestricted use, distribution, and reproduction in any medium, provided the original work is properly cited.

This research proposes a correlation coefficient for detecting and evaluating defects in beams, which brings about a positive outcome in terms of accuracy and efficiency. This parameter surpasses other parameters, such as natural frequency and damping coefficient, thanks to its sensitivity to structural changes. Our results show that although the damping coefficient had more variation than the natural frequency value in the same experiment, its changes were insufficient and unstable at different levels of defects. In addition, the proposed correlation coefficient parameter has a linear characteristic and always changes significantly according to increasing levels of defects. The results outweigh damping coefficient and natural frequency values. Furthermore, this value is always sensitive to measurement channels, which could be an important factor in locating defects in beams. The testing index is statistically evaluated by a normal distribution of the amplitude value of vibration measurement signals. Changes and shifts in this distribution are the basis for evaluating beam defects. Thus, the suggested parameter is a reliable alternative for assessing the defects of a structure.

1. Introduction

Mathematically, research on detecting defects in bridge beams and other construction components has taken place in two major areas. The first study uses mathematical models to simulate the structures of mechanical systems. Researchers do not focus on characteristics of defects but on their general specifications in terms of kinematic and dynamic responses. The defects caused by changes in geometric dimensions, geometric shapes, or materials might include cracks, such as horizontal cracks [1–4] or vertical cracks [5, 6], geometric shapes, [7, 8] such as circles, ovals, or obliques, a reduction of mechanical characteristics, such as elastic, torsional, or bending modulus [9–11] or a combination of the above factors. These studies use certain parameters to evaluate the overall stiffness level, EJ_x . The second research area, which seeks to obtain a solution to the inverse problem, is aimed at determining structural characteristics by using algorithms to retrieve relevant

information. Some of these algorithms also evaluate the performance of a structure under actual working conditions. In order to increase the accuracy of parameters collected from different measurement signals, researchers have developed different mathematical methods, for example, statistical methods [12, 13] or combination with optimization algorithms [14–16], algorithms of artificial neural networks [17–19], wavelet transformation [20, 21], or neuron-fuzz [15, 22]. Figure 1 shows the steps involved in detecting and forecasting defects in a structure.

The procedure goes from the lowest to highest level, in detail:

- (i) Detecting: to inspect and confirm the presence of defects
- (ii) Locating: to localize defects
- (iii) Evaluating: to assess the impact of these defects on the structure and determine their degrees in order to organize periodic tests and inspection

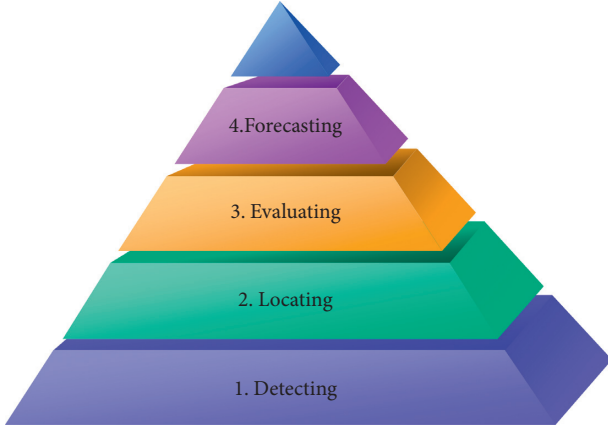


FIGURE 1: The sequence of detecting and evaluating defects.

- (iv) Forecasting: to promptly forecast defects, minimizing loss and damage to personnel and assets

As detecting is very important, it has attracted the interest of researchers all over the world. Researchers have mostly opted for reliable signals, such as vibration measurement signals, deformation measurement signals, and transposition signals (deflection).

Some outstanding examples using vibration measurement signals are found in [23, 24]. Parameters related to these signals, such as natural frequencies, mode shapes, vibration amplitudes, and damping coefficients, were commonly used in [25, 26]; among these, natural frequency was one of the most popular. Many of the above studies have shown that natural frequency does not express changes in the overall stiffness of mechanical systems very well, as it is not sensitive enough in practice. For example, in [27], when the beam had three cracks that accounted for 50% of its thickness, the natural frequency was reduced by less than 5%. Salawu [28] measured the status of a concrete bridge before and after the trimmer beam was replaced and realized that the frequency of the first six segments changed by 1.7% on average. The results from Salawu show that natural frequency can only detect relatively large defects but cannot locate them due to the same changes in frequency [29]. Other researchers, such as Loland [30], Fox [31], Meneghetti and Maggiore [32], and Choy et al. [33], also had the same viewpoint [34–38]. Therefore, we must discover new characteristics that are sensitive enough to exploit.

This article proposes a new characteristic built on actual vibration signals and, specifically, on the correlation coefficient. Changes in this parameter are the basis for evaluating the existence and development of defects or locating defects inside structures. Using test beam models, this study not only determines the natural frequencies and damping coefficients of mechanical systems suffering from different extents of defects but also compares their changes to the new proposed parameter using mathematical statistics. In addition, it also defines the normal distribution of vibration measurement signals through experimentation. Most importantly, this new parameter can be applied to complex structural models.

2. Theoretical Basis

2.1. Theoretical Vibration of Beam Model. Any vibration in a mechanical system is considered to be a linear combination of basic vibrations. In this investigation, a bar type is used with a basic load-bearing state of compression and tension at the center, bending, torsion, or a combination of different kinds of vibration. However, every vibration can be composed of each type of basic vibration. They are usually represented by the harmonic vibration formula:

$$\omega_i = W_i \cos(\omega_{Ni}t), \quad (1)$$

in which ω_{Ni} is the i^{th} natural frequency. Vectors following the order of W_i are called i^{th} private vectors and are assigned so that

$$\omega_{N1} < \omega_{N2} < \omega_{N3} < \dots < \omega_{Ni}. \quad (2)$$

These values depend on the geometric dimensions of bridge span, material characteristics, and sectional structure. Technically, natural frequency has a special feature: when the frequency of a constraining force is equal to the natural frequency value, the amplitude of the corresponding response will sharply increase due to resonance. Determining the natural frequency of basic vibrations of elastic beams applies the formulas below.

- (i) Natural frequency of the bending vibration of a simply supported beam:

$$\omega_{Bi} = (i\pi)^2 \sqrt{\frac{EJ_z}{\rho \cdot A \cdot l^4}}, \quad (3)$$

in which l is the length of the structure, EJ_z is its bending stiffness, A is its sectional area, and ρ is its net weight.

- (ii) Natural frequency of torsional vibration:

$$\omega_{Ti} = (i\pi) \sqrt{\frac{GJ_z}{J_0}}, \quad (4)$$

in which GJ_z is the convolution stiffness and J_0 is the area of the cross-section.

- (iii) Natural frequency of torsional-bending vibration:

$$\omega_{B-T-i}^2 = \frac{(\omega_{Ti}^2 + \omega_{Bi}^2) \pm \sqrt{(\omega_{Ti}^2 - \omega_{Bi}^2)^2 + 4\lambda\omega_{Ti}^2\omega_{Bi}^2}}{2(1-\lambda)}, \quad (5)$$

in which $\omega_{Bi}^2 = (EI_z i^4 \pi^4) / (l^4 \rho F)$, $\omega_{Ti}^2 = ((GJ_z i^2 \pi^2 l^2 + EJ_z i^4 \pi^4) / (l^4 \rho (I + Fc^2)))$, and $\lambda = (Fc^2 / (I + Fc^2))$.

When $\lambda = 0$, the torsional-bending frequency (5) is determined by

$$\omega_{B-T-i}^2 = \frac{(\omega_{Ti}^2 + \omega_{Bi}^2) \pm (\omega_{Ti}^2 - \omega_{Bi}^2)}{2}, \quad (6)$$

in which $\omega_{B-T-1i} = \omega_{B-i}$ and $\omega_{B-T-2i} = \omega_{T-i}$.

Equations (3), (4), and (6) show that if the mechanical system vibrates, the impact of impeding factors will make the amplitude decrease over time. The vibration energy in the system is gradually lost until it vanishes (becomes equal to 0). The decreasing energy directly affects the overall stiffness of the beams. However, the natural frequency value rarely changes with respect to the stiffness reduction of structures, which means the energy loss is unable to change the natural frequency value. To evaluate the energy loss mentioned above, researchers focus on examining the damping coefficient. When a mechanical system vibrates under bending, torsion, or a torsional-bending state, the vibration equation is

$$q(t) = A_0 e^{-\zeta \omega_n t} \cos(\sqrt{1 - \zeta^2} \omega_n t - \Phi_0). \quad (7)$$

When a mechanical system suffers from damping vibrations, the natural frequency is reduced. To evaluate the new vibration state (commonly called vibration damping), studies have examined the damping frequency of mechanical systems. ω_d is the damped natural frequency. Therefore,

$$\omega_d = \sqrt{1 - \zeta^2} \omega_n \Leftrightarrow q(t) = A_0 e^{-\zeta \omega_n t} \cos(\omega_d t - \Phi_0). \quad (8)$$

To determine the damping coefficient ζ , experimental methods record the decreasing vibration graphs of the system. q_1 and q_2 represent two adjacent peaks of the decreasing vibration graph (Figure 2). At the recorded time, the two peaks are t_1 and t_2 . We thus have a ratio:

$$\frac{q_1}{q_2} = \frac{Ae^{-\zeta \omega_n t_1} \cos(\omega_d t_1 - \Phi_0)}{Ae^{-\zeta \omega_n t_2} \cos(\omega_d t_2 - \Phi_0)}. \quad (9)$$

As q_1 and q_2 are two adjacent peaks of the graph, $t_2 = t_1 + T_d$:

$$\omega_d t_2 = \omega_d t_1 + \omega_d T_d = \omega_d t_1 + 2\pi. \quad (10)$$

Noting equation (10), when applying the damped vibration equation to equation (8), we get the following equation:

$$\cos(\omega_d t_2 - \Phi_0) = \cos(\omega_d t_1 + 2\pi - \Phi_0) = \cos(\omega_d t_1 - \Phi_0). \quad (11)$$

Equation (9) then becomes equation (12). This is the basis for determining energy loss through vibration amplitude:

$$\frac{q_1}{q_2} = e^{\zeta \omega_n T_d}. \quad (12)$$

The natural logarithm of the above equation is called the logarithmic decrement and is symbolized as δ . This coefficient expresses the loss of energy during vibration as

$$\delta = \ln \frac{q_1}{q_2} = \zeta \omega_n T_d. \quad (13)$$

Provided that $\begin{cases} T_d = 2\pi/\omega_d \\ \omega_d = \omega_n \sqrt{1 - \zeta^2} \end{cases}$, the final expression becomes $\delta = (2\pi/\sqrt{1 - \zeta^2})$.

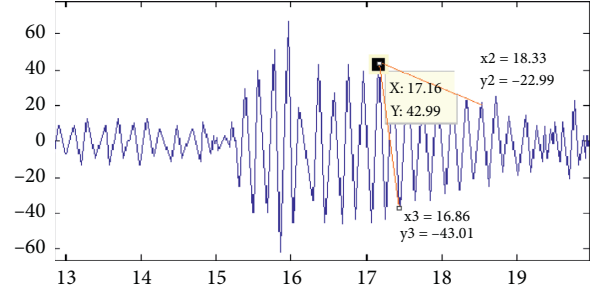


FIGURE 2: Levels of cracks in the beam.

If $\zeta \ll 1$, then the above expression can be written as $\delta \approx 2\pi\zeta$.

In order to increase the accuracy of determining the ζ value, instead of two adjacent peaks, we propose to take two peaks at m intervals. Thus, the ratio between q_1 and q_m is

$$\frac{q_1}{q_{1+m}} = \frac{q_1}{q_2} \cdot \frac{q_2}{q_3} \cdot \dots \cdot \frac{q_m}{q_{1+m}}. \quad (14)$$

We combine equation (14) with equation (13) to determine the damping coefficient under all circumstances:

$$\delta = \frac{1}{m} \ln \left(\frac{q_1}{q_{1+m}} \right). \quad (15)$$

However, the results of calculating the damping coefficient ζ usually contain errors. During actual experimentation, we have identified two common cases:

- The calculated results have higher values than the reality. This case usually occurs when the test beam is overloaded at a low velocity. In this circumstance, the deflection of the beam suddenly increases to maximum, while the vibration decreases quickly.
- The calculated results have smaller values than the reality. This case usually occurs when the beam suffers from forced vibration, with its frequency approaching its natural frequency. The load and velocity on the beam are sufficient to make the bridge vibrate drastically. At that point, the forced vibration lasts longer than the decreasing vibration. As such, the test beam vibrates harshly, and forced vibration in beams creates large vibration amplitudes. This phenomenon causes a deterioration in the bridge capability and destroys the structure.

Therefore, calculating the actual damping value is relatively difficult with remaining deviations. This is why we propose a new parameter to evaluate the energy loss of structural vibration. This parameter must simplify both calculation and measurement.

2.2. Proposal of Correlation Coefficient Model. Correlation coefficients are commonly used in cases of studying the relation between two parameter sets with the same number of samples X and Y. There are different types of calculations based on usage. The most popular correlation coefficient is the Pearson correlation coefficient, which is calculated by

dividing the covariances of two variables by their multiplied standard deviations. This calculation is shown as

$$r = \rho_{X,Y} = \frac{\text{Cov}(X,Y)}{\sigma_X \sigma_Y} = \frac{E[(X - \mu_X)(Y - \mu_Y)]}{\sigma_X \sigma_Y}, \quad (16)$$

in which E is the operator of expected value and Cov is the covariance. Another formula is widely applied according to equation (16):

$$\text{Corr}(X,Y) = \rho_{X,Y}. \quad (17)$$

As

$$\mu_X = E(X), \sigma_X^2 = E[(X - E(X))^2] = E(X^2) - E^2(X), \text{ and so is } Y.$$

On the contrary,

$$E[(X - \mu_X)(Y - \mu_Y)] = E(XY) - E(X) \cdot E(Y). \quad (18)$$

Therefore, equation (16) is rewritten as

$$r = \rho_{X,Y} = \frac{E(XY) - E(X)E(Y)}{\sqrt{E(X^2) - E^2(X)} \cdot \sqrt{E(Y^2) - E^2(Y)}}. \quad (19)$$

The correlation coefficient shall only be defined as above if the standard deviation is bounded and not equal to zero. Mathematically, the correlation coefficient is equal to one in the case of covariant linear correlation and -1 in the case of contravariant linear correlation. Other values ranging from $[-1, 1]$ show the level of linear dependence between variables. The closer the correlation coefficients are to -1 and 1 , the stronger the correlation between variables. However, the values in mechanical fields only range between $[0, 1]$. It can be concluded that the correlation coefficient is equal to 1 when no energy loss occurs and equal to 0 when no energy exists after vibration transmission.

3. Experimental Model

The experimental model was created at the Laboratory of Applied Mechanics (LAM), Ho Chi Minh City University of Technology (Figure 3), utilizing three groups of equipment: a model group, excitation-creating group, and signal-receiving group.

The model group includes a steel plate with a 0.9 m length, 0.01 m width, and 0.005 m height (see Table 1) to simulate the load-bearing beam. The steel beam rests on two trimmer beams, as shown in Figure 4(a). Additionally, a deceleration part is installed at each head of the test beam to make the model more realistic. When a vehicle approaches, passes through the beam, and finishes its movement, it does not make the steel beam become tight. To simulate a complicated force acting on the test beam, the study installed one more thin homogeneous plate that creates eccentric vibrations. Thus, this experiment can change not only the running velocity of vehicles but also the rotating velocity of vehicle engines (Figure 4(b)).

The excitation-creating group consists of one engine driven by a belt-drive system. This system lets the vehicle run over the beam in one direction at a steady velocity, as shown in Figure 5(a). When the vehicle moves, the velocity is



FIGURE 3: Experimental model of travel load on beams (obtained from LAM).

controlled by two inverter machines that can change the rotating velocity of the engine and the running velocity of the vehicles (Figure 5(b)).

The signal-receiving group measures various kinds of parameters, including the velocity, acceleration, deformation, and transposition-meter measurement signals. The transposition meter is directly attached to the middle point of the beam (Figure 6(a)). For vibration signals, parameters from velocity and acceleration sensors were collected. There are four acceleration sensors and four velocity sensors attached to the beam at four locations. The measurement points are distributed evenly on the beam, as shown in Figure 6(b). At each point, we arranged one velocity sensor and one acceleration sensor to simultaneously measure both signals. Finally, a strain gauge was installed at the center of the beam, as shown in Figure 6(c).

The experiment evaluated six different velocities: $V50 = 18.84$ cm/s, $V60 = 25.12$ cm/s, $V70 = 28.26$ cm/s, $V80 = 31.4$ cm/s, $V90 = 35.3$ cm/s, and $V100 = 39.2$ cm/s. Each velocity responded to eight different levels of defects created in the beam (according to Table 2). We treated cracks as defects. At each stage of the experiment, the cracks were deepened, until the beam was nearly destroyed. The moving loads from left abutments to right abutments on the beams and sample parameters are shown in Table 3.

4. Results and Discussion

4.1. Stability of Natural Frequency. A power spectrum for the test beam was created, ranging from nondefective to different levels of defects. The results, shown in Figure 7, include Figure 7(a): a free vibration of the intact beam, Figure 7(b): a free vibration of the beam with a 0.4 mm deep and 0.3 mm wide crack, Figure 7(c): a free vibration of the beam with a 0.8 mm deep and 0.3 mm wide crack, Figure 7(d): a free vibration of the beam with a 1.2 mm deep and 0.3 mm wide crack, Figure 7(e): a free vibration of the beam with a 1.6 mm deep and 0.3 mm wide crack, Figure 7(f): a free vibration of the beam with a 2.4 mm deep and 0.3 mm wide crack, Figure 7(g): a free vibration of the beam with a 2.6 mm deep and 0.3 mm wide crack, and Figure 7(h): a free vibration of the beam with two defects of

TABLE 1: Basic parameters of beams.

Type	Geometric parameters ($l \times d \times w$)	Material parameters	Specific weight
Steel beam	0.9 m \times 0.005 m \times 0.1 m	Steel CT3	7,800 kg/m ³

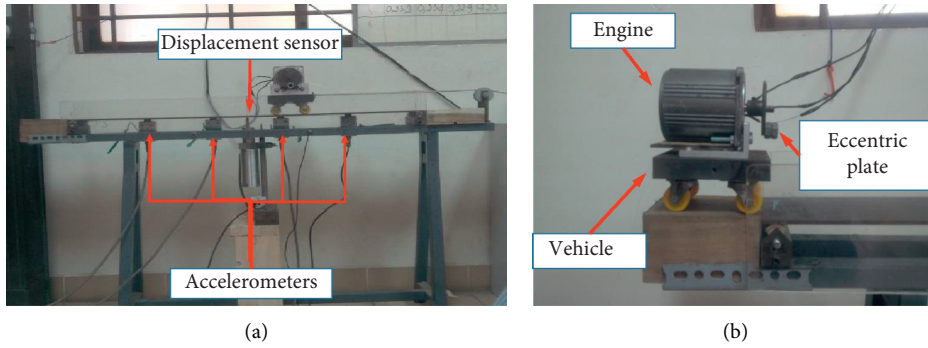


FIGURE 4: The beam model and the model simulating a vehicle passing through the beam. (a) Beam. (b) Vehicle.



FIGURE 5: (a) Transmission and (b) inverter machines from the excitation-creating group.

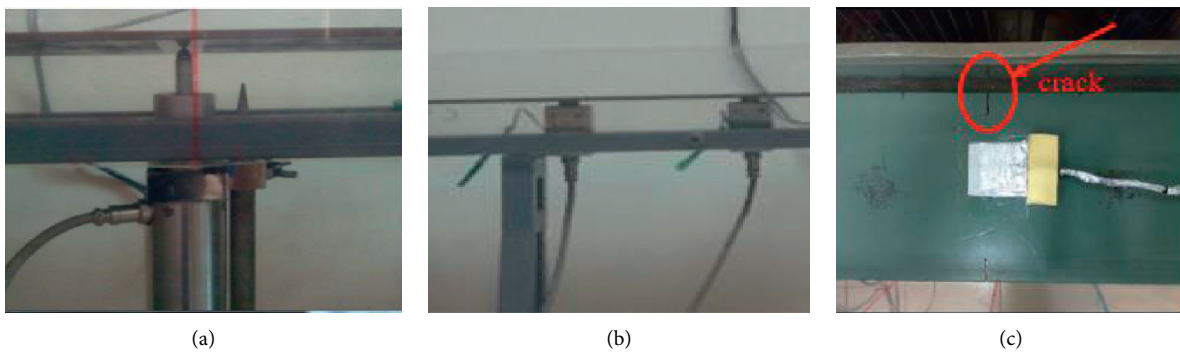
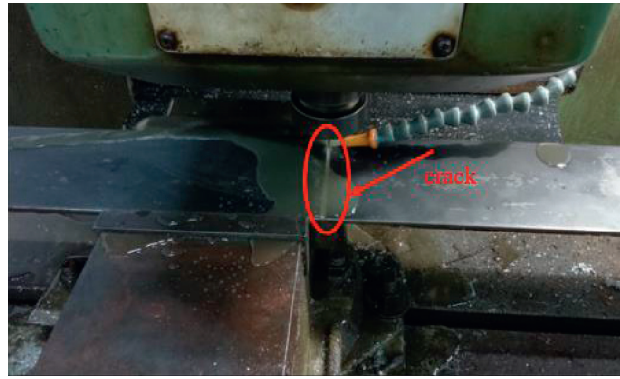


FIGURE 6: Continued.



(d)

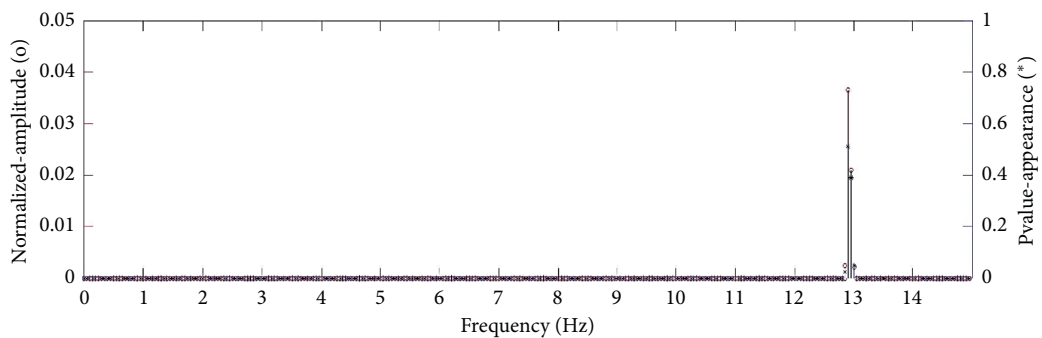
FIGURE 6: Sensors installed on test beam: (a) displacement sensor; (b) accelerometer; (c) strain-gauge; (d) the position of the cut.

TABLE 2: Levels of cracks in the beam.

No.	Label	Depth of crack (mm)	Width of crack (mm)
1	H ₀	0	0
2	H ₄	0.4	0.3
3	H ₈	0.8	0.3
4	H ₁₂	1.2	0.3
5	H ₁₆	1.6	0.3
6	H ₂₀	2.0	0.3
7	H ₂₄	2.4	0.3
8	H ₂₆	2.6	0.3

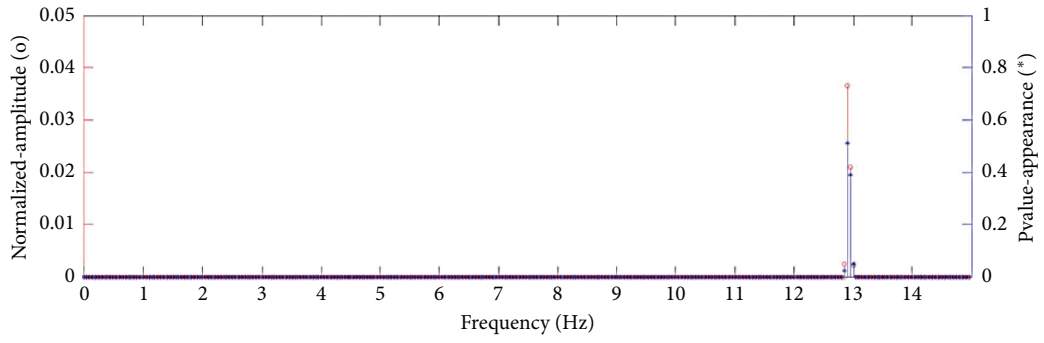
TABLE 3: Sample signal parameters.

Sample frequency	100 sample/seconds
Time to collect a file	1,920 seconds
Total measurement points	4 measurement points
Number of files in a measurement point	96
Number of samples in a measurement point	192,000 sample
Total samples in four measurement points	960,000 sample

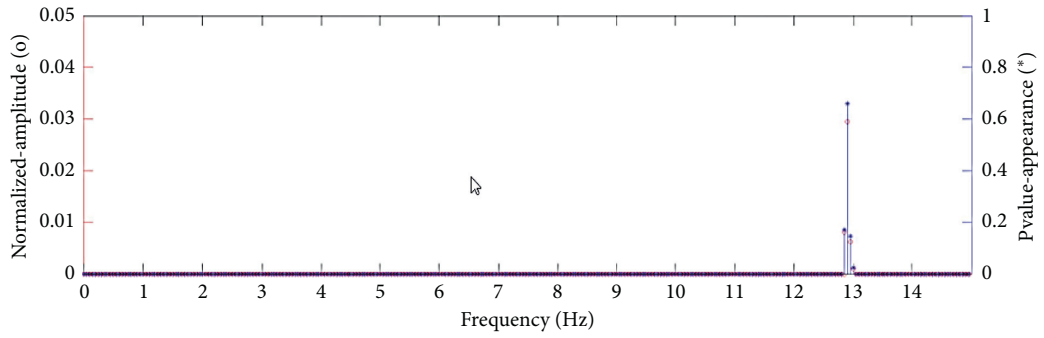


(a)

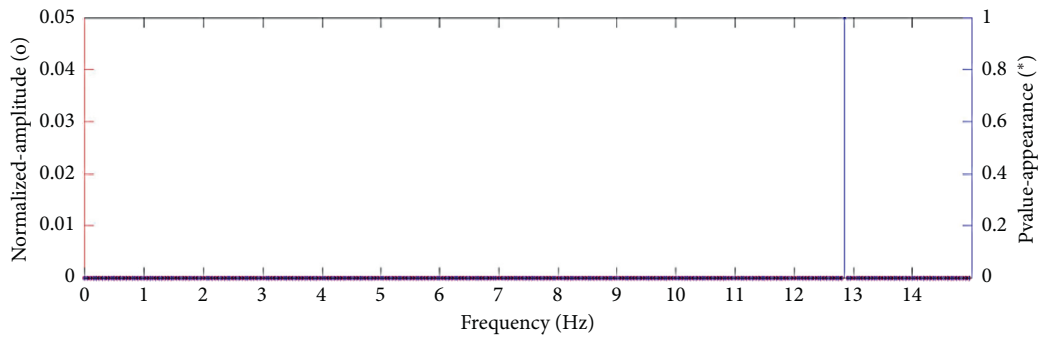
FIGURE 7: Continued.



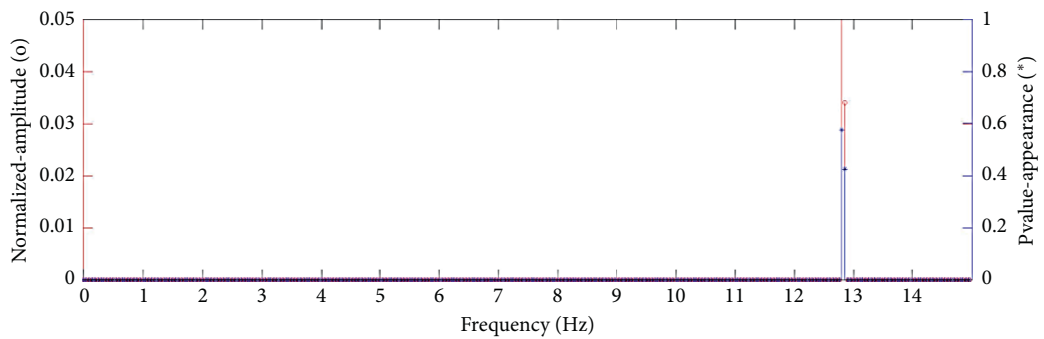
(b)



(c)



(d)



(e)

FIGURE 7: Continued.

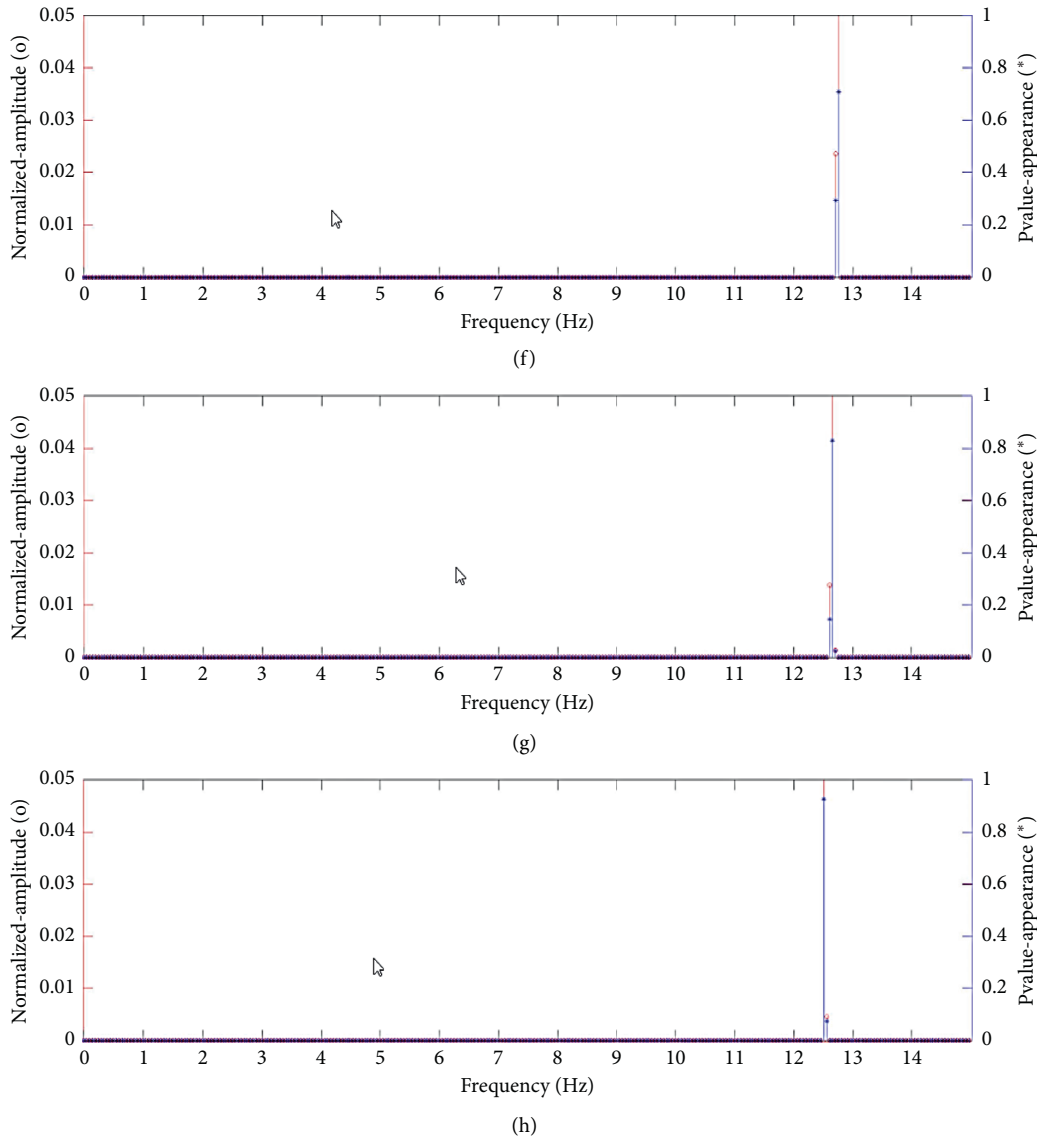
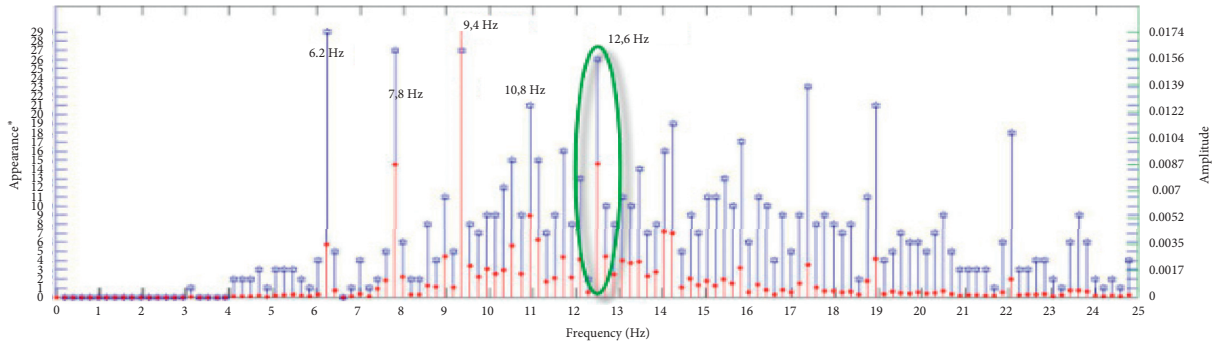


FIGURE 7: Natural frequencies of the free vibration beam corresponding to different levels of defects.

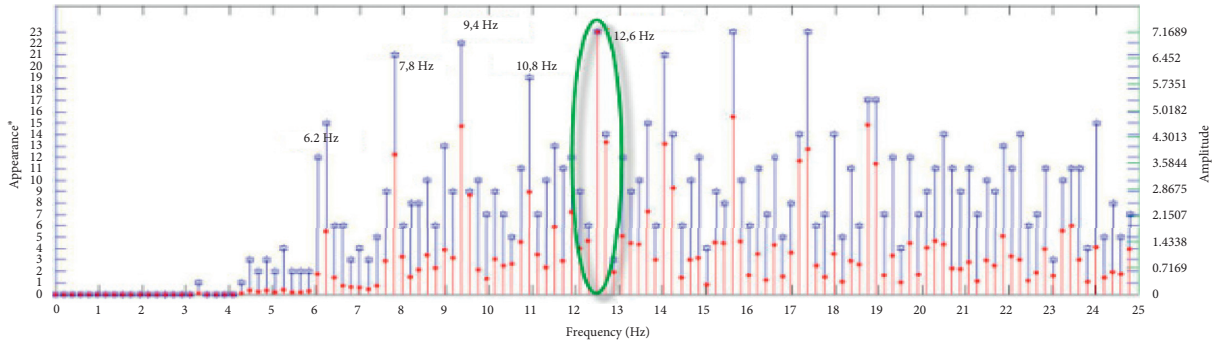
0.3 mm width wherein the first crack is 2.6 mm deep and the second crack is 0.8 mm deep.

Changes in the natural frequency value were too small (not exceeding 4%) during the experiment. They were not adequate for determining the existence of defects in the beam. Furthermore, under free vibration, not only one natural frequency but also others nearby on the spectrum appeared. These frequencies had almost identical values (with only a 0.05 Hz differential), and the amplitudes of different spectra corresponded to different levels of cracks. The natural frequency tended to continuously reduce together with the levels of cracks. However, this reduction was too small in comparison with the changes in the defects. From the intact level (beam with no crack) to the maximum level of defect (H26), the value of the frequency was reduced by no more than 0.5 Hz. Therefore, changes in natural frequency cannot evaluate, locate, or determine the level of defects in the beam.

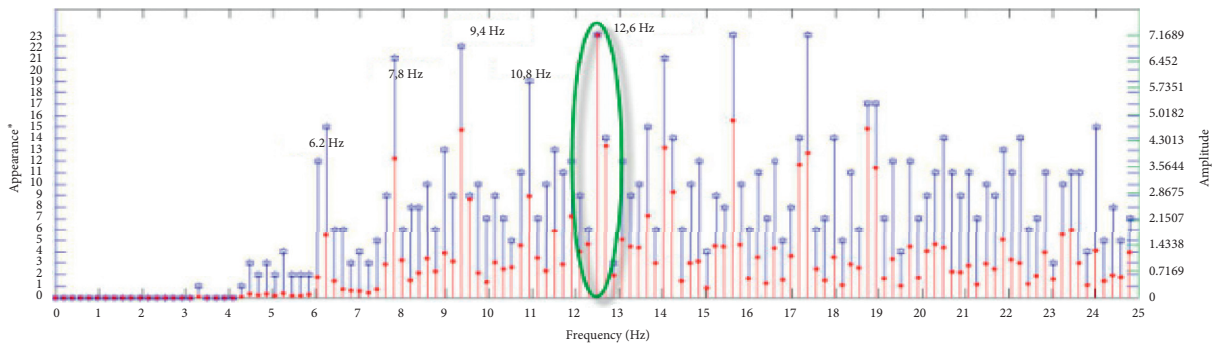
Figures 8(a)–8(h) show the frequency values of the power spectra under forced action when the vehicle model passes through the beam. These values correspond to the levels of defects (as shown in Table 2) at different velocities ($V_{50} = 18.84$ cm/s, $V_{60} = 25.12$ cm/s, $V_{70} = 28.26$ cm/s, $V_{80} = 31.4$ cm/s, $V_{90} = 35.3$ cm/s, and $V_{100} = 39.2$ cm/s). When the vehicle moved on the beam, together with a basic natural frequency (determined when the beam vibrates freely), there were more forced frequencies, such as $f_1 = 6.2$ Hz, $f_2 = 7.8$ Hz, $f_3 = 9.4$ Hz, and $f_4 = 10.8$ Hz, and higher frequencies beyond the natural frequency value. Corresponding to different levels of defects, the natural frequency remains nearly unchanged, which is similar to the free vibration of beams. This result accords with prior research [27, 28, 39, 40]. Most researchers conclude that changes in natural frequency are not sensitive enough to determine a partial breakdown of the test or actual beams. The problem is the accuracy of measurement equipment: it is



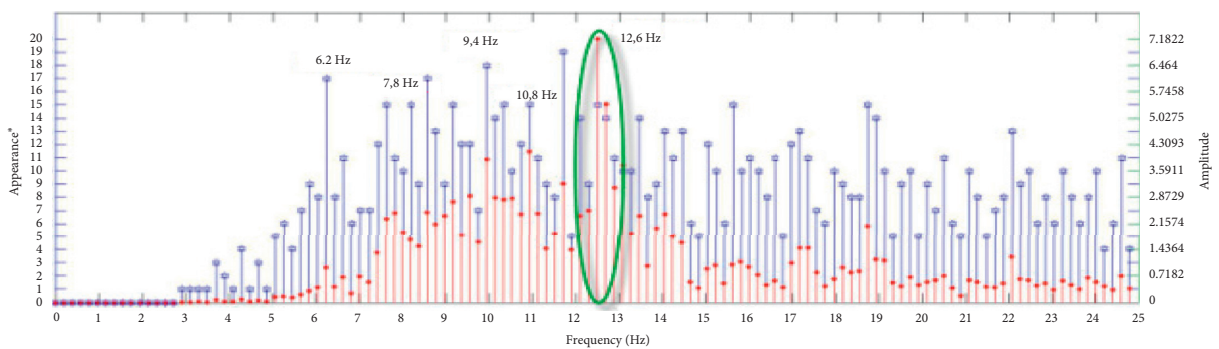
(a)



(b)



(c)



(d)

FIGURE 8: Continued.

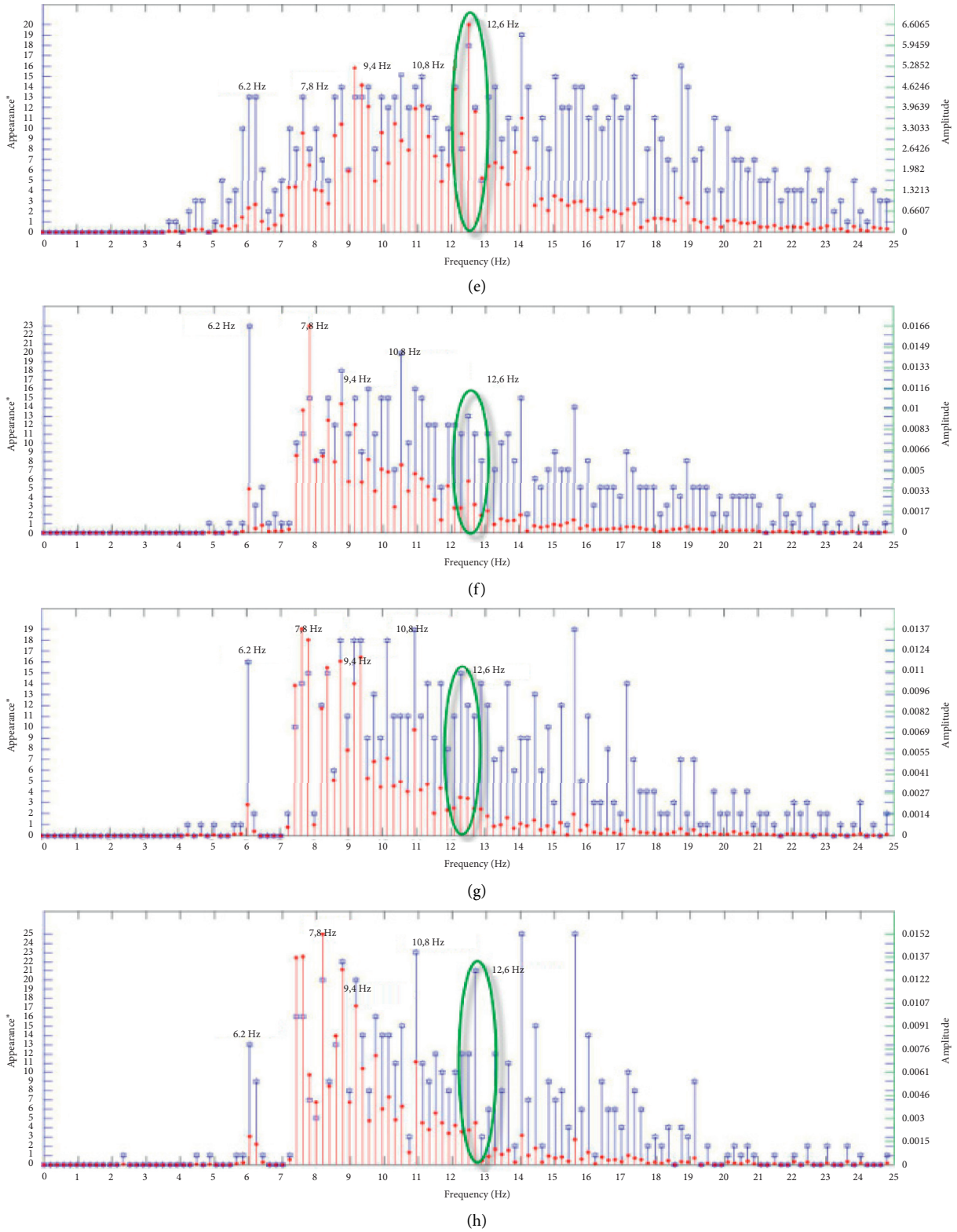


FIGURE 8: Natural frequencies of the beam under acting vehicular force corresponding to different levels of defect.

unable to spot these small differences. Furthermore, frequency is an overall quantity: it is not sensitive to partial changes. Thus, natural frequency does not provide enough information on structural changes.

4.2. Changes of Damping Coefficient. This research also studied changes in damping components at different levels of defects. In general, damping coefficients collected from vibrations of sensors always vary in a similar way. The results show that

- (i) From defect level H_0 to level H_{12} , the damping coefficient tended to increase and reached a maximum value of 0.3. This change was relatively larger and more distinct than natural frequency values, as shown in Figures 9–14. However, under different circumstances of defects, such as H_{16} , the value was reduced to 0.15, lower than that of the intact beam (with no defect). Further investigation showed that this coefficient increased slightly until level H_{26} , where the beam was entirely destroyed. Moreover, there was no difference in damping coefficients at each measurement point (sensor location) according to Table 3.
- (ii) The velocity of the experiment did not significantly affect the value of the damping. Figures 9–14 show the damping coefficient values at six different velocities corresponding to each level of defects.

In general, the change in the damping coefficient is insufficient and unstable. Therefore, we can hardly recognize the existence of defects, especially in beams suffering from major defects. In addition, the changes in the damping coefficients at four measurement points were relatively the same, which made it difficult to locate cracks in the beam. Although it performs better than natural frequency, the damping coefficient is still an impractical, low-sensitivity parameter. This conclusion is accepted in other studies [25, 26], in which the damping coefficient value is affected by the mechanical characteristics of the material. The structural changes in the experimental models only have impacts on small parts, not the whole beam structure.

4.3. Changes in Correlation Coefficient

4.3.1. Changes in Correlation Coefficient. Due to insufficient damping coefficients and natural frequencies, we propose to use correlation coefficients. Both Figure 15 and Table 2 show the relation between two measurements (Figure 4(a)) channels through correlation coefficients. The new proposed parameter has always shown a significant linear change corresponding to the increase in defect degree. According to Figure 15, when correlation coefficients decreased, the level of cracks was found to have increased. They decreased within the range of $[1, 0]$. If the correlation coefficient is equal to 1, there is perfect correlation. This usually happens to correlation coefficients of measurements at the same point (autocorrelation). On the contrary, when the correlation coefficient between two points is equal to 0, there is no

binding relation. In terms of energy distribution in beams, the reduction of correlation coefficients implies energy loss at each level of defects. The correlation coefficient is influenced by velocities during the experiment. This means that the velocity in the experimental model scatters the vibrating energy. It changes the fluctuating values of consecutive elements. As defined in the draft, the more the value of the velocity increased, the more the value of the correlation coefficient decreased. In the manuscript, we want to define the relationship between these two parameters (correlation coefficient value and experimental velocity). Hence, the existence of defects is the main reason for this loss. In each case, we have the following comments:

- (i) Figure 15 shows changes in correlation coefficients between channel 1 and the remaining channels. The value of channel 1 had significant changes compared with other channels (100%), from a non-defective level to defect level H_{26} . This change is the rule and remains steady throughout the extent of defects. It also surpasses the results of the damping coefficient and natural frequency values. This research will delve into the effective usage of this parameter at different levels of defects.
- (ii) Figures 16–18 show changes in correlation values in channel 2 compared with the remaining channels as well as in channel 3 with the remaining channels. The results indicate the symmetric characteristics of the two measurement channels throughout different levels. In other words, the distribution of measurement channels in the model can affect this value during evaluation. Therefore, this value is sensitive to the measurement channel and crucial for locating defects in the beam. Similar conclusions can be made upon investigating the correlation values of channels R_{1-4} (between channel 1 and channel 4) and channels R_{4-1} (between channel 4 and channel 1).
- (iii) When the velocity changed, the correlation coefficients sped up rapidly (Figures 15–18). This suggests that the relation between correlation coefficients and velocity corresponds linearly to each level of defects. The impact of velocity on this parameter increased the feasibility of detecting defects, as it can show the overall condition of a structure under acting force.

4.3.2. The Relation between Correlation Coefficients and Defects. Corresponding to different levels of defects, correlation coefficients are distributed in pairs as follows:

- (i) Regarding the value of correlation coefficients between two consecutive channels (R_{1-2} and R_{3-4}) without cracks, Figure 19 shows almost no connection with the levels of cracks in the beam. When the cracks were at the highest level (H_{26}) and V100 velocity, the changes in channel R_{1-2} were approximately 40% in comparison with the intact beam. The change was nearly 38% in channel R_{3-4} .

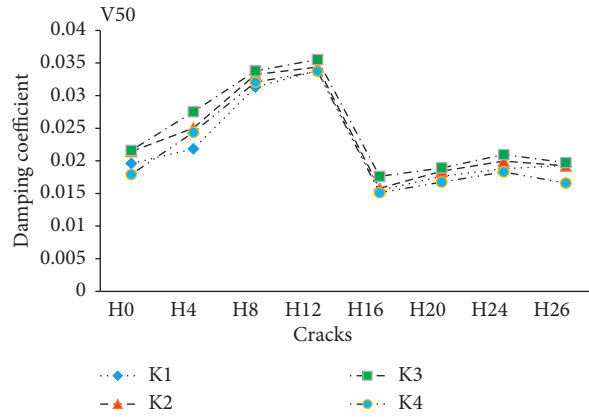


FIGURE 9: Damping coefficients under acting vehicular force (V50) corresponding to different levels of defects.

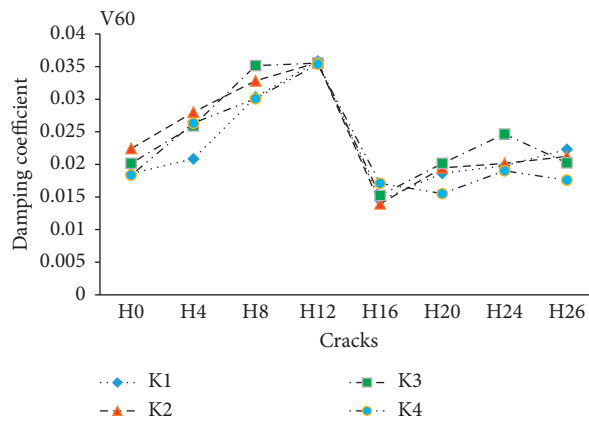


FIGURE 10: Damping coefficients under acting vehicular force (V60) corresponding to different levels of defects.

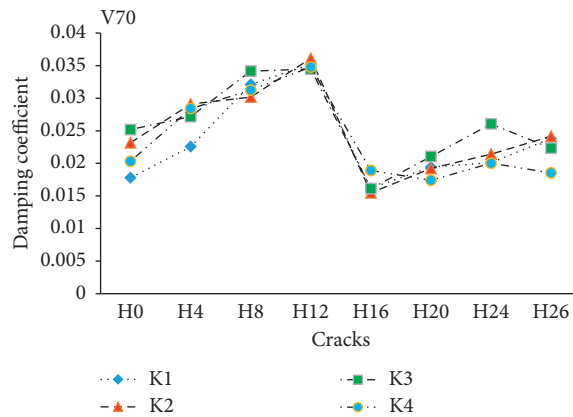


FIGURE 11: Damping coefficients under acting vehicular force (V70) corresponding to different levels of defects.

The distribution of the correlation coefficient rule in these similar channels is equivalent and relatively linear at each level of cracks. This is the standard input for evaluating the presence of cracks in beams.

(ii) Regarding the correlation coefficient values of two consecutive channels (R_{2-3}) with cracks (Figure 20), the correlation value changed quickly according to the increase in the cracks. This change was

significant (over 90%) between the intact beams after they reached the level (H_{26}) at V100 velocity. In the first (R_{1-2} and R_{3-4}) and second (R_{2-3}) circumstances with the same level of defects, the changes were sufficient for determining the location of the cracks in the beam.

(iii) Regarding the correlation coefficients of two channels that were far away from each other (R_{1-3}

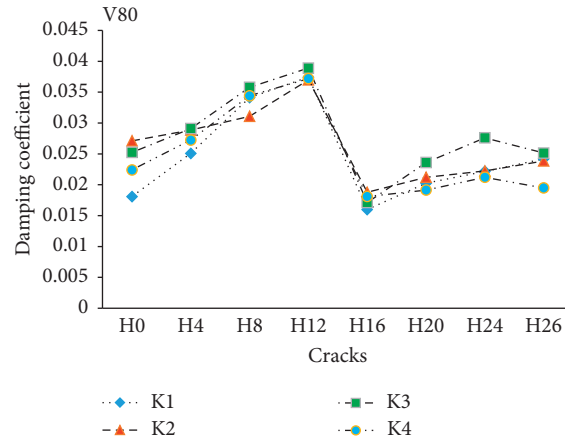


FIGURE 12: Damping coefficients under acting vehicular force (V80) corresponding to different levels of defects.

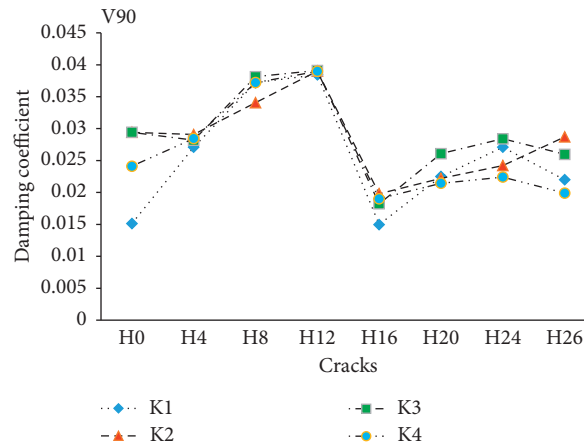


FIGURE 13: Damping coefficients under acting vehicular force (V90) corresponding to different levels of defects.

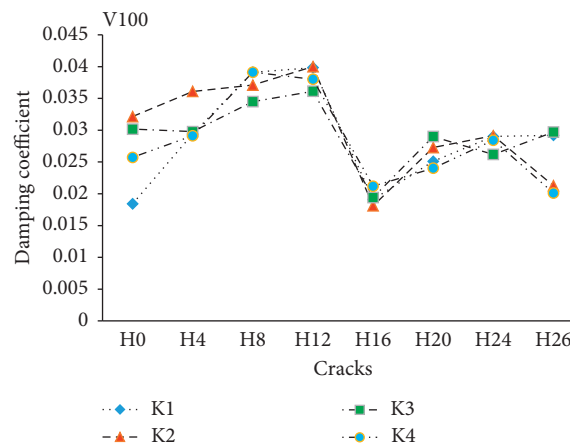


FIGURE 14: Damping coefficients under acting vehicular force (V100) corresponding to different levels of defects.

and R_{2-4}) (see Figure 21) with defects in between, their values among these channels were relatively different. Under forced vibration, the vibration energy was transmitted from channel 1 to channel 2,

passing through the defect and finally to channel 3. As analyzed above, the energy was partially lost during transmission from one point to another according to the direction of vibration. It

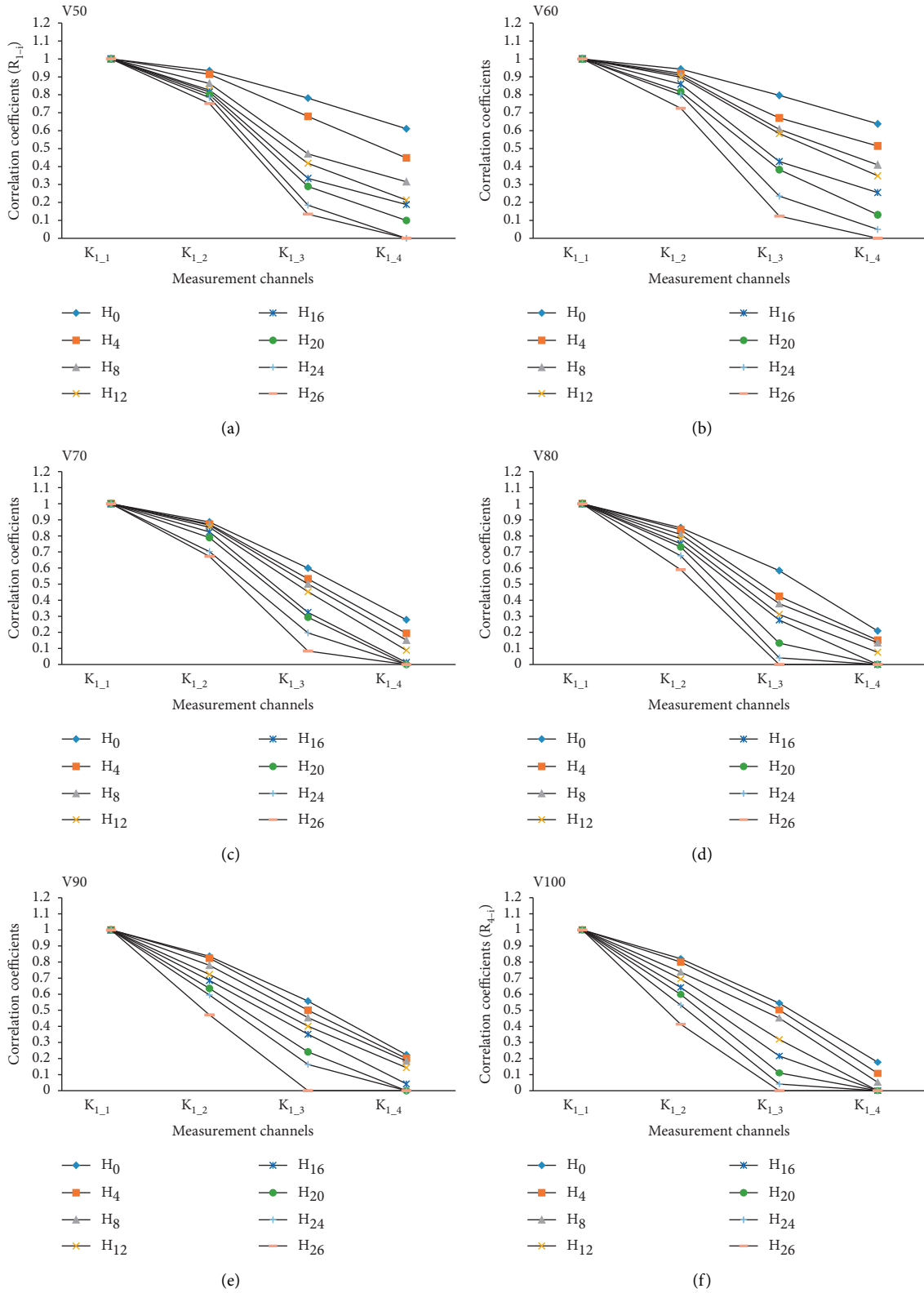


FIGURE 15: Changes of correlation coefficients R_{1-i} (between channel 1 and the remaining channels) corresponding to the levels of defects and different velocities.

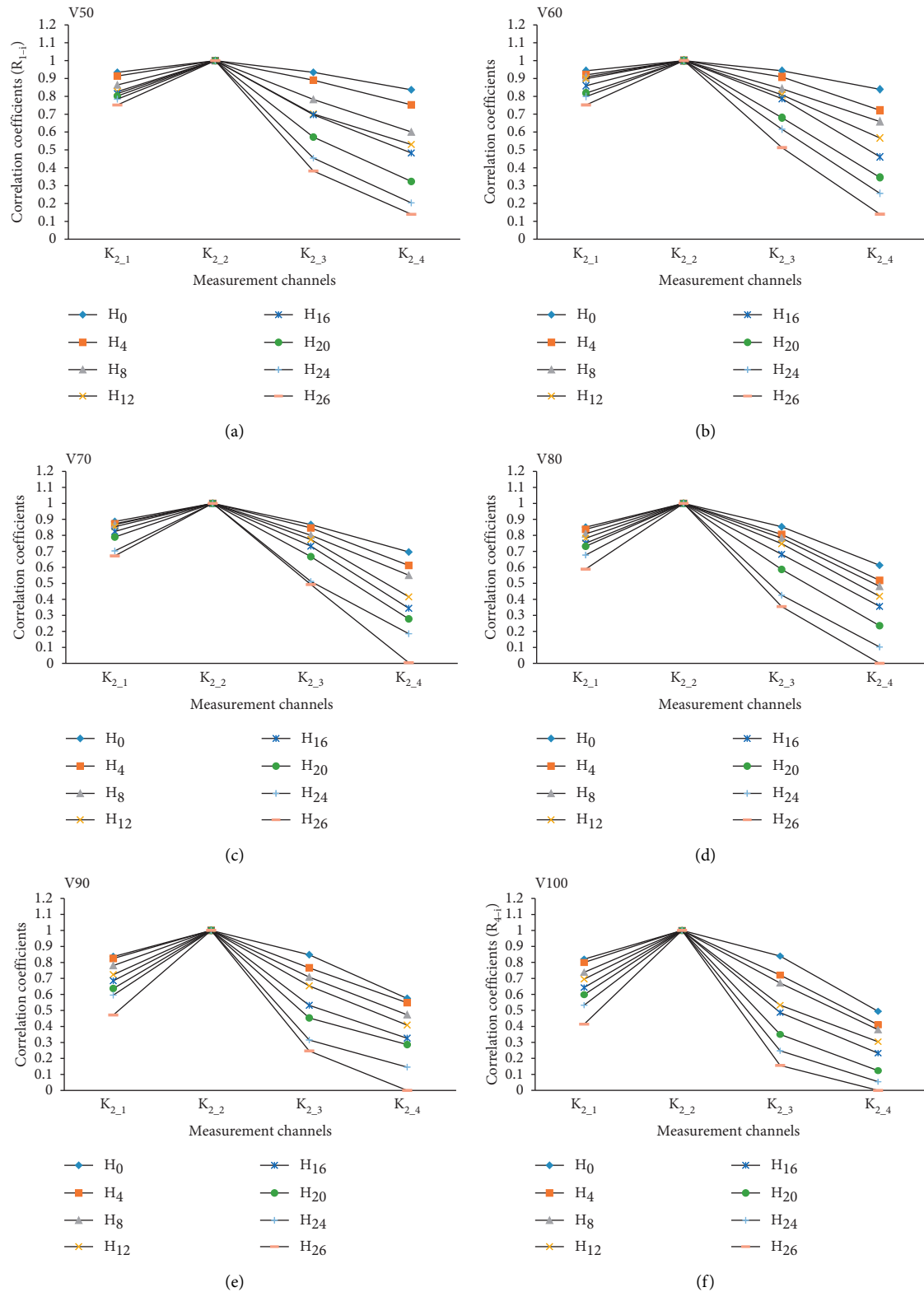


FIGURE 16: Changes of correlation coefficients R_{2-i} (between channel 2 and the remaining channels) corresponding to the levels of defects and different velocities.

experienced maximum loss when passing by the defect location. However, the correlation coefficients of ($R_{1,3}$) had lower energy loss because the

distance between channel 1 and the defect location was large. When it passed the defect location, the remaining energy was not large enough to result in

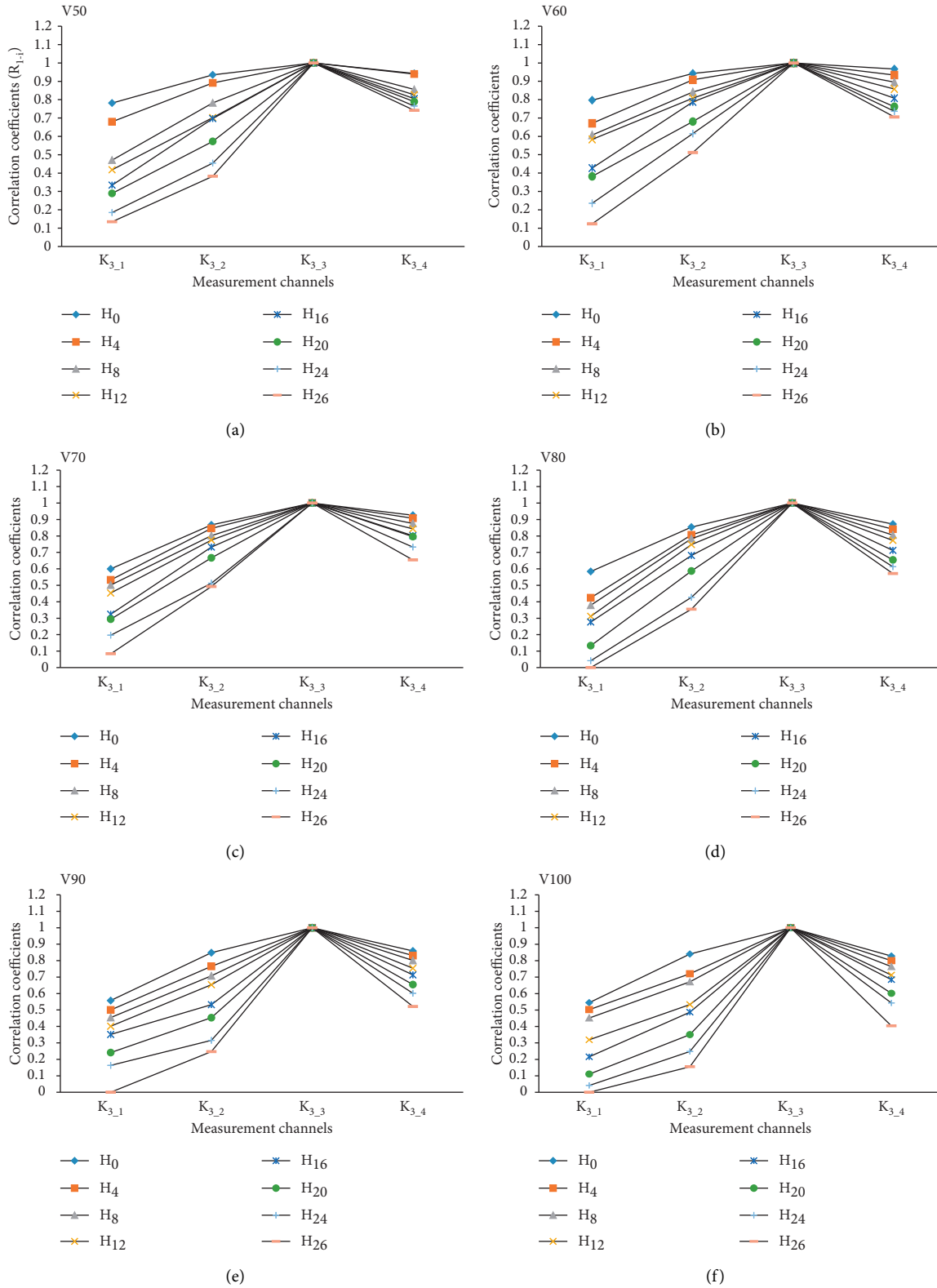


FIGURE 17: Changes of correlation coefficients R_{3-i} (between channel 3 and the remaining channels) corresponding to the levels of defects and different velocities.

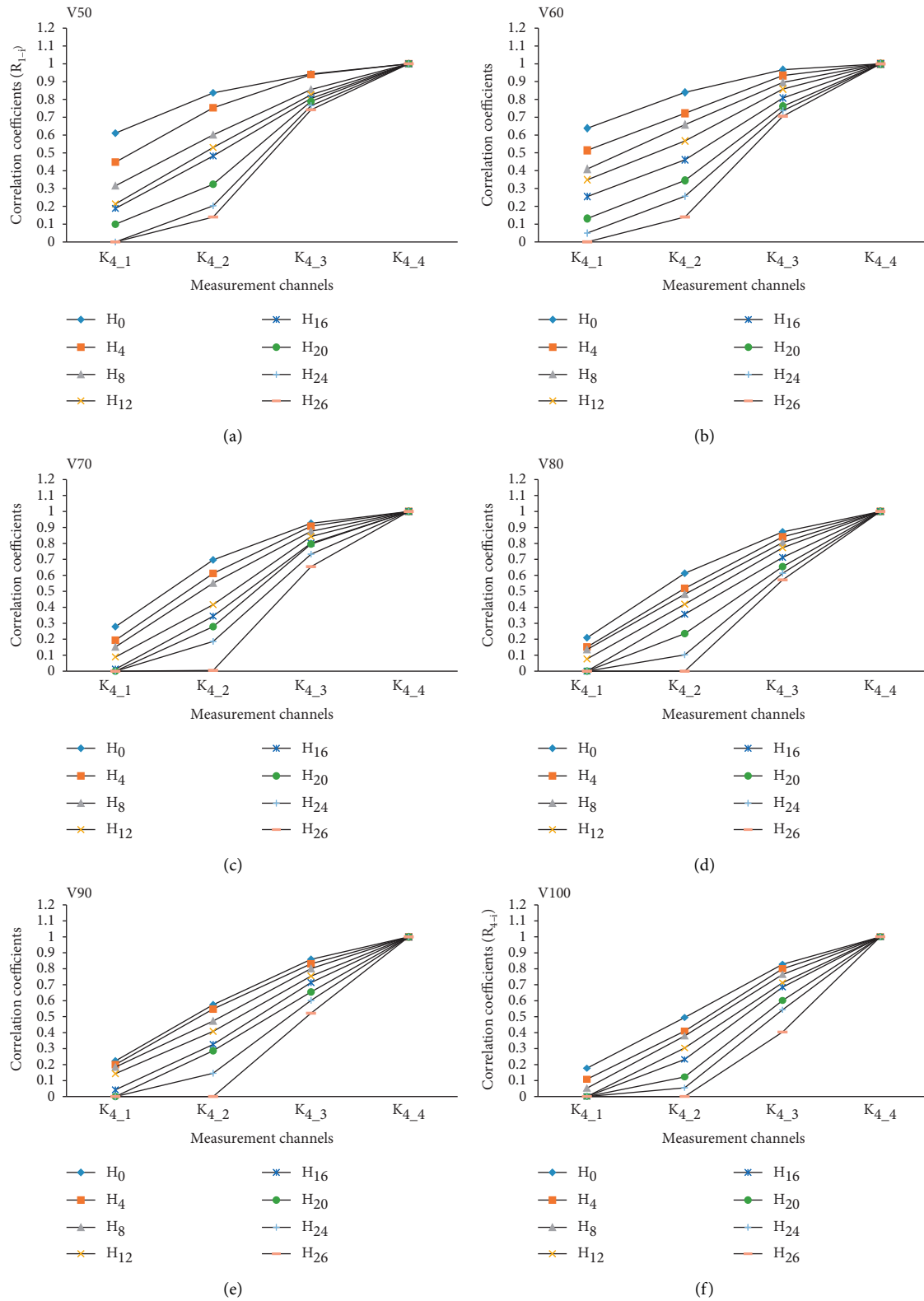


FIGURE 18: Changes of correlation coefficients R_{4-i} (between channel 4 and the remaining channels) corresponding to the levels of defects and different velocities.

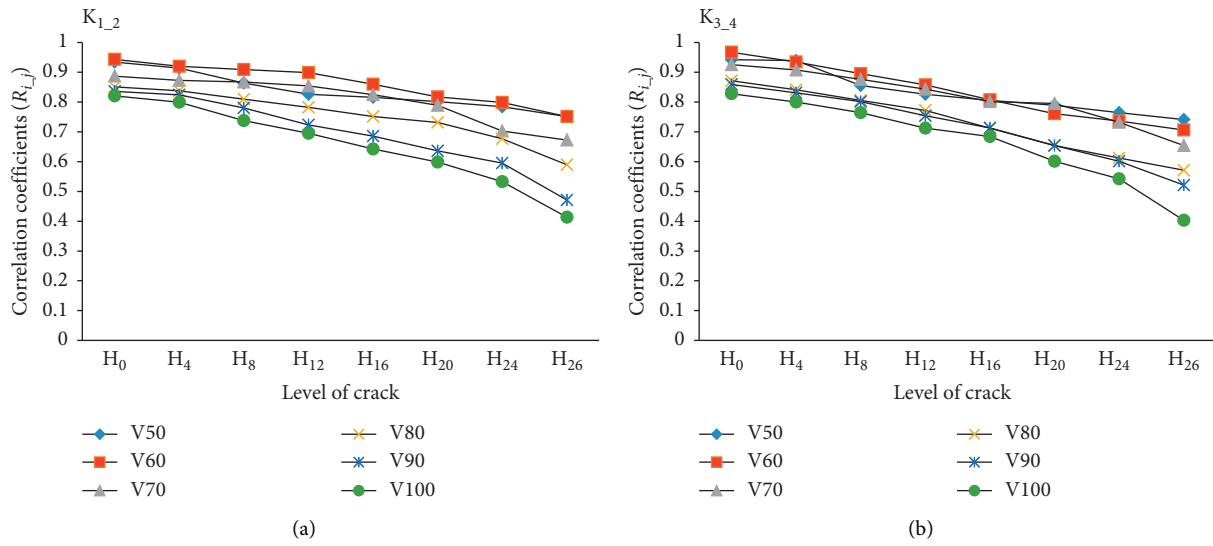


FIGURE 19: Relation between correlation coefficients of two consecutive channels ($R_{1,2}$ and $R_{3,4}$) without cracks and the levels of cracks.

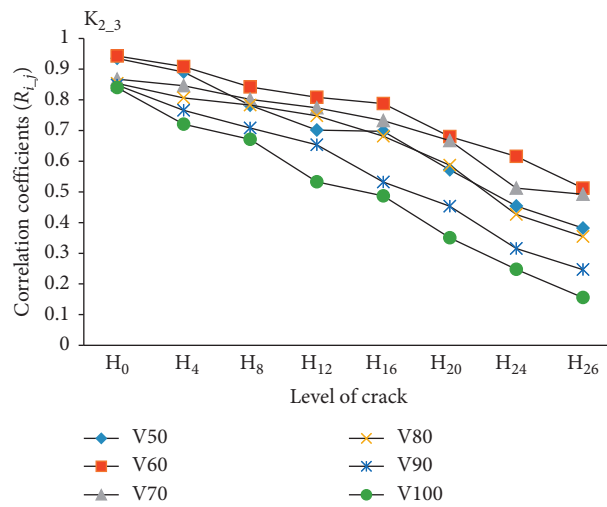


FIGURE 20: Relation between correlation coefficients of two consecutive channels ($R_{2,3}$) with cracks and the levels of cracks.

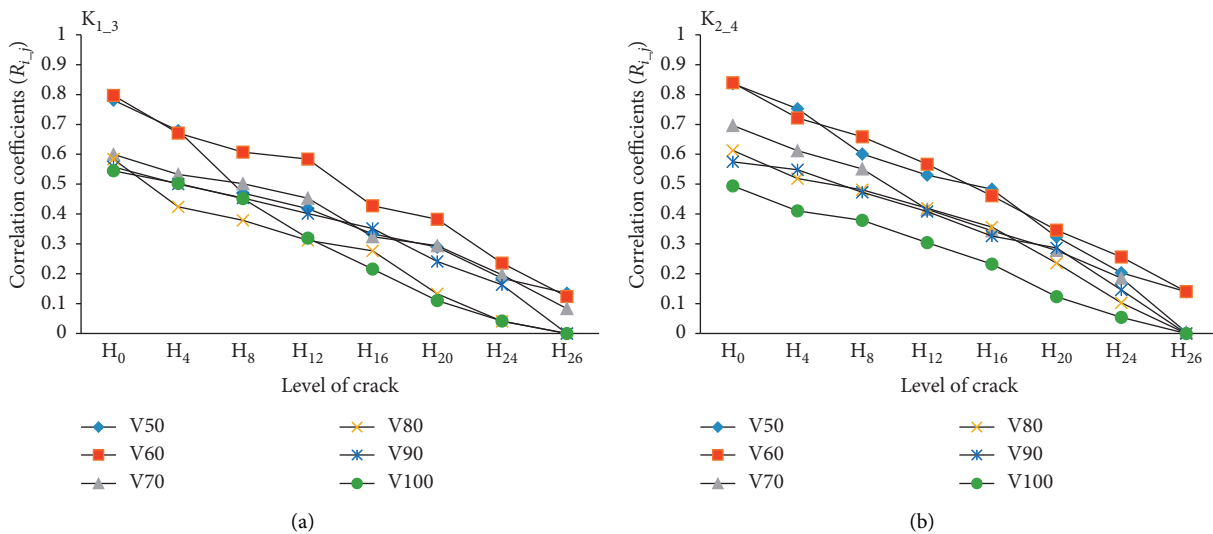


FIGURE 21: Relation between correlation coefficients of two channels ($R_{1,3}$ and $R_{2,4}$) with cracks and the levels of cracks.

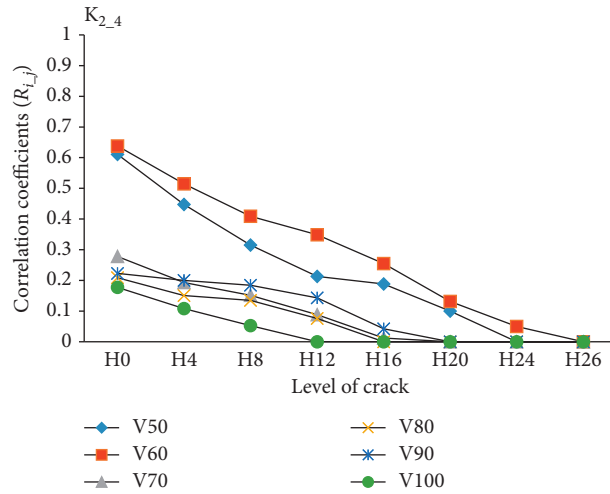


FIGURE 22: Relation between correlation coefficients of two channels (R_{1-4}) with cracks and the levels of cracks.

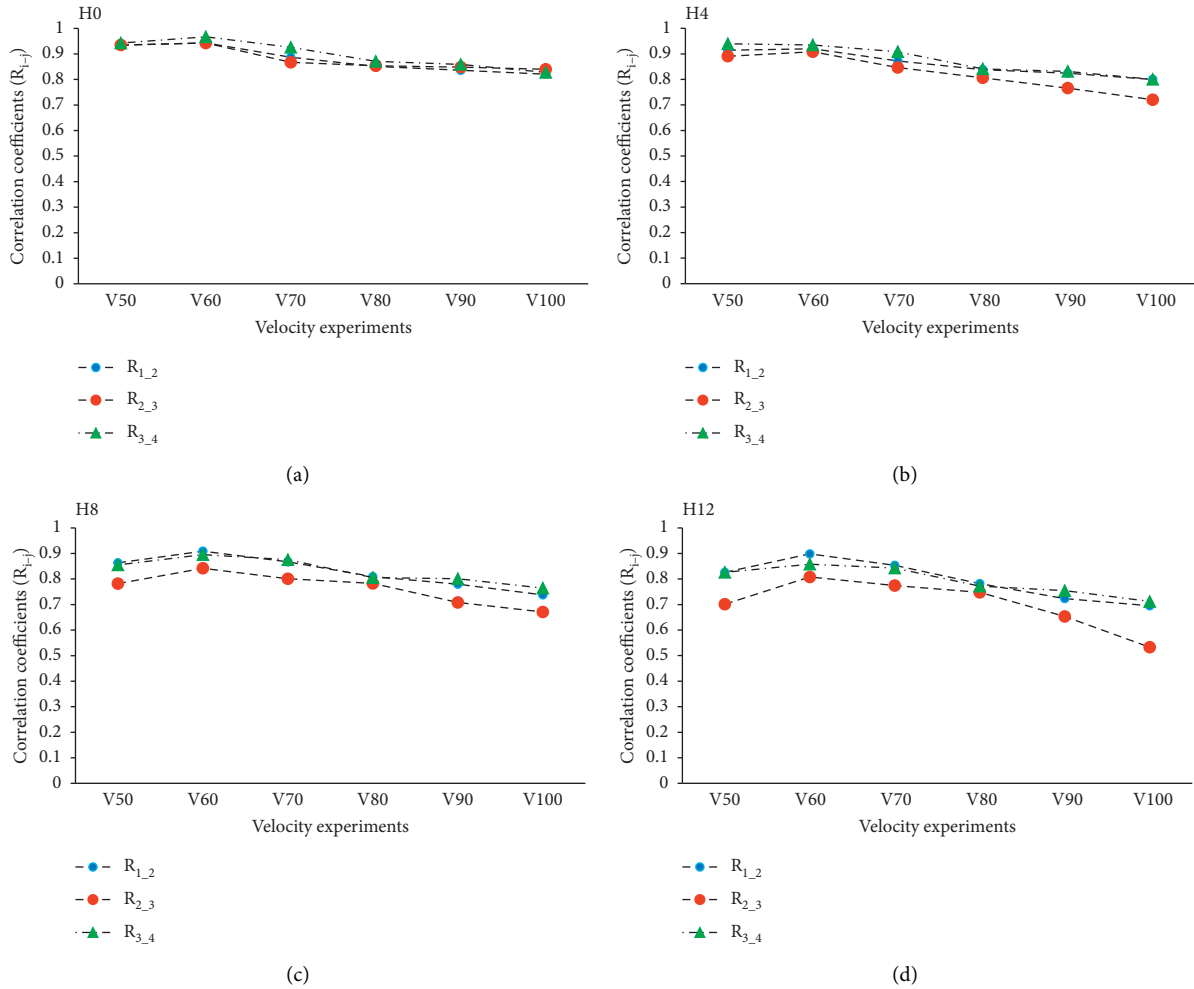


FIGURE 23: Continued.

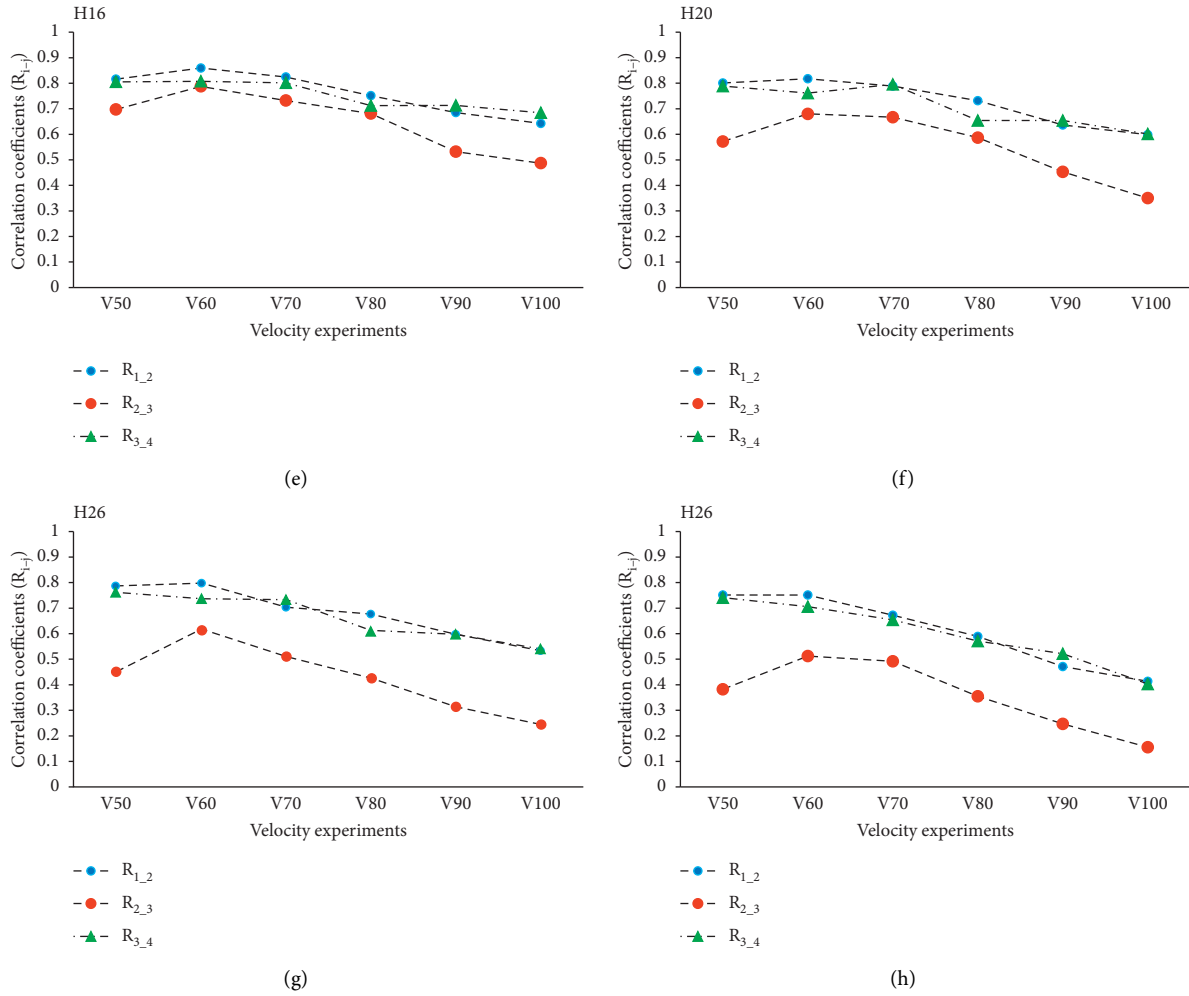


FIGURE 23: Relation between velocity and correlation coefficient values.

such a significant loss. Contrary to $(R_{1,3})$, the correlation value of $(R_{2,4})$ clearly increased at each level of defects. This meant that the distance between the measurement point of channel 2 and the defect location was shorter, causing more significant losses. We can immediately notice the impact of defects on the correlation coefficients.

Figure 22 shows the changes in the correlation coefficient values at different levels of defects in the beam. This is evidence that affirms the sensitivity of this parameter to defects. These changes, compared with the changes in natural frequency values and damping coefficients, are relatively large. Therefore, they support the application of this coefficient for detecting and evaluating defects in structures.

4.3.3. The Impact of Velocity on Correlation Coefficients and the Development of Defects. Velocity has a significant impact on changes in correlation coefficient values at different levels of defects in beams. In order to simplify the evaluation process, this study only investigated a case of two

consecutive channels with the presence of $(R_{2,3})$ or the absence of $(R_{1,2})$ and $(R_{3,4})$ defects. The results show that

- (i) For intact beams (beams without defects), as shown in Figure 23(a), or beams with some defects (H4, H8, H12), as in Figure 23(b), the impact of velocity was insignificant. The defect was not enough to reduce the correlation coefficients. The impact of velocity shows that the energy consumed when passing through the defect location is small.
- (ii) On the contrary, at the high scale of defects, the impact of velocity was more significant. Figures 23(e)–23(h) show that the higher the velocity, the more energy in the beam. However, the higher the levels of defects, the more energy is lost. Thus, there is a large difference in energy loss between intact beams and defective beams, which is an important point to evaluate in the study of defects in beams.

5. Conclusion

In this research, we proposed a new parameter—the correlation coefficient—to detect and evaluate defects in beams.

It is much more sensitive to defects than the natural frequency or the damping coefficient. This research has raised four prominent points:

- (i) The natural frequency values in the experimental model were not sensitive enough to detect defects in the beam. The changes in this value were too small compared to the development of defects. Therefore, natural frequency measurements hardly meet the requirements of detecting defects in structures.
- (ii) Although the damping coefficient had more variation than the natural frequency value in the same experiment, its changes were also insufficient and unstable at different levels of defects. Therefore, it is difficult to apply the damping coefficient method to detect the existence of defects, especially in beams suffering from major defects. In addition, changes in the damping coefficients at four measurement channels were relatively the same, so this characteristic makes it hard to locate cracks in the beam. Thus, the damping coefficient is still a low-sensitivity parameter that is difficult to apply.
- (iii) The new proposed parameter has a linear characteristic and always significantly changes according to increasing levels of defects. The results show that the measurability of the changes using this method outweighs those from damping coefficient and natural frequency values. Furthermore, this value is always sensitive to measurement channels, which could be an important factor in locating defects in beams.
- (iv) However, this research has limited value for investigating the relation between correlation coefficients and changes in beam stiffness due to cracks. Future research needs to be conducted to look into the quantitative evaluation of correlation coefficients to clarify that relation in the monitoring and identification of defects in structures.

Data Availability

All data generated or analysed during this study are included in this published article.

Conflicts of Interest

The authors declare that they have no conflicts of interest.

Acknowledgments

The authors wish to thank various people for their contribution towards this work. Mr. Lam Q. Tran and Mr. Vien N. Le contributed for technical support on this project. Prof. Nhi K. Ngo, staff of Applied Mechanics (LAM), Ho Chi Minh City University of Technology, contributed in collecting the plant data and all the technicians helped in handling the instruments. The authors would like to specially thank Prof. Nhi K. Ngo, research project supervisor,

for her professional guidance and valuable support and constructive recommendations on this project.

References

- [1] G. Bhardwaj, I. V. Singh, and B. K. Mishra, "Stochastic fatigue crack growth simulation of interfacial crack in bi-layered FGMs using XIGA," *Computer Methods in Applied Mechanics and Engineering*, vol. 284, pp. 186–229, 2015.
- [2] B. Kunin, "Stochastic model of brittle crack growth under cyclic load," *International Journal of Pure and Applied Mathematics*, vol. 84, no. 3, pp. 163–174, 2013.
- [3] X. Yan, "A boundary element modeling of fatigue crack growth in a plane elastic plate," *Mechanics Research Communications*, vol. 33, no. 4, pp. 470–481, 2006.
- [4] T. Belytschko and T. Black, "Elastic crack growth in finite elements with minimal remeshing," *International Journal for Numerical Methods in Engineering*, vol. 45, no. 5, pp. 601–620, 1999.
- [5] T. Rabczuk and T. Belytschko, "Cracking particles: a simplified meshfree method for arbitrary evolving cracks," *International Journal for Numerical Methods in Engineering*, vol. 61, no. 13, pp. 2316–2343, 2004.
- [6] T. Rabczuk and T. Belytschko, "A three dimensional large deformation meshfree method for arbitrary evolving cracks," *Computer Methods in Applied Mechanics and Engineering*, vol. 196, no. 29–30, pp. 2777–2799, 2007.
- [7] H. Yu, L. Wu, L. Guo, H. Wu, and S. Du, "An interaction integral method for 3D curved cracks in nonhomogeneous materials with complex interfaces," *International Journal of Solids and Structures*, vol. 47, no. 16, pp. 2178–2189, 2010.
- [8] T. N. Bittencourt, P. A. Wawrzynek, A. R. Ingraffea, and J. L. Sousa, "Quasi-automatic simulation of crack propagation for 2D LEFM problems," *Engineering Fracture Mechanics*, vol. 55, no. 2, pp. 321–334, 1996.
- [9] R. J. Price and J. Trevelyan, "Boundary element simulation of fatigue crack growth in multi-site damage," *Engineering Analysis with Boundary Elements*, vol. 43, pp. 67–75, 2014.
- [10] N. Moës, J. Dolbow, and T. Belytschko, "A finite element method for crack growth without re-meshing," *International Journal for Numerical Methods in Engineering*, vol. 46, no. 1, pp. 131–150, 1999.
- [11] K. Tanaka, "Fatigue crack propagation from a crack inclined to the cyclic tensile axis," *Engineering Fracture Mechanics*, vol. 6, no. 3, pp. 493–498, 1974.
- [12] Q. W. Zhang, "Statistical damage identification for bridges using ambient vibration data," *Computer and Structures*, vol. 85, no. 7–8, pp. 476–485, 2007.
- [13] Z. X. Li, T. H. T. Chan, and R. Zheng, "Statistical analysis of online strain response and its application in fatigue assessment of a long-span steel bridge," *Engineering Structures*, vol. 25, no. 14, pp. 1731–1741, 2003.
- [14] A. Miyamoto, K. Kawamura, and H. Nakamura, "Bridge management system and maintenance optimization for existing bridges," *Computer-Aided Civil and Infrastructure Engineering*, vol. 15, no. 1, pp. 45–55, 2000.
- [15] H. Furuta, J. He, and E. Watanabe, "A fuzzy expert system for damage assessment using genetic algorithms and neural networks," *Computer-Aided Civil and Infrastructure Engineering*, vol. 11, no. 1, pp. 37–45, 1996.
- [16] C. Mares and C. Surace, "An application of genetic algorithms to identify damage in elastic structures," *Journal of Sound and Vibration*, vol. 195, no. 2, pp. 195–215, 1996.
- [17] C.-B. Yun and E. Y. Bahng, "Substructural identification using neural networks," *Computers & Structures*, vol. 77, no. 1, pp. 41–52, 2000.

- [18] C. C. Chang, T. Y. P. Chang, Y. G. Xu, and M. L. Wang, "Structural damage detection using an iterative neural network," *Journal of Intelligent Material Systems and Structures*, vol. 11, no. 1, pp. 32–42, 2000.
- [19] C. S. Huang, S. L. Hung, C. M. Wen, and T. T. Tu, "A neural network approach for structural identification and diagnosis of a building from seismic response data," *Earthquake Engineering & Structural Dynamics*, vol. 32, no. 2, pp. 187–206, 2003.
- [20] X. Q. Zhu and S. S. Law, "Wavelet-based crack identification of bridge beam from operational deflection time history," *International Journal of Solids and Structures*, vol. 43, no. 7–8, pp. 2299–2317, 2006.
- [21] E. Douka, S. Loutridis, and A. Trochidis, "Crack identification in beams using wavelet analysis," *International Journal of Solids and Structures*, vol. 40, no. 13–14, pp. 3557–3569, 2003.
- [22] S. A. Ramu and V. T. Johnson, "Damage assessment of composite structures-A fuzzy logic integrated neural network approach," *Computers & Structures*, vol. 57, no. 3, pp. 491–502, 1995.
- [23] S. W. Doebling, C. R. Farrar, and M. B. Prime, "A summary review of vibration-based damage identification methods," *The Shock and Vibration Digest*, vol. 30, no. 2, pp. 91–105, 1998.
- [24] S. W. Doebling, C. Farrar, M. B. Prime, and D. W. Shevitz, *Damage Identification and Health Monitoring of Structural and Mechanical Systems from Changes in Their Vibration Characteristics: A Literature Review*, Los Alamos National Laboratory, Los Alamos, New Mexico, 1996.
- [25] A. Furukawa, H. Otsuka, and J. Kiyono, "Structural damage detection method using uncertain frequency response functions," *Computer-Aided Civil and Infrastructure Engineering*, vol. 21, no. 4, pp. 292–305, 2006.
- [26] P. Cawley and R. D. Adams, "The location of defects in structures from measurements of natural frequencies," *The Journal of Strain Analysis for Engineering Design*, vol. 14, no. 2, pp. 49–57, 1979.
- [27] N. T. Khiem and L. K. Toan, "A novel method for crack detection in beam-like structures by measurements of natural frequencies," *Journal of Sound and Vibration*, vol. 333, no. 18, pp. 4084–4103, 2014.
- [28] O. S. Salawu, "Assessment of bridges: use of dynamic testing," *Canadian Journal of Civil Engineering*, vol. 24, no. 2, pp. 218–228, 1997.
- [29] A. Shahdin, J. Morlier, and Y. Gourinat, "Damage monitoring in sandwich beams by modal parameter shifts: a comparative study of burst random and sine dwell vibration testing," *Journal of Sound and Vibration*, vol. 329, no. 5, pp. 566–584, 2010.
- [30] J. C. Dodds Loland, "Experiment in developing and operating integrity," in *Experiment in Developing and Operating Integrity*, pp. 313–319, 1976.
- [31] C. H. J. Fox, "The location of defects in structure: a compare of the use of natural frequency and mode shape data," in *Proceedings of the 10th International Modal Analysis*, pp. 522–528, San Diego, California, 1992.
- [32] U. Meneghetti and A. Maggiore, "Crack detection by sensitivity analysis," in *Proceedings of the 12th International Modal Analysis Conference*, pp. 1292–1298, Honolulu, HI, USA, January 1994.
- [33] F. K. Choy, R. Liang, and P. Xu, "Fault identification of beams on elastic foundation," *Computers and Geotechnics*, vol. 17, no. 2, pp. 157–176, 1995.
- [34] T. Q. Nguyen, T. T. D. Nguyen, H. Nguyen-Xuan, and N. K. Ngo, "A correlation coefficient approach for evaluation of stiffness degradation of beams under moving load," *Computers, Materials and Continua*, vol. 61, no. 1, pp. 27–53, 2019.
- [35] T. Q. Nguyen, L. Q. Tran, H. Nguyen-Xuan, and N. K. Ngo, "A statistical approach for evaluating crack defects in structures under dynamic responses," *Nondestructive Testing and Evaluation*, p. 1, 2019.
- [36] T. Q. Nguyen, H. C. Doan, L. C. Vuong, H. Nguyen-Xuan, and N. K. Ngo, "Fretting fatigue damage nucleation and propagation lifetime using a central point movement of power spectral density," *Shock and Vibration*, vol. 2020, no. 4, 16 pages, Article ID 4985134, 2020.
- [37] Z. Yang, Z. Yu, and H. Sun, "On the cross correlation function amplitude vector and its application to structural damage detection," *Mechanical Systems and Signal Processing*, vol. 21, no. 7, pp. 2918–2932, 2007.
- [38] F. Asma, "Damage detection by updating using correlation functions," *Mechanical Engineering*, vol. 73, no. 1, pp. 31–42, 2011.
- [39] N. T. Khiem and T. V. Lien, "A simplified method for natural frequency analysis of a multiple cracked beam," *Journal of Sound and Vibration*, vol. 245, no. 4, pp. 737–751, 2001.
- [40] N. T. Khiem and D. D. Khang, "Structural damage detection by measurements of vibration characteristics," in *Proceedings of the International Operational Model Ananysis Conference*, pp. 789–801, Portonovo, Italy, May 2009.

Research Article

Vibrations of Plates with Complex Shape: Experimental Modal Analysis, Finite Element Method, and *R*-Functions Method

Antonio Zippo ^{1,2} Giovanni Iarriccio ^{1,2} Francesco Pellicano ^{1,2}
and Tetyana Shmatko ³

¹Department of Engineering “Enzo Ferrari”, University of Modena and Reggio Emilia, Via P. Vivarelli 10, Modena 41124, Italy

²Centre InterMech MoRe, University of Modena and Reggio Emilia, V. P. Vivarelli, 2, Modena 41124, Italy

³Department of Higher Mathematics, National Technical University “KhPI”, 2 Kyrpychova Str., Kharkov 61002, Ukraine

Correspondence should be addressed to Antonio Zippo; antonio.zippo@unimore.it

Received 14 August 2020; Revised 5 October 2020; Accepted 9 October 2020; Published 3 December 2020

Academic Editor: Jorge P. Arenas

Copyright © 2020 Antonio Zippo et al. This is an open access article distributed under the Creative Commons Attribution License, which permits unrestricted use, distribution, and reproduction in any medium, provided the original work is properly cited.

In this paper, the dynamic behavior of 3D-printed plates with different shapes and boundary conditions is investigated. The natural frequencies and mode shapes were determined using three different methods: the experimental analysis, the finite element method, using Nastran, and the *R*-functions method. The experimental and theoretical results are compared. The specimens tested included four cases. The test procedure is deeply described, and the material properties of the plates are given. The fixed-fixed configuration shows a better agreement both in the rectangular plate and in the plate with rectangular cuts, and the *R*-functions method gives better convergence with respect to the experimental and finite element analysis. The simply supported arrangement indicates some uncertainty in the boundary realization of the specimen.

1. Introduction

Today, composite and innovative materials are distributed very intensively through many industries, using even more polymeric and plastic materials that are becoming increasingly popular and are gaining more and more technical concern. They find applications in aerospace, automobile, medicine, sport, optoelectronics, and so on. Often, designing elements are plates and shallow shells. One of the main problems arising at the investigation of the structural elements is their dynamic behavior. Therefore, application of a new modern technology or practical and theoretical investigation of linear and nonlinear vibrations of composite plates and shallow shells with a complex form, various boundary conditions, and different properties of materials is a very actual problem. To model properly, the structural response of a system is needed to take into account several aspects of the environmental condition that can drastically affect the results. Theoretical and experimental aspects of nonlinear vibration and stability of shells and plates are explained in [1], where the author

investigates, in a comprehensive and detailed approach, several traits of shells and plates from the design of traditional and advanced materials to fluid-structure interaction problems of shells.

In [2], the effect of the temperature has been studied on a thin circular cylindrical shell made of polyethylene terephthalate (PET) showing that temperature variations highlight the complex dynamics of the shell, as in [3], where the thermal gradient was applied. In [4], the role of the boundary conditions is highlighted by the authors that provided in a nonideal realization of the fixed-fixed joint, a possible reason for the difference between the experimental data and the modelling. Moreover, the outcome of the different boundary conditions has a lead role in annular sector plates as shown by Shi et al. [5], and in a recent work, Joubaneh et al. [6] studied the effect of various boundary conditions both analytically and experimentally.

In recent years, the use of innovative methods and technologies such as additive manufacturing and 3D printers is becoming increasingly popular both in the design phase and in the production phase. The use of these technologies

allows on the one side the possibility to create prototypes or components faster and on the other to give the designer greater freedom in the use of shapes and profiles that cannot be achieved with traditional production methods. This freedom, however, translates into more complex structures with boundary conditions that are often difficult to define in the creation of models that can correctly describe their dynamic behavior. For this reason, it is necessary to have available, reliable, and versatile methods that allow to simulate the behavior of composite structures with complex shapes and boundary conditions.

The study of structural dynamics is essential to understand and evaluate the performances of any engineering product. The experimental modal analysis of the data obtained from the structural tests provides us with a definitive description of the response of a structure, which can be assessed based on the project specifications. Moreover, it is not always possible to perform experimental analysis during the design process due to budget limitations or uncertainty of technical specification; certain cases having available methods, experimentally validated, that allow to forecast the behavior of the structures under investigation and predict how the structure will behave under different operating conditions could speed up the design and development process.

One of the effective methods for realization of this problem is the R -functions theory. It is used as a numerical and analytical method for calculation of mode shapes and natural frequencies of the plates and shallow shells of a complex form with various boundary conditions. The main feature of the R -functions theory is that it can present the solution in an analytical form for developing nonlinear models, what differs it essentially from other methods [7–9]. This theory has a well-known abbreviation RFM (R -functions method). Earlier, this method was applied in the papers [10–13]. Now, RFM is useful for verification of experimental data obtained by 3D printer application.

1.1. Application of the R-Functions Theory to Solution of Boundary Value Problems. The R -functions theory combined with the Ritz method (RFM) is an effective approach for the investigation of vibration characteristics of elastic structures having a complex geometry. The goal of this paper is to prove the efficiency and accuracy of the R -functions method of the solution of the boundary value problem by comparing with experimental data and other numerical methods in a particular case with FEM.

Let us consider a composite plate. To construct the mathematical model of the plate under experimental investigation, we use a classical plate theory based on the hypothesis Kirchhoff–Love. In the framework of this theory, the motion equation is the following:

$$M_{11,xx} + M_{12,xy} + M_{22,yy} = \rho h w_{,tt}, \quad (1)$$

where ρ and h are the density and thickness of the plate relatively.

M_{11} , M_{22} , and M_{12} are the stress resultants:

$$\vec{M} = \begin{pmatrix} M_{11} \\ M_{22} \\ M_{12} \end{pmatrix} = \begin{pmatrix} D_{11} & D_{12} & D_{16} \\ D_{12} & D_{22} & D_{26} \\ D_{16} & D_{26} & D_{66} \end{pmatrix} \begin{pmatrix} -w_{,xx} \\ -w_{,yy} \\ -2w_{,xy} \end{pmatrix}. \quad (2)$$

For isotropic plates, the elements of matrix (2) have the following form:

$$\vec{M} = \begin{pmatrix} M_{11} \\ M_{22} \\ M_{12} \end{pmatrix} = \frac{Eh^3}{12(1-\nu^2)} \begin{pmatrix} 1 & \nu & 0 \\ \nu & 1 & 0 \\ 0 & 0 & \frac{1-\nu}{2} \end{pmatrix} \begin{pmatrix} -w_{,xx} \\ -w_{,yy} \\ -2w_{,xy} \end{pmatrix}. \quad (3)$$

Motion equation is supplemented by corresponding boundary conditions. For the thin plates, two boundary conditions are set. Type of the boundary condition is determined by the fixing way of a plate edge. The boundary conditions for the most frequent ways of fixing for the curvilinear contour of the plate are as follows:

(i) Clamped edge:

$$\begin{aligned} w &= 0, \\ \frac{\partial w}{\partial n} &= 0, \end{aligned} \quad (4)$$

where n is an external normal to the boundary $\partial\Omega$ of the domain Ω of the plate.

(ii) Simply supported edge:

$$\begin{aligned} w &= 0, \\ M_n &= 0, \end{aligned} \quad (5)$$

where

$$M_n = M_1 \cos^2 \alpha + M_2 \sin^2 \alpha + 2M_{12} \cos \alpha \sin \alpha, \quad (6)$$

$\alpha = (n, Ox)$ is an angle between normal n and the Ox axis.

(iii) Free edge:

$$\begin{aligned} M_n &= 0, \\ Q_n - \frac{\partial M_{nr}}{\partial S} &= 0, \end{aligned} \quad (7)$$

where

$$\begin{aligned} M_{nr} &= (M_2 - M_1) \cos \alpha \sin \alpha + M_{12} (\cos^2 \alpha - \sin^2 \alpha), \\ Q_n &= Q_1 \cos \alpha + Q_2 \sin \alpha. \end{aligned} \quad (8)$$

According to the Ritz method solution of the motion, equation (1) is reduced to find the minimum of the following functional equation:

$$I = U - V, \quad (9)$$

that is, to the solution of the variational equation:

$$\delta(U - V) = 0, \quad (10)$$

where U and V are the potential and kinetic energy of a plate relatively. They have the following type for isotropic plates:

$$U(w) = \frac{1}{2} \iint_{\Omega} \left((\Delta w)^2 + 2(1 - \nu) \left((w_{,xy})^2 - w_{,xx} w_{,yy} \right) \right) d\Omega, \quad (11)$$

$$V(w) = \frac{\rho h \Omega_L^2}{2} \iint_{\Omega} w^2 d\Omega, \quad (12)$$

where ρ is a curvature radius of the edge curve and ν is Poisson's ratio.

By Ritz's approach, the function w is presented in the following type:

$$w = \sum_{k=1}^N c_k w_k, \quad (13)$$

where functions w_k are the admissible functions satisfying given boundary conditions and c_k , $k = \overline{1, N}$, are unknown constants that can be found from the following condition:

$$\frac{\partial}{\partial c_k} (U - \Omega_L^2 V) = 0. \quad (14)$$

For the case of plates and shallow shells of complex shape, the difficulties are usually connected with the construction of an admissible functions system. These functions should be linearly independent and differentiable, generate the complete system, and satisfy at least the geometrical boundary conditions. Applying the R -functions theory, we can construct the sequence of the admissible functions for an arbitrary shape and different boundary conditions. At first, the corresponding solution structure should be built. Solution structure is defined as [14] the following expression:

$$W = B(\Phi_1, \Phi_2, \dots, \Phi_k, \omega, \omega_i). \quad (15)$$

Here, $W(x, y)$ is a displacement; B is an operator depending on the system and its boundary conditions; Φ_k , $k = \overline{1, m}$, are the indefinite components that are expanded into truncated series along some full system of functions $\{\varphi_i(x, y)\}$. For a complete system of functions

$\varphi_i(x, y)$, power polynomials, Chebyshev's polynomials, trigonometric polynomials, splines, and others can be used. Functions $\omega(x, y) = 0$ and $\omega_i(x, y) = 0$ describe an equation of the domain boundary and some parts of the domain boundary. These functions are constructed by the R -functions theory and presented in analytical form.

The function $\omega(x, y)$ satisfies the following conditions:

$$\begin{aligned} \omega(x, y) &> 0, \quad \forall (x, y) \in \Omega, \\ \omega(x, y) &< 0, \quad \forall (x, y) \notin \Omega, \\ \omega(x, y) &= 0, \quad \forall (x, y) \in \partial\Omega, \end{aligned} \quad (16)$$

$$\frac{\partial \omega(x, y)}{\partial n} = -1, \quad \forall (x, y) \in \partial\Omega.$$

Functions satisfying condition (16) are constructed using the main system of the R -functions R_0 :

$$\begin{aligned} f_1 \wedge_{\alpha} f_2 &\equiv \frac{1}{1 + \alpha} \left(f_1 + f_2 - \sqrt{f_1^2 + f_2^2 - 2\alpha f_1 f_2} \right), \\ f_1 \vee_{\alpha} f_2 &\equiv \frac{1}{1 + \alpha} \left(f_1 + f_2 + \sqrt{f_1^2 + f_2^2 - 2\alpha f_1 f_2} \right), \\ \bar{f} &= -f. \end{aligned} \quad (17)$$

In practice, usually, the value $-1 < \alpha(x_1, x_2) \leq 1$ is assumed to be zero, and the main system R_0 takes the more simple form ($\alpha \equiv 0$):

$$\begin{aligned} \bar{f} &\equiv -f, \\ f_1 \wedge_0 f_2 &\equiv f_1 + f_2 - \sqrt{f_1^2 + f_2^2}, \\ f_1 \vee_0 f_2 &\equiv f_1 + f_2 + \sqrt{f_1^2 + f_2^2}, \end{aligned} \quad (18)$$

where functions $f_1(x, y) \geq 0$ and $f_2(x, y) \geq 0$ define domains Ω_1 and Ω_2 . Note that formulas (17) and (18) define a region Ω that is the intersection, union of the regions Ω_1 and outside of the region Ω .

Let us present solution structures for boundary conditions (4), (5), and (7) which satisfy all boundary conditions [15].

(i) Clamped edge:

$$w = \omega^2 \Phi_1. \quad (19)$$

(ii) Simply supported edge:

$$w = \omega \Phi_1 - \frac{1}{2} \omega^2 \left(\Phi_1 - \left(D_2 \omega - \frac{\nu}{\rho_c} \right) + 2D_1 \Phi_1 \right). \quad (20)$$

(iii) Free edge:

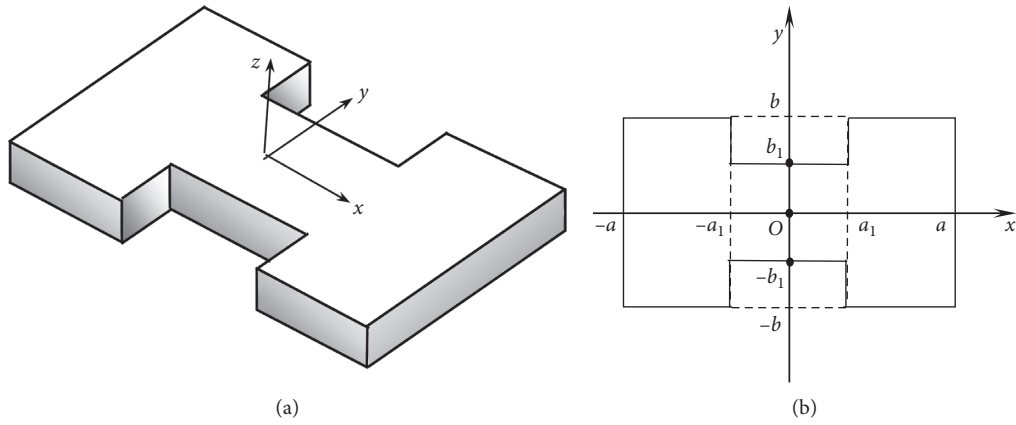


FIGURE 1: Planform of the composite plate with rectangular cuts.



FIGURE 2: 3D printer, Delta Wasp 2040 Turbo 2.

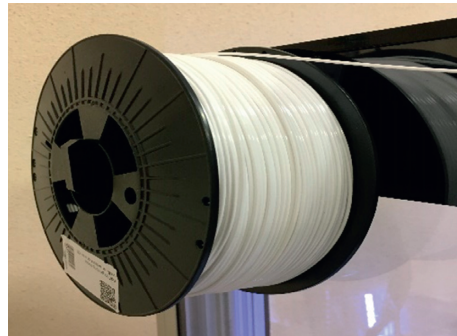


FIGURE 3: Detail of the printer: wire of PETG used for the 3D printing process.

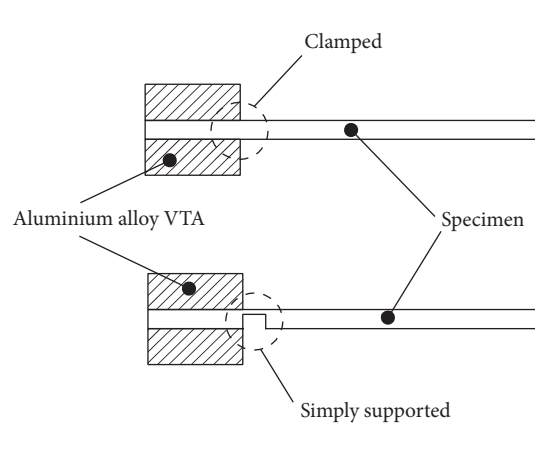


FIGURE 4: Drawing of clamped and simply supported BC.

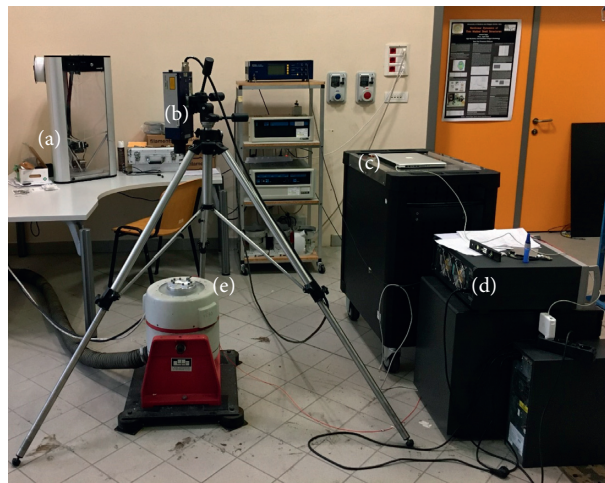


FIGURE 5: Picture of the experimental setup: (a) 3D printer, (b) laser vibrometer, (c) computer, (d) SCANDAS III, and (e) electrodynamic shaker.

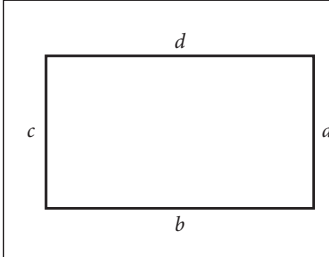
TABLE 1: Test cases.

Case	Shape description	Boundary conditions
1	Rectangular	2 opposite sides clamped; 2 sides free
2	Rectangular	All sides clamped
3	Rectangular	All sides simply supported
4	Rectangular with rectangular cut	2 opposite sides clamped, other sides free

TABLE 2: Material properties used for FEM and RFM simulation.

Feature	G PET
Mass density	1.20 g/cm ³
Yield strength	50 MPa
Ultimate tensile strength	26 MPa
Young's modulus	1.6 GPa
Poisson's ratio	0.417 su
Shear modulus	0.564573 GPa

TABLE 3: Geometrical properties and boundary conditions (Case 1).

		Size	
		$a = c = 37.60 \text{ mm}$ $b = d = 74.70 \text{ mm}$ $h \text{ (thickness)} = 0.90 \text{ mm}$	
Side	Boundary condition		
a	clamped		
b	free		
c	clamped		
d	free		

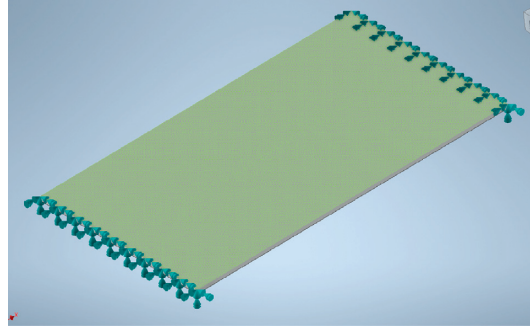


FIGURE 6: Numerical simulation: mesh and clamped edges.

$$w = \Phi_1 - \frac{1}{2}\omega^2 \left(R + \frac{\omega}{3} \left(D_3 + (2 - \nu)D_1T_2 - \frac{\nu - 1}{\rho_c} (D_2 - T_2) - 3D_1R \right) \Phi_1 + R \left(3D_2\omega - \frac{1}{\rho_c} \right) \right). \quad (21)$$

Operators D_m , $m = 1, 2, 3$, in formulas (19)–(21) are defined as

$$D_m f = (\nabla \omega, \nabla)^m = \left(\frac{\partial \omega}{\partial x} \frac{\partial}{\partial x} + \frac{\partial \omega}{\partial y} \frac{\partial}{\partial y} \right)^m f,$$

$$T_2 f = \frac{\partial^2 f}{\partial x^2} \left(\frac{\partial \omega}{\partial y} \right)^2 - 2 \frac{\partial^2 f}{\partial x \partial y} \left(\frac{\partial \omega}{\partial x} \right) \left(\frac{\partial \omega}{\partial y} \right) + \frac{\partial^2 f}{\partial y^2} \left(\frac{\partial \omega}{\partial x} \right)^2,$$

$$Rf = (D_2 + \nu T_2)f. \quad (22)$$

Φ_1 is an indefinite component.

Solution structures (19)–(21) contain function $\omega(x, y) = 0$.

Now, let us take the following example. Considering a composite plate with the planform shown in Figure 1, where $a = 37.5 \times 10^{-3} \text{ m}$; $b = 8.75 \times 10^{-3} \text{ m}$; $a_1 = 12.5 \times 10^{-3} \text{ m}$; $b_1 = 9.25 \times 10^{-3} \text{ m}$.

Suppose that the plate is clamped along all the borders. In order to obtain the admissible functions, it is necessary to construct a solution structure (19), and the equation of the border $\omega(x, y) = 0$. Using the R -operations \wedge_0 and \vee_0 , the equation of the boundary is built in the following form:

$$\omega = (f_1 \wedge_0 f_2) \wedge_0 (f_3 \vee_0 f_4), \quad (23)$$

where $f_1 = ((a^2 - x^2)/2a) \geq 0$ is the vertical band bounded by straight lines $x = \pm a$, $f_2 = ((b^2 - y^2)/2b) \geq 0$ is the horizontal band bounded by straight lines $y = \pm b$, $f_3 = ((x^2 - a_1^2)/2a_1) \geq 0$ is an outside domain of the vertical band bounded by straight lines $x = \pm a_1$, $f_4 = ((b_1^2 - y^2)/2b_1) \geq 0$ is the horizontal band bounded by straight lines $y = \pm b_1$, and $\omega = 0$ is the equation of the whole boundary domain.

Numerical implementation of the method of solving problems of linear vibrations of FG plates and shallow shells has been done in the system POLE-RL.

2. Specimens Preparation

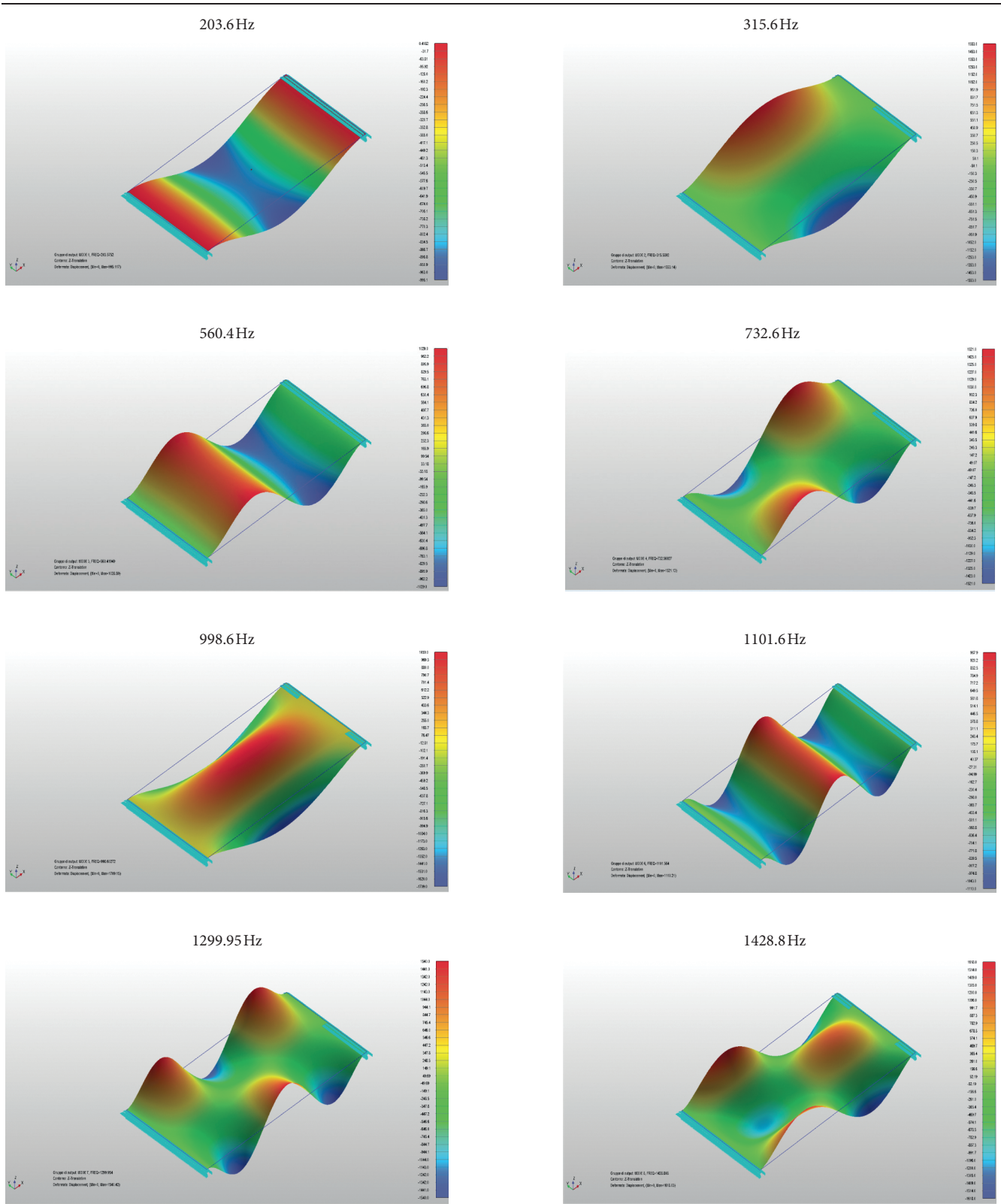
As the goal of this work is the experimental validation of the R -functions method, the activity started with the definition of four geometries with different boundary conditions. Such structures were experimentally prototyped. Then, the finite element method and the R -functions method were used for modelling the system.

A 3D printer has been used to create the specimens, in such a way it was possible to obtain better accuracy and precise, clamped, and simply supported boundary conditions, as well as a complex shape.

The printer used, see Figure 2, is the Delta WASP 2040 Turbo2 that has been set with the following technical specification:

- (i) Layer height: 0.15 mm

TABLE 4: FEM simulation: mode shapes and natural frequencies (Case 1).



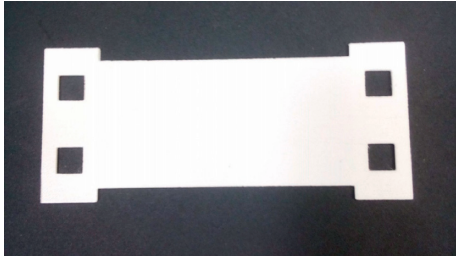


FIGURE 7: Specimen for experimental modal analysis (Case 1).

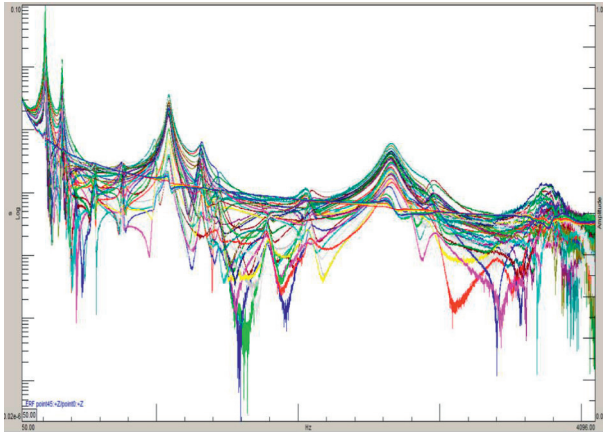


FIGURE 8: Experimental frequency response function base excitation vs velocity.

- (ii) Print speed: 50 mm/s
- (iii) Travel speed: 80 mm/s
- (iv) Bed temperature: 60°C
- (v) Extruder temperature: 245°C
- (vi) Extruder/nozzle diameter: 0.4 mm

All specimens have been made using the PETG filament of TREED, see Figure 3, with the following mechanical properties:

- (i) Density: 1.20 g/cm³
- (ii) Young's modulus: 1.6 GPa
- (iii) Water absorption: 0.13%

As water absorption can affect the real weight of the specimen, in order to avoid unwanted mass variation, each specimen has been weighed before and after the testing process. Moreover, in order to avoid Young's modulus change, the same filament reel has been used for all the specimens.

The main issue in the prototype creation is the determination of the correct boundary condition. Figure 4 shows the drawing section of half of the samples, note that the dash-dot line is a symmetry axis, to highlight the realization of the fixed joint by locking the specimen between the VTA (vibration table adapter) made with two aluminum frames, suitably shaped, while the simply supported joint has been made by printing a thinner outline to allow rotations and lock displacements; indeed, super flexible joints behave similarly to hinges.

3. Experimental Set-Up

The equipment used for this experiment shown in Figure 5 consists of an electrodynamic shaker LDS V530 (Figure 5(e)) controlled with the SCADAS III data acquisition system (Figure 5(d)) and Siemens LMS Test Lab software: the bare table vibration is monitored with a Dytran monoaxial accelerometer model 3097a2, and the response is measured by a laser vibrometer OFV-505 by POLYTEC (Figure 5(b)). The shaker and cooling fan are powered by a power amplifier.

Specimens have been designed with a 3D cad and realized with a 3D printer using a slicing software; for each plate, an ad hoc aluminum VTA has been made to rigidly connect the specimen to the shaker. The printing process was repeated iteratively, modifying the printing parameters (extruder speed and temperature) in order to obtain homogeneous and uniform specimens. The dimensions of the specimens were carefully measured and used for the FEM and RFM simulations. The specimens were experimentally tested, and modal analysis was performed using about 45 measuring points for each plate. Experimental modal analysis by base excitation has been chosen due to the small size, the high damping, and the low stiffness of the samples: the measurement location has been accurately set; the base acceleration was carried out using sine sweep, allowing uniform energy distribution in the frequency range of interest; contactless sensors were used to avoid excessive perturbation of the system.

4. Results and Discussion

Four test cases are considered; for each one, the general properties and operating conditions were defined, the numerical modal analysis is reported, and afterward the experimental modal analysis is presented. The four cases differ in geometry and boundary conditions. Table 1 reports the definition of each test case and the relative boundary conditions, while Table 2 reports the reference material properties that have been used to investigate the cases with finite element simulation using Nastran and RFM simulations. Material properties could be subjected to small variations due to the 3D printing pattern and process such as water absorption or extruding temperature.

Case 1. Rectangular plate with 2 clamped edges.

In Table 3, the measured geometrical properties and the boundary conditions of the plate for the first case are listed.

4.1. FEM Simulation. For the finite element simulation, the Nastran solver has been used; in Figure 6, the mesh and the opposite clamped edges are shown; results are given in Table 4.

4.2. Experimental Modal Analysis. In Figure 7, the specimen realized with the 3D printer for the experimental modal analysis is shown, while in Figure 8, the experimental FRF (frequency response function) between the base acceleration of the excitation and the measured velocity response of each point is presented. In Table 5, experimental results are given.

TABLE 5: Experimental modal analysis: mode shapes and natural frequencies (Case 1).

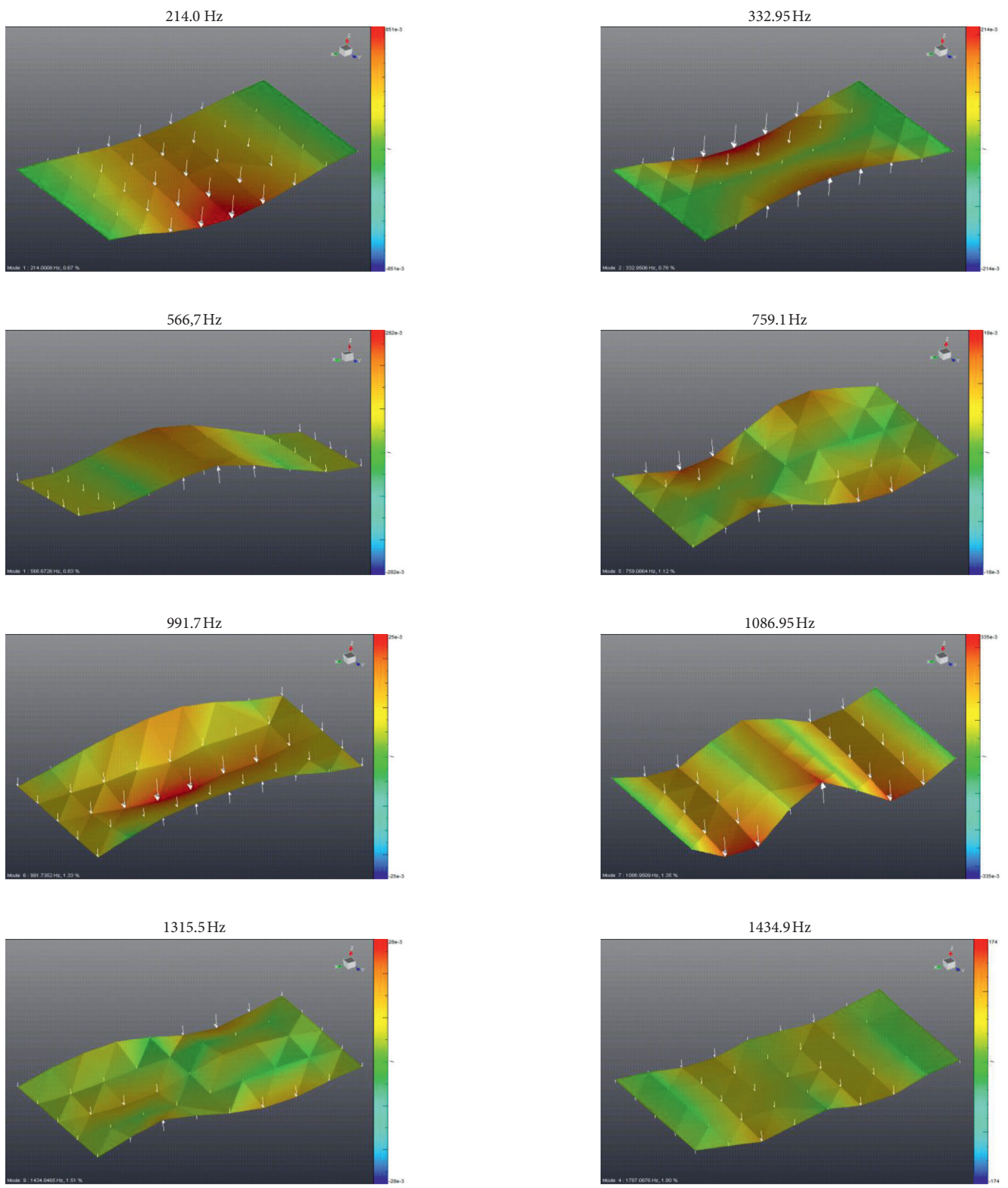
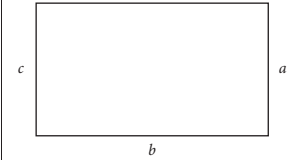


TABLE 6: Comparison of numerical and experimental frequencies (Case 1).

FEM (Hz)	Experimental (Hz)	Difference (%)
203,58	214,00	4,87
315,59	332,95	5,21
560,42	566,67	1,10
732,57	759,09	3,49
998,60	991,74	-0,69
1101,56	1086,95	-1,34
1299,95	1315,54	1,19
1428,81	1434,85	0,42

TABLE 7: Geometrical properties and boundary conditions (Case 2).

	Size $a = c = 40,8 \text{ mm}$ $b = d = 79,00 \text{ mm}$ h (thickness) = 0,93 mm	
	Side	Boundary condition
a	clamped	
b	clamped	
c	clamped	
d	clamped	

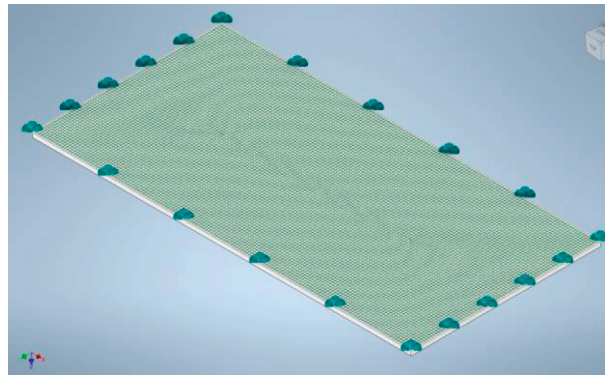


FIGURE 9: Numerical simulation: mesh and clamped edges.

From Table 6, it could be seen that the percental difference is less than 6% for the first cases, and it is decreasing for subsequent cases.

The analysis confirms a good agreement from finite element analysis and experimental modal analysis. In this test, the purpose is to verify that the identified material properties and the 3D printed boundary conditions are accurately made and that the specimen is realized with a pattern that allows to obtain global uniform structural properties of the specimen.

In the modelling process, it is well known that the most comfortable boundary conditions are the fixed joints because they allow to simplify the analysis reducing the complexity of the calculations; vice-versa in the experimental analysis, the free-free configurations result to be the easier to test because they reduce drastically the influence of the interaction of supporting frames or structural coupling with vibration table adapters.

These considerations are relevant from both the scientific point of view, when the experimental validation of a model is needed and when is required to model a real

structure that is connected to a more complex system. This series of tests are used to validate reciprocally the FEM model, due to material uncertainties, and the experimental setup, due to the very critical experimental realization of clamping and hinges.

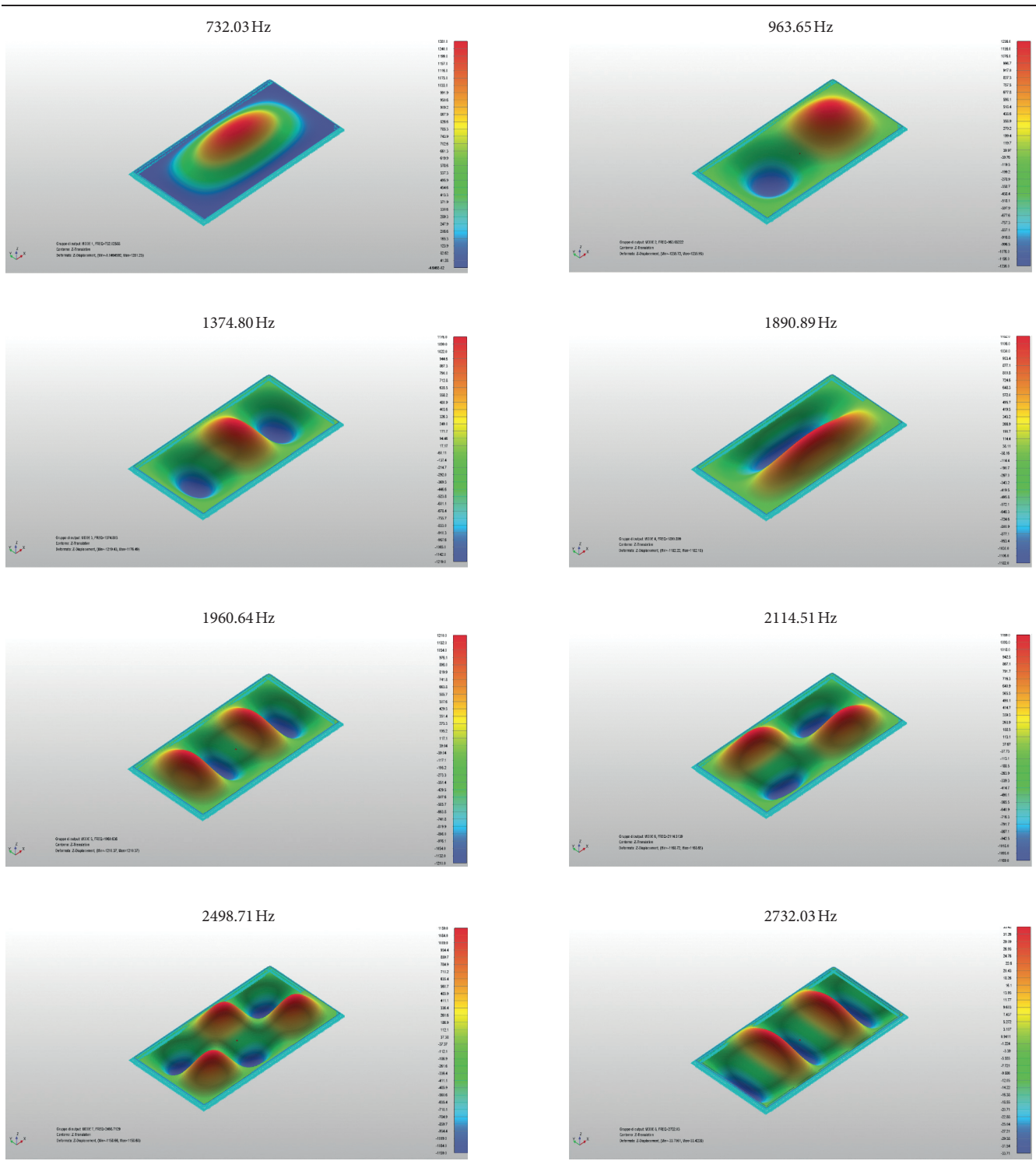
In particular, the 3D printing process provides a high versatility allowing to choose different materials and several patterns and parameters during the creation of the specimens; this, however, increases the complexity of the specimens introducing uncertainties that need to be taken into account during the modelling process.

Case 2. Rectangular plate with all edges clamped

In Table 7, the measured geometrical properties and the boundary conditions of the plate for the second case are listed.

4.3. FEM Simulation. For the finite element simulation, the Nastran solver has been used; in Figure 9, the mesh and the clamped edges are shown; results are given in Table 8.

TABLE 8: FEM simulation: mode shapes and natural frequencies (Case 2).



4.4. *Experimental Modal Analysis.* In Figure 10, the specimen mounted through the VTA (vibration table adapter) to the shaker is shown, and the laser spot during the measuring process is visible. In Figure 11, the experimental FRF (frequency response function) between base acceleration of the

excitation and the measured velocity response of each point is presented. In Table 9, results are given.

In Table 10, the 2nd, 4th, and 7th modes have a low correspondence probably due to a nonideal uniform clamping configuration along the specimen edges.

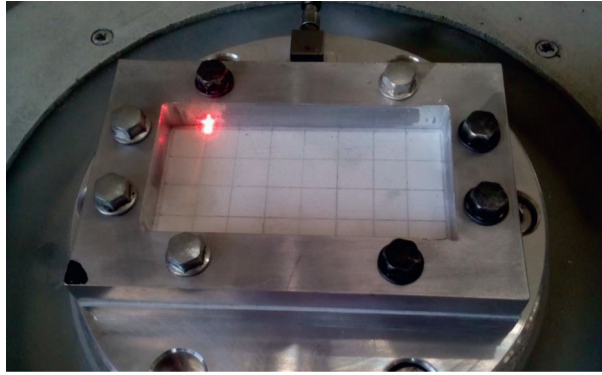


FIGURE 10: Specimen for experimental modal analysis (Case 2).

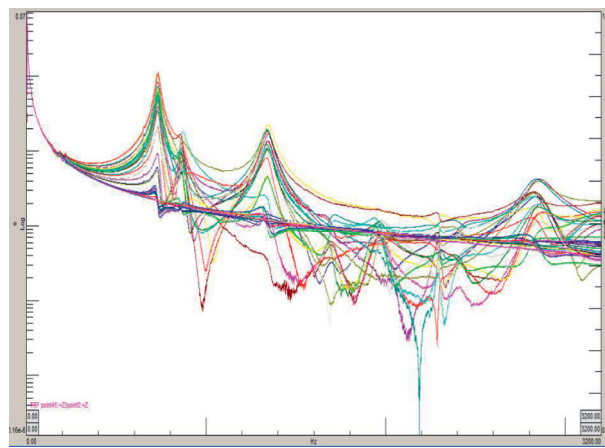


FIGURE 11: Experimental frequency response function base excitation vs velocity.

TABLE 9: Experimental modal analysis: mode shapes and natural frequencies (Case 2).

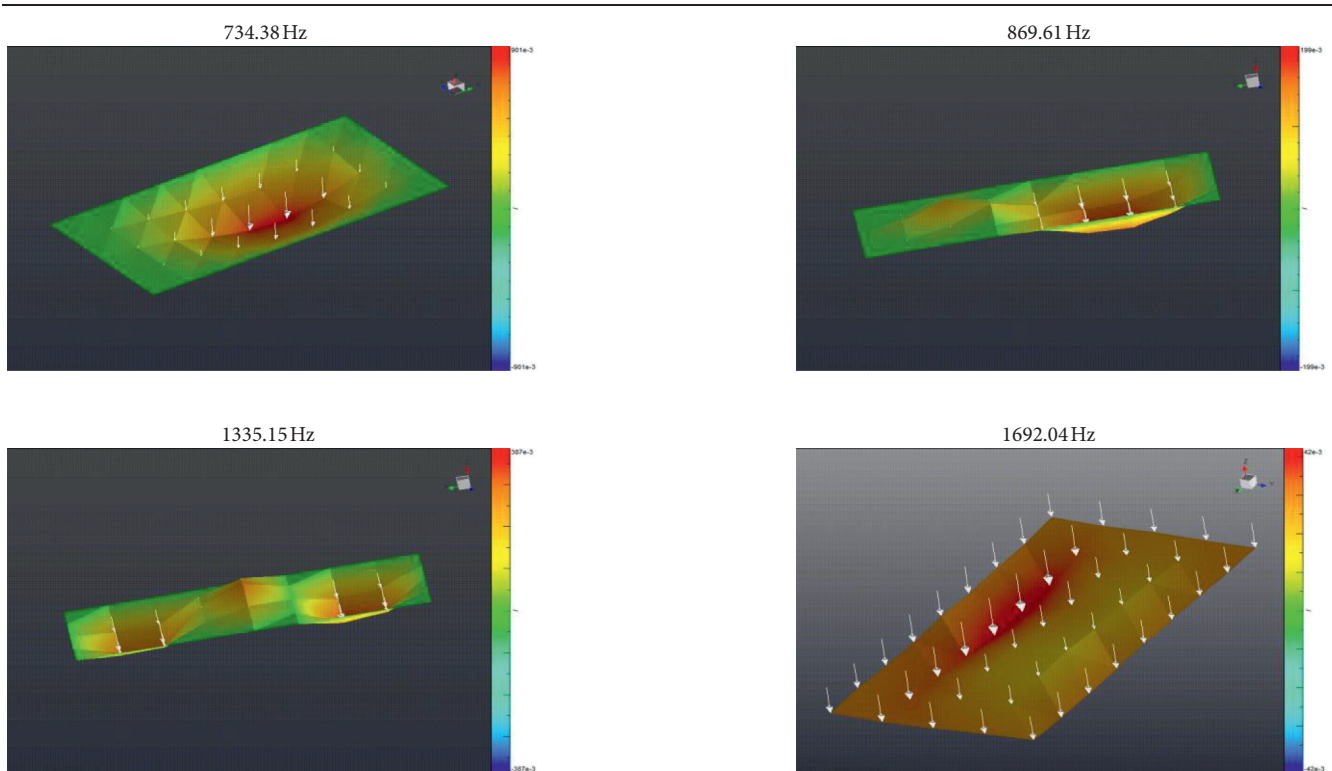


TABLE 9: Continued.

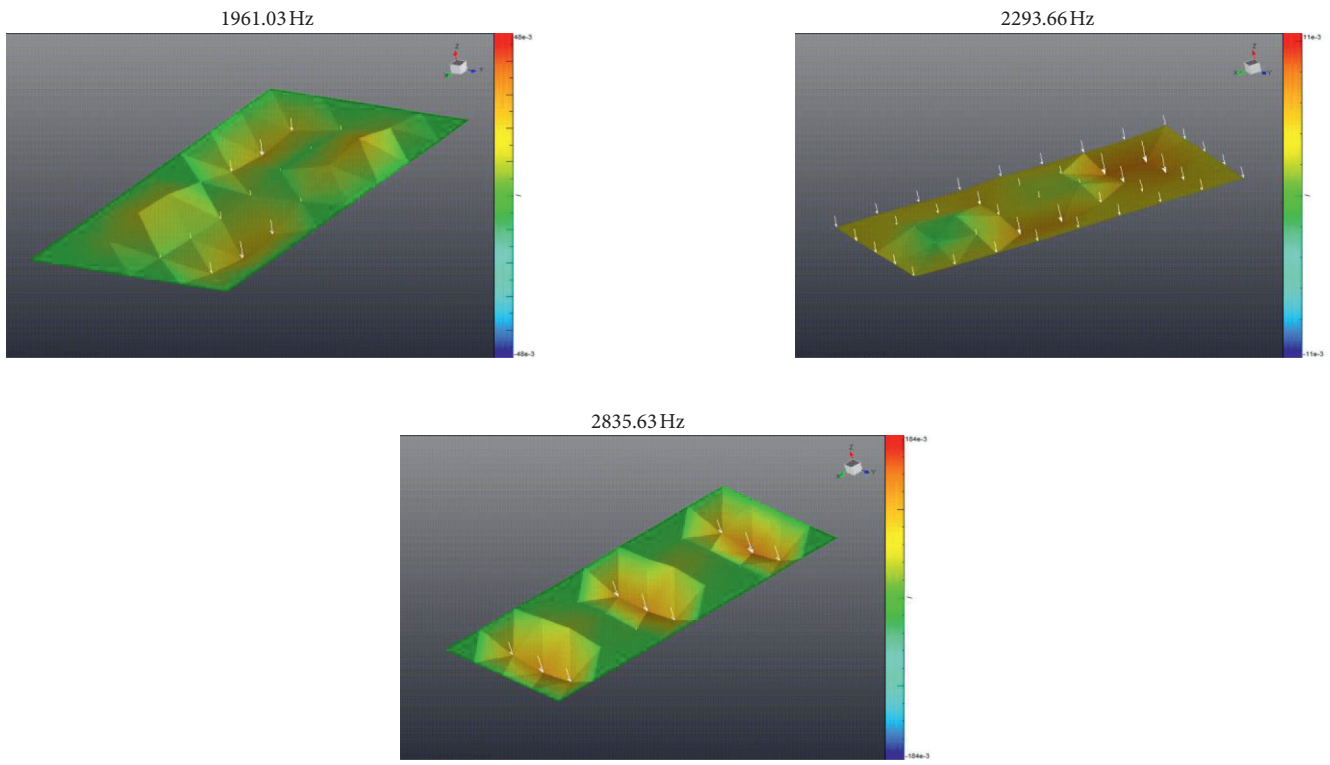


TABLE 10: Comparison of numerical and experimental frequencies (Case 2).

FEM simulation (Hz)	Experimental (Hz)	Difference (%)
732,03	734,38	0,32
963,65	869,61	-10,81
1374,80	1335,15	-2,97
1890,89	1692,04	-11,75
1960,64	1961,03	0,02
2114,51	2293,66	7,81
2498,71	2835,63	11,88

TABLE 11: Geometrical properties and boundary conditions (Case 3).

	Size $a = c = 37.50 \text{ mm}$ $b = d = 75.00 \text{ mm}$ $h \text{ (thickness)} = 0,90 \text{ mm}$	
	Side	Boundary condition
a	simply supported	
b	simply supported	
c	simply supported	
d	simply supported	

Case 3. Rectangular plate with all edges simply supported

In Table 11, the measured geometrical properties and the boundary conditions of the plate for the first case are listed.

4.5. FEM Simulation. For the finite element simulation, the Nastran solver has been used; in Figure 12, the mesh and the simply supported edges are shown; experimental results are given in Table 12.

4.6. Experimental Modal Analysis. In Figure 13, the specimen realized with the 3D printer for the experimental modal analysis is shown, and a thinner boundary contour made to simulate the continuous hinge joint is clearly visible, while in Figure 14, the experimental FRF (frequency response function) between base acceleration of the excitation and the measured velocity response of each point is presented; it seems that the structure has a more dampened response due to the more smoothed curves

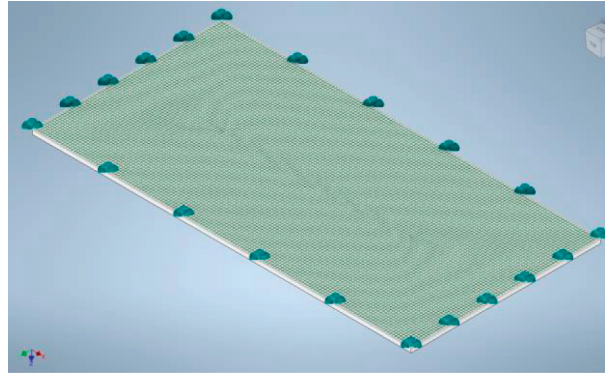


FIGURE 12: Numerical simulation: mesh and simply supported edges.

TABLE 12: FEM simulation: mode shapes and natural frequencies (Case 3).

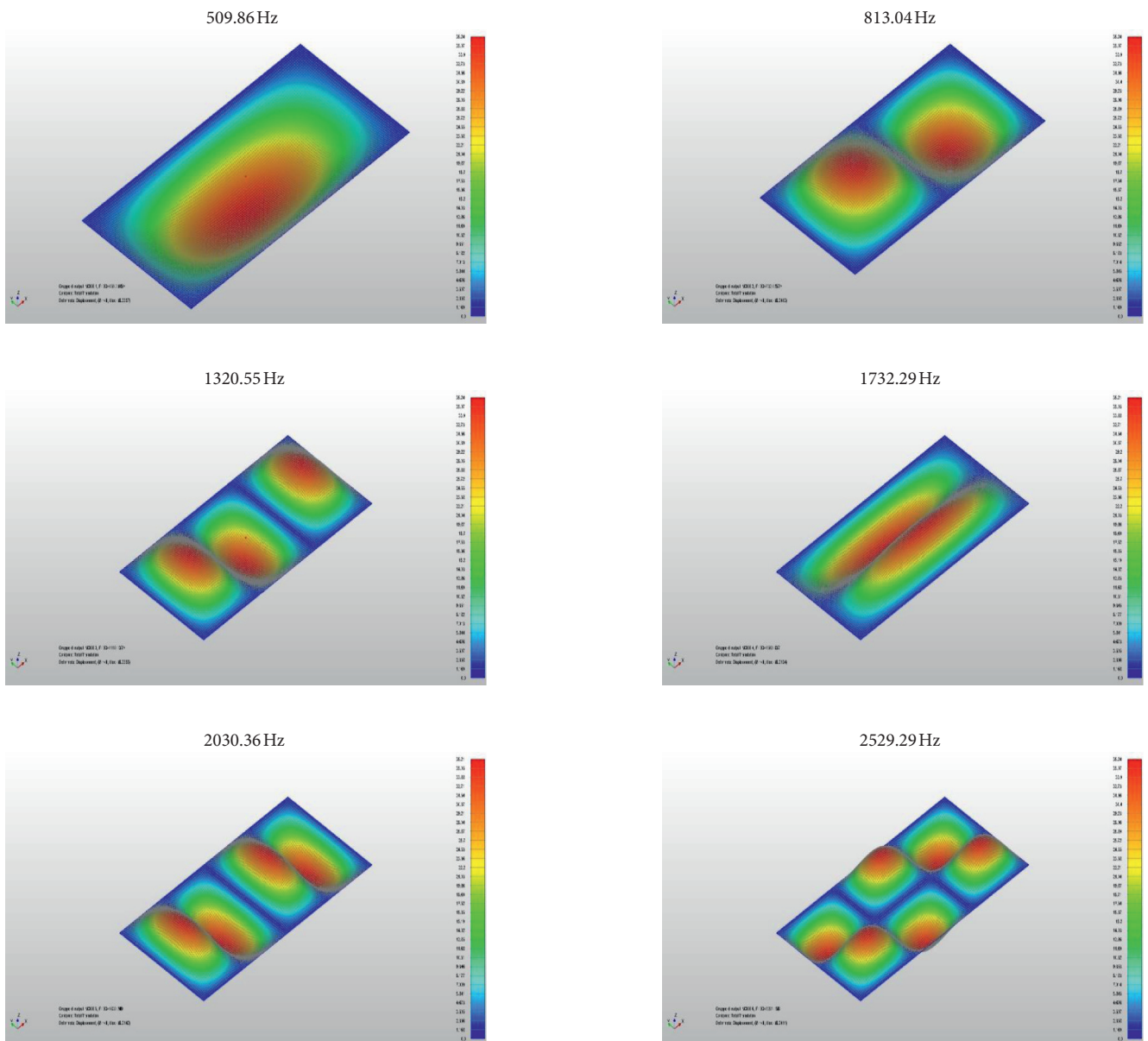


TABLE 12: Continued.

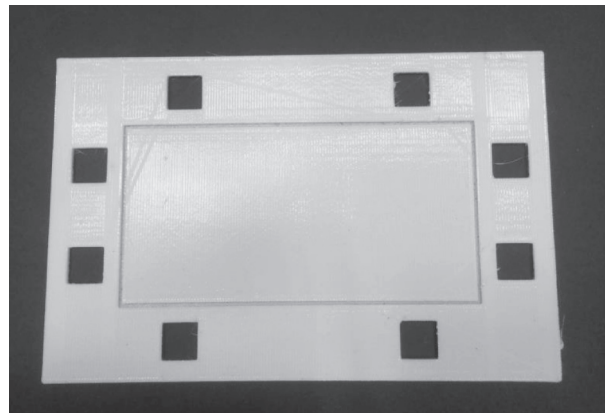
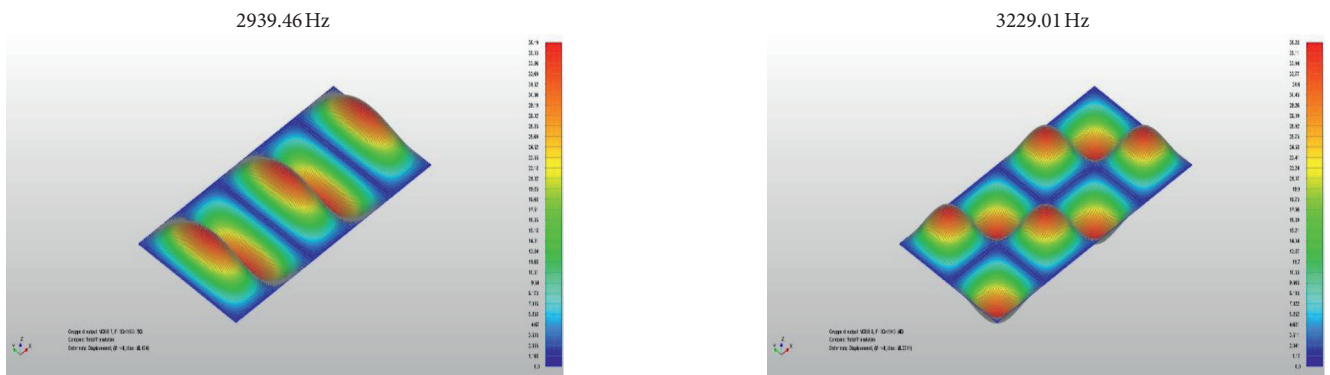


FIGURE 13: Specimen for experimental modal analysis (Case 3).

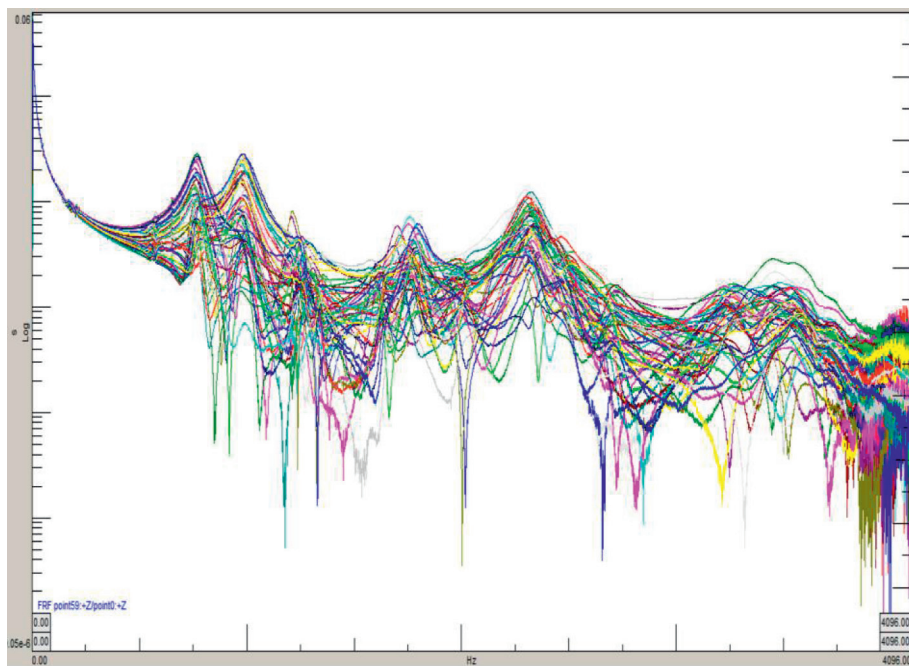


FIGURE 14: Experimental frequency response function base excitation vs velocity.

TABLE 13: Experimental modal analysis: mode shapes and natural frequencies (Case 3).

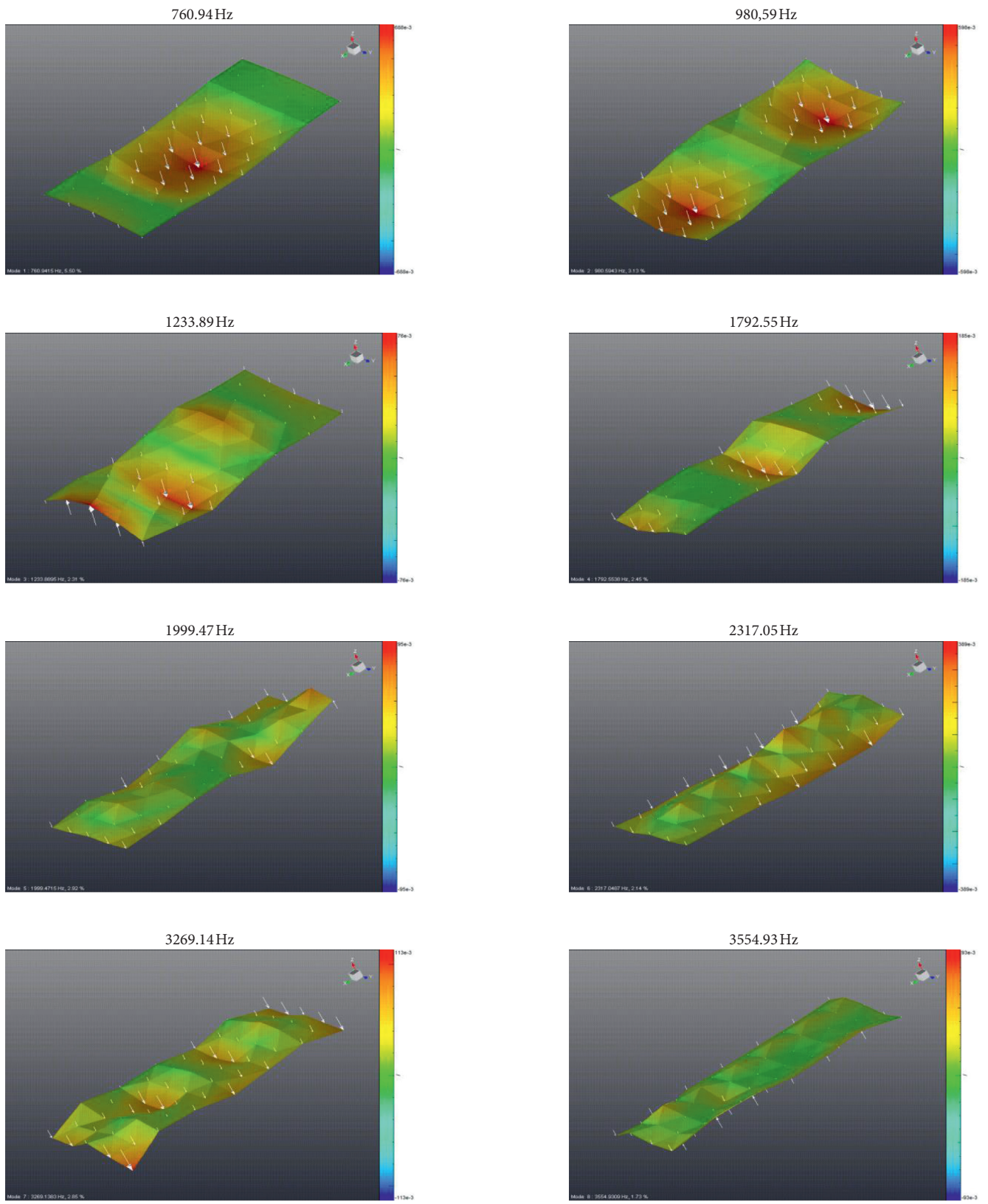


TABLE 14: Comparison of numerical and experimental frequencies (Case 3).

FEM simulation (Hz)	Experimental (Hz)	Difference (%)
509,86	760,94	33,00
813,04	980,59	17,09
1320,55	1233,89	-7,02
1732,29	1792,55	3,36
2030,36	1999,47	-1,54
2529,29	2317,05	-9,16
2939,46	3269,14	10,08
3229,01	3554,93	9,17

TABLE 15: Geometrical properties and boundary conditions (Case 4).

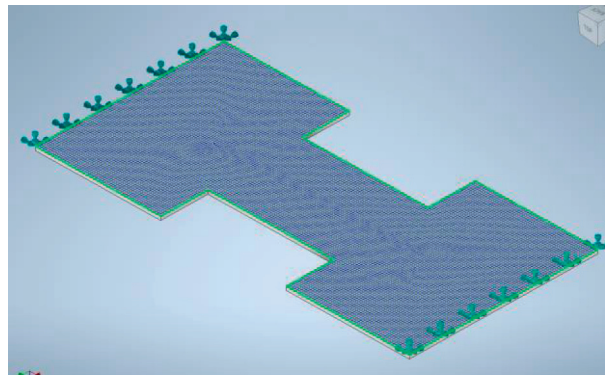
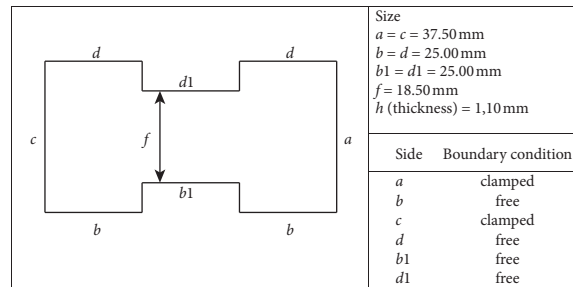


FIGURE 15: Numerical simulation: mesh and clamped edges.

TABLE 16: FEM simulation: mode shapes and natural frequencies (Case 4).

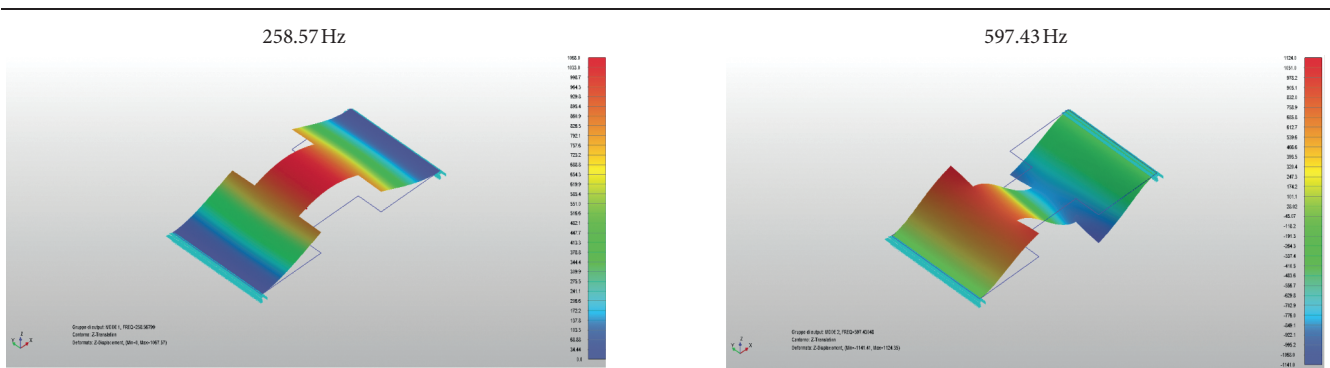


TABLE 16: Continued.

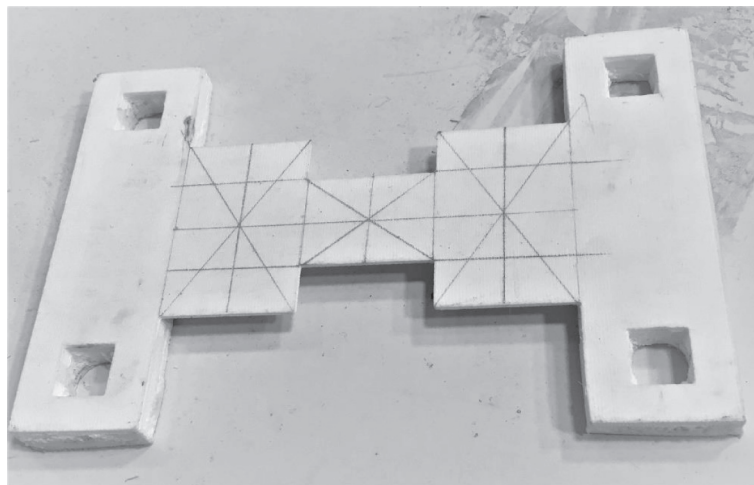
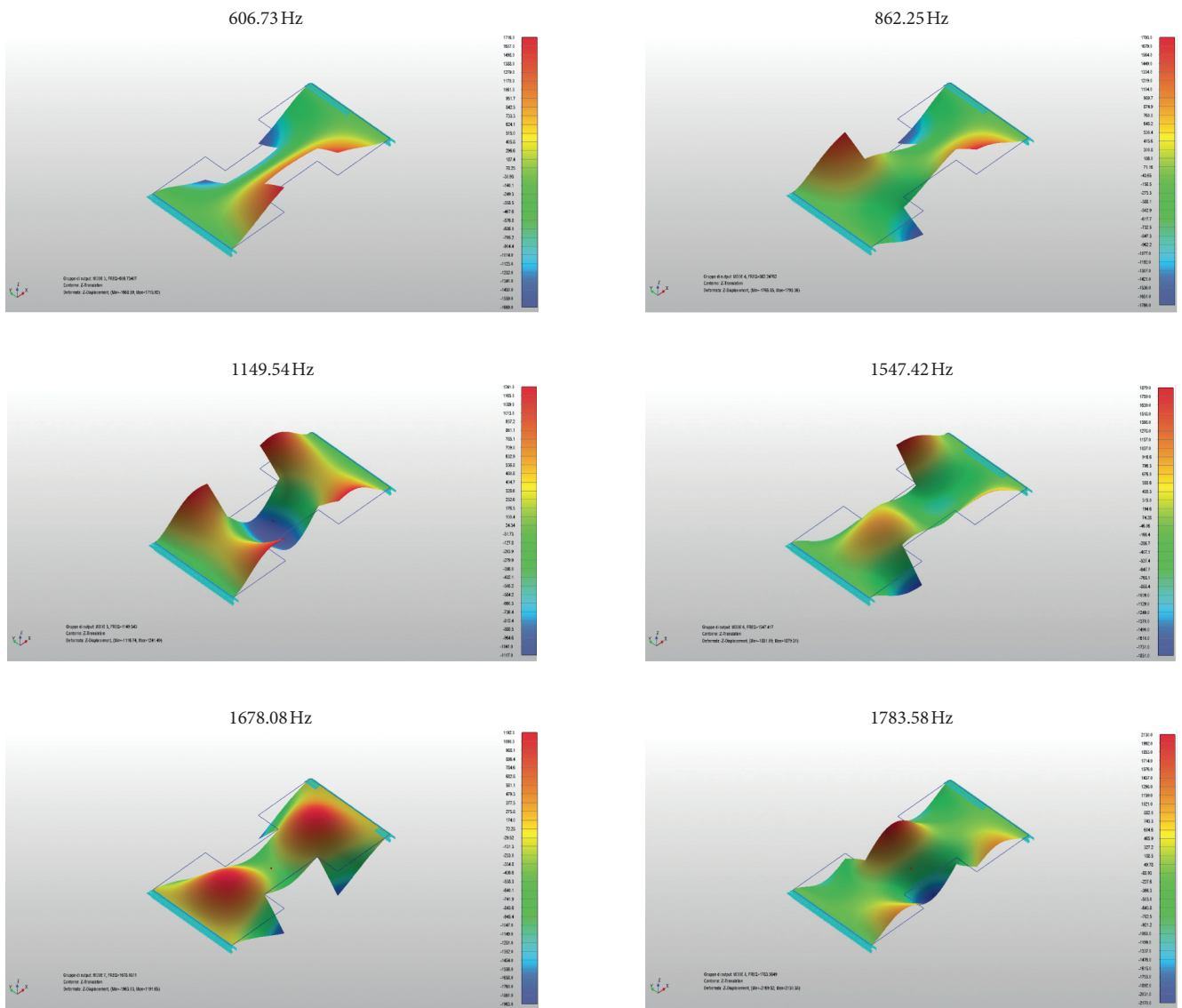


FIGURE 16: Specimen for experimental modal analysis (Case 4).

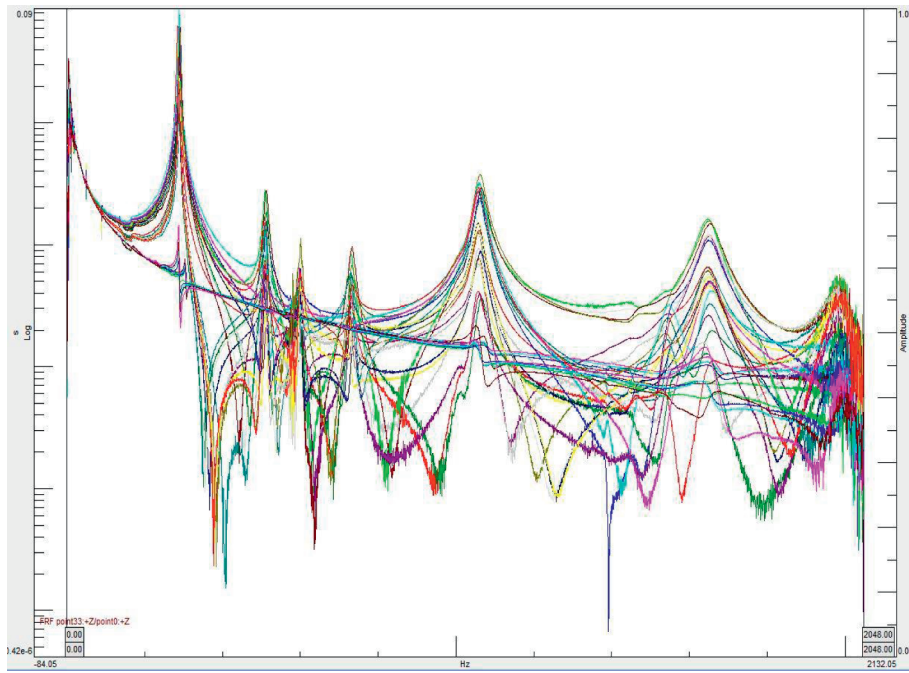


FIGURE 17: Experimental frequency response function base excitation vs velocity.

TABLE 17: Experimental modal analysis: mode shapes and natural frequencies (Case 4).

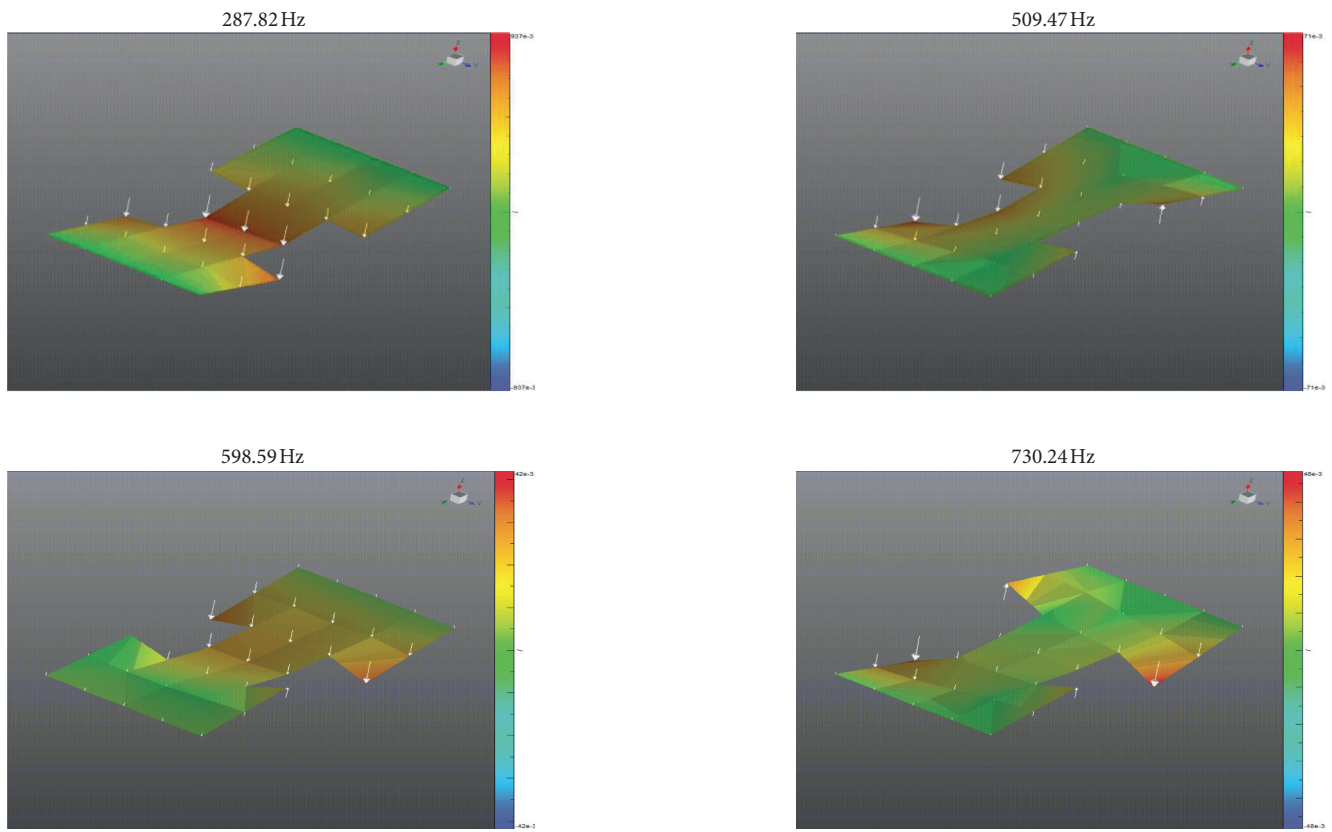


TABLE 17: Continued.

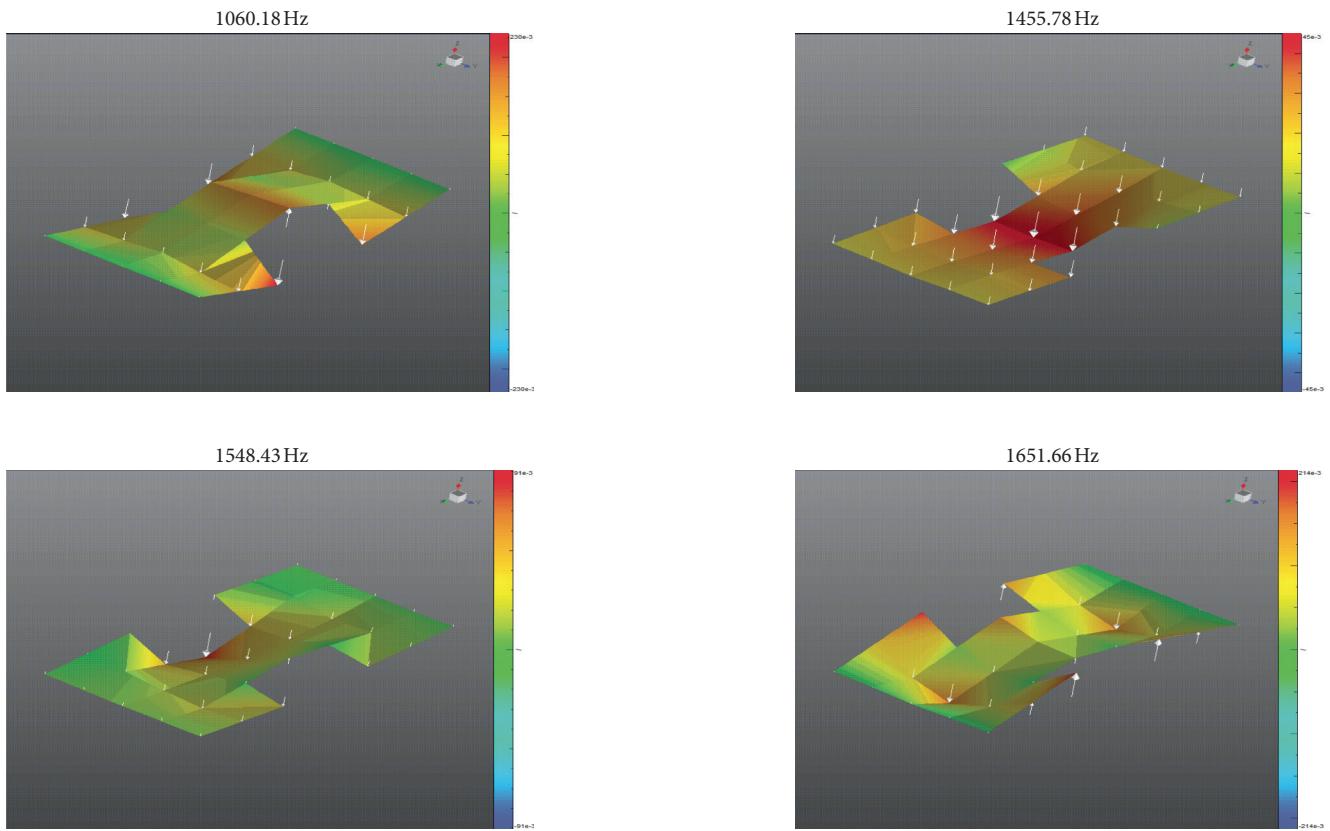


TABLE 18: Comparison of FEM and experimental frequencies (Case 4).

FEM simulation (Hz)	Experimental (Hz)	Difference (%)
258,57	287,82	10,16
597,43	509,47	-17,27
606,73	598,59	-1,36
862,25	730,24	-18,08
1149,54	1060,18	-8,43
1547,42	1455,78	-6,29
1678,08	1548,43	-8,37
1783,58	1651,66	-7,99

TABLE 19: R-functions method: mode shapes and natural frequencies (Case 4).

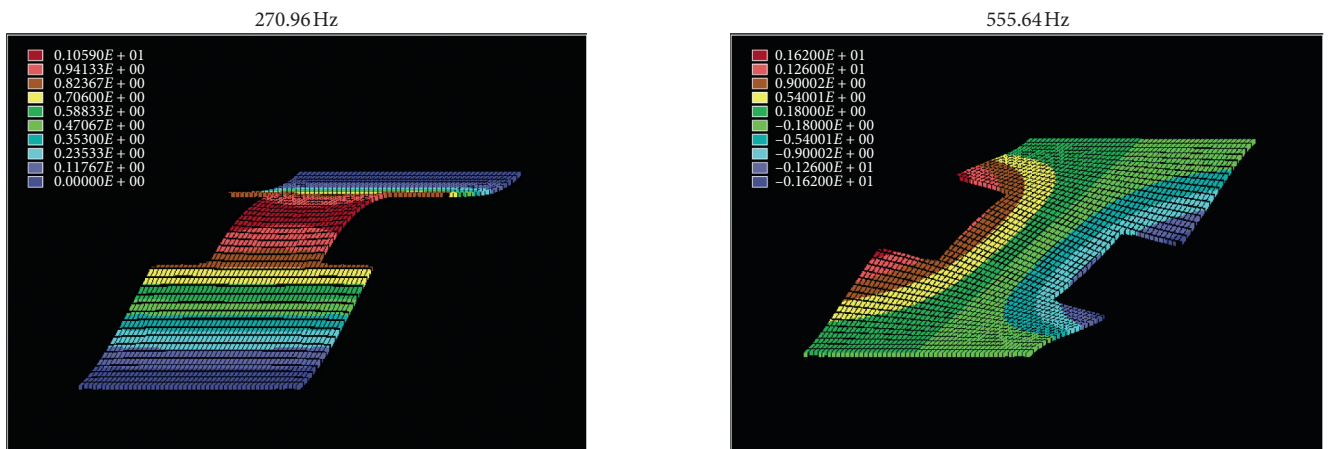
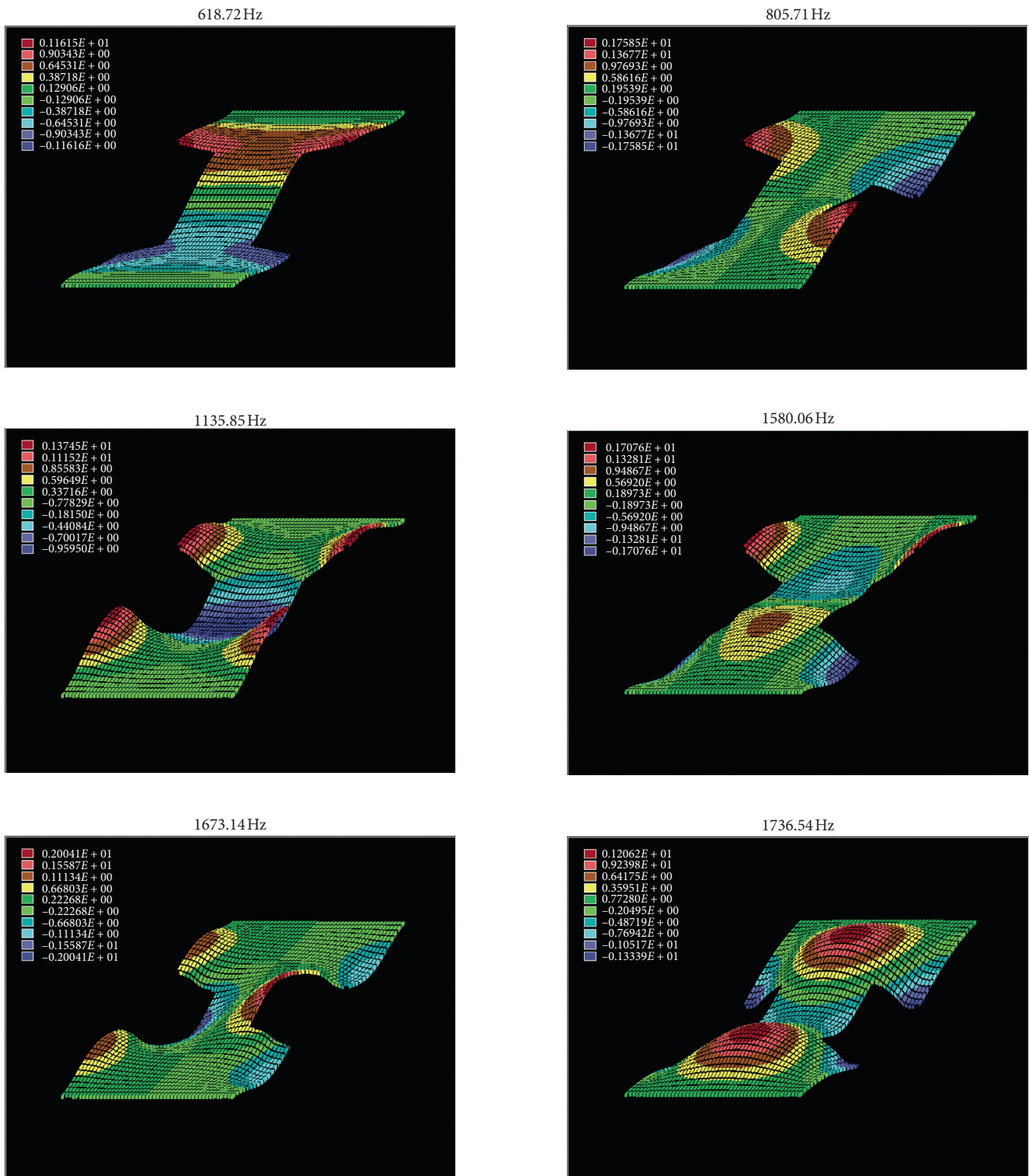


TABLE 19: Continued.



near the resonances. In Table 13, experimental results are given.

As it can be seen from the percentage differences, in Table 14, the effect of the boundary condition is present in

the lowest and higher modes, the frequency of the first mode has a difference value more than 30% that exceeds an acceptable value, the second mode halved the percentual difference with respect to the experimental analysis, and the

TABLE 20: Comparison of experimental, FEM, and RFM frequencies (Case 4).

Experimental (Hz)	FEM simulation (Hz)	Difference (%) (exp-FEM)	RFM (Hz)	Difference (%) (exp-RFM)
287,82	258,57	10,16	270,96	5,86%
509,47	597,43	-17,27	555,64	-9,06%
598,59	606,73	-1,36	618,72	-3,36%
730,24	862,25	-18,08	805,71	-10,33%
1060,18	1149,54	-8,43	1135,85	-7,14%
1455,78	1547,42	-6,29	1580,06	-8,54%
1548,43	1678,08	-8,37	1673,14	-8,05%
1651,66	1783,58	-7,99	1736,54	-5,14%

other modes are not uniform, and we can assume that this is due to the fact that the constraint has not been modelled exactly or vice-versa that the creation of the specimen hinge joint is too much stiff and interacts with the frame structure.

Case 4. Rectangular plate with symmetric rectangular cuts

In Table 15, the measured geometrical properties and the boundary conditions of the plate for the first case are listed.

4.7. FEM Simulation. For the finite element simulation, the Nastran solver has been used; in Figure 15, the mesh and the opposite clamped edges are shown; experimental results are given in Table 16.

4.8. Experimental Modal Analysis. In Figure 16, the specimen realized with the 3D printer for the experimental modal analysis is shown, while in Figure 17, the experimental FRF (frequency response function) between base acceleration of the excitation and the measured velocity response of each point is presented. In Table 17, experimental results are given.

In Table 18, a comparison between the finite element method and the experimental modal analysis is given.

4.9. R-Functions Simulation. In Table 19, the results of the simulation using the *R*-functions method are given.

The proposed case takes an advantage of the previous analysis, used for the mutual validation of the fixed-fixed configuration, for testing a plate with a complex form and two clamped sides. In Table 20, the comparison of the experimental modal analysis with respect to the finite element method and the *R*-functions method is presented. The *R*-functions method shows better correspondence, an average difference of 7.2%, concerning the finite element modelling that presents an average difference of 9.7%. Moreover, the first and second modes are better modelled, as well as the 4th mode. These discrepancies could be addressed to the difficulty in modelling and realizing an ideal boundary condition.

5. Conclusion

In this work, a comparison of three methods to analyze the dynamic behavior of 3D-printed specimens with complex plate

shapes and different boundary conditions is fulfilled. The used method and the experimental procedure and facilities are accurately reported, and the material properties of the plates are described. The 2 fixed-sided configuration presents a more solid agreement both in the rectangular plate and in the plate with rectangular cuts, and the *R*-functions method seems to be more similar with respect to the experimental test in comparison with the finite element analysis. The simply supported configuration shows difficulties in the continuous hinge joint realization of the specimen to be correctly modelled.

The experimental analysis reflects the complexity to rightly make a fixed or hinge joint in a real test case, and the finite element method reveals these challenges to the modelling point of view. Since the *R*-functions method represents the solution in an analytical form, this distinguishes it favorably from the finite element method when solving nonlinear problems.

Data Availability

The experimental data used to support the findings of this study are available from the corresponding author upon request.

Conflicts of Interest

The authors declare that there are no conflicts of interest regarding the publication of this paper.

Acknowledgments

The authors would like to thank InterMech MO.RE. Center. This research received the support of the project DiaPro4.0: "Cost-effective" Multisensor Diagnostic-Prognostic Integrated System in Mechanical Drives for Industry 4.0 (PG/2018/632156)-CUP F44I18000030009.

References

- [1] M. Amabili, *Nonlinear Vibrations and Stability of Shells and Plates*, Cambridge University Press, Cambridge, UK, 2008.
- [2] A. Zippo, M. Barbieri, G. Iarriccio, and F. Pellicano, "Non-linear vibrations of circular cylindrical shells with thermal effects: an experimental study," *Nonlinear Dynamics*, vol. 99, no. 1, p. 373, 2020.
- [3] G. Iarriccio, A. Zippo, F. Pellicano, and M. Barbieri, "Resonances and nonlinear vibrations of circular cylindrical shells, effects of thermal gradients," *Proceedings of the Institution of*

Mechanical Engineers, Part C: Journal of Mechanical Engineering Science, 2020.

- [4] T. J. Anderson and A. H. Nayfeh, "Natural frequencies and mode shapes of laminated composite plates: experiments and FEA," *Journal of Vibration and Control*, vol. 2, no. 4, pp. 381–414, 1996.
- [5] D. Shi, X. Shi, W. L. Li, Q. Wang, and J. Han, "Vibration analysis of annular sector plates under different boundary conditions," *Shock and Vibration*, vol. 2014, p. 1, Article ID 517946, 2014.
- [6] E. F. Joubaneh, O. R. Barry, and H. E. Tanbour, "Analytical and experimental vibration of sandwich beams having various boundary conditions," *Shock and Vibration*, vol. 2018, p. 1, Article ID 3682370, 2018.
- [7] F. Tornabene and E. Viola, "Vibration analysis of spherical structures elements using the GDQ method," *Computers and Mathematics with Applications*, vol. 53, pp. 1538–1560, 2007.
- [8] S. Pradyumna and J. N. Bandyopadhyay, "Free vibration analysis of functionally graded curved panels using a higher-order finite element formulation," *Journal of Sound and Vibration*, vol. 318, no. 1-2, pp. 176–192, 2008.
- [9] A. M. A. Neves, A. J. M. Ferreira, E. Carrera, M. Cinefra, C. M. C. Roque, and R. M. N. Jorge, "Free vibration analysis of functionally graded shells by a higher-order shear deformation theory and radial basis functions collocation accounting for through the thickness deformations," *European Journal of Mechanics-A/Solids*, vol. 37, pp. 24–34, 2013.
- [10] J. Awrejcewicz, L. Kurpa, and T. Shmatko, "Investigating geometrically nonlinear vibrations of laminated shallow shells with layers of variable thickness via the R-functions theory," *Composite Structures*, vol. 125, pp. 575–585, 2015.
- [11] G. Pilgun and M. Amabili, "Non-linear vibrations of shallow circular cylindrical panels with complex geometry. Meshless discretization with the R-functions method," *International Journal of Non-linear Mechanics*, vol. 47, no. 3, pp. 137–152, 2012.
- [12] J. Awrejcewicz, L. Kurpa, and T. Shmatko, "Linear and nonlinear free vibration analysis of laminated functionally graded shallow shells with complex plan form and different boundary conditions," *International Journal of Non-linear Mechanics*, vol. 107, p. 161, 2018.
- [13] L. Kurpa, G. Pilgun, and M. Amabili, "Nonlinear vibrations of shallow shells with complex boundary: R-functions method and experiments," *Journal of Sound and Vibration*, vol. 306, no. 3–5, pp. 580–600, 2007.
- [14] V. L. Rvachev, *The R-Functions Theory and its Some Application*, Naukova Dumka, Kiev, Ukraine, in Russian, 1982.
- [15] L. V. Kurpa, *R-functions Method for Solving Linear Problems of Bending and Vibrations of Shallow Shells*, Kharkiv NTU Press, Kharkiv, Ukraine, in Russian, 2009.

Research Article

Probabilistic Assessment of Damage from Same Shock Response Spectra due to Variations in Damping

Arup Maji 

Org 1557, Sandia National Laboratories, Albuquerque, NM, USA

Correspondence should be addressed to Arup Maji; amaji@sandia.gov

Received 14 April 2020; Revised 6 August 2020; Accepted 15 November 2020; Published 28 November 2020

Academic Editor: Matteo Strozzi

Copyright © 2020 Arup Maji. This is an open access article distributed under the Creative Commons Attribution License, which permits unrestricted use, distribution, and reproduction in any medium, provided the original work is properly cited.

Interpretation of field data from shock tests and subsequent assessment of product safety margins via laboratory testing are based on the shock response spectra (SRS). The SRS capture how a single degree of freedom (SDOF) structure responds to the shock at differing frequencies and, therefore, no longer contain the duration or other temporal parameters pertaining to the shock. A single duration can often be included in the technical specification or in the recreation of acceleration vs. time history from the specified SRS; however, there is little basis for that beyond technical judgment. The loss of such temporal information can result in the recreated SRS being the same while its effect on a system or component can be different. This paper attempts to quantify this deficiency as well as propose a simple method of capturing damping from shock waves that can allow the original waveform to be more accurately reconstructed from the SRS. In this study the decay rate associated with various frequencies that comprise the overall shock was varied. This variation in the decay rate leads to a variation in the acceleration vs. time history, which can be correlated to a “Damage Index” that captures the fatigue damage imparted to the object under shock. Several waveforms that have the same SRS but varying rates of decay for either high- or low-frequency components of the shock were investigated. The resulting variation in stress cycles and Damage Index is discussed in the context of the lognormal distribution of fatigue failure data. It is proposed that, along with the SRS, the decay rate is also captured to minimize the discrepancy between field data and representative laboratory tests.

1. Introduction

Mechanical vibration and shock have a detrimental effect on components or systems. Therefore, shock tests are conducted to ensure items can survive the repeated shocks that they are expected to endure during their lifetime. The level of shock to be applied in the shock tests is prescribed in terms of the shock response spectra (SRS). The SRS levels used for testing are typically prescribed in the terms of P99 or P95 levels (for example, P99 implies that the shock applied in the test will exceed 95% of the shock the item may see in its lifetime).

An issue that arises with this approach is that SRS are not a unique representation of shock; various shock events can have the same SRS. The different shocks (decaying acceleration vs. time) corresponding to the same SRS will inflict a different amount of damage to the item of interest. In this study, the effect of 4 shocks (Trials 1–4) that have identical

SRS was investigated to quantify the consequence in such variations. The 4 shocks were generated by varying the decay rate (damping) of the underlying shock acceleration vs. time.

The SRS quantify the input shock, and “damping” relates to the decay rate of the input shock. Damage, on the contrary, is a consequence of the shock applied. The consequence of the shock can be measured in terms of a “Damage Index”. In this paper, a “Damage Index” is quantified in terms of the magnitude and number of stress cycles as per equation (1). Its absolute value is significant only when a specific material/structure is being considered and the stress cycles needed to cause failure are known. In the context of this paper, the absolute value of the “Damage Index” is not significant, and only the relative differences between Trial 1 through Trial 4 are significant. Damping (of the input shock) is constant for each frequency but varies among the 5 frequencies and from Trial 1 to Trial 4.

Statistical data are available in the literature on how the Damage Index at failure (# of stress cycles leading to failure) varies among tests. This information can be used to assess how a variation in the number and magnitude of stress cycles relates to the probability of failure. This, in turn, allows the variation in stress cycles from the 4 trials to be related to the consequent variation in the probability of failure. The various sources of data and the analytical methods are presented in the next section.

2. Implications of Fatigue Test Data

In this section, test data from several sources in the literature were examined for variation in fatigue damage from test data, as defined by the standard deviation of the \log_{10} (damage).

The basic relationship between cyclic stress (ΔS) and number of cycles to failure (N) is provided by Basquin's power law [1], also referred to as the Miner–Palmgren relation [2]:

$$\Delta S^\beta N = C, \quad (1)$$

where the constant C can be thought of as a “Damage Index” or measure of accumulated damage leading to failure. The dimensional units of this parameter C are dependent on those of the underlying parameter (ΔS has units of stress, typically in MPa, and N is unitless) and hence can be converted to other units accordingly. The unitless parameter β is determined from test data using linear regression on a semilog scale ($\beta = 6.66$ was used in this paper).

Paris and Erdogan [3] provided an analogous expression or slow fatigue crack growth per cycle $\delta a/\delta N$ as a function of the stress intensity factor (K) instead of stress and the material constant A replacing C in the Miner–Palmgren relation:

$$\frac{\delta a}{\delta N} = A\Delta K^m. \quad (2)$$

These relations form the basis for statistical analyses of fatigue data for various material-structural systems [4, 5] and standard practices used in the industry. Equation (1) is also expressed in the following form:

$$\begin{aligned} \log N &= \frac{1}{\beta} \log\left(\frac{C}{\Delta S}\right) \text{ or } \log(\text{damage}) \\ &= \log(C) = \log(N) + \beta \log(\Delta S). \end{aligned} \quad (3)$$

The standard deviations of the quantities are thus related by the following equation:

$$\sigma(\text{damage}) = \sigma(\log N) + \beta\sigma(\log \Delta S). \quad (4)$$

Szala and Szala [6] investigated the fatigue life of D16CzATW aluminum alloy using fatigue test data on structural elements subject to different types of cyclic loads. Using a fatigue model based on equation (1), they arrived at a mean fatigue life parameter Nc from 6 tests. The normalized (to the mean) fatigue life parameter was calculated, and the standard deviation of $\log(\text{normalized-}Nc)$ was determined to be 10.4% (Table 1).

TABLE 1: Mean number of fatigue life cycles from test data from Szala and Szala [6].

Test #	Normalized (Nc)	Log(Nc)
1	1.24	0.094
2	0.75	-0.128
3	0.91	-0.043
4	0.75	-0.125
5	1.08	0.034
6	1.27	0.105
Mean		-0.010
St. deviation		10.4%

Leonetti et al. [7] fit fatigue test data to the Miner–Palmgren cumulative damage law and looked at the deviations for butt weld joints and cover-plated beams of steel for a large number (>500) of tests. Based on the standard deviation σ_w of $\log_{10}N$, the standard deviation of fatigue damage was determined to be 29% and 19%, respectively, for the butt joint and cover plates tested.

Peng et al. [8] investigated fatigue failure under combinations of small and large amplitude cyclic loading with cumulative damage defined as the summation of damage for each type of loading. Damage for each type of load was defined in terms of the Miner–Palmgren relation. The damage for various load combinations was normalized to their corresponding mean values and evaluated using a lognormal distribution, as shown in Table 2, which summarizes the variation in total damage for 3 types of metals. The standard deviation of the lognormal distribution shown in Table 2 was determined to be 14.7%, 12.3%, and 11.4%, respectively.

Shen [9] provided an extensive database of fatigue failure of the aluminum 2023-T4 alloy. Figure 1 shows the data on a log-log scale and the best-fit straight line. Using the inverse of the slope of this line as the measure of β ($1/0.11 = 9.1$), damage was calculated for each data point. The standard deviation of $\log(\text{damage})$ was determined to be 0.27. It can be noted in Figure 1 that the scatter in data is much higher for the low-stress cycles. Therefore, this analysis was repeated using only the data ≥ 371.7 MPa ($\log \Delta S \geq 2.57$), as shown in Figure 2. The slope of the line has changed to 0.18 and $\beta = 5.57$. The standard deviation of $\log(\text{damage})$ is now only 3.7% due to the lower scatter (note the small stress range for these data). Figure 3 shows how the damage remains constant in spite of the variation in the stress range due to the corresponding changes in the number of cycles to failure.

Overall, the standard deviation of $\log(\text{damage})$ varies from 10% to 30%, and smaller standard deviations are possible when the range of stress cycles is small. Therefore, the analyses in the next section will be based on the assumptions of the standard deviation $\sigma(\log_{10}\text{damage}) = 10\%$ to 30%. A comprehensive literature survey of fatigue test data is beyond the scope of this paper; the reader can use the analyses presented, henceforth, to assess the consequences for any fatigue test data relevant to their specific application.

TABLE 2: Fatigue damage data for various materials by Peng et al. [8].

300CVM steel		Aluminum-2024-T42		30NiCrMoV12 steel	
Normalized damage	Log(damage)	Normalized damage	Log(damage)	Normalized damage	Log(damage)
0.76	-0.121	0.85	-0.072	0.58	-0.238
0.82	-0.087	0.78	-0.106	0.78	-0.107
1.03	0.012	0.69	-0.164	0.83	-0.083
1.22	0.086	0.64	-0.192	0.80	-0.095
1.03	0.011	0.66	-0.178	0.74	-0.133
1.61	0.207	0.70	-0.153	1.04	0.019
1.11	0.045	0.84	-0.074	0.91	-0.041
1.30	0.114	0.74	-0.133	0.69	-0.162
1.10	0.043	0.88	-0.057	0.86	-0.068
0.46	-0.341	1.18	0.072	1.17	0.069
0.51	-0.296	1.24	0.095	1.27	0.105
0.77	-0.112	1.25	0.098	1.54	0.187
1.05	0.023	1.39	0.144	1.07	0.028
1.45	0.160	1.40	0.147	1.28	0.106
0.90	-0.046	1.29	0.109	1.41	0.150
0.76	-0.120	1.26	0.100	1.08	0.035
1.13	0.055	1.20	0.080	0.95	-0.022
		1.16	0.064	0.85	-0.072
Standard deviation	14.7%		12.3%		11.4%

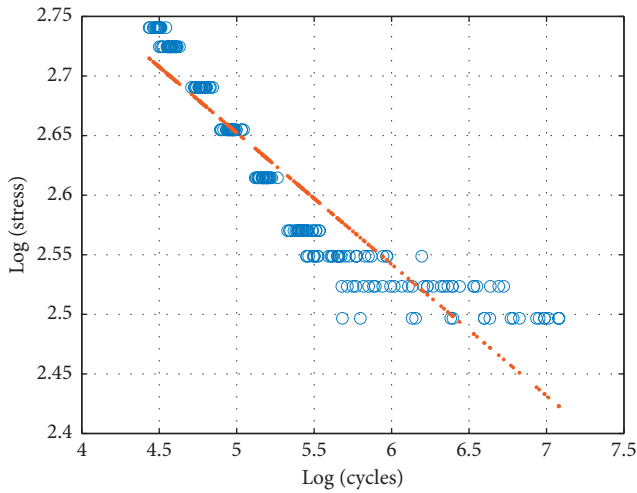


FIGURE 1: Linear fit to fatigue failure test data (entire stress range).

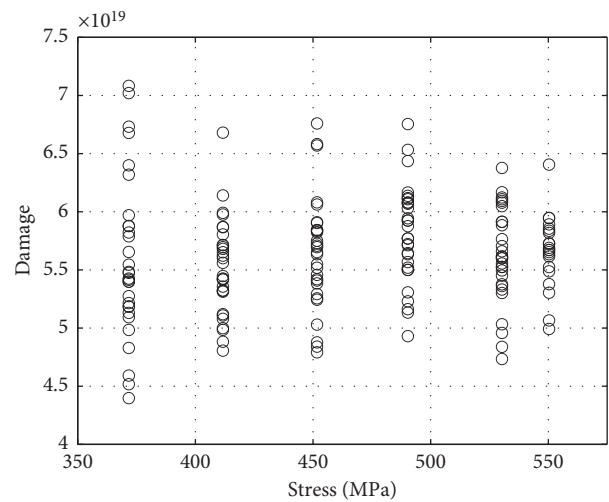


FIGURE 3: Variation in damage for various stress ranges.

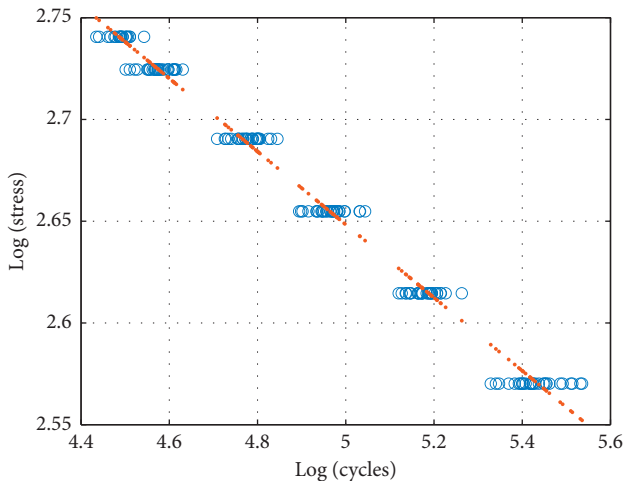


FIGURE 2: Linear fit to fatigue failure test data (higher stress range).

3. Damage Corresponding to Different Decay Rates for the Same SRS

Shock testing specifications are based on the concept of the shock response spectra (SRS) which no longer contains the time history. The SRS were originally conceived to address the need to convey the effect of earthquake damage to civil infrastructure [10, 11] in a concise manner. The SRS are typically based on the maxi-max absolute acceleration (MMAA) of the response of an SDOF (single degree of freedom) structure to the shock acceleration vs. time. As a result, the SRS do not contain any information on the decay rate of the original wave. Different component frequencies in a shock wave may attenuate at different rates. For instance, the high-frequency component typically attenuates faster; however, the decay at different frequencies is also dependent on through what media or structure the shock wave has been

transmitted. Therefore, the issues addressed in this paper pertain to the following.

Damage Index (DI) is defined in the context of Miner's rule for low-cycle fatigue damage as discussed earlier (parameter C in equation (1)). For the same SRS, how is the imparted "Damage Index" (C) affected by the varying decay rate of the different component frequencies? An implicit part of this question is the determination of what causes differences in SRS and DI as the decay rate changes. The value of the material-dependent exponent β was chosen to be 6.66.

While this paper studies the influence of damping as an input parameter to shock and consequent damage, damping has also been extensively studied as a consequence of damage. Kouris et al. [12] investigated the variation in modal damping as a measure of structural damage by applying progressively greater vibration load to a building leading to "near-collapse damage state." Variation in damping was proven to be a better measure of structural damage than the shift in natural frequency/modes [13].

3.1. Effect of Damping on the SRS. Four different acceleration time-histories with the same SRS were investigated. These acceleration vs. time data $\ddot{x}(t)$ were generated using decayed sines (equation (5)), where ω is the frequency in radians and ξ is damping. The exponential decay parameter α represents the final amplitude/initial amplitude ratio after a certain time period. Five sine waves (at 100, 200, 400, 650, and 950 Hz) were added to create the total acceleration time history. Trial 1 had the amplitude of each of the 5 sine waves (acc 1–5) set to 10. As shown in Table 3, the damping of each frequency ξ was inversely proportional to the frequency as per equation (5). The exponential decay parameter α determines how the sine waves decay as per equation (5). Therefore, since $\xi\omega = \alpha$ was constant for each of the 5 constituent sine waves, each of them decay to the same level at the end of the 0.08 sec duration under consideration. Figure 4 shows 3 of the 5 sine waves each decaying to the same amplitude after 0.08 sec.

$$\begin{aligned} \ddot{x}(t) &= \sin \omega t e^{-\xi \omega t}, \quad \text{where } \xi \omega \\ &= \alpha = \text{Constant Exp Decay.} \end{aligned} \quad (5)$$

For Trial 2, the damping of the 2 highest frequencies (650 and 950 Hz) was increased by a factor of 3. As a result, these waves decayed faster (Figure 5). However, the amplitude of these two components was increased (Table 3) such that the resulting SRS were identical to that of Trial 1. Figure 5, therefore, shows a higher amplitude for the 950 Hz signal (blue); note that the actual peak is somewhat less than that of the table because of the rapid decay of the high-frequency content.

For Trial 3, the damping of the 2 highest frequencies (650 and 950 Hz) was increased by a factor of 4 relative to Trial 1. Once again, the amplitude of these two components was increased (Table 3) such that the resulting SRS were identical to that of Trial 1. The SRS of Trials 1–3 are shown in Figure 6. The 2 waveforms (Trial 1 and Trial 2) are shown side by side in Figure 7. Due to the increase in the amplitude of the high-frequency component, Trial 2 had a higher maximum

TABLE 3: Synthesis of four waveforms with the same SRS.

Frequency (Hz)	100	200	400	650	950
Trial 1: proportional damping to get the same decay					
Damping	0.07500	0.03750	0.01875	0.01154	0.00750
Amplitude	10	10	10	10	10
Trial 2: X3 damping of Trial 1 at 650 and 950 Hz					
Damping	0.075	0.0375	0.01875	0.03462	0.0225
Amplitude	10	10	10	13.6	13.2
Trial 3: X4 damping of Trial 1 at 650 and 950 Hz					
Damping	0.075	0.0375	0.01875	0.04616	0.03
Amplitude	10	10	10	15.4	14.7
Trial 4: X2 damping of Trial 1 at 100 and 200 Hz					
Damping	0.15	0.075	0.01875	0.01154	0.0075
Amplitude	14	14	10	10	10

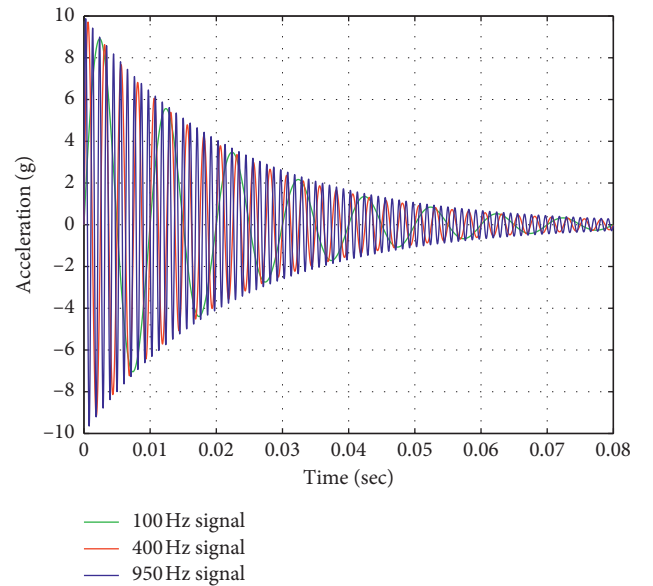


FIGURE 4: Accelerations at 100, 400, and 950 Hz decaying to the same final amplitude.

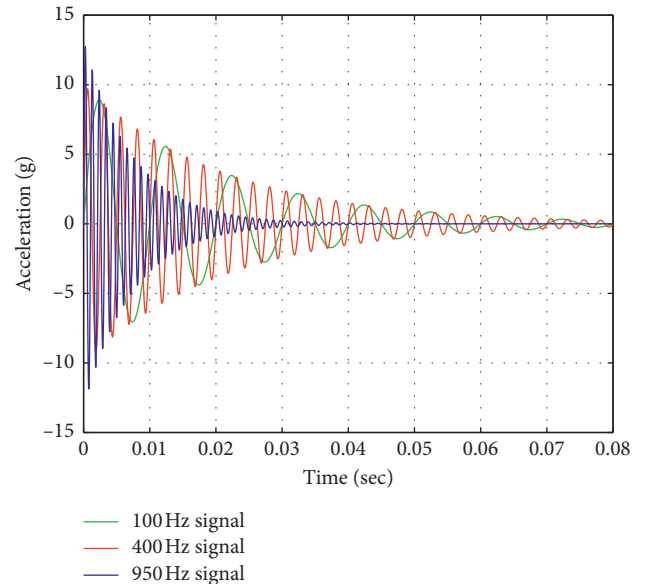


FIGURE 5: Accelerations at 950 Hz decaying faster than 100 and 400 Hz.

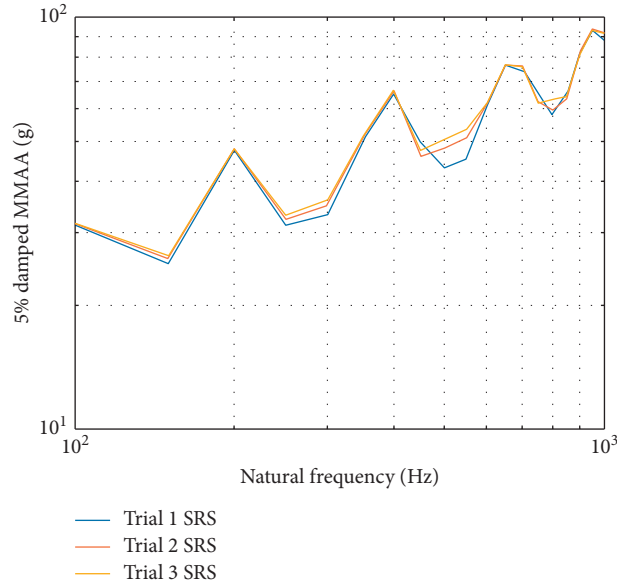


FIGURE 6: SRS of waveforms from Trial 1, Trial 2, and Trial 3.

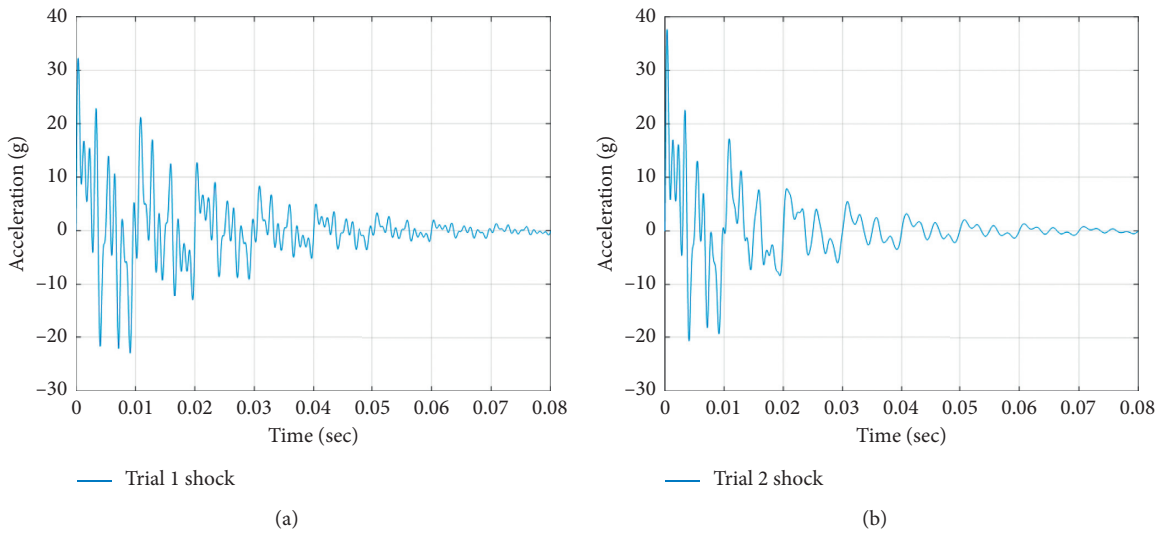


FIGURE 7: Waveforms from Trial 1 vs. Trial 2.

acceleration, which contributed to a greater Damage Index as will be discussed next.

The SRS were computed using the MMAA after the following convolution integral that captures the response of a single degree of freedom (SDOF) spring-mass structure $\ddot{y}(t)$ due to input acceleration $\ddot{x}(t)$ shown in the following equation, where ω is the natural frequency of the SDOF structure and ξ is the damping constant:

$$\ddot{y}(t) = \frac{-\omega}{\sqrt{1-\xi^2}} \int_0^t \ddot{x}(\tau) e^{-\xi\omega(t-\tau)} \sin \omega\sqrt{1-\xi^2}(t-\tau) d\tau. \quad (6)$$

Next, using the rain flow count algorithm in Matlab™, the # and amplitude of cycles (N and σ in equation (1)) were

determined from the acceleration vs. time such as those shown in Figure 7. The results for all 4 trials are shown in Figure 8. Using these data and equation (1), the Damage Index (DI) was determined to be 2.90×10^{11} , 3.39×10^{11} , 3.99×10^{11} , and 3.24×10^{11} for Trial 1 through Trial 4, respectively. The approximately 17% increase in DI for Trial 2 is due to the higher initial peak in the shock wave leading to more high-stress cycles (50–60); note that Trial 2 has a smaller # of cycles at the stress range of 0–10. The contribution of low-stress cycles to the DI is minimal due to the exponent $\beta = 6.66$ in the equation for DI. Likewise, the 38% increase in DI for Trial 3 is due to the high-stress cycle (60–70) which was not present for Trial 1.

For Trial 4, the damping of the two lowest frequencies was increased by a factor of 2 (Table 3). Figure 9 shows the

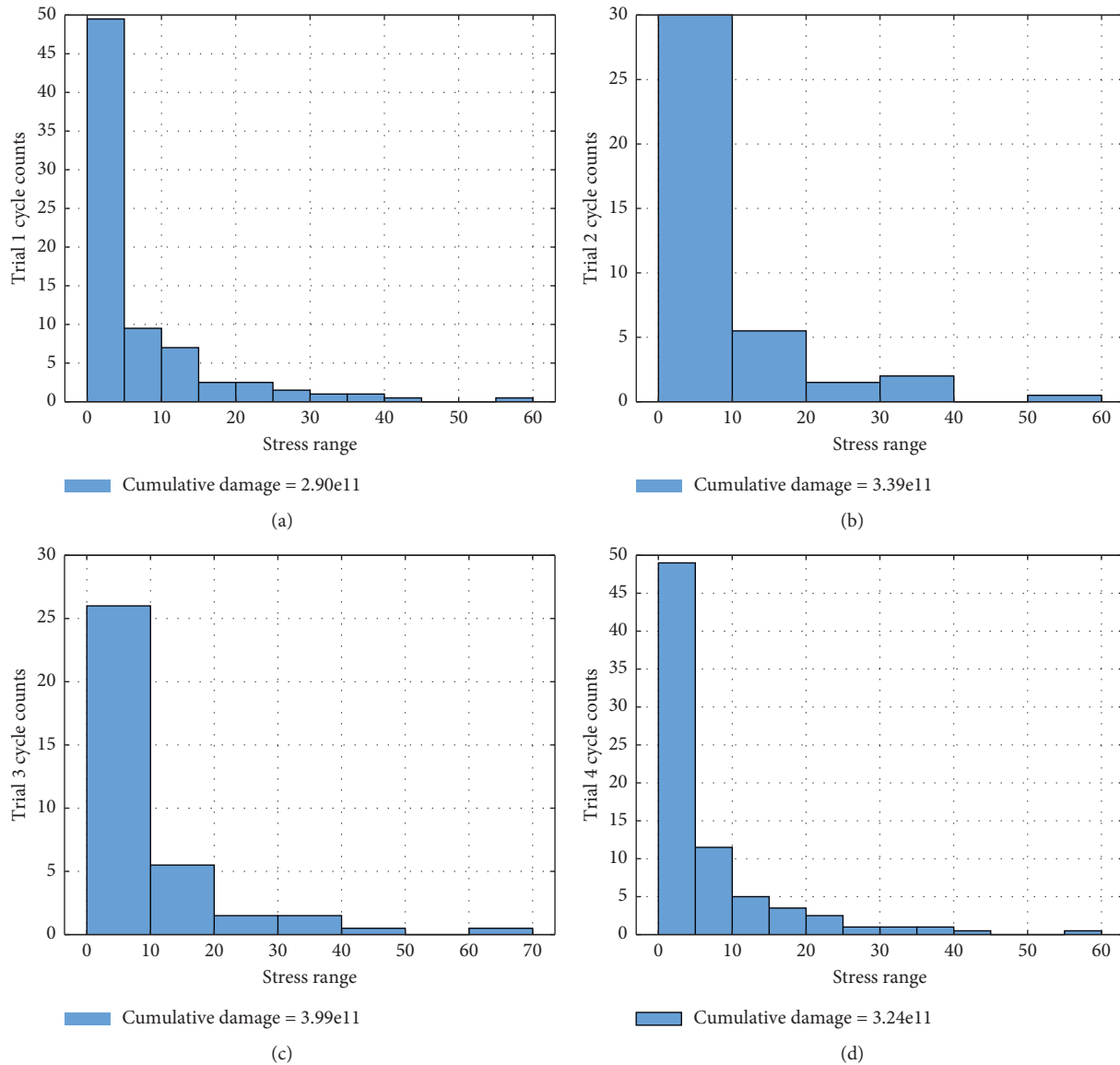


FIGURE 8: Stress range (σ) and corresponding cycle count (n) from 4 trials.

resulting shock wave and the rapidly decayed 100 Hz component, which required the amplitude at that frequency to increase (to keep the same SRS). This led to the DI increasing to 3.24×10^{11} (12% higher than that of Trial 1).

4. Consequence of Damage Variations in Test Reliability Levels

4.1. *Probability of Exceeding Damage Threshold.* The previous sections showed the following:

- (i) Different acceleration vs. time data from the same SRS can lead to differences in the “Damage Index.”
- (ii) Variations in materials and structures result in a variation in the “Damage Index” at failure (for static loads, this is analogous to failure of any material at different stress levels).

This section provides a discussion on how a variation in the fatigue-based “Damage Index” in the previous section affects the overall assessment of the probability failure. We will use the concept of P99 level as the probability of failure less than 1%. Conducting a shock test to P99 level implies that the test exceeds the real-life environment 99% of the time. So, when there is a 20% variation in the Damage Index from the different recreations of acceleration vs. time from the same SRS (based on the range of 12% to 38% variations in DI discussed earlier), how does that affect the probability of failure? This issue will be investigated in the next section considering the effect of 20% variation in the fatigue damage imparted during a test.

First, lognormal statistics is discussed briefly in terms of natural log(base e), defined as $y = \ln(x)$, where x is lognormal if y follows the normal distribution. Closed-form equations provided below provide some valuable insights that can then

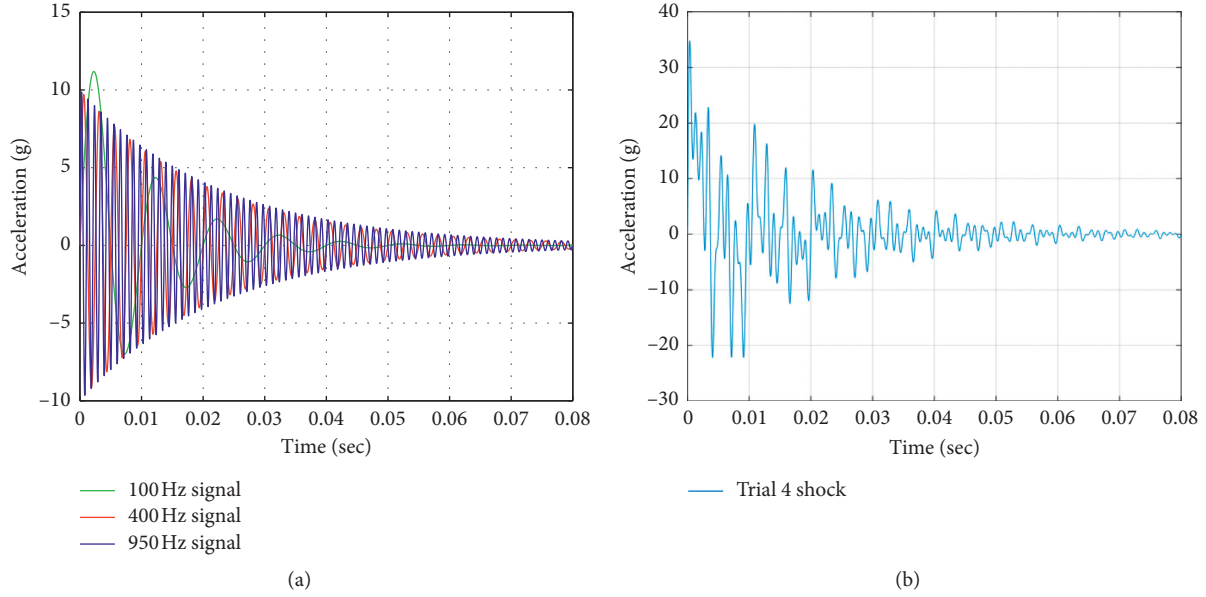


FIGURE 9: Trial 4: amplified peak at 100 Hz component and overall signal.

be extended to the definition of lognormal statistics $y = \log_{10}(x)$. If the mean and standard deviation of y is μ and σ , the mean and standard deviation of $x (=e^y)$ is μ' and σ' . Equations for probability distribution function (PDF) and cumulative PDF (CDF) are also provided as follows:

$$\text{mean of } x: \mu' = e^{(\mu + \sigma^2/2)}, \quad (7)$$

$$\text{standard deviation of } x: \sigma' = \sqrt{[e^{\sigma^2} - 1]} e^{(2\mu + \sigma^2)},$$

$$\text{coefficient of variation in } x: \frac{\sigma'}{\mu'} = \sqrt{[e^{\sigma^2} - 1]}, \quad (8)$$

$$\begin{aligned} &\text{probability distribution function (PDF): PDF}(x) \\ &= \frac{1}{x\sigma\sqrt{2\pi}} e^{-(\ln(x) - \mu)^2/2\sigma^2}, \end{aligned} \quad (9)$$

$$\text{cumulative PDF (CDF): CDF}(x) = \frac{1}{2} + \frac{1}{2} \operatorname{erf} \left[\frac{\ln(x) - \mu}{\sqrt{2}\sigma} \right]. \quad (10)$$

As per equation (8), the coefficient of variation in x is independent of the mean μ of the underlying data y . Consequently, a change in μ only leads to a stretching of the CDF, which is also evident from equation (10) since a change in μ is offset by a corresponding change in $\ln(x) = y$. Figure 10 shows this for a simulation using 10^6 randomly generated values of y (using MatLab™ randn) from which x is computed ($=e^y$). The PDF and CDF (vs. x) are shown for $\sigma = 0.25$ and $\mu = 0$, and 1. The larger $\mu (=1)$ shows a larger spread in the lognormal data as well as a shift in the mean value to the right. The CDF shows that the 50% values for both equal $x = e^\mu (=1.0$ and 2.72 , respectively; red lines). If the value of x is increased by 20% to 1.2 and 3.26 (red dotted

lines), the corresponding CDFs remain the same (0.77). Hence, a proportionate change in x leads to the same change in CDF. This will also be observed when the definition is changed to $\log_{10}(x) = y$.

In order to investigate how the Matlab™ simulation of statistical distribution converges with an increase in the number of data (varied from 10^3 to 10^7), the theoretical values of the mean and standard deviation of x (μ' and σ') were obtained using equation (7) and normally distributed y (with $\mu = 0$ and $\sigma = 1$). These were then compared with the mean and standard deviation of x based on the Matlab™ random number generator to create y . Figure 11 shows how this ratio converges to 1.0 for 10^7 data points. Henceforth, simulations were conducted with 10^7 data points.

4.2. Simulation of the Effect of a 20% Change in C on Probability of Failure. The simulation involved the following steps.

The PDF and CDF of 10^7 data points were generated using $\mu = 0$ and varying σ (0.1 to 0.3).

Using the CRF, the value of x corresponding to a 1% probability of failure (1% probability of the material's fatigue life being below that of the fatigue damage corresponding to the SRS) was determined. Note that this corresponds to the P99 level (99% probability of the material's fatigue life being higher than that of the fatigue damage corresponding to the SRS).

For a 20% increase in x (i.e., $1.2x$), the probability of failure was determined. For instance, if the new probability of failure corresponding to $1.2x$ is 5%, it means that the 20% increase in x resulted in the P99 changing to P95. Figure 12 shows the probability of failure for different combinations of μ and σ (10 simulations for each). Note that an increase in σ from 0.25 to 1.0 reduces the probability of failure. This is because with increased scatter in the fatigue strength of the material, a 20% change in the damage imparted is less

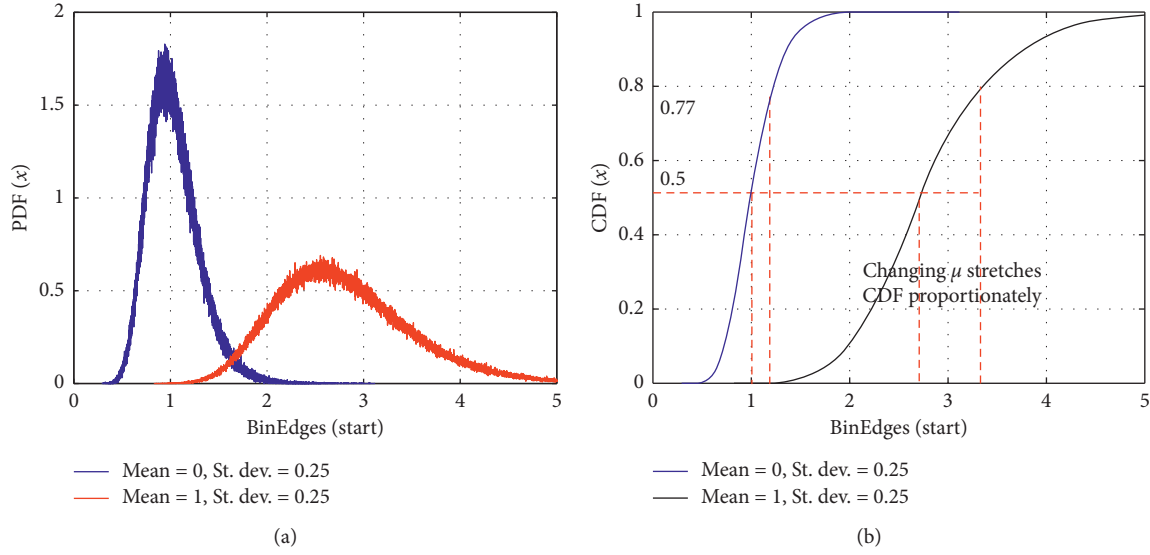


FIGURE 10: PDF and CDF with changing mean (0 and 1) and same standard deviation.

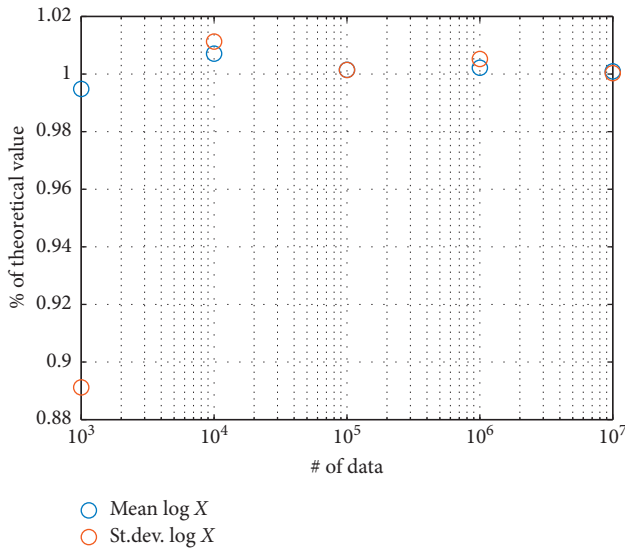


FIGURE 11: Convergence of mean and standard deviation to theoretical values.

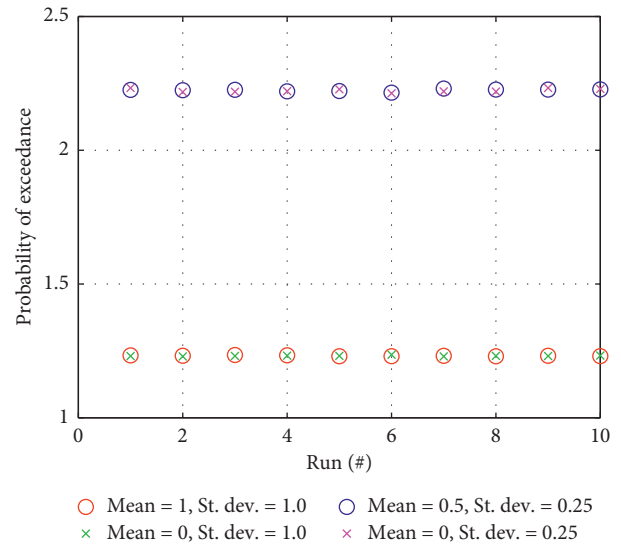


FIGURE 12: Probability of failure (damage exceeding material capacity).

consequential. Note that the change in the mean value is inconsequential due to reasons discussed in the previous section (coefficient of variation is independent of the mean).

Therefore, the remaining simulations (10 runs each) were done with $\mu = 0$ and varying σ from 0.1 to 0.3; results are shown in Figure 13. As the scatter in the material's fatigue strength decreases (decreasing σ), the consequence of the 20% change in x is progressively more consequential. For $\sigma = 0.1$, P99 changes to worse than P94, while for $\sigma = 0.3$, P99 changes only to P98.

5. Capturing Rate of Decay of Shock

A method is suggested for capturing the decay rate associated with the different component frequencies. This would allow

the original waveform to be replicated more accurately. The SRS at each frequency are a function of both the amplitude and damping associated with that frequency. The same is also true for the FFT of a decaying shock wave. As the shock wave decays with time, the amplitude of the FFT decreases; this can be utilized to capture the damping at each frequency.

The input signal at each frequency ω is a decaying sine wave of amplitude A enveloped by an exponential decay. The decaying envelope I of each sine wave can be characterized by the damping parameter ξ according to the following equation:

$$I = Ae^{-\xi\omega t}. \tag{11}$$

Integrating equation (11) from the start to time T , one obtains the mean value of the envelope over the time period

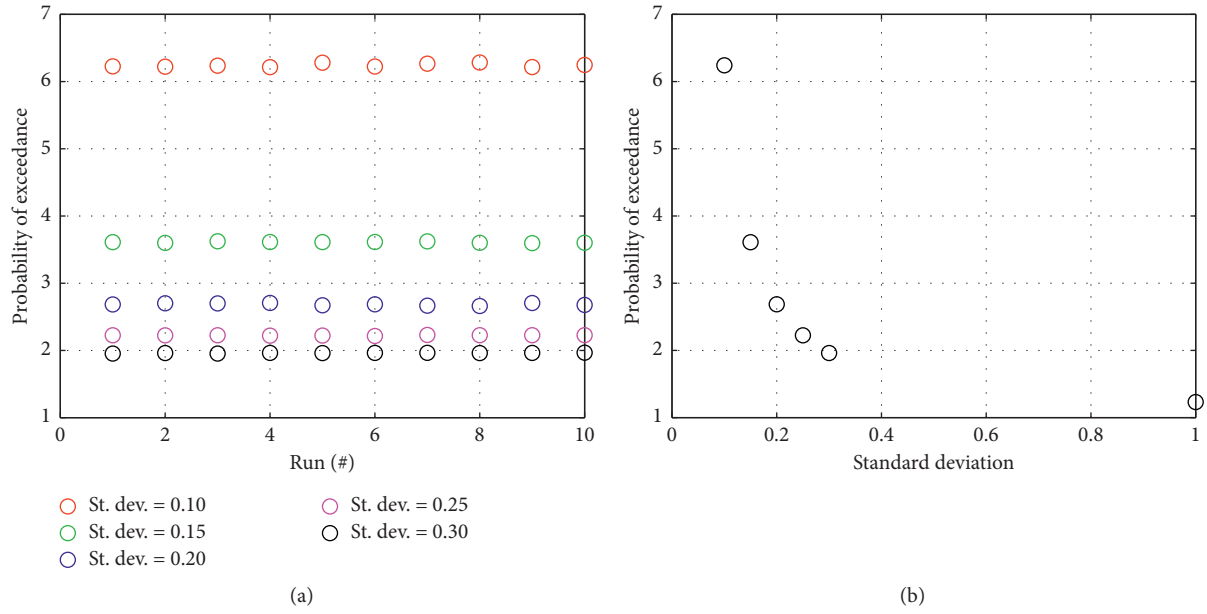


FIGURE 13: Probability of failure (damage exceeding material capacity).

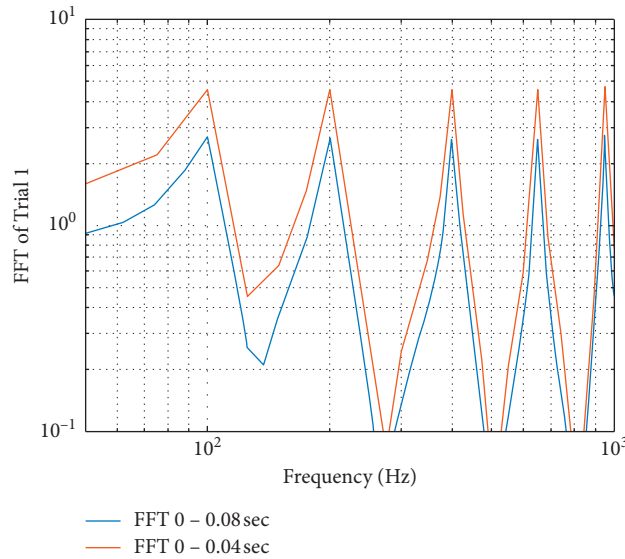


FIGURE 14: FFT of Trial 1 signal (full and 1/2 duration).

$[0, T]$, as shown in equation (2). This mean value represents the amplitude of the Fourier transform of the decaying sine wave over this interval ($P/A < 1$ because of the decay):

$$P = \frac{A}{T} \int_0^T e^{-\xi\omega t} dt = \frac{A}{\xi\omega T} (1 - e^{-\xi\omega T}). \quad (12)$$

Equation (12) has two unknowns: amplitude A and damping ξ of the sine wave and, therefore, needs to be evaluated at two different points. Therefore, by conducting a fast Fourier transform (FFT) of the shock wave at two different time intervals $[0, T_1]$ and $[0, T_2]$, one can obtain two corresponding values of the mean amplitude of the sine waves P_1 and P_2 . Based on equation (2), equation (3)

represents these two specific situations. The unknown damping ξ is then evaluated by numerically solving the following equation:

$$\frac{1 - e^{-\xi\omega T_1}}{1 - e^{-\xi\omega T_2}} = \frac{P_1 T_1}{P_2 T_2}. \quad (13)$$

Figures 14 and 15 show the FFT of the input signal from Trial 1 and Trial 2, respectively, from 0 to 0.08 sec and from 0 to 0.04 sec, respectively. The lower numbers for 0–0.08 sec are due to the greater decay over the full duration. The peak values in Figure 14 are the same for both durations due to proportional damping and constant amplitude of each sine wave. The peak values in Figure 15 are lower for the 2 high

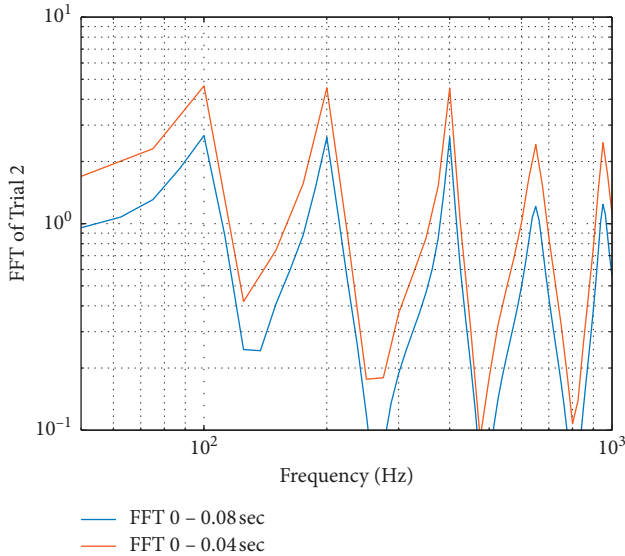


FIGURE 15: FFT of Trial 2 signal (full and 1/2 duration).

TABLE 4: Comparison of actual decay rates with those computed from FFT.

	Frequencies				
	100 Hz	200 Hz	400 Hz	650 Hz	950 Hz
Trial 1 actual	0.07500	0.03750	0.01875	0.01154	0.00750
Trial 1 from FFT	0.07499	0.03750	0.01875	0.01154	0.00750
Trial 2 actual	0.075	0.0375	0.01875	0.03462	0.0225
Trial 2 from FFT	0.0756	0.0376	0.0188	0.0346	0.0222
Trial 3 actual	0.075	0.0375	0.01875	0.04616	0.03
Trial 3 from FFT	0.0757	0.0377	0.0189	0.0496	0.0280
Trial 4 actual	0.15	0.075	0.01875	0.01154	0.0075
Trial 4 from FFT	0.1433	0.0741	0.0188	0.0115	0.0075

frequencies due to the larger damping; the values for the full duration are even lower. The damping values determined using the methodology described above are shown in Table 4; both the actual and the estimated damping values are provided for comparison. The method captures the damping values very accurately for all 4 trials. The only time the estimated damping is slightly different (shaded orange) is when the duration of 0.04 sec does not include sufficient waves to be statistically representative.

6. Conclusions

- (i) Assuming longer duration equates to a smaller damping for the same SRS. This leads to a lower Damage Index (DI) and unconservative test (high-stress cycles are eliminated).
- (ii) An increase in damping leads to an increase in DI (approximately 17% and 38% for Trial 2 and Trial 3 compared to Trial 1) due to an increase in peak acceleration values. A few high cycles can dominate the Damage Index due to the exponent β .

- (iii) An increase in DI can significantly impact the estimated reliability of the test for realistic lognormal statistics of fatigue test data observed in tests of different materials. A perceived P99 test can become a P95 test or worse.
- (iv) The influence of an increase in DI on reliability is less if the underlying data correlating DI to failure have a larger scatter (higher σ). Large variation in material property makes the accuracy of the test specification less consequential. The analysis process presented in this paper provides a methodology to evaluate the appropriate level of rigor and accuracy for shock test specification.
- (v) The coefficient of variation in a lognormal distribution is independent of the mean of the underlying normal distribution. This implies that the mean fatigue damage μ is of no consequence to the issue (changes in the PXX level) discussed in this paper.
- (vi) Using the Fourier transform of shock signals over two different durations, it is possible to compute the damping associated with the frequencies of interest with high accuracy. This would allow original waveforms to be captured more accurately vs. just the SRS.

Data Availability

All data in the paper unless explicitly cited and referenced were generated in this study by the author.

Disclosure

Sandia National Laboratories is a multimission laboratory managed and operated by National Technology and Engineering Solutions of Sandia, LLC, a wholly owned subsidiary of Honeywell International Inc., for the U.S. Department of Energy's National Nuclear Security Administration under contract DE-NA0003525. This paper describes objective technical results and analysis. Any subjective views or opinions that might be expressed in the paper do not necessarily represent the views of the U.S. Department of Energy or the United States Government.

Conflicts of Interest

The authors declare that they have no conflicts of interest.

References

- [1] O. H. Basquin, *The Exponential Law of Endurance Tests*, American Society for Testing Materials, Philadelphia, PA, USA, 1910.
- [2] M. A. Miner, "Cumulative damage in fatigue," *Journal of Applied Mechanics*, vol. 3, pp. 159–164, 1945.
- [3] P. Paris and F. Erdogan, "A critical analysis of crack propagation laws," *Journal of Basic Engineering*, vol. 85, no. 4, pp. 528–533, 1963.
- [4] ASTM, *ASTM Practice for Statistical Analysis of Linear or Linearized Stress-Life (S-N) and Strain-Life (ϵ -N) Fatigue*

- Data*, ASTM E-739-91, ASTM, West Conshohocken, PA, USA, 1998.
- [5] J. Brozzetti, M. A. Hirt, I. Ryan, G. Sedlacek, and I. Smith, *Background Information on Fatigue Design Rules-Statistical Evaluation-Chapter 9-Document 9.01*, ECCS, Colorado Springs, CO, USA, 1989.
 - [6] J. Szala and G. Szala, "A fatigue life calculation method for structural elements made of D16CzATW aluminum alloy," *Polish Maritime Research*, vol. 17, no. 3, 2010.
 - [7] D. Leonetti, S. B. Hashemi, D. Allaix, and J. Maljaars, "Fatigue damage evaluation using S-N curves obtained by different data fitting methods," in *Proceedings of the 39th IABSE Symposium*, Vancouver, Canada, September 2017.
 - [8] Z. Peng, H.-Z. Huang, J. Zhou, and Y.-F. Li, "A new cumulative fatigue damage rule based on dynamic residual S-N curve and material memory concept," *Metals*, vol. 8, no. 6, p. 456, 2018.
 - [9] C. Shen, *The Statistical Analysis of Fatigue Data*, University Microfilms International, Ann Arbor, MI, USA, 1994.
 - [10] C. Lalanne, "Shock and vibration," in *Vibration and Shock Handbook*, C. De Silva, Ed., McGraw-Hill, New York, NY, USA, 2005.
 - [11] J. Edward Alexander, "Shock response spectrum-a primer," *Sound and Vibration*, vol. 43, no. 6, pp. 5–14, 2009.
 - [12] L. A. S. Kouris, A. Penna, and G. Magenes, "Seismic damage diagnosis of a masonry building using short-term damping measurements," *Journal of Sound and Vibration*, vol. 394, pp. 366–391, 2017.
 - [13] L. A. S. Kouris, A. Penna, and G. Magenes, "Dynamic modification and damage propagation of a two-storey full-scale masonry building," *Advances in Civil Engineering*, vol. 2019, Article ID 2396452, 21 pages, 2019.

Research Article

Numerical Study on Acoustic Resonance Excitation in Closed Side Branch Pipeline Conveying Natural Gas

Liuyi Jiang ¹, Hong Zhang,² Qingquan Duan,¹ and Yulong Zhang ^{1,3}

¹College of Safety and Ocean Engineering, China University of Petroleum, Beijing 102249, China

²National Engineering Laboratory for Pipeline Safety, MOE Key Laboratory of Petroleum Engineering, Beijing Key Laboratory of Urban Oil and Gas Distribution Technology, China University of Petroleum (Beijing), Beijing 102249, China

³Australian Maritime College, Newnham, Tasmania 7248, Australia

Correspondence should be addressed to Liuyi Jiang; jiangliuyi409@163.com

Received 23 April 2020; Revised 20 September 2020; Accepted 22 September 2020; Published 23 October 2020

Academic Editor: Sinniah Ilanko

Copyright © 2020 Liuyi Jiang et al. This is an open access article distributed under the Creative Commons Attribution License, which permits unrestricted use, distribution, and reproduction in any medium, provided the original work is properly cited.

Flow-induced acoustic resonance in the closed side branch of a natural gas pipeline can cause intensive vibration which threatens the safe operation of the pipeline. Accurately modeling this excitation process is necessary for a workable understanding of the genetic mechanism to resolve this problem. A realizable $k-\varepsilon$ Delayed Detached Eddy Simulation (DDES) model was conducted in this study to numerically simulate the acoustic resonance problem. The model is shown to accurately capture the acoustic resonance phenomenon and self-excited vibration characteristics with low calculation cost. The pressure pulsation component of the acoustic resonance frequency is gradually amplified and transformed into a narrowband dominant frequency in the process of acoustic resonance excitation, forming a so-called “frequency lock-in phenomenon.” The gas is pressed into and out of the branch in sinusoidal mode during excitation. The first-order frequency, single vortex moves at the branch inlet following the same pattern. A quarter wavelength steady standing wave forms in the branch. The mechanism and characteristics presented in this paper may provide guidelines for developing new excitation suppression methods.

1. Introduction

Natural gas is a clean, efficient, and high-quality energy resource which is a preferred fuel by many countries across the globe [1, 2]. The mileage of natural gas pipeline construction projects has rapidly increased alongside the demand for fuel in recent decades. For example, the length of natural gas pipeline in-service has reached 81,000 km in China; 3,233 km of this length was newly built in 2019. The closed side branch of a natural gas pipeline is a commonly used unit of gas transmission. Flow-induced acoustic resonance occurs as gas flows through the mouth of a closed branch at a certain velocity, causing intensive and continuous gas pressure pulsations that may result severe pipeline vibration and even fatigue damage [3–6]. These pulsations are also noisy and intense enough to endanger the physical and mental health of workers. A serious acoustic resonance event occurred in the WKC2 gas transmission station of China in 2012 which fractured a tee connector (Figure 1).

There is substantial practical importance in accurately, comprehensively understanding the mechanism of acoustic resonance and the most effective approaches to suppressing it [7–12]. The essential mechanism of acoustic resonance in the closed side branch is the coupling effect of the flow field and sound field. The shear layer detaches from the upstream pipe wall, exciting a sound vortex that travels downstream and is coupled with the gas in the side branch; this causes acoustic vortex convection along the branch. The sound vortex is gradually excited as it detaches. The convection of the vortex (vortices) generates and absorbs sound energy to maintain continuous pressure pulsation [13].

The key to effectively understanding the shear layer detachment process lies in accurately modeling the sound source excitation and hydrodynamic modal in the branch mouth. Deriving a solvable differential equation of sound source excitation analytically is almost impossible, as the turbulence flow in the main pipe is excessively complex. The vortex acoustic

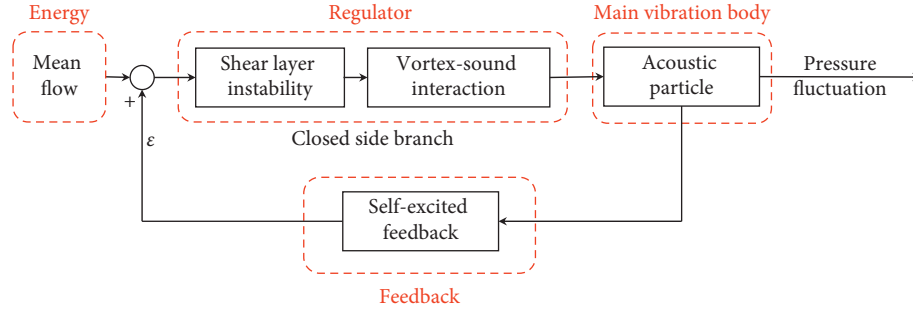


FIGURE 1: Schematic diagram of feedback mechanism.

theory developed by Powell [14] and Howe [15] has been widely used in the acoustic field, including acoustic resonance problems, but it is still difficult to solve vortex acoustic equations. Michalke [16] used linear stability theory to model a shear layer flow. Karlsson and Åbom [17] developed expressions for the side branch acoustic impedance under various velocities, and investigated the interaction between acoustic impedance and sound source excitation. Considering the nonlinearity of this problem, Graf and Ziada [18] proposed a semiempirical model for predicting the amplitude and phase of pressure fluctuations in tandem side branches and coaxial branches. Their model includes sound source excitation as the nonlinear pressure difference between the upper side and lower side of the detached shear layer in the branch mouth and can predict the acoustic amplitude and frequency of the pressure in the two branches.

Visual flow experiments and computational fluid dynamics (CFD) are the most common approaches to hydrodynamic modal analysis. In visual experiments, the morphology of the acoustic vortex and flow patterns of the fluid during the acoustic resonance can be clearly observed via high-speed camera. Ziada [19], for example, found that the mechanism of acoustic resonance is different from that of nonresonant oscillation of impact shear flow; visual analysis revealed that pressure fluctuation in closed side branches was caused by the coupling of the unstable detachment of shear layer from the upstream wall and standing acoustic waves in the side branch. During the unstable detachment of the shear layer, an acoustic vortex is excited as it is trapped in the mouth of the side branch. Li et al. [20–22] studied the flow patterns of acoustic resonance in tandem side branches and coaxial side branches using a high time-resolved particle image velocimetry (PIV) technique. They captured the velocity distribution in the flow field and constructed a phase delay diagram. Salt et al. [23, 24] also used PIV to observe the acoustic energy transfer pattern during an acoustic resonance cycle as per the sound source generation and absorption with shear layer oscillation. Xiao et al. [25] similarly obtained a multimodal image of shear layer detachment under the acoustic resonance of a square single closed side branch.

Flow patterns in closed side branches can be analyzed effectively via CFD methods. For example, Tamura et al. [26] modeled the acoustic resonance in three side branches based on a three-dimensional (3D) model using the finite difference lattice Boltzmann method. Kriesels et al. [5] simulated the gas

flow and calculated the sound power generated by a vortex using the vortex-blob method based on a 2D potential flow model. Radavich et al. [27] simulated the 2D flow of a single closed side branch by solving Navier–Stokes equations of unsteady and compressible turbulence. Dequand et al. [28] simulated a 2D compressible coaxial closed side branch flow via Euler equation. Numerical simulations accurately predicted the range of frequency lock-in velocity and flow patterns.

Previous research has mainly centered on the formation conditions, pressure fluctuation amplitudes, and frequencies of acoustic resonance. Few scholars have modeled the acoustic resonance excitation process. Radavich et al. [27] briefly discussed the coupling of sound waves and flow in the excitation process and simulated the variations in pressure pulsation during excitation, but there has been no extensive research on the mechanism and excitation process of acoustic resonance. Such knowledge has great significance in regards to establishing an accurate, descriptive model.

This paper presents a numerical simulation of the excitation process of acoustic resonance in a closed side branch of natural gas pipeline using the commercial CFD code FLUENT. Due to safety concerns, researchers often use air instead of natural gas as a fluid medium in physical tests. Our findings show that the ingredients of the fluid medium have a pronounced impact on acoustic resonance characteristics.

Figure 1 shows a functional block diagram of the feedback mechanism of the system under analysis here. The red dotted frame marks the self-excitation system given by Ding [29], and the black solid frame is the feedback mechanism of acoustic resonance in the closed side branch. The mean flow kinetic energy in the main pipeline provides constant energy for the system. The closed side branch structure is a regulator. The acoustic particles in the pipe are the main vibration body. The pressure fluctuation (acoustic standing wave) in the closed side branch is fed back to the regulator to control the continuity of the fluctuation. The flow-induced acoustic resonance has self-excited vibration characteristics, so a self-excited vibration model was used in this study.

2. Mathematical Models

2.1. Geometry Model Simplification. Figure 2(a) shows a typical closed side branch of a natural gas pipeline in which acoustic resonance occurs. Considering its actual dimensions, which are usually larger than 0.5 m in diameter and

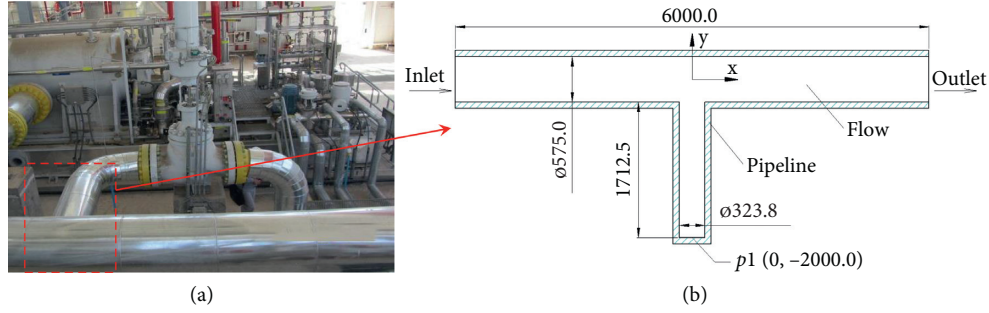


FIGURE 2: Schematic diagram showing the geometry of the closed side branch of a natural gas pipeline: (a) physical structure of the branch pipe in situ; (b) simplified geometry of the branch pipe (unit: mm).

1.5 m in length, the elbow at the end of the side branch can be neglected. The simplified geometry of closed side branch is shown in Figure 2(b). The model consists of two parts: the main pipe and the closed side branch. The length and inner diameter of the main pipe are 6000.0 mm and 575.0 mm, respectively. The branch pipe is located at the center of the main pipe and has a length and inner diameter of 1712.5 mm and 323.8 mm, respectively. The flow medium is methane (the main component of natural gas), which is input steadily from the inlet side and flows continuously to the outlet side. The coordinate system is shown in Figure 2(b), where the x -axis falls along the center line of the main pipe and the y -axis along the center line of the branch pipe. The pressure-monitoring point $p1 (0, -2000, 0)$ is located at the bottom of the center of the side branch.

2.2. CFD Turbulence Model Configuration. Reynolds Average Navier–Stokes (RANS), Detached Eddy Simulation (DES), and Large Eddy Simulation (LES) [30, 31] are the most commonly used CFD models. Among them, RANS is most often applied due to its minimal computational cost. However, it is often unable to accurately predict pressure fluctuations in transient flow fields. We found that the pressure fluctuation amplitude of acoustic resonance in a closed side branch, as calculated by RANS, gradually decreases over time and ultimately attenuates to 0. We considered a hybrid model of the subregional computation of RANS and LES, in this study, so DES was a workable solution. DES solves near-wall flow field by RANS and other flow fields by LES, thus avoiding the need for an overly fine grid near the LES wall and striking a balance between numerical calculation cost and accuracy [32]. In near-wall flow fields, a realizable k - ε model can accurately simulate boundary-free shear flows [33]. A realizable k - ε DDES model [34–36] was used in this study to investigate acoustic resonance in the closed side branch.

3. Governing Equations for the Acoustic Resonance Process

3.1. Conservation Equations. The mass, momentum, and energy conservation equations as well as ideal gas law that the acoustic resonance process complies with can be written as follows:

$$\frac{\partial \rho}{\partial t} + \frac{\partial}{\partial x_j} (\rho u_j) = 0, \quad (1)$$

$$\frac{\partial}{\partial t} (\rho u_i) + \frac{\partial}{\partial x_j} (\rho u_i u_j) = -\frac{\partial p}{\partial x_i} + \frac{\partial \tau_{ij}}{\partial x_j}, \quad (2)$$

$$\frac{\partial}{\partial t} (\rho E) + \frac{\partial}{\partial x_i} (u_i (\rho E + p)) = \frac{\partial}{\partial x_i} \left(k_{\text{eff}} \frac{\partial T}{\partial x_i} - hJ + u_j (\tau_{ij})_{\text{eff}} \right), \quad (3)$$

$$p = \rho T \frac{R}{M}, \quad (4)$$

where ρ is the gas density, t is the time, p is the pressure, τ is the viscous stress tensor, E is the sum of internal energy and kinetic energy, T is the temperature, h is the gas enthalpy, J is the diffusion energy, k_{eff} is the effective thermal conductivity, τ_{eff} is the effective viscous dissipation coefficient, R is the universal gas constant, and M is the molecular weight.

3.2. Transport Equations. The flows discussed here are characterized by high Reynolds number turbulence, as their Reynolds numbers range from $2.03 \text{E}+07$ to $1.42 \text{E}+08$. Additional transport equations are needed to construct the turbulence closure models. The DDES model adopts the following dual realizable k - ε equations [34]:

$$\frac{\partial (\rho k)}{\partial t} + \frac{\partial (\rho k u_i)}{\partial x_i} = \frac{\partial}{\partial x_j} \left[\left(\mu + \frac{\mu_t}{\sigma_k} \right) \frac{\partial k}{\partial x_j} \right] + G_k - \rho \varepsilon - Y_M, \quad (5)$$

$$\begin{aligned} \frac{\partial (\rho \varepsilon)}{\partial t} + \frac{\partial (\rho \varepsilon u_i)}{\partial x_i} = & \frac{\partial}{\partial x_j} \left[\left(\mu + \frac{\mu_t}{\sigma_\varepsilon} \right) \frac{\partial \varepsilon}{\partial x_j} \right] + \rho C_{1\varepsilon} S \varepsilon \\ & - C_{2\varepsilon} \rho \frac{\varepsilon^2}{k + \sqrt{\nu \varepsilon}} + C_{1\varepsilon} \frac{\varepsilon}{k} C_{3\varepsilon} G_b, \end{aligned} \quad (6)$$

where $Y_M = \rho k^{3/2} / l_{\text{des}}$, $l_{\text{des}} = l_{rke} - f_d \max(0, l_{rke} - C_{\text{des}} \Delta_{\text{max}})$, $l_{rke} = k^{3/2} / \varepsilon$, $f_d = 1 - \tanh(20r_d)^3$, $r_d = (\nu_t + \nu) / (\sqrt{|U_{i,j} U_{i,j}|} k^2 d)$, $\mu_t = \rho C_\mu k^2 / \varepsilon$, $C_\mu = 1 / (A_0 + A_S k \nu^2 / \varepsilon)$, $A_0 = 4.04$, $A_S = \sqrt{6} \cos \phi$, $\phi = 1/3 \cos^{-1}(\sqrt{6} W)$, $W = (S_{ij} S_{jk} S_{ki}) / S$, $S = \sqrt{2 S_{ij} S_{ij}}$, $S_{ij} = 1/2 ((\partial u_j / \partial x_i) + (\partial u_i / \partial x_j))$,

$C_{1\varepsilon} = \max(0.43, (\eta/(\eta + 5)))$, $C_{2\varepsilon} = 1.9$, $C_{3\varepsilon} = \tanh(|v/u|)$, $\eta = Sk/\varepsilon$, G_k denotes the turbulent kinetic energy due to the mean velocity, $Pr_t = 0.85$ in the realizable $k-\varepsilon$ model, $C_{des} = 0.61$, and Δ_{\max} is the grid spacing, which in the case of a rectilinear hexahedral cell is the maximum edge length. In the region far away from the wall, r_d is far less than 1 and f_d is equal to 1, then the governing equation changes to LES; in the region near the wall, f_d is equal to 0, and then the governing equation is in the RANS form of the realizable $k-\varepsilon$ model. In short, Y_M thus controls the transformation of RANS to LES.

3.3. Grid Partition. A hexahedral structured grid was selected to improve the accuracy and convergence of the computation. All block grids in the pipeline were made O-shaped to improve the quality of the grid, as shown in Figure 3. The grid was refined in the side branch mouth and parts adjacent to the main pipe as the acoustic vortices are mainly located in these areas when acoustic resonance occurs. The thickness of the first layer near the wall was set to 0.04 mm, and the internal area grid increased inward at a growth rate of 1.2.

3.4. Boundary Conditions and Solver. The inlet boundary condition was considered a velocity inlet. The inlet velocities of all cases were configured with a mean flow and without fluctuation (Table 1) and represented by Strouhal number S_f . The Strouhal number is a dimensionless number that characterizes the unsteady similarity of fluid flow and is calculated as $S_f = fd/v$, where d is the mouth diameter of the side branch, v is the mean flow velocity of the main pipe, and f is the first-order acoustic resonance frequency calculated as follows [37]:

$$f_n = \frac{(2n-1)c}{4(L+Le)} \quad (7)$$

$n = 1, 2, 3, \dots$, is the order of the frequency, c is the flow field sound velocity, L is the branch length, and Le is correction factor, 0.4–0.425 times the diameter of the branch.

The outlet boundary condition was considered a pressure outlet with a pressure of 0 Pa and operating pressure of 6 MPa. The methane gas (CH_4 , the main component of natural gas) in the pipe was assumed to be compressible ideal gas. The wall temperature was set to 293.15 K. The walls were designed as rigid and non-permeable, so heat does not transfer through them. It should be noted that although there was no heat exchange between the fluid and the environment through the wall in the simulation, energy conversion did exist in the flow (e.g., the conversion of pressure potential energy to heat energy, molecular friction leading to heat generation), so equation (3) is a necessary component of the CFD model.

The PISO algorithm coupled with neighbour and skewness corrections was adopted as the conservation equation solver. The conservation equations were spatially discretized by the finite volume method with the discretization schemes shown in Table 2.

The parameters of the mean flow velocity, pressure, and flow time were normalized as the dimensionless parameters Strouhal number St , normalized pressure p^* , and normalized time t^* , respectively. These parameters are calculated as follows:

$$St = \frac{fd}{v}, \quad (8)$$

$$p^* = \frac{p}{(1/2)\rho v^2}, \quad (9)$$

$$t^* = \frac{vt}{l}, \quad (10)$$

where f is the first-order frequency of acoustic resonance, d is the diameter of the side branch, v is the mean flow velocity, p is the pressure amplitude, ρ is the gas density, t is the flow time, and l is the distance from the inlet to the branch.

4. Validation

4.1. Grid Independent Solution Validation. It is necessary to verify the grid independence to prevent grid quality from affecting the accuracy of the numerical computation. For grid independence verification, the number of adjacent grids is usually set to be approximately twice as large as that of adjacent grids [38, 39]. Four sets of grids were prepared to compute with the boundary condition with a 40 m/s inlet velocity. The cell number of grids was about 159151, 354435, 790423, and 1494845, respectively. All the cases were simulated to 2 s, at which point the quasisteady state of acoustic resonance was reached. The pressure fluctuation at the monitoring point $p1$ of the four sets of grids is shown in Figure 4(a). The dominant frequency of all pressure fluctuations was equal to 50.6 Hz by FFT analysis, which shows that the four sets of grids did not affect the pressure fluctuation frequency in this case.

As shown in Figure 4(a), the pressure fluctuation waveforms of 159151 grids have larger errors than those of other grids while the pressure fluctuation results of 354435, 790423, and 1494845 grids are basically the same, with nearly coincident curves. The amplitude and phase of the dominant frequency pressure fluctuation of four sets of grids were obtained by FFT as shown in Figure 4(b), where though the pressure fluctuations of the four sets of grids are similar, the phase differences among them are stark. There are small phase changes in the 790423 and 1494 845 grids, so 790 and 423 grids can be considered grid independent solutions.

4.2. Frequency Validation. According to equation (7), $f_1 = 64.7$ Hz and $f_3 = 194.1$ Hz based on the simulated flow conditions (the natural gas adiabatic index $K = 1.479$, and the gas constant $R = 518.2$ J/(kg·K)). The sound velocity $c = 471.4$ m/s as per $c = \sqrt{KRT}$. The simulation results show a first-order frequency $f_{1s} = 50.8$ Hz at the mean flow velocity of $v = 20$ m/s and a first-order frequency $f_{2s} = 185.0$ Hz at the mean flow velocity of $v = 70$ m/s. These theoretical calculation results are in good agreement with the simulation results.

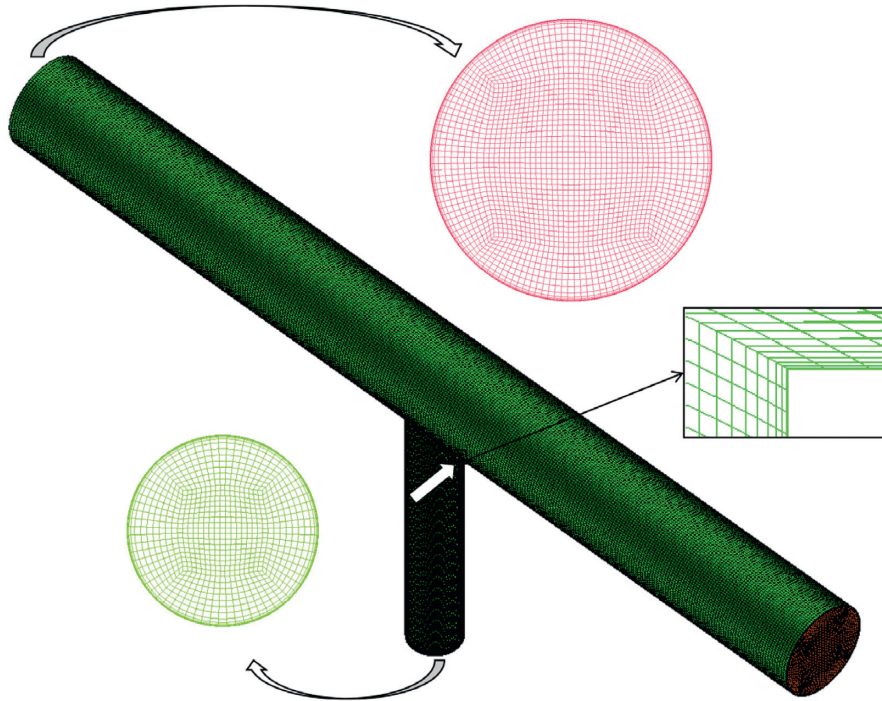


FIGURE 3: Grid area.

TABLE 1: Parameters of the cases.

Case	Velocity (m/s)	St	Re
1	10	2.00	$2.03E+07$
2	15	1.34	$3.04E+07$
3	20	1.00	$4.05E+07$
4	30	0.67	$6.08E+07$
5	40	0.50	$8.11E+07$
6	50	0.40	$1.01E+08$
7	60	0.33	$1.22E+08$
8	70	0.29	$1.42E+08$

TABLE 2: Spatial discretization schemes for the governing equations.

Governing equations	Schemes
Gradient	Least squares cell-based
Pressure	Second order
Momentum	Bounded central difference
Turbulent kinetic energy	Second-order upwind
Turbulent dissipation rate	Second-order upwind
Energy	Second-order upwind

4.3. Experimental Validation. It is difficult to do experiments under pressure as high as 6 MPa. We compared our simulation results of 0.3 MPa with the experimental results of Ziada Shine [11]. As shown in Figure 5, the CFD simulation pressure is generally higher than the experimental pressure, as the wall was rigid and impenetrable in the CFD simulation. The pipe absorbed vibration energy in the experiment, however, so the acoustic energy could propagate outward through the pipe wall. The simulation result is basically consistent with the experimental result at the Strouhal number (St)

range of acoustic resonance, which indicates that our model can effectively simulate the acoustic resonance in the closed side branch.

5. Results and Analysis

5.1. Pressure Fluctuation and FFT Analysis. Figure 6 shows the time history of pressure fluctuation in monitoring point $p1$ at different mean flow velocities. All of these cases were initialized from the inlet of the main pipe at the corresponding velocity and were calculated until a stable acoustic resonance formed. The acoustic resonance excitation process initially attenuated at various flow velocities, presenting cluttered signals. The difference was whether acoustic resonance finally formed. For $St > 1$, as shown in Figures 6(a) and 6(b)), acoustic resonance did not occur and the pressure fluctuation amplitude was low. For $St < 1$, as shown in Figures 6(c)–6(h)), acoustic resonance did occur and the amplitude of pressure fluctuation was higher. It appears to take some time for stable acoustic resonance to form, less time when the mean flow velocity is relatively large.

For main pipe mean flow velocity of $v > 40$ m/s, the pressure fluctuation shows beat vibration characteristics indicative of unstable self-excited vibration, though continuous fluctuations were maintained in this case.

According to the FFT analysis (Figure 7), all the cases contain a frequency component of approximately 50 Hz. More low frequency, small amplitude components were observed when mean flow velocity $v = 10$ m/s and 20 m/s (Figures 5(a) and 5(b)). Although there is a component of approximately 50 Hz ($f = 49.1$ Hz and 48.7 Hz correspondingly), the amplitude is much smaller than that of other cases. In the case of the

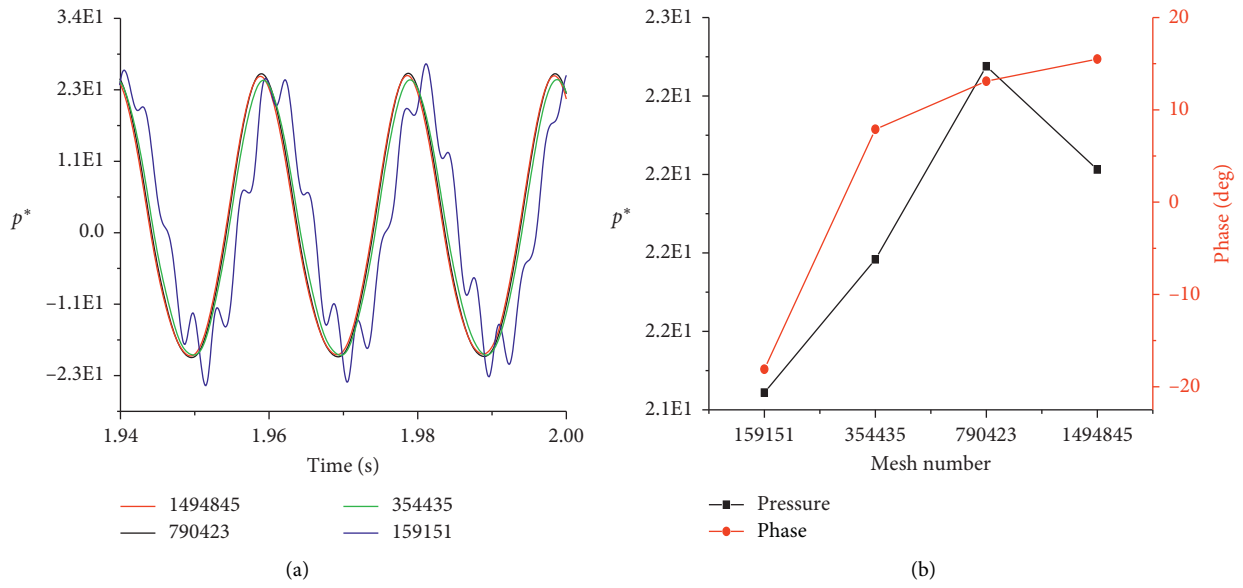


FIGURE 4: Verification for grid independent solutions.

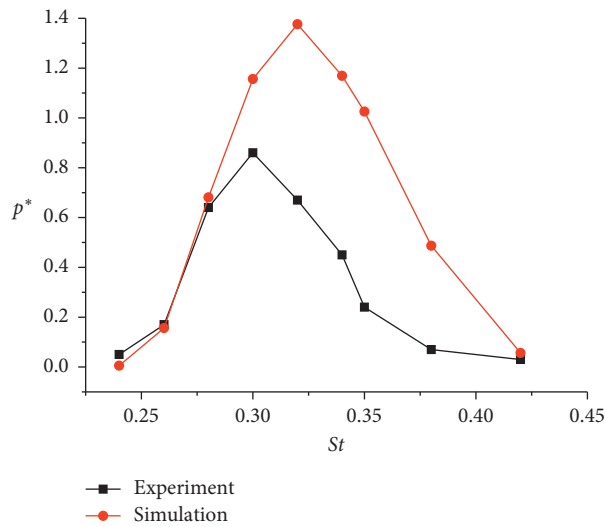


FIGURE 5: Comparison between Ziada and Shine [11] results and current simulation results.

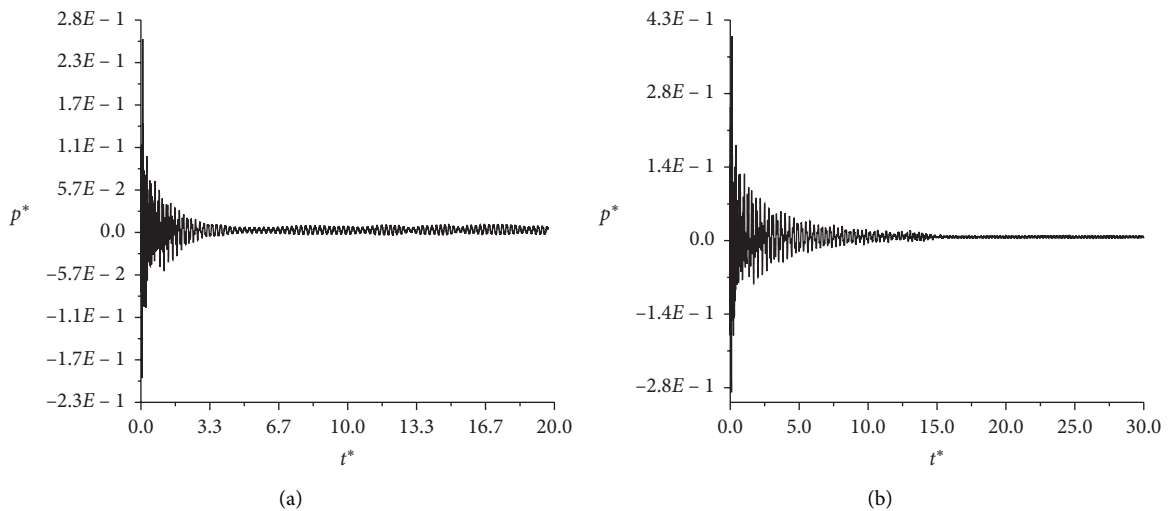


FIGURE 6: Continued.

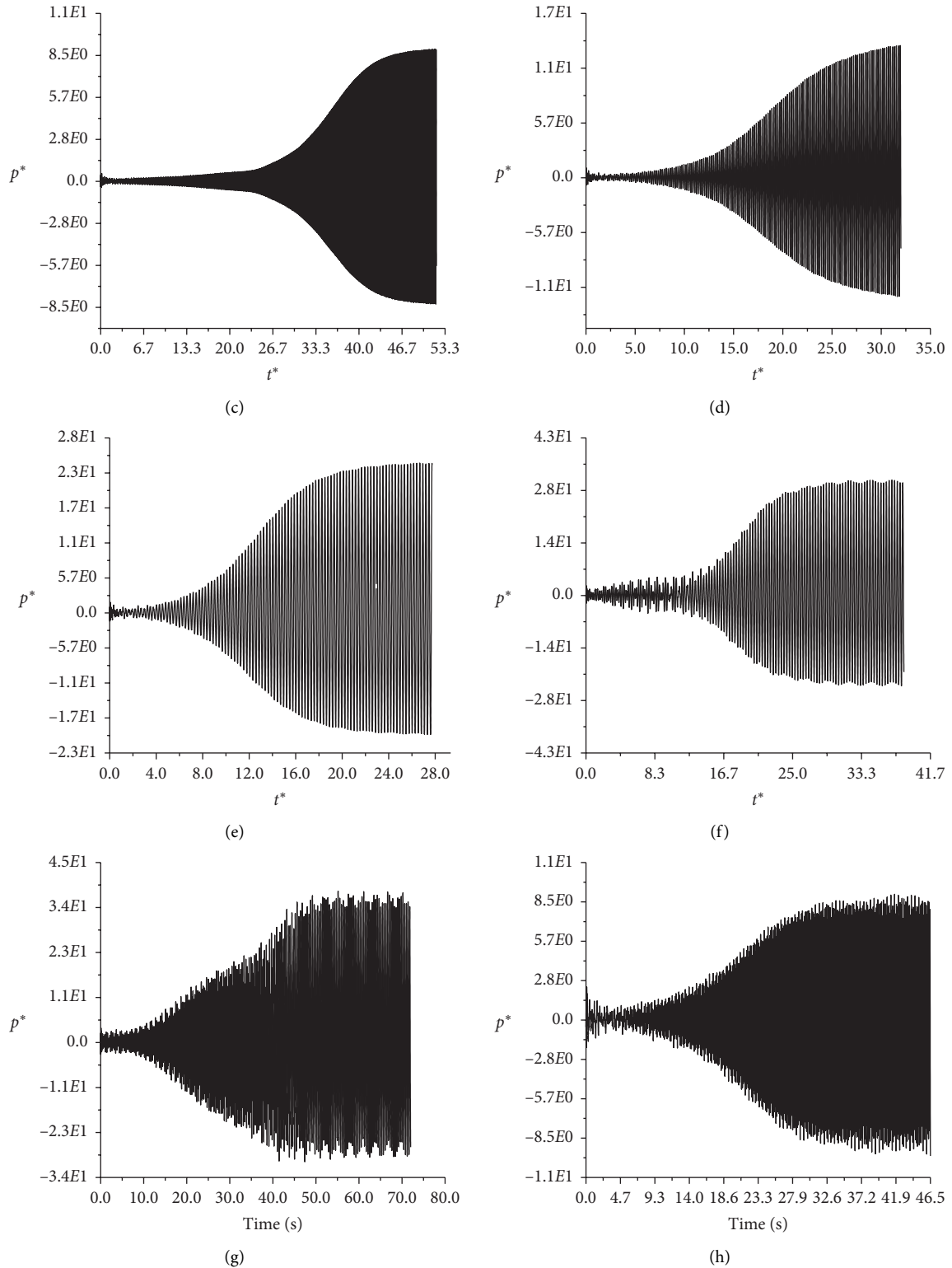
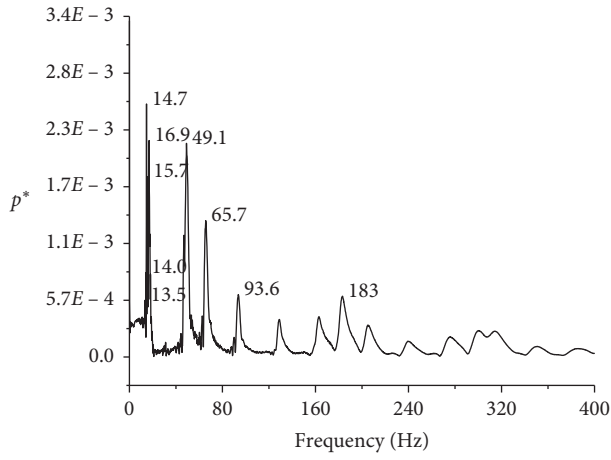


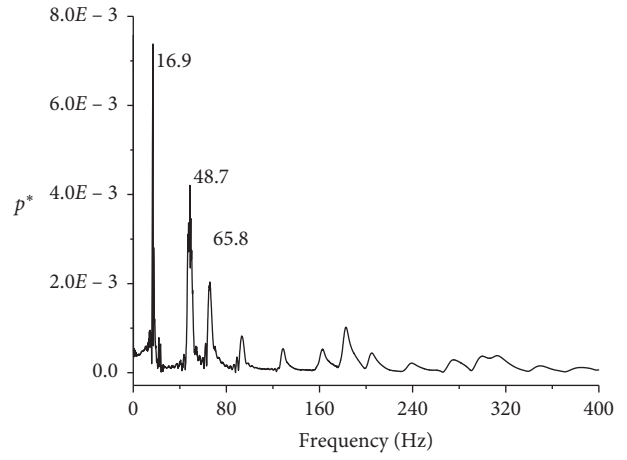
FIGURE 6: Pressure fluctuation: (a) $v = 10$ m/s, (b) $v = 15$ m/s, (c) $v = 20$ m/s, (d) $v = 30$ m/s, (e) $v = 40$ m/s, (f) $v = 50$ m/s, (g) $v = 60$ m/s, and (h) $v = 70$ m/s.

mean flow velocity $v = 20$ m/s, 30 m/s, 40 m/s, and 50 m/s (Figures 5(c)–5(f)), the dominant frequency of pressure fluctuation was approximately 50.8 Hz of the first order of the

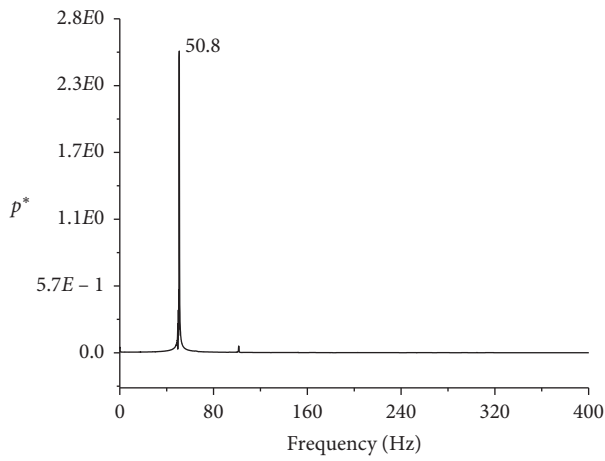
acoustic resonance, with narrow frequency characteristics, while the other components had smaller amplitudes. This indicates a pure-tone acoustic resonance. In the case of the



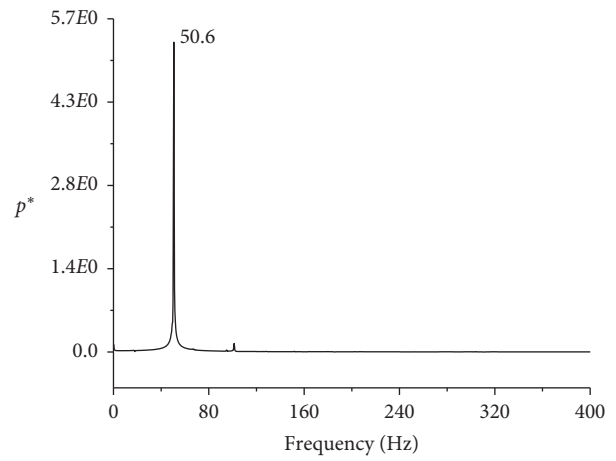
(a)



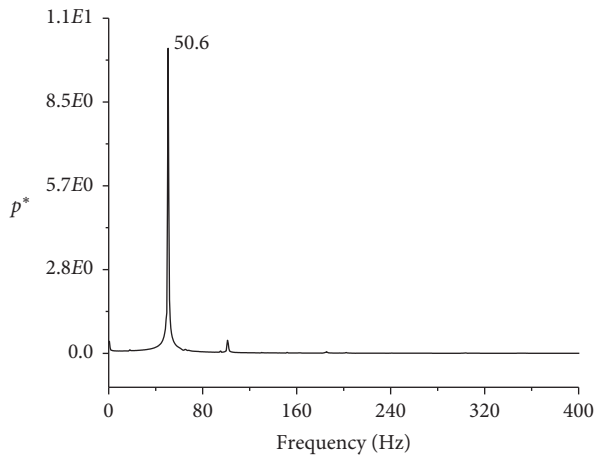
(b)



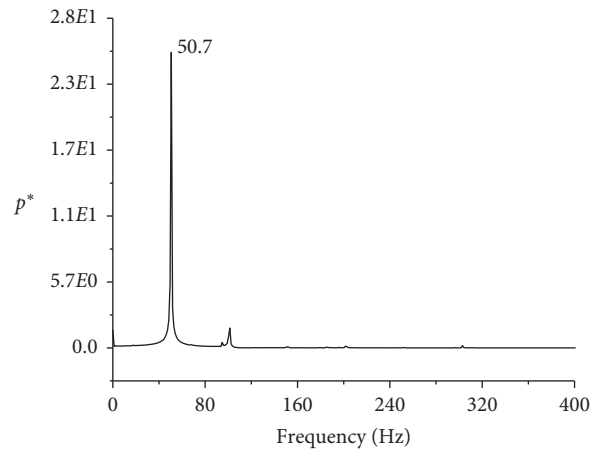
(c)



(d)



(e)



(f)

FIGURE 7: Continued.

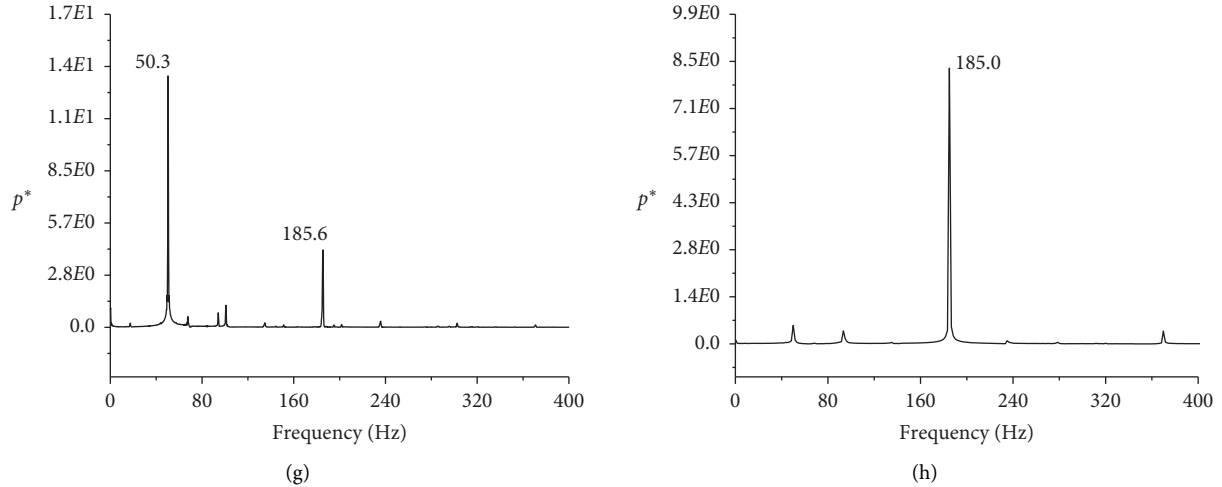


FIGURE 7: Pressure fluctuation FFT analysis: (a) $v=10$ m/s, (b) $v=15$ m/s, (c) $v=20$ m/s, (d) $v=30$ m/s, (e) $v=40$ m/s, (f) $v=50$ m/s, (g) $v=60$ m/s, and (h) $v=70$ m/s.

mean flow velocity $v=70$ m/s (Figure 7(h)), the dominant frequency of pressure fluctuation was 185.0 Hz of the second order, but the component amplitude of 50.7 Hz was not obvious; the acoustic resonance transformed into a pure tone of the second order. In the case of the mean flow velocity $v=60$ m/s (Figure 7(g)), unlike other cases where acoustic resonance occurred, the frequencies of pressure fluctuation contained two frequencies: a dominant frequency of 50.3 Hz and a secondary frequency of 185.6 Hz. These results indicate that the mean flow velocity $v=60$ m/s fell in the transitional velocity range from the first-order acoustic resonance to the second. The order of the acoustic resonance frequency is defined by the parameter n in equation (7).

5.2. Frequency and Amplitude Characteristics of Excitation Process. The dominant frequency and its pressure amplitude are presented in Figure 8 as function of St and velocity. The dominant frequencies in the cases of $0.3 < St < 1$ showed a frequency lock-in phenomenon, which has been found in previous experimental studies. In the cases of $St > 1$, the dominant frequency and its amplitude were lower and the pressure fluctuation amplitude could be neglected. The pressure fluctuation amplitude reached its maximum when $St=0.4$, which is consistent previous experimental results wherein the peak pressure fluctuation amplitude appears around St of 0.4 or 0.45 [37]. Previously published experiments have generally shown that acoustic resonance occurs in the range of $0.2 < St < 0.6$ when the fluid medium is air. In the present study, acoustic resonance still occurred when St reaches 1.0 for the fluid medium of methane. This indicates that the fluid medium affects the value of St at which acoustic resonance occurs. The fluid medium of methane acoustic resonance occurs at a higher St (lower mean flow velocity) than air, so the natural gas pipeline is a riskier environment in terms of acoustic resonance in closed side branches.

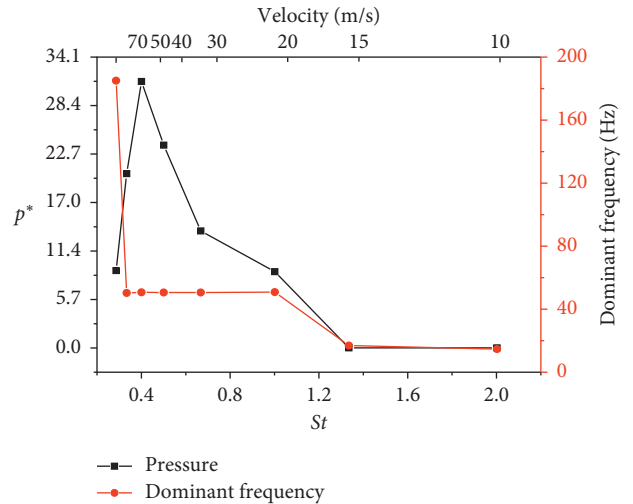


FIGURE 8: Dominant frequency (right) and pressure amplitude (left) as function of St (bottom) and velocity (top).

Figures 9(a)–9(e) show the spectra corresponding to the time intervals $\Delta t=0-0.2$ s, $0.2-0.6$ s, $0.6-0.8$ s, $0.8-1.0$ s, and $1.4-2.0$ s with mean flow velocity $v=50$ m/s. Figure 9(f) shows where the dominant frequency amplitude varies within different time intervals. Both the frequency of pressure fluctuation and the amplitude of each dominant frequency changed during the acoustic resonance excitation process. Before 0.8 s, there were dominant frequency components of 50 Hz, 65 Hz, and 185 Hz in the pressure fluctuations (Figures 9(a)–9(c)). Over time, the component frequency of 50 Hz was continuously amplified until it became the only dominant frequency (Figures 9(d) and 9(e)). The 185 Hz pressure fluctuation component increased slowly before 1.0 s slowly and was not obvious compared to the 50 Hz component. After 0.8 s, the 65 Hz component disappeared in the dominant frequencies. The 185 Hz component did not disappear until 1.0 s. It appears that the dominant acoustic resonance frequency is selectively

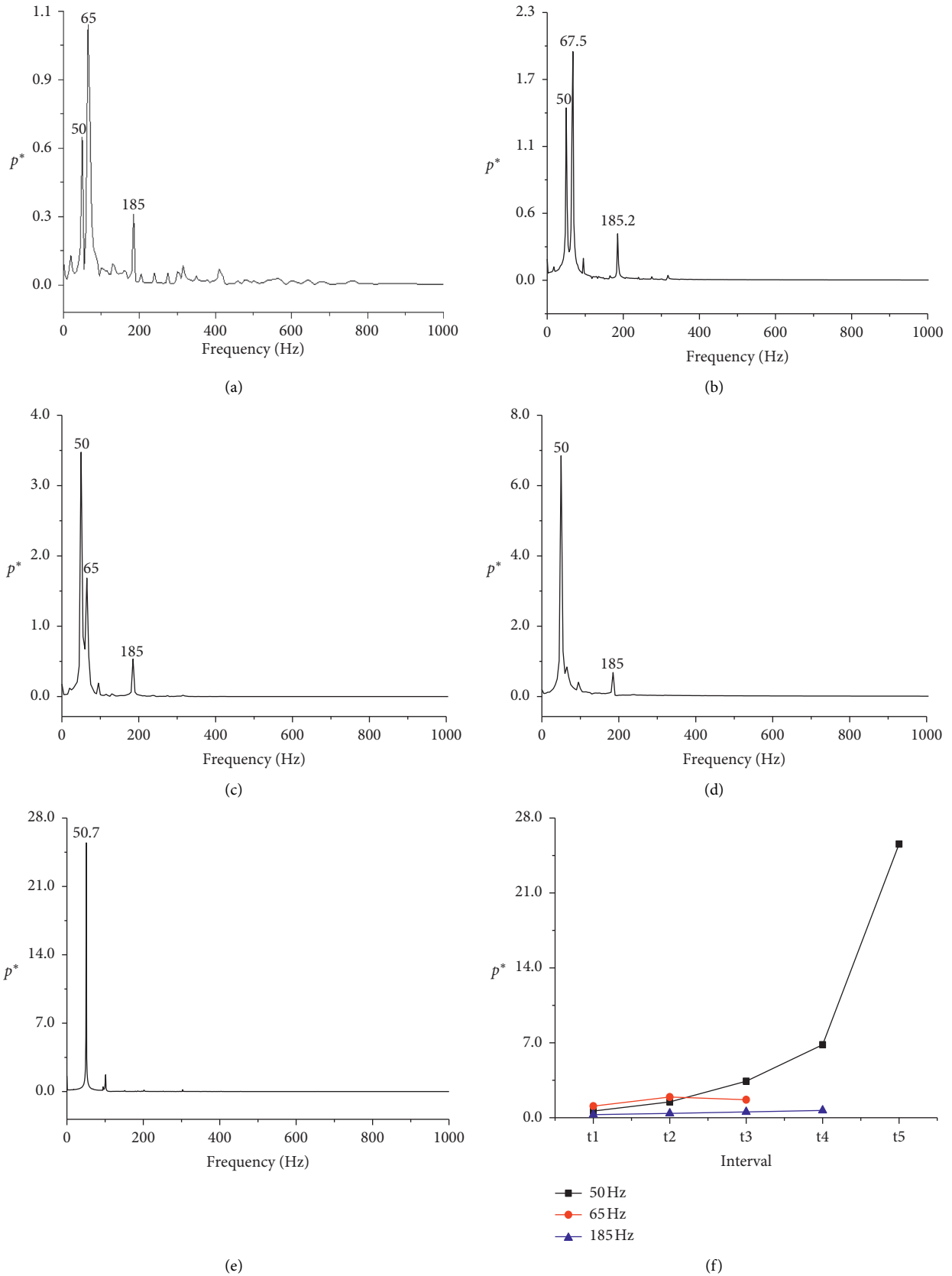


FIGURE 9: Pressure amplitude of dominant frequency with corresponding time intervals ($v = 50$ m/s): (a) pressure fluctuation FFT analysis ($v = 50$ m/s, $t_1 = 0-0.2$ s), (b) pressure fluctuation FFT analysis ($v = 50$ m/s, $t_2 = 0.2-0.6$ s), (c) pressure fluctuation FFT analysis ($v = 50$ m/s, $t_3 = 0.6-0.8$ s), (d) pressure fluctuation FFT analysis ($v = 50$ m/s, $t_4 = 0.8-1.0$ s), (e) pressure fluctuation FFT analysis ($v = 50$ m/s, $t_5 = 1.4-2.0$ s), and (f) variation of pressure amplitude of dominant frequency with the corresponding time interval ($v = 50$ m/s).

amplified in the excitation process while other components gradually disappear in the dominant frequencies.

The pressure fluctuations in other cases were analyzed using the same method to find that the excitation processes follow the same mode as the case of $v = 50$ m/s. As shown in Figures 5(a) and 5(b)), in the case of the mean flow velocity $v = 10$ m/s and 15 m/s, the pressure fluctuation still had a component of approximately 50 Hz but no acoustic resonance occurred. Comparison with Figure 9(a) indicates that in the case of mean flow velocity $v = 10$ m/s and 15 m/s, the power of the 50 Hz component was too small to excite the gas acoustic resonance in the closed side branch.

5.3. Mass Flow Rate into Branch. Figures 10(a)–10(c) show the mass flow rate from the side branch mouth into the branch and the pressure of the monitoring point $p1$ at three time intervals, $t1$ – $t3$, where $t1 = 0.1$ – 0.12 s, $t2 = 0.6123$ – 0.6323 s, and $t3 = 1.7$ – 1.72 s in the case of mean flow velocity $v = 40$ m/s. All the time intervals contain 200 time steps allowing for an approximately sinusoidal wave time of an acoustic resonance period. As shown in Figure 10, the mass flow rate into the closed side branch was sinusoidal; the amplitude increased gradually with time until a stable acoustic resonance formed. The pressure at the bottom of the branch appears to be positively correlated with the mass flow rate into the branch. The pressure increased when the mass flow rate was positive, and vice versa. Acoustic resonance excitation is essentially a process in which the gas is pressed into and out of the branch in accordance with the sinusoidal mode.

5.4. Vortex Modes. The 200 time steps shown in Figure 10 were evenly divided into eight parts corresponding to the $0T/8$ – $8T/8$ of the period. The vorticity on the $z = 0$ plane of the dividing time points ($0T/8$ – $8T/8$) is shown in Figures 11–13 for the three time intervals and the velocity curl:

$$\omega = \frac{\partial v}{\partial x} - \frac{\partial u}{\partial y}. \quad (11)$$

The vorticity around the mouth of the branch increased with the flow time (Figures 11–13). The vorticity shows three distinct vortex modes at the three time intervals. At $t1 = 0.1$ – 0.12 s, the detached shear layer beat the air at the branch mouth with low amplitudes; the vortex mode at most moments was similar to that of backward-facing step flow. At $t2 = 0.6123$ – 0.6323 s, the detached shear layer formed a large vortex at the branch mouth which then impinged on the downstream wall. Small vortices were transmitted to the bottom of the branch at this time in a mode similar to shallow cavity flow. At $t3 = 1.7$ – 1.72 s, the detached shear layer formed a larger vortex that was pushed out of the branch mouth without impingement on the downstream wall. This is a unique vortex mode.

We conclude that the acoustic resonance excitation process in the closed side branch can be divided into three steps: (1) the shear layer is free to detach from the upstream wall, (2) the detached shear layer interacts with the

downstream wall at the branch mouth, and (3) the detached shear layers are coupled to the gas column resonance to form a periodic large vortex, which is excited in the branch as the shear layer no longer interacts with the downstream wall of the branch.

At the time ($6T/8 \rightarrow 7T/8 \rightarrow 8T/8 \rightarrow 0T/8 \rightarrow 1T/8$), the shear layer gradually detached from the upstream wall to form a large vortex. This large vortex propagated from the main pipe to the branch, pressing the gas into the branch. We define this as the “former vortex.” At the time ($2T/8 \rightarrow 3T/8 \rightarrow 4T/8 \rightarrow 5T/8 \rightarrow 6T/8$), the large vortex was gradually pushed to the main pipe by the compressed gas in the branch, accompanied by the gas moving out of the branch. The “later detached shear layer” from the upstream wall was brought upwards by the former vortex.

At $4T/8$ (Figure 13(e)), the later detached shear layer was almost perpendicular to the flow direction. At $5T/8$ (Figure 13(f)), the later detached shear layer was broken into an independent vortex (the later detached vortex) by the former detached vortex. At $6T/8$ (Figure 13(g)), the vorticity of the later detached vortex began to exceed the former detached vortex. At $7T/8$ (Figure 13(h)), the trajectory of the later vortex and former vortex intersected; the two vortices integrated to a certain extent. In this unique mode, the vortex mode repeats periodically so that a stable acoustic resonance forms. We found that after this formation, the center of the large vortex is located in the upstream half around the branch mouth and the large eddy does not impinge the downstream wall.

5.5. Standing Wave. The pressure appeared to form a standing wave in the branch (Figure 14), so we further examined this aspect of the excitation process. The pressure along the branch axis at three time intervals is shown in Figure 15. At $t1$, there is no obvious standing wave phenomenon but the wave node is clearly located near the inner side of the branch mouth. At $t2$, the wave node obviously falls near the inner side of the branch mouth and the antinode is at the bottom of the branch. At $t3$, the antinode is located at the bottom of the branch and there are no obvious nodes; all are located near to the outer side of the branch mouth. As shown in Figure 15(c), the pressure near the branch mouth steeply dropped off at this point.

The pressure drop was located in the branch and during the negative pressure time ($3T/8 \rightarrow 7T/8$) and in the main pipe (out of the branch) during the positive pressure time ($8T/8 \rightarrow 2T/8$). The reason for the irregularity of the standing wave node is observable in Figure 13. During the positive pressure time, the vortex moved toward the branch pipe, which contributed to the pressure drop; during the negative pressure time, the vortex moved toward the main pipe. The motion of the vortex prevented the sound source from being fixed. The distance from the branch mouth to the main pipe was greater than that to the branch, which is why equation (7) needs to contain the correction coefficient Le .

The frequency validation result $f_{lc} = 50.8$ Hz, which is smaller than the result predicted by equation (7), $f_1 = 61.8$ Hz. This is because the acoustic vortex (sound

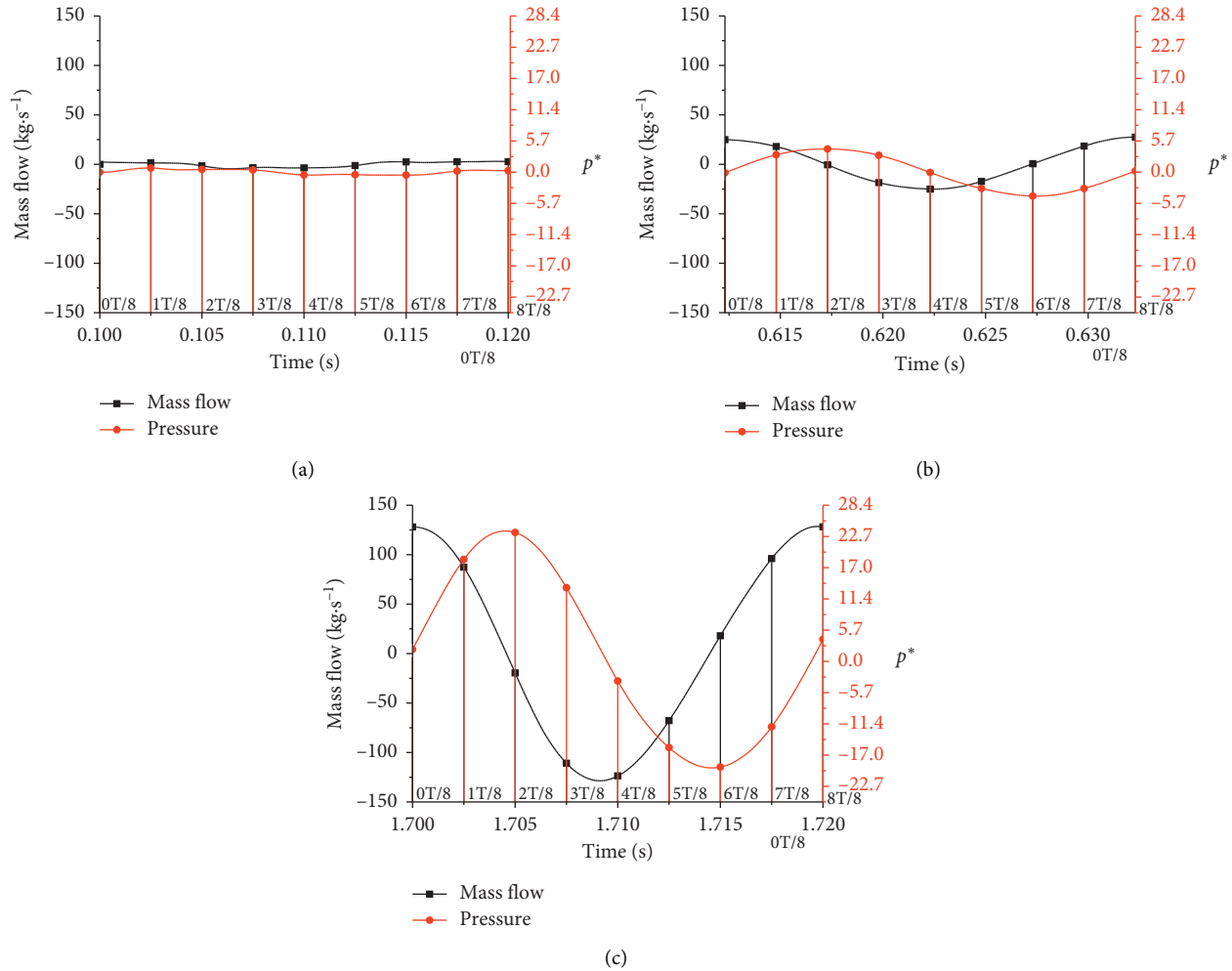


FIGURE 10: Mass flow rate into branch and pressure of monitoring point p_1 ($v = 40$ m/s): (a) $t_1 = 0.1$ s– 0.12 s, (b) $t_2 = 0.6123$ s– 0.6323 s, and (c) $t_3 = 1.7$ s– 1.72 s.

source) moved toward the main pipe, so that the wavelength of the standing wave increased and the frequency decreased significantly. At the time intervals of t_1 and t_2 , the standing wave length was shorter due to the effect of the 65 Hz pressure fluctuation component. Figures 9(a) and 9(c) illustrate this phenomenon. At the t_1 time interval, 65 Hz was the dominant frequency. At t_2 , the 65 Hz component persisted but had become the secondary frequency while the approximately 50 Hz component became the dominant frequency. At t_3 , the 65 Hz component disappeared and the 50 Hz component was completely dominant.

5.6. Phase Plane Characteristics. Shaaban and Mohany [40] pointed out that the energy transfer from the flow field to the sound field can overcome the energy taken away by sound damping and radiation, maintaining high-pressure fluctuations. The mechanism of self-excited resonance in the closed side branch is similar to that around inline cylinders.

Figure 16 shows the phase trajectories of all the cases in the phase plane, where it appears that whether acoustic

resonance is formed determines the final shape of the phase trajectory. When acoustic resonance can be formed, the limit cycle exists and the phase trajectory eventually converges to the limit cycle. When acoustic resonance cannot form, the limit cycle does not exist and the phase trajectory converges to the equilibrium point. In the case of the mean flow velocity $v = 10$ m/s and 20 m/s, the phase trajectory tended toward the coordinate origin (0, 0) from the outside to the center, indicating that the equilibrium point fell at the approximate coordinate origin (Figures 16(a) and 16(b)). In the other cases, the phase trajectories converged to a limit cycle from the center to the outside. A curve direction toward the center (limit cycle) reflects the consumption (production) of source energy. Again, whether acoustic resonance occurs depends on whether the sound source energy is greater than the energy taken away by the sound damping and radiation, and the area of this curve illustrates the strength of the source.

However, in the cases of convergence toward the limit cycle (Figure 16(c)–16(h)), different oval shapes appear to form. In cases of mean flow velocity $v = 30$ m/s, 40 m/s, or 50 m/s, the oval long axis is on the left side; with mean flow

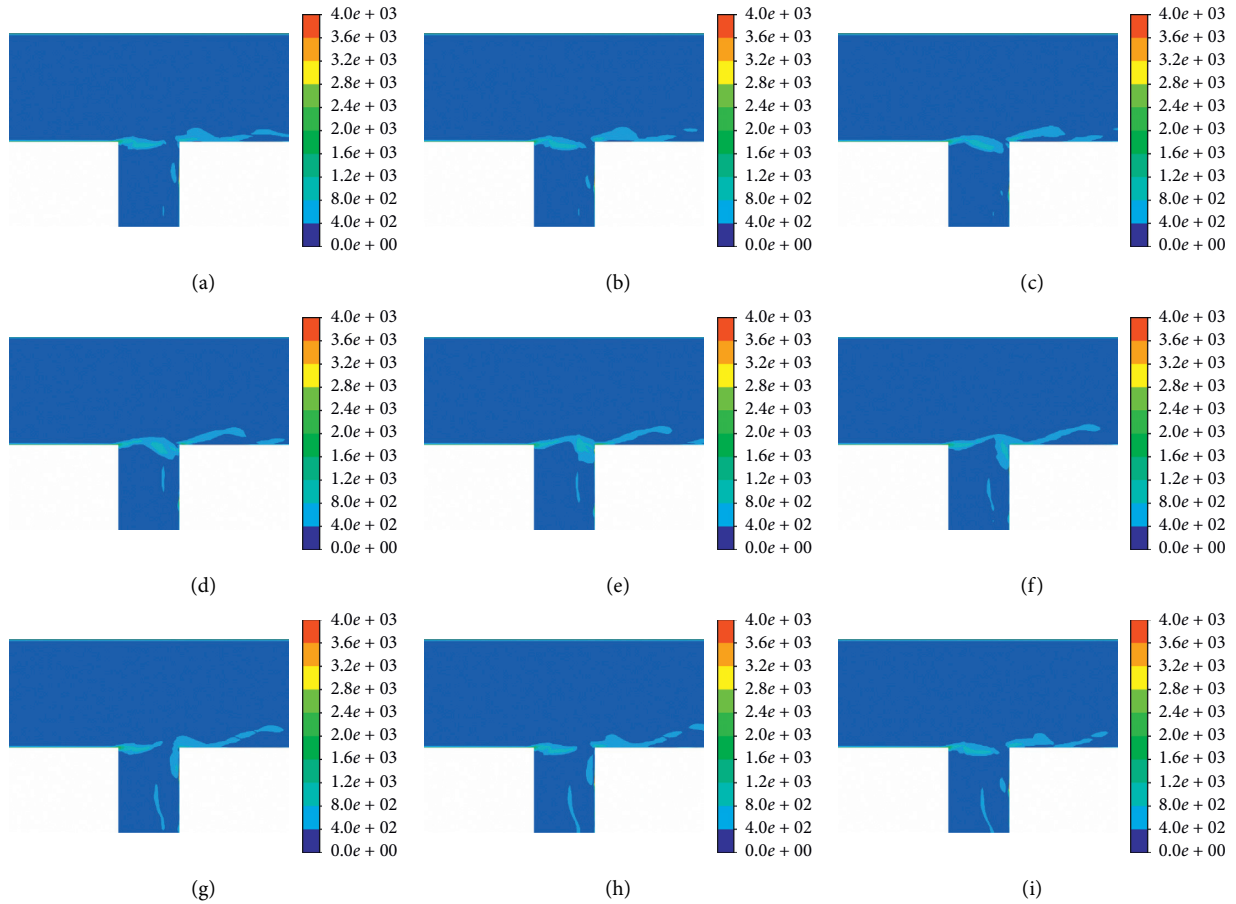


FIGURE 11: Vorticity ($t_1 = 0.1-0.12$ s unit: s^{-1}): (a) $0T/8$, (b) $1T/8$, (c) $2T/8$, (d) $3T/8$, (e) $4T/8$, (f) $5T/8$, (g) $6T/8$, (h) $7T/8$ and (i) $8T/8$.

velocity $v = 60$ m/s or 70 m/s, the oval long axis is on the right side. The limit cycle is a regular oval in the case of the mean flow velocity $v = 20$ m/s and 30 m/s. The limit cycle is relatively regular but oval in the case of the mean flow velocity $v = 40$ m/s and an irregular oval in the case of the mean flow velocity $v = 50$ m/s and 60 m/s. The limit cycle is also relatively oval in the case of the mean flow velocity $v = 70$ m/s. This phase shape ovality was expected due to harmonics, as is also shown in Figure 7.

Figure 16 with Figure 7 together show that the shape of the limit cycle is affected by the second-order dominant frequency component. The limit cycle appears to grow more irregular the more obvious the second-order dominant frequency component is. Furthermore, the influence of the second-order dominant frequency intensifies when closer to the mean flow velocity; the limit cycle also grows more irregular. The phase trajectories were similar to the shape of the final limit cycle in all cases except for mean flow velocity $v = 60$ m/s (Figure 16(g)). In the case of the mean flow velocity $v = 60$ m/s (Figure 16(g)), the phase trajectory in the phase plane first shows an oval long axis along the direction of Y , and then ultimately the oval long axis falls along the direction of X . These two different trends illustrate that the excitation process of the oval long axis is relatively unstable. The amount of regularity should indicate whether the coupling is stable or not.

The stability of the above process is related to the approximation of the second-order acoustic resonance velocity. The phase trajectory appears to grow less stable as the mean flow velocity grows closer to the second-order acoustic resonance velocity. As shown in Figure 16(g), the phase trajectory was extremely unstable in the case of the mean flow $v = 60$ m/s. This indicates that the instability factor increased with flow velocity during the transition from first-order acoustic resonance to second-order acoustic resonance. However, the process recovered a great deal of its stability in the case of mean flow $v = 70$ m/s.

5.7. Self-Excited Vibration Characteristics of Acoustic Resonance. The acoustic resonance in the closed side branch presented self-excited vibration (SEV) in our simulation. The SEV and acoustic resonance characteristics discussed above suggest that acoustic resonance is an SEV system in which the pressure fluctuation of the gas is a vibration variable. In an actual system, the gas conveyed in the pipeline and the pipe can also be regarded as an SEV system. We did not build vibration of the pipeline into our simulation, so this is not discussed here.

The mathematical model of the SEV system must be a nonlinear differential equation [29]. As an SEV system, the acoustic resonance in the closed side branch shows pure-

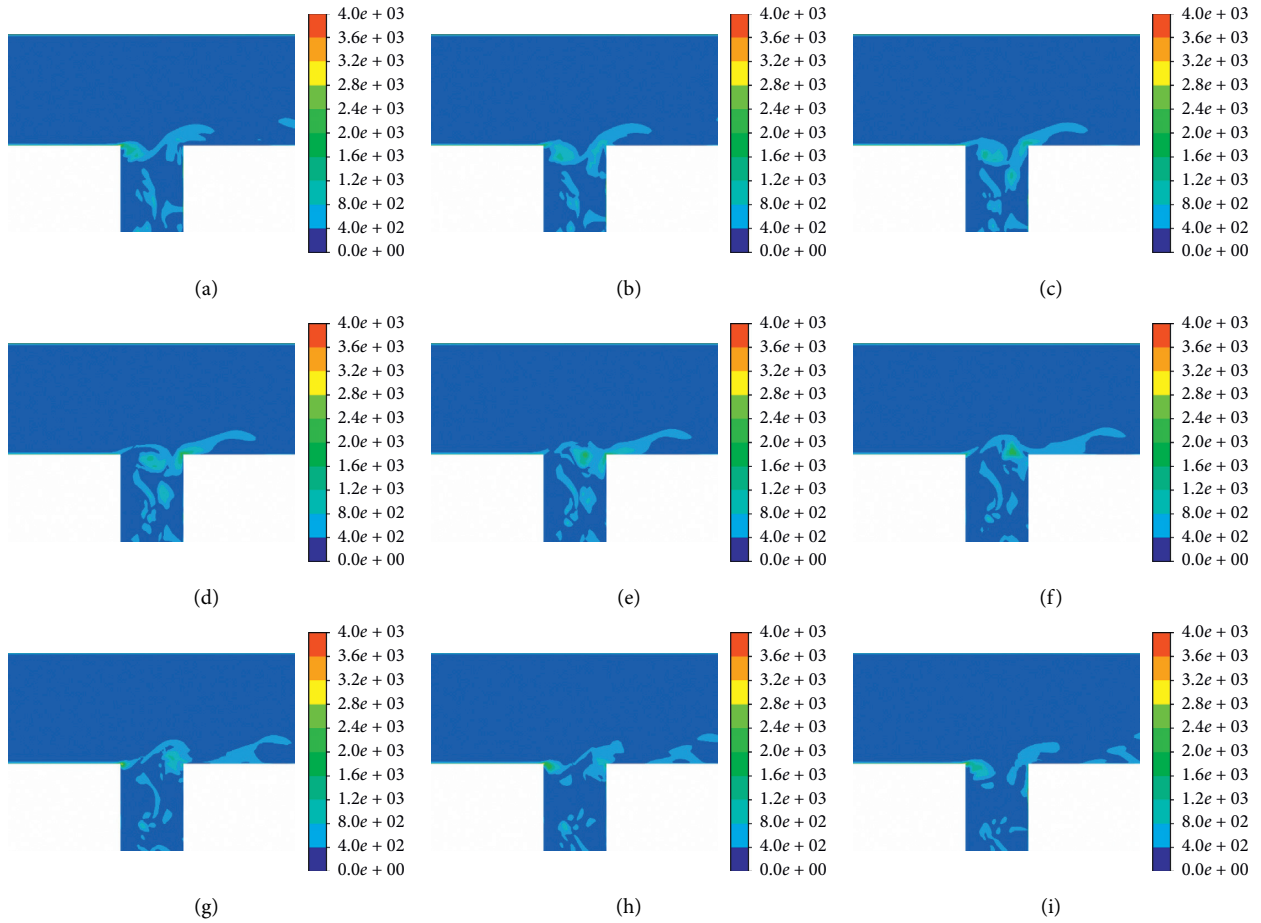


FIGURE 12: Vorticity ($t_2 = 0.6123 - 0.6323$ s unit: s^{-1}): (a) $0T/8$, (b) $1T/8$, (c) $2T/8$, (d) $3T/8$, (e) $4T/8$, (f) $5T/8$, (g) $6T/8$, (h) $7T/8$, and (i) $8T/8$.

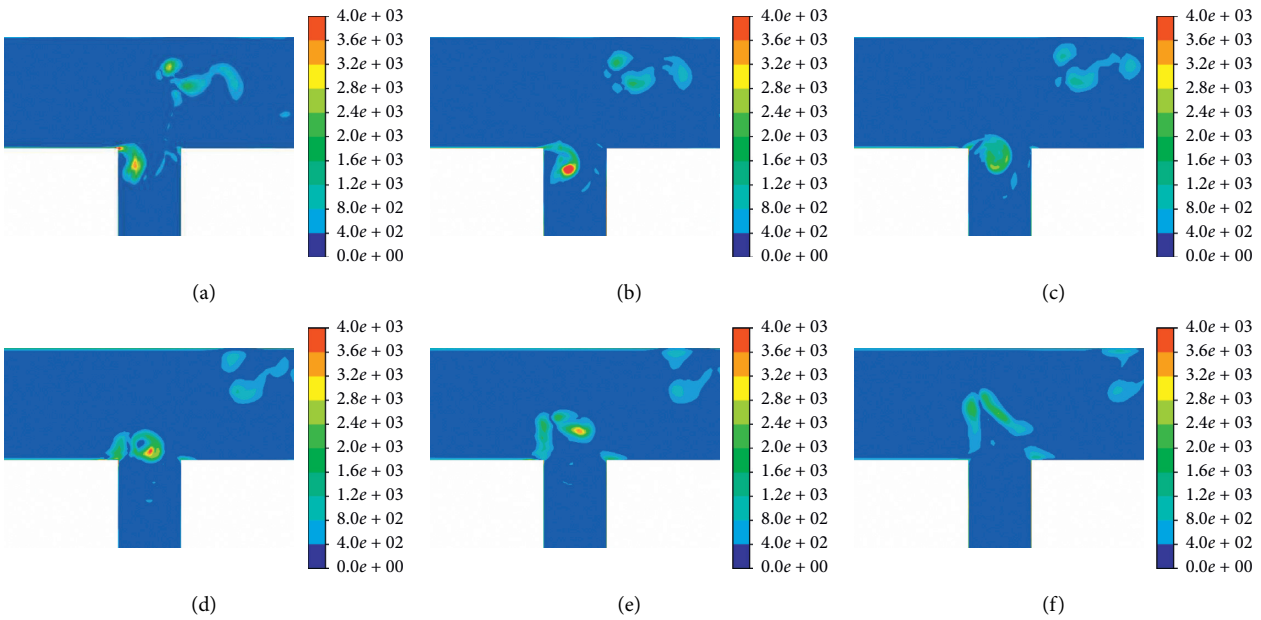


FIGURE 13: Continued.

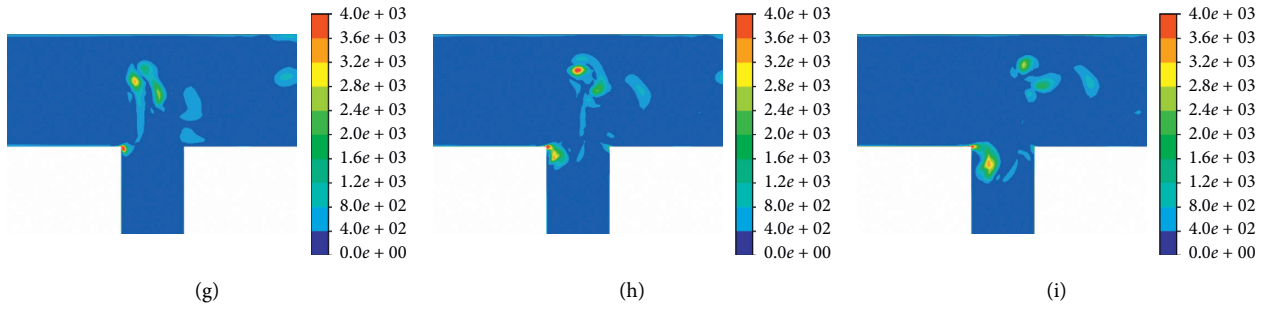


FIGURE 13: Vorticity ($t_3 = 1.7\text{--}1.72$ s unit: s^{-1}): (a) $0T/8$, (b) $1T/8$, (c) $2T/8$, (d) $3T/8$, (e) $4T/8$, (f) $5T/8$, (g) $6T/8$, (h) $7T/8$, and (i) $8T/8$.

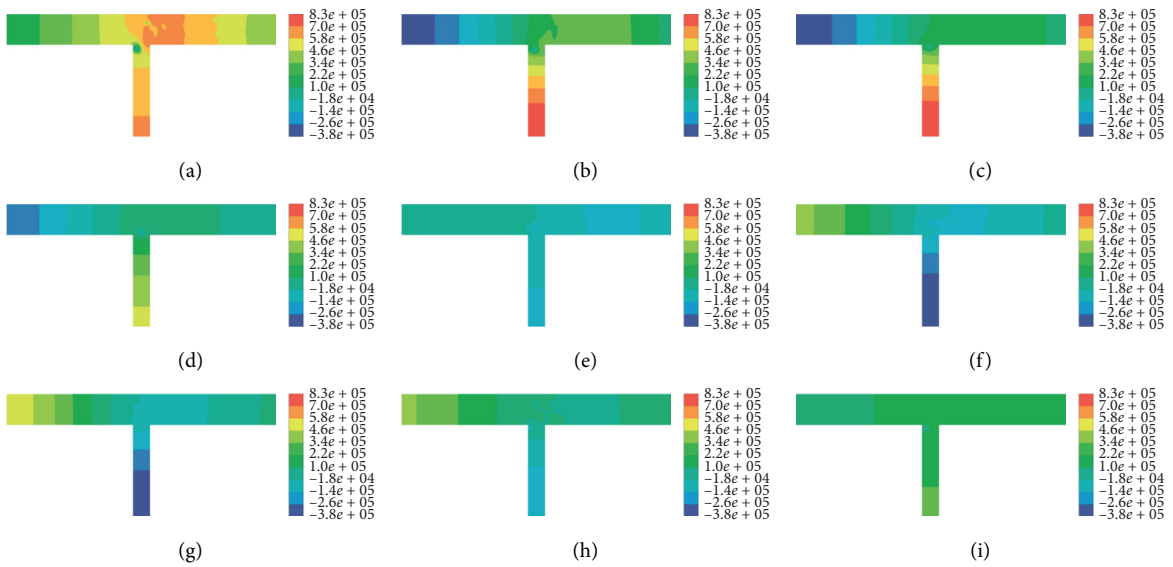


FIGURE 14: Pressure contour ($t_3 = 1.7\text{--}1.72$ s, unit: Pa): (a) $0T/8$, (b) $1T/8$, (c) $2T/8$, (d) $3T/8$, (e) $4T/8$, (f) $5T/8$, (g) $6T/8$, (h) $7T/8$, and (i) $8T/8$.

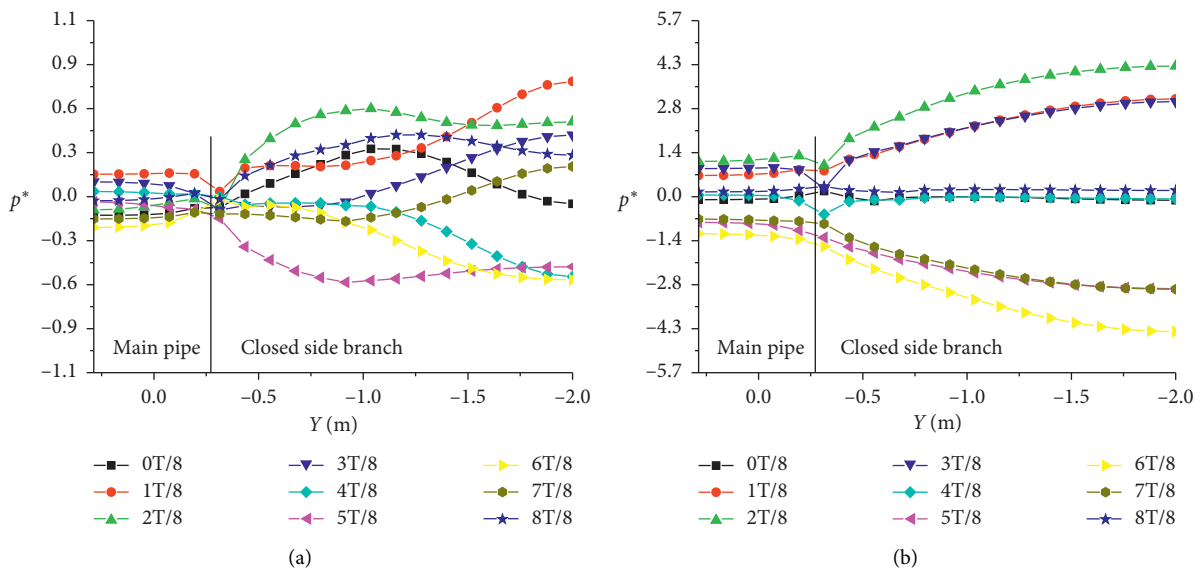


FIGURE 15: Continued.

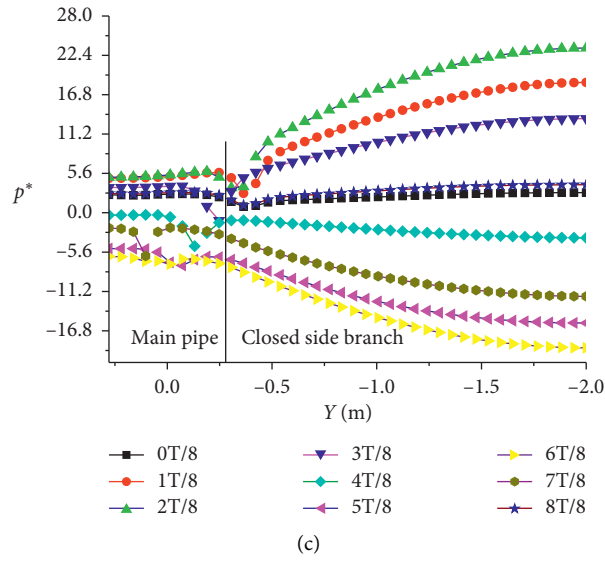


FIGURE 15: Standing wave along closed side branch: (a) $t_1 = 0.1$ s– 0.12 s, (b) $t_2 = 0.6123$ s– 0.6323 s, and (c) $t_3 = 1.7$ s– 1.72 s.

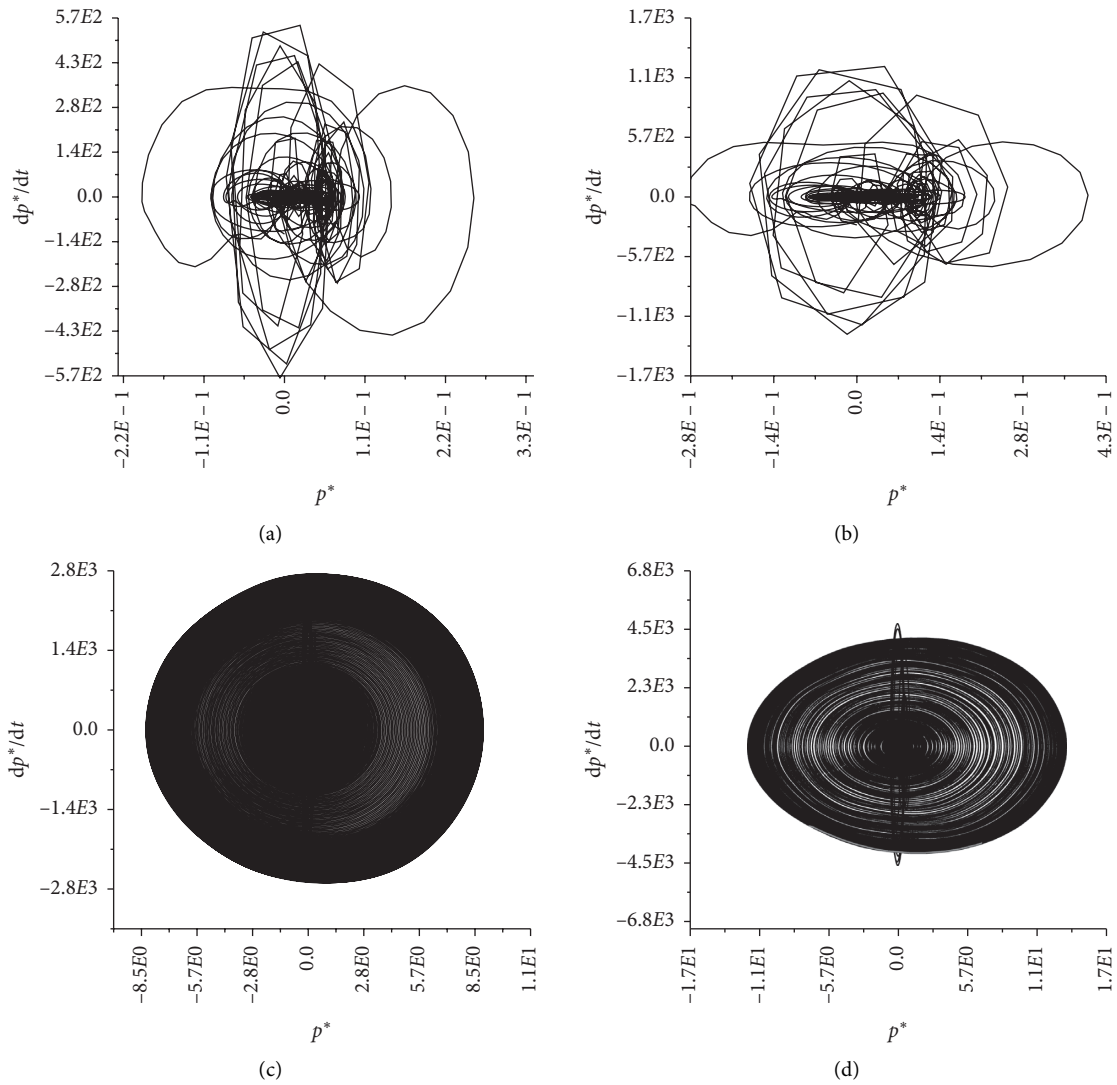


FIGURE 16: Continued.

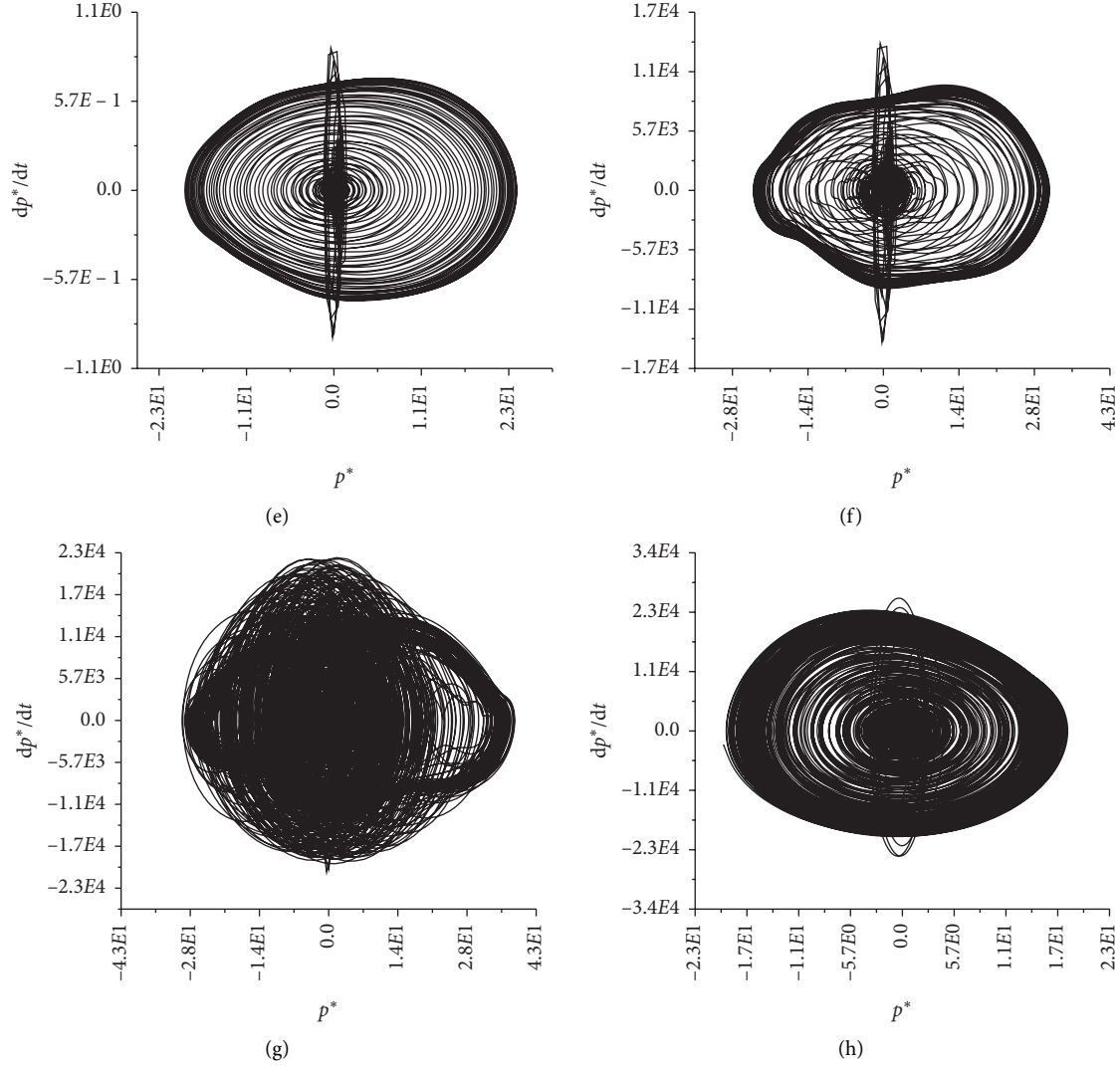


FIGURE 16: Phase plane: (a) $v = 10$ m/s, (b) $v = 15$ m/s, (c) $v = 20$ m/s, (d) $v = 30$ m/s, (e) $v = 40$ m/s, (f) $v = 50$ m/s, (g) $v = 60$ m/s, and (h) $v = 70$ m/s.

tone characteristics which approximate the simple harmonic function, so it is a quasiharmonic SEV system (weakly nonlinear autonomous system). The natural frequency of a weakly nonlinear SEV system is ω_0 , so the equation of motion is as follows:

$$\ddot{x} + \omega_0^2 x = \mu f(x, \dot{x}), \quad (12)$$

where $f(x, \dot{x})$ is a nonlinear function that does not contain the linear term of x , and μ is a small constant. A larger μ value makes the phase trajectory tend toward the limit cycle (or the equilibrium point) more quickly. Our simulation results show that the mean flow velocity in the main pipe v affects the speed of the phase trajectory approaching the limit cycle as well as the shape of the limit cycle. We conclude that the mean flow velocity v in the main pipe should be within the nonlinear damping force system of SEV system equation (12) and positively correlated with μ . The length of the closed side branch and the acoustic velocity of

the fluid determine the frequency of acoustic resonance (equation (7)), so the length of the branch and the acoustic velocity determine the ω_0 in equation (12).

6. Conclusion

We simulated acoustic resonance in a single closed side branch of a natural gas pipeline based on a realizable $k-\epsilon$ DDES turbulence model in this study. We investigated flow characteristics of the acoustic resonance excitation process accordingly via the phase plane method from the SEV perspective. Our conclusions can be summarized as follows:

- (1) In the excitation process, the dominant acoustic resonance frequency of the closed side branch can be selected and amplified while other components gradually disappear. The acoustic resonance frequency ultimately dominates the pure-tone characteristic.

- (2) A large vortex forms around the branch mouth which brings the gas in to (out of) the branch pipe with a sinusoidal periodic mass. The vortex mode is unique from the background step flow and shallow cavity flow, but the excitation process successively experiences the characteristics of both flows.
- (3) The excitation time and stability of acoustic resonance are related to the mean flow velocity. The excitation time is negatively correlated with the mean flow velocity; it is shorter when the mean flow velocity is relatively large. The stability of acoustic resonance decreases with the mean flow velocity during the transition from the first-order acoustic resonance to the second order, and then the second-order acoustic resonance recovers the stability.
- (4) Acoustic resonance is an SEV system. We recommend modeling the acoustic resonance as a weakly nonlinear SEV equation.

Data Availability

The data used to support the findings of this study are available from the corresponding author upon request.

Conflicts of Interest

The authors declare that they have no conflicts of interest.

Acknowledgments

This research acknowledges the financial support provided by the China National Key Research and Development Plan (no. 2016YFC0802105).

References

- [1] M. Su, Z. Zhang, Y. Zhu, and D. Zha, "Data-driven natural gas spot price forecasting with least squares regression boosting algorithm," *Energies*, vol. 12, no. 6, p. 1094, 2019.
- [2] L. S. Tiewsoh, J. Jirásek, and M. Sivek, "Electricity generation in India: Present state, future outlook and policy implications," *Energies*, vol. 12, no. 7, p. 1361, 2019.
- [3] R. M. Baldwin and H. R. Simmons, "Flow-induced vibration in safety relief valves," *Journal of Pressure Vessel Technology*, vol. 108, no. 3, pp. 267–272, 2009.
- [4] G. DeBoo, R. Gesior, K. Ramsden, and B. Strub, "Identification of quad cities main steam line acoustic sources and vibration reduction," *American Society of Mechanical Engineers*, vol. 4, pp. 485–491, 2008.
- [5] P. C. Kriesels, M. C. A. M. Peters, A. Hirschberg et al., "High amplitude vortex-induced pulsations in a gas transport system," *Journal of Sound and Vibration*, vol. 184, no. 2, pp. 343–368, 1995.
- [6] D. Tonon, A. Hirschberg, J. Golliard, and S. Ziada, "Aeroacoustics of pipe systems with closed branches," *Noise Notes*, vol. 10, no. 3, pp. 27–88, 2011.
- [7] C. Q. Howard and R. A. Craig, "Noise reduction using a quarter wave tube with different orifice geometries," *Applied Acoustics*, vol. 76, pp. 180–186, 2014.
- [8] Y. Xiao, W. Zhao, H. Gu, and X. Gao, "Effects of branch length and chamfer on flow-induced acoustic resonance in closed side branches," *Annals of Nuclear Energy*, vol. 121, pp. 186–193, 2018.
- [9] M. Shaaban and A. Mohany, "Passive control of flow-excited acoustic resonance in rectangular cavities using upstream mounted blocks," *Experiments in Fluids*, vol. 56, no. 4, 2015.
- [10] B. D. Knotts and A. Selamat, "Suppression of flow-acoustic coupling in sidebranch ducts by interface modification," *Journal of Sound and Vibration*, vol. 265, no. 5, pp. 1025–1045, 2003.
- [11] S. Ziada and S. Shine, "Strouhal numbers of flow-excited acoustic resonance of closed side branches," *Journal of Fluids and Structures*, vol. 13, no. 1, pp. 127–142, 1999.
- [12] K. Okuyama, A. Tamura, S. Takahashi, M. Ohtsuka, and M. Tsubaki, "Flow-induced acoustic resonance at the mouth of one or two side branches," *Nuclear Engineering and Design*, vol. 249, pp. 154–158, 2012.
- [13] S. Ziada, A. Scott, and D. Arthurs, "Acoustic excitation by flow in T-junctions," *Journal of Pressure Vessel Technology*, vol. 129, no. 1, pp. 14–20, 2007.
- [14] A. Powell, "Theory of vortex sound," *The Journal of the Acoustical Society of America*, vol. 36, no. 1, pp. 177–195, 1964.
- [15] M. S. Howe, "Vorticity and the theory of aerodynamic sound," *Journal of Engineering Mathematics*, vol. 27, no. 3, pp. 143–204, 2001.
- [16] A. Michalke, "On spatially growing disturbances in an inviscid shear layer," *Journal of Fluid Mechanics*, vol. 23, no. 3, p. 521, 1965.
- [17] M. Karlsson and M. Åbom, "Aeroacoustics of T-junctions - an experimental investigation," *Journal of Sound and Vibration*, vol. 329, no. 10, pp. 1793–1808, 2010.
- [18] H. R. Graf and S. Ziada, "Excitation source of a side-branch shear layer," *Journal of Sound and Vibration*, vol. 329, no. 10, pp. 1793–1808, 2010.
- [19] S. Ziada, "A flow visualization study of flow-acoustic coupling at the mouth of a resonant side-branch," *Journal of Fluids and Structures*, vol. 8, no. 4, pp. 391–416, 1994.
- [20] Y. R. Li, S. Someya, and K. Okamoto, "An experimental investigation of flow-induced acoustic resonance and flow field in a closed side branch system using a high time-resolved PIV technique," *Journal of Visualization*, vol. 13, no. 1, pp. 7–16, 2010.
- [21] Y. Li, S. Someya, K. Okamoto, T. Inagaki, and Y. Nishi, "Study on flow-induced acoustic resonance in symmetrically located side-branches using dynamic PIV technique," *Journal of Fluid Science and Technology*, vol. 9, no. 2, 2014.
- [22] Y. Li, S. Someya, K. Okamoto, T. Inagaki, and Y. Nishi, "Visualization study of flow-excited acoustic resonance in closed tandem side branches using high time-resolved particle image velocimetry," *Journal of Mechanical Science and Technology*, vol. 29, no. 3, pp. 989–999, 2015.
- [23] E. Salt, S. Mohamed, D. Arthurs, and S. Ziada, "Identification of aeroacoustic sources in a T-junction," *American Society of Mechanical Engineers*, vol. 4, 2014.
- [24] E. Salt, S. Mohamed, D. Arthurs, and S. Ziada, "Aeroacoustic sources generated by flow-sound interaction in a T-junction," *Journal of Fluids and Structures*, vol. 51, pp. 116–131, 2014.
- [25] Y. Xiao, H. Gu, X. Gao, H. Zhang, and W. Zhao, "Flow visualization study of flow-induced acoustic resonance in closed side branches," *Annals of Nuclear Energy*, vol. 121, pp. 186–193, 2018.
- [26] A. Tamura, K. Okuyama, S. Takahashi, and M. Ohtsuka, "Development of numerical analysis method of flow-acoustic resonance in stub pipes of safety relief valves," *Journal of*

- Nuclear Science and Technology*, vol. 49, no. 8, pp. 793–803, 2012.
- [27] P. M. Radavich, A. Selamet, and J. M. Novak, “A computational approach for flow–acoustic coupling in closed side branches,” *The Journal of the Acoustical Society of America*, vol. 109, no. 4, pp. 1343–1353, 2002.
- [28] S. Dequand, S. J. Hulshoff, and A. Hirschberg, “Self-sustained oscillations in a closed side branch system,” *Journal of Sound and Vibration*, 2003;vol. 265, no. 2, pp. 359–386.
- [29] W. Ding, *Self-excited Vibration: Theory, Paradigms, and Research Methods*, Springer Science and Business Media, Berlin, Germany, 2013.
- [30] V. M. Calo, Y. Bazilevs, T. J. R. Hughes, and R. Moser, “Turbulence modeling for large eddy simulations,” *Computer Methods in Applied Mechanics and Engineering*, vol. 199, no. 13–16, p. 779, 2010.
- [31] M. Lesieur and O. Métais, “New trends in large-eddy simulations of turbulence,” *Annual Review of Fluid Mechanics*, vol. 28, no. 1, pp. 45–82, 1996.
- [32] P. R. Spalart, W. H. Jou, M. K. Strelets, and S. R. Allmaras, “Comments on the feasibility of LES for wings and on a hybrid RANS/LES approach,” in *Proceedings of the First AFOSR International Conference on DNS/LES*, Ruston, LA, USA, August 1997.
- [33] T. H. Shih, W. W. Liou, A. Shabbir, Z. Yang, and J. Zhu, “A new $k-\epsilon$ eddy viscosity model for high Reynolds number turbulent flows,” *Computers and Fluids*, vol. 24, no. 3, pp. 227–238, 1995.
- [34] P. R. Spalart, S. Deck, M. L. Shur, K. D. Squires, M. K. Strelets, and A. Travin, “A new version of detached-eddy simulation, resistant to ambiguous grid densities,” *Theoretical and Computational Fluid Dynamics*, vol. 20, no. 3, pp. 181–195, 2006.
- [35] X. M. Tan, P. P. Xie, Z. G. Yang, and J. Y. Gao, “Adaptability of turbulence models for pantograph aerodynamic noise simulation,” *Shock and Vibration*, vol. 2019, pp. 1–20, Article ID 6405809, 2019.
- [36] Y. Zhang, J. Zhang, T. Li, L. Zhang, and W. Zhang, “Research on aerodynamic noise reduction for high-speed trains,” *Shock and Vibration*, vol. 2016, pp. 1–21, Article ID 6031893, 2016.
- [37] S. Takahashi, M. Ohtsuka, K. Okuyama, T. Ito, and K. Yoshikawa, “Experimental study of acoustic and flow-induced vibrations in BWR main steam lines and steam dryers,” *American Society of Mechanical Engineers*, vol. 4, pp. 41–47, 2008.
- [38] Q. Yuan, B. Yu, J. Li, D. Han, and W. Zhang, “Study on the restart algorithm for a buried hot oil pipeline based on wavelet collocation method,” *International Journal of Heat and Mass Transfer*, vol. 125, pp. 891–907, 2018.
- [39] K. Zhang, J. Li, B. Yu, D. Han, and Y. Chen, “Fast prediction of the replacement process of oil vapor in horizontal tank and its improved safety evaluation method,” *Process Safety and Environmental Protection*, vol. 122, pp. 298–306, 2019.
- [40] M. Shaaban and A. Mohany, “Experimental study of the self-excited resonance effect on the dynamic lift and flow structure around inline cylinders,” *Journal of Fluids and Structures*, vol. 96, Article ID 103015, 2020.

Research Article

Steady-State Dynamical Response of a Strongly Nonlinear System with Impact and Coulomb Friction Subjected to Gaussian White Noise Excitation

Guidong Yang ¹, Dongmei Huang,¹ Wei Li,¹ and Meng Su²

¹School of Mathematics and Statistics, Xidian University, No. 2 South Taibai Road, Xi'an, Shaanxi 710071, China

²Department of Applied Mathematics, Northwestern Polytechnical University, Xi'an, Shaanxi 710072, China

Correspondence should be addressed to Guidong Yang; gdyang@xidian.edu.cn

Received 12 April 2020; Revised 30 July 2020; Accepted 17 September 2020; Published 28 September 2020

Academic Editor: Francesco Pellicano

Copyright © 2020 Guidong Yang et al. This is an open access article distributed under the Creative Commons Attribution License, which permits unrestricted use, distribution, and reproduction in any medium, provided the original work is properly cited.

The paper is devoted to the steady-state dynamical response analysis of a strongly nonlinear system with impact and Coulomb friction subjected to Gaussian white noise excitation. The Zhuravlev nonsmooth transformation of the state variables combined with the Dirac delta function is utilized to simplify the original system to one without velocity jump. Then, the steady-state probability density functions of the transformed system are derived in terms of the stochastic averaging method of energy envelope. The effectiveness of the presented analytical procedure is verified by those from the Monte Carlo simulation based on the original system. Effects of different restitution coefficients, amplitudes of friction, and noise intensities on the steady-state dynamical responses are investigated in detail. Results show different intensities of Gaussian white noise can affect the peaks value of the probability density functions, whereas the variations of restitution coefficients and amplitudes of friction can induce the occurrence of stochastic P-bifurcation.

1. Introduction

Nowadays, mechanical systems have become more and more intricate due to the rapid development of science and technology [1–4]. Impact and friction, as two types of inevitable nonsmooth factors in engineering and structural applications, may change the dynamical properties of mechanical systems significantly and even result in the structural insecurity [5]. On the one hand, gaps are widely distributed in the components of mechanical equipment as a result of manufacturing errors. They may bring about collision and friction among different components, which can cause noises and reduce the working efficiency of the devices [6]. On the other hand, engineering structures usually work in complex external environment and are inevitably affected by random excitations such as ground motion, atmospheric turbulence, wind, and road unevenness. [7–9]. The random excitations owing to impact and friction or environment may also play important roles in responses of mechanical

systems [10, 11]. Hence, it is of great urgency and cardinal significance to study the dynamical behaviors of systems with impact and friction under random excitations.

As systems with impact and friction are notorious for their inherent nonsmooth features which lead to the difficulties of analytical study [12, 13], a large number of experts and scholars at home and abroad have to appeal to the numerical investigation. Accordingly, abundant achievements are gained about chaotic motions, Hopf bifurcations, and subharmonic oscillation [14–17]. Furthermore, some particular dynamical phenomena are observed such as grazing bifurcation, chatter, and sticking motions [18–20]. In terms of the mean Poincaré mapping, Feng and He [21] investigated the stochastic stick-slip motion of a random friction model. With the help of the generalized cell mapping method, Sun [22] studied random response problems on systems with Coulomb friction. Virgin and Begley [23] showed the basin of attraction due to friction and impact of a vibro-impact system with Coulomb friction damping based

on the global dynamical analysis. Zhang et al. [24] discussed the evolution process to the chaos of a single-degree-of-freedom vibro-impact system while Yue et al. [25] focused on the coexistence of strange nonchaotic attractors and a novel mixed attractor in a periodically driven three-degree-of-freedom vibro-impact system with symmetry.

In recent years, more and more attention has been paid to the analytical study of the nonsmooth system. Several different models were established for impact system and frictional systems separately to make the response analysis tractable. For systems with impact, one relatively easy model was based on the Hertzian contact law. The response's closed-form solutions were presented by Jing and Sheu [26] for a single-degree-of-freedom vibro-impact system. Using the stochastic averaging technique, Huang et al. [27] obtained the stationary responses of a multi-degree-of-freedom vibro-impact system with clearance. To overcome the disadvantage that the Hertzian contact model is impotent for dissipated contact problem, Xu et al. [28] developed a modified Hertzian contact model and analysed random vibration problems of inelastic vibro-impact systems. Another impact model commonly used was the classical impact which could depict the energy loss but was not easy to obtain the analytical solutions of responses. A nonsmooth coordinate transformation contributed to Zhuravlev [29] was introduced to transform the vibro-impact system to one without velocity jump. By this transformation, some analytical methods applicable to smooth systems were extended to the vibro-impact ones. By means of the stochastic averaging method and energy balance method, Dimentberg et al. [30–32] investigated the response probability density function, energy loss, and first passage problem of the “pseudolinear” vibro-impact system. Zhu [33] obtained one solution of stationary response for the single-degree-of-freedom vibro-impact system by the exponential-polynomial closure method. With the help of Zhuravlev-Ivanov transformation and the iterative method of weighted residue, Chen et al. [34] discussed the closed-form stationary probability distribution for stochastically excited vibro-impact oscillators. Based on the framework of Galerkin technique, Xie et al. [35] studied the transient response of a vibro-impact system under random excitation. For frictional systems, more than ten models were developed for different cases. The most commonly used one was the Coulomb friction model. Ding [36] discussed the calculation for an ideal dry friction system. Sun et al. [37] investigated the reliability of a nonlinear damped friction oscillator under combined additive and multiplicative Gaussian white noise excitations by the stochastic averaging method and obtained satisfactory results.

Although the problems of the vibro-impact system and friction system have been studied by many experts and scholars with different methods, most of them are limited to separate research. The analytical studies for the vibro-impact system with friction under random excitations are far from enough and there are numerous problems need to be solved. Recently, Su et al. [38] combined the nonsmooth coordinate

transformation and the stochastic method of the amplitude to study the stationary responses of a weakly nonlinear system with impact and Coulomb friction under Gaussian white noise. The proposed method was quite effective. However, in the case of strongly nonlinear restoring force, the stochastic method of the amplitude may be invalid to obtain accurate results. To deal with this problem, the research is performed in this paper, and the layout is as follows. The problems for a strongly nonlinear system with impact and Coulomb friction subjected to Gaussian white noise excitation are formulated in Section 2. The approximately equivalent system is obtained by the nonsmooth coordinate transformation. In Section 3, the steady-state responses' probability density functions are derived analytically by means of the stochastic averaging method of energy envelope. The effectiveness of the proposed method is verified in Section 4. Additionally, in this section, the influences of impact, friction, and random excitation on the system's responses are discussed in detail. At last, the paper is ended with conclusions.

2. Problem Formulation

Consider a randomly excited single-degree-of-freedom Van der Pol-Duffing vibro-impact system with Coulomb friction whose schematic model is displayed in Figure 1. The motion of the system is governed by

$$\ddot{x} + \varepsilon(c_2 x^2 - c_1)\dot{x} + \varepsilon f_k \text{sgn}(\dot{x}) + x^3 = \varepsilon^{1/2} \xi(t), \quad x > 0, \quad (1)$$

$$\dot{x}_+ = -r\dot{x}_-, \quad x = 0, \quad (2)$$

where ε is a small positive number used to limit the scale of other parameters, c_2 and c_1 are the nonlinear and linear damping coefficients, respectively, f_k indicates the amplitude of friction and $\text{sgn}(\dot{x})$ represents the signum function with respect to the velocity x , $\xi(t)$ denotes a Gaussian white noise process with zero mean and correlation function $R(t_2 - t_1) = 2D\delta(t_2 - t_1)$, in which $\delta(\bullet)$ is the Dirac delta function, meaning that the noise intensity is $2D$, \dot{x}_- and \dot{x}_+ refer to values of velocity at the instants right before and after the impact, respectively, r is the impact restitution coefficient satisfying $0 < r \leq 1$, which depicts the energy loss due to impact, and $x = 0$ describes the impact condition, that is, when the oscillator arrives at the position $x = 0$, the impact happens.

From equations (1) and (2), the motion of the oscillator is performed in two steps. The oscillator moves freely between two consecutive impacts. Then, its velocity changes suddenly at the static equilibrium position of the system. Besides, the dry friction force also has a discontinuous variety in terms of the direction of velocity. Thus, the vibro-impact system with dry friction is strongly nonlinear as well as nonsmooth.

To overcome the difficulty due to the nonsmooth characteristics of the vibro-impact system, the nonsmooth variable transformation proposed by Zhuravlev [29] is introduced as follows:

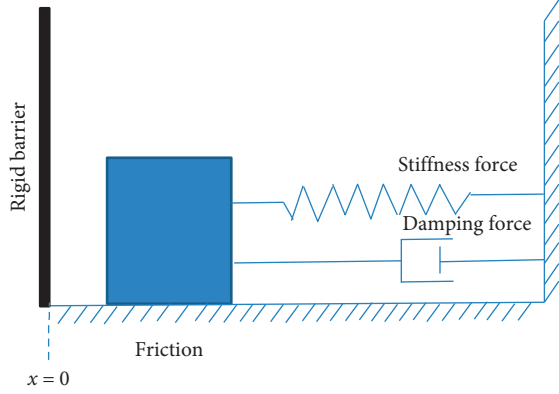


FIGURE 1: Schematic model of the system with impact and friction.

$$\begin{aligned} x &= x_1 = |y|, \\ \dot{x} &= x_2 = \dot{y} \operatorname{sgn} y, \\ \ddot{x} &= \ddot{y} \operatorname{sgn} y, \end{aligned} \quad (3)$$

in which

$$\operatorname{sgn} y = \begin{cases} 1, & y > 0, \\ -1, & y < 0. \end{cases} \quad (4)$$

Obviously, the original phase plane (x, \dot{x}) is mapped to the whole phase plane (y, \dot{y}) by the nonsmooth variable transformation, in which the restrictive condition $x > 0$ is removed.

Substituting equation (3) into equations (1) and (2) results in the following expressions:

$$\dot{y} + \varepsilon(c_2 y^2 - c_1)\dot{y} + \varepsilon f_k \operatorname{sgn}(\dot{y}) + y^3 = \varepsilon^{1/2} \operatorname{sgn} y \xi(t), \quad t \neq t_*, \quad (5)$$

$$\begin{aligned} \ddot{y}_+ &= r \dot{y}_-, \\ t &= t_*, \end{aligned} \quad (6)$$

where $t = t_*$ indicates the time when impact occurs, corresponding to $x = 0$. Comparing equation (6) with equation (2), it is easy to see that the velocity jump of the original variable at the rigid barrier is $\Delta \dot{x} = \dot{x}_+ - \dot{x}_- = (-r - 1)\dot{x}_-$, whereas the velocity jump for new variable is $\Delta \dot{y} = \dot{y}_+ - \dot{y}_- = (r - 1)\dot{y}_-$. The closer r is to one, the smaller the velocity jump of the new variable is. In terms of the properties of the Dirac delta function, the following equation could be derived:

$$(\dot{y}_- - \dot{y}_+)\delta(t - t_*) = (1 - r)\dot{y}|\dot{y}|\delta(y), \quad (7)$$

which can be combined into equation (5) as an additional impulsive term. Arranging them yields

$$\begin{aligned} \dot{y} + \varepsilon(c_2 y^2 - c_1)\dot{y} + \varepsilon f_k \operatorname{sgn}(\dot{y}) - (r - 1)\dot{y}|\dot{y}|\delta(y) \\ + y^3 = \varepsilon^{1/2} \operatorname{sgn} y \xi(t). \end{aligned} \quad (8)$$

It is obvious that the new equation does not include the velocity jump, which may permit us to study it by taking advantage of some analytical methods applicable to the smooth system.

3. Stochastic Averaging Method of Energy Envelope

Considering the case that the energy change is caused by the linear damping, the nonlinear damping, the impact, and friction as well as random excitation is far less than the original energy of the system. Herein, the system could be quasiconservative. Thus, the stochastic averaging method of energy envelope may be feasible to deal with the approximately equivalent system described by equation (8).

The corresponding undamped system of equation (8) is

$$\ddot{y} + y^3 = 0. \quad (9)$$

Letting $y = y_1$, $\dot{y} = y_2$, $g(y_1) = y_1^3$, the energy envelope of the system is written as

$$H = \frac{1}{2}y_2^2 + G(y_1), \quad (10)$$

$$G(y_1) = \int_0^{y_1} g(u)du,$$

where $G(y_1)$ is the potential energy.

Equation (8) is equivalent to the following set of Itô stochastic differential equations:

$$\begin{aligned} dy_1 &= y_2 dt, \\ dy_2 &= [-f(y_1, y_2) - g(y_1)]dt + \sigma(y_1, y_2)dW(t), \end{aligned} \quad (11)$$

in which $f(y_1, y_2) = \varepsilon(c_2 y_1^2 - c_1)y_2 + \varepsilon f_k \operatorname{sgn}(y_2) - (r - 1)y_2|y_2|\delta(y_1)$ represents the effective damping, $g(y_1)$ is the effective conservative force, $-f(y_1, y_2) - g(y_1)$ is the drift coefficient and $\sigma(y_1, y_2)$ is called the diffusion coefficient, and $W(t)$ denotes the Wiener process.

The Itô stochastic differential equations for the displacement y_1 and velocity y_2 can be transformed into the following Itô equations for displacement y_1 and the energy envelope $H(t)$ by the transformation equation (10) and the Itô's differential rule.

$$\begin{aligned} dy_1 &= \pm \sqrt{2H - 2G(y_1)}dt, \\ dH &= \left[\mp \varepsilon^2 \sqrt{2H - 2G(y_1)} f\left(y_1, \pm \sqrt{2H - 2G(y_1)}\right) \right. \\ &\quad \left. + \frac{1}{2}\sigma^2\left(y_1, \pm \sqrt{2H - 2G(y_1)}\right) \right]dt \\ &\quad \pm \sqrt{2H - 2G(y_1)}\sigma\left(y_1, \pm \sqrt{2H - 2G(y_1)}\right)dW(t). \end{aligned} \quad (12)$$

Noting that the displacement process y_1 is rapidly varying and the energy envelope process H is a slowly varying one, according to the Khasminskii theorem [39], the H process converges weakly to a one-dimensional Markov process as $\varepsilon \rightarrow 0$, in a time interval $0 < t < T$, where $T \sim o(1/\varepsilon)$. Here, we also use the symbol H to represent this one-dimensional Markov process.

Averaging to equation (12), the resulting Itô equation is given by

$$dH = U(H)dt + V(H)dW(t), \quad (13)$$

in which

$$T = 4T_{1/4} = 4 \int_0^A \frac{dy}{\sqrt{2H - 1/2y_1^4}} = \sqrt{\pi}H^{-1/4} \frac{\Gamma(1/4)}{\Gamma(3/4)}, \quad (14)$$

$$U(H) = -\frac{32}{5} \varepsilon c_2 \frac{\Gamma^2(3/4)}{\Gamma^2(1/4)} H^{3/2} + \frac{4}{3} \varepsilon c_1 H - \frac{4\sqrt[4]{4}}{\sqrt{\pi}} \varepsilon f_k \frac{\Gamma(3/4)}{\Gamma(1/4)} H^{1/2} + \frac{4}{\sqrt{\pi}} (r-1) \frac{\Gamma(3/4)}{\Gamma(1/4)} H^{5/4} + \varepsilon D, \\ V^2(H) = \frac{8}{3} \varepsilon DH, \quad (15)$$

where T is a pseudoperiod, A denotes the amplitude, and $U(H)V^2(H)$ represent the averaged drift coefficient and diffusion coefficient, respectively.

During the calculation process, some points may be noted. Firstly, the averaging to the impact damping term should be done in half pseudoperiod since there are two impacts during this time. Secondly, the following formula is used to simplify the integral calculation:

$$\int_0^{\pi/2} \sin^{m-1} \theta \cos^{n-1} \theta d\theta = \frac{1}{2} B\left(\frac{m}{2}, \frac{n}{2}\right), \quad (16)$$

where $B(\cdot, \cdot)$ is the beta function.

The Fokker-Planck-Kolmogorov (FPK) equation corresponding to Itô equation (13) is easy to obtain as

$$\frac{\partial p}{\partial t} = -\frac{\partial}{\partial H} [u(H)p] + \frac{1}{2} \frac{\partial^2}{\partial H^2} [v^2(H)p], \quad (17)$$

in which the boundary condition is

$$\left\{ \begin{array}{l} 0 \leq p < \infty, \\ H = 0, \\ p \rightarrow 0, \\ \frac{dp}{dH} \rightarrow 0, \\ H \rightarrow \infty. \end{array} \right. \quad (18)$$

The instantaneous response of equation (17) is usually difficult to obtain due to the existence of strongly nonlinear factors, although some special cases could be solved by the Galerkin procedure. We herein study the stationary dynamical response analytically.

Taking the left side of equation (17) to be zero and integrating at both sides, the stationary probability density function of energy envelope H is deduced as

$$p(H) = \frac{C}{K} H^{-1/4} \exp(MH^{3/2} + NH + OH^{1/2} + QH^{5/4}), \quad (19)$$

in which C is a normalization constant and

$$K = \frac{8}{3} \varepsilon D, \\ M = -\frac{16c_2}{5D} \frac{\Gamma^2(3/4)}{\Gamma^2(1/4)}, \\ N = \frac{c_1}{D}, \\ O = \frac{-6\sqrt{2}f_k}{\sqrt{\pi}D} \frac{\Gamma(3/4)}{\Gamma(1/4)}, \\ Q = \frac{12(r-1)}{5\sqrt{\pi}\varepsilon D} \frac{\Gamma(3/4)}{\Gamma(1/4)}. \quad (20)$$

As is shown by Stratonovitch [40], the corresponding first approximation for the joint probability density function of the displacement y_1 and velocity y_2 can be obtained as follows in terms of equations (7) and (14):

$$p(y_1, y_2) \approx \frac{p(H)}{T(H)} \Big|_{H=(1/2)y_2^2+(1/4)y_1^2}. \quad (21)$$

Note that $g(y_1) = y_1^3$ has only one zero, then the transformation from $p(H)$ to $p(y_1, y_2)$ is one-to-one for each level of H [41].

Since the displacement y_1 and velocity y_2 are the variables of the transformed system, the original system's joint probability density function for the displacement x_1 and velocity x_2 can be derived by means of the inverse transformation of equation (2).

$$p(x_1, x_2) = p_s(y_1, y_2) \left| \frac{\partial(y_1, y_2)}{\partial(x_1, x_2)} \right| = p_{Y_1, Y_2}(x_1, x_2) \\ + p_{Y_1, Y_2}(-x_1, -x_2) = 2p(y_1, y_2). \quad (22)$$

According to the formula between the joint probability density function and the marginal probability density function, the resulting stationary probability density function for displacement x_1 and velocity x_2 are given by

$$p_{X_1}(x_1) = \int_R p(x_1, s) ds, \\ p_{X_2}(x_2) = \int_{R^+} p(s, x_2) ds. \quad (23)$$

4. Response Analysis

In order to validate the analytical results of the system's stationary responses obtained via the nonsmooth transformation and stochastic averaging method of energy envelope, numerical simulations by fourth-order stochastic Runge-Kutta algorithm and Monte Carlo methods are performed, and herein the procedure is based on the original

vibro-impact system with dry friction under white noise excitation. To judge the instants of impacts more accurately, two different time step sizes are used in the Runge–Kutta algorithm: before the oscillator moves to the barrier, the larger time step is chosen to reduce simulation time; once the oscillator arrives at the position $x = 0$, the smaller time step is selected to improve the precision. Seeing the stochastic response, we are interested in is the stationary one, the frontal data should not be considered.

4.1. Effectiveness of the Procedure. In this subsection, the agreement between the analytical results and numerical results is under consideration. Fixing the scale parameter $\varepsilon = 0.01$, since the analytical results are derived in the case that the energy loss due to the linear damping, the nonlinear damping, the impact, and friction as well as random excitation is far less than the system's original energy. Other parameters are as follows: $c_1 = 3.0$, $c_2 = 1.0$, $f_k = 1.0$, $r = 0.99$, and $D = 1.0$. Figure 2 presents the analytical results and Monte Carlo simulation results of stationary PDFs for total energy H , where the line denotes the analytical results and the bullet means the numerical results. By comparing them with each other, excellent agreement can be found easily. The stationary joint PDFs for displacement x_1 and velocity x_2 are shown in Figure 3. It is obvious that the analytical result in Figure 3(a) agrees well with the Monte Carlo result in Figure 3(b). To reveal the effectiveness of the analytical procedure more clearly, the contour plots of joint PDFs corresponding to Figures 3(a) and 3(b) are depicted in Figures 4(a) and 4(b), respectively. The error is inconspicuous between the analytical result and Monte Carlo simulation result.

4.2. The Influence of Nonsmooth Factors. In virtue of the nonsmooth characteristics caused by impact and dry friction, the dynamical behaviour of the system becomes quite complex. Hence, the influences of nonsmooth factors on the system's responses would be investigated in detail.

First of all, we consider the changes of system response when the restitution coefficient r varies as well as other system parameters keep unchanged. As mentioned above, the value of restitution coefficient r depicts the energy loss due to impact. The closer r is to 1, the less energy loss is. Here, $r > 0.9$ is considered to make the system quasi-conservative, and thus, the analytical results are effective. The curves of stationary PDFs for total energy are shown in Figure 5 as the restitution coefficient r equals to 0.95, and herein other parameters remain unchanged. The line represents the analytical results and the bullet denotes the numerical results. It is obvious that they agree well with each other. The peak of the PDFs for total energy is at the position $H = 0$ in Figure 5, that is, the oscillator would stay at the system's static equilibrium with a high probability. However, it is not the case shown in Figure 2, where r equals to 0.99. It is intuitively believable that the smaller r is, the larger energy loss is; consequently, the probability that the oscillator stays at the system's static equilibrium is higher. On the other hand, the results indicate the occurrence of stochastic

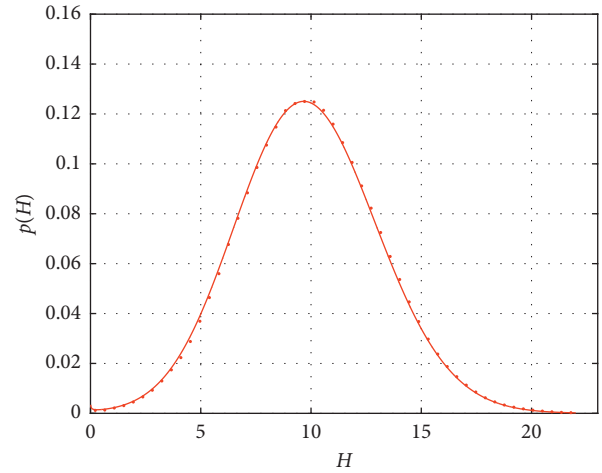


FIGURE 2: Stationary PDFs for total energy H . (—), analytical results; (·), Monte Carlo results.

P-bifurcation. In order to present this phenomenon more clearly, Figures 6(a) and 6(b) show the analytical results and numerical results of stationary joint PDFs for displacement x_1 and velocity x_2 , respectively, as $r = 0.95$. Also, Figures 7(a) and 7(b) are the corresponding contour plots. It is easy to find that the stochastic P-bifurcation happens by comparing Figures 6 and 7 with Figures 3 and 4, respectively, since the image in Figure 3 presents the shape of the crater while there is a singular peak in Figure 6. Furthermore, the section graphs of joint PDFs on the surface $x_1 = 0$ for different restitution coefficients r are presented in Figure 8, who clearly demonstrate the evolution process of PDFs' images with r varying. When $r = 0.95$, the PDF only has one peak. Then, it peaks to three peaks as r increases and finally becomes two peaks. This phenomenon is indicative of stochastic P-bifurcation, that is, the change of the restitution coefficient r can induce the occurrence of stochastic P-bifurcation.

The dry friction is another significant nonsmooth factor which may have a great influence on the dynamical properties of the system. Therefore, we explore the changes of stationary joint PDFs for displacement x_1 and velocity x_2 when the amplitude of Coulomb friction f_k varies. For this purpose, we fix other parameters as $c_1 = 3.0$, $c_2 = 1.0$, $r = 0.99$, and $D = 1.0$ and only modify the value of f_k . Analytical results of stationary joint PDFs for displacement x_1 and velocity x_2 for different amplitudes of friction are shown in Figure 9. It can be seen from Figure 9(a), the image of the system's response presents the shape of the crater when $f_k = 0$, that is, there is no friction. The result with $f_k = 2$ in Figure 9(b) is different from the case of $f_k = 0$ in Figure 9(a), since at this time, a new peak arises. As for the case $f_k = 2.5$ in Figure 9(c), the new peak becomes higher, and two other peaks become quite lower, and when $f_k = 3$, there is only one singular peak in Figure 9(d). It is obvious that stochastic P-bifurcation happens as the amplitude of Coulomb friction varies. By the way of understanding the evolution process of stochastic P-bifurcation, the section graphs of joint PDFs on the surface $x_1 = 0$ for different

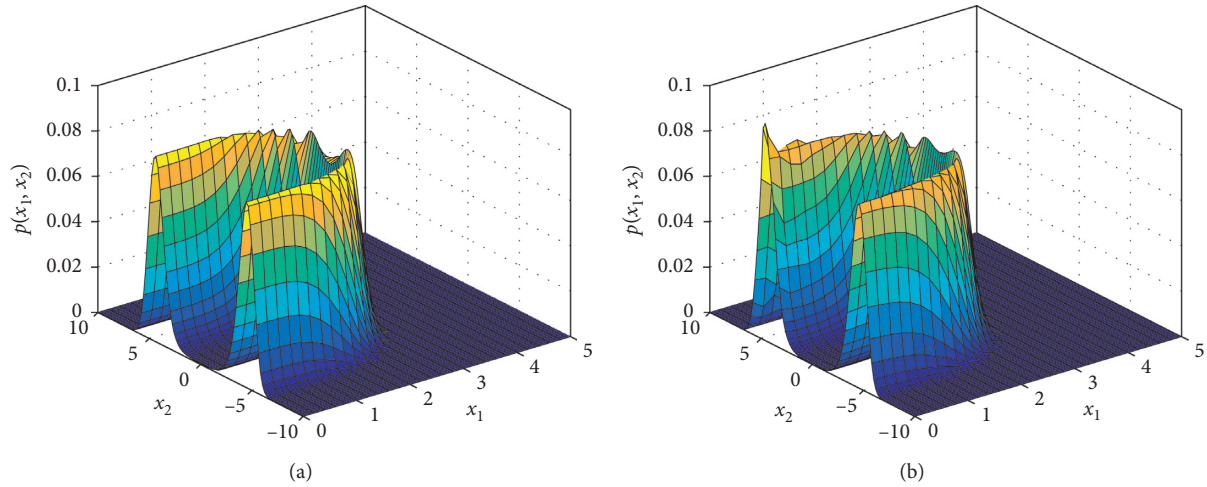


FIGURE 3: Stationary joint PDFs for displacement x_1 and velocity x_2 : (a) analytical results; (b) Monte Carlo results.

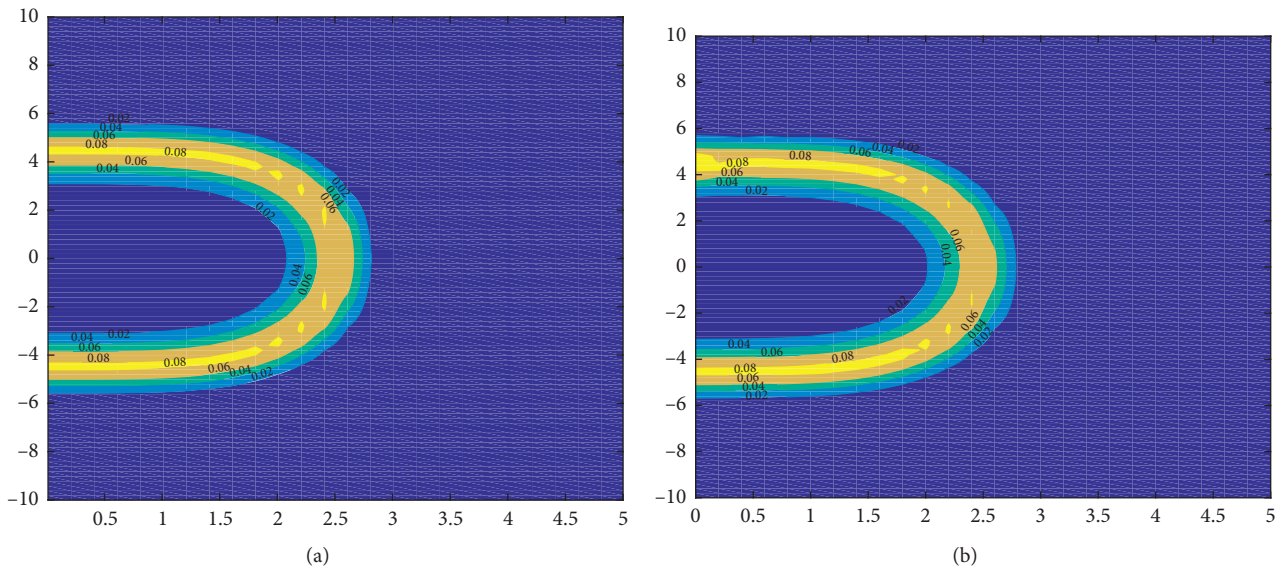


FIGURE 4: Contour plots of stationary joint PDFs for displacement x_1 and velocity x_2 : (a) analytical results; (b) Monte Carlo results.

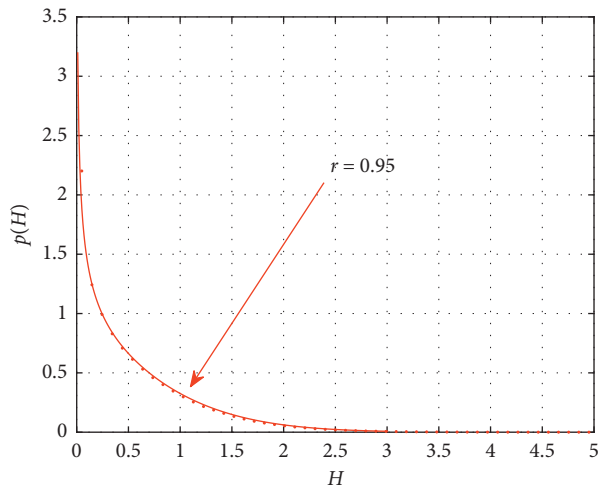


FIGURE 5: Stationary PDFs for total energy H . (—), analytical results; (·), Monte Carlo results.

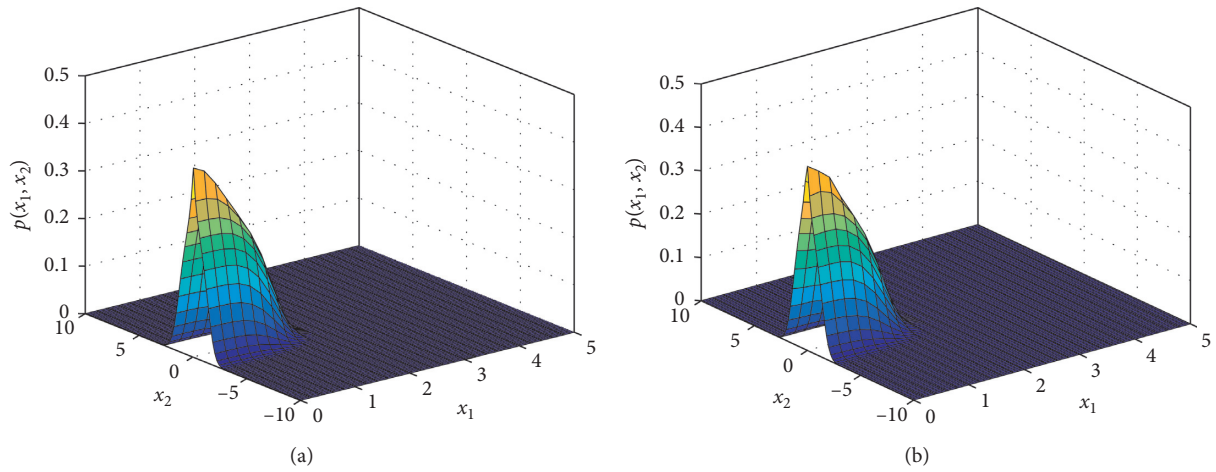


FIGURE 6: Stationary joint PDFs for displacement x_1 and velocity x_2 as $r = 0.95$: (a) analytical results; (b) Monte Carlo results.

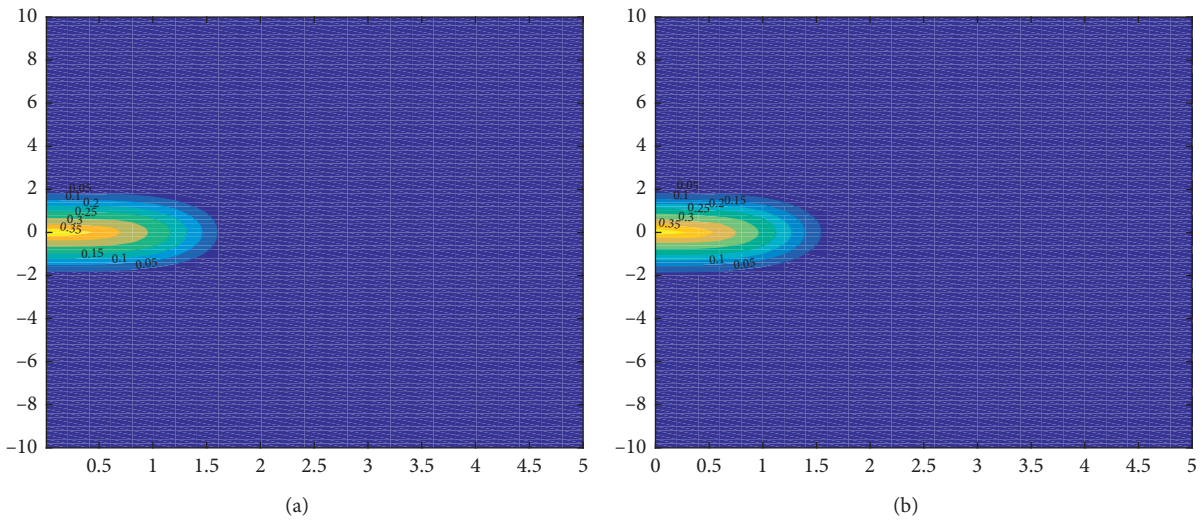


FIGURE 7: Contour plots of stationary joint PDFs for displacement x_1 and velocity x_2 as $r = 0.95$: (a) analytical results; (b) Monte Carlo results.

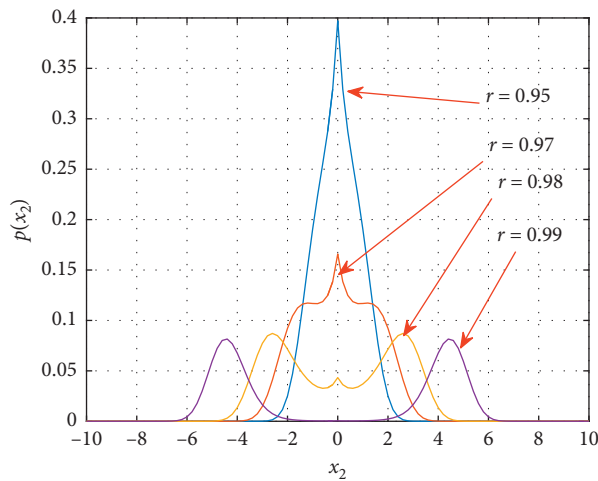


FIGURE 8: Section graphs of joint PDFs on the surface $x_1 = 0$ for different restitution coefficients r .

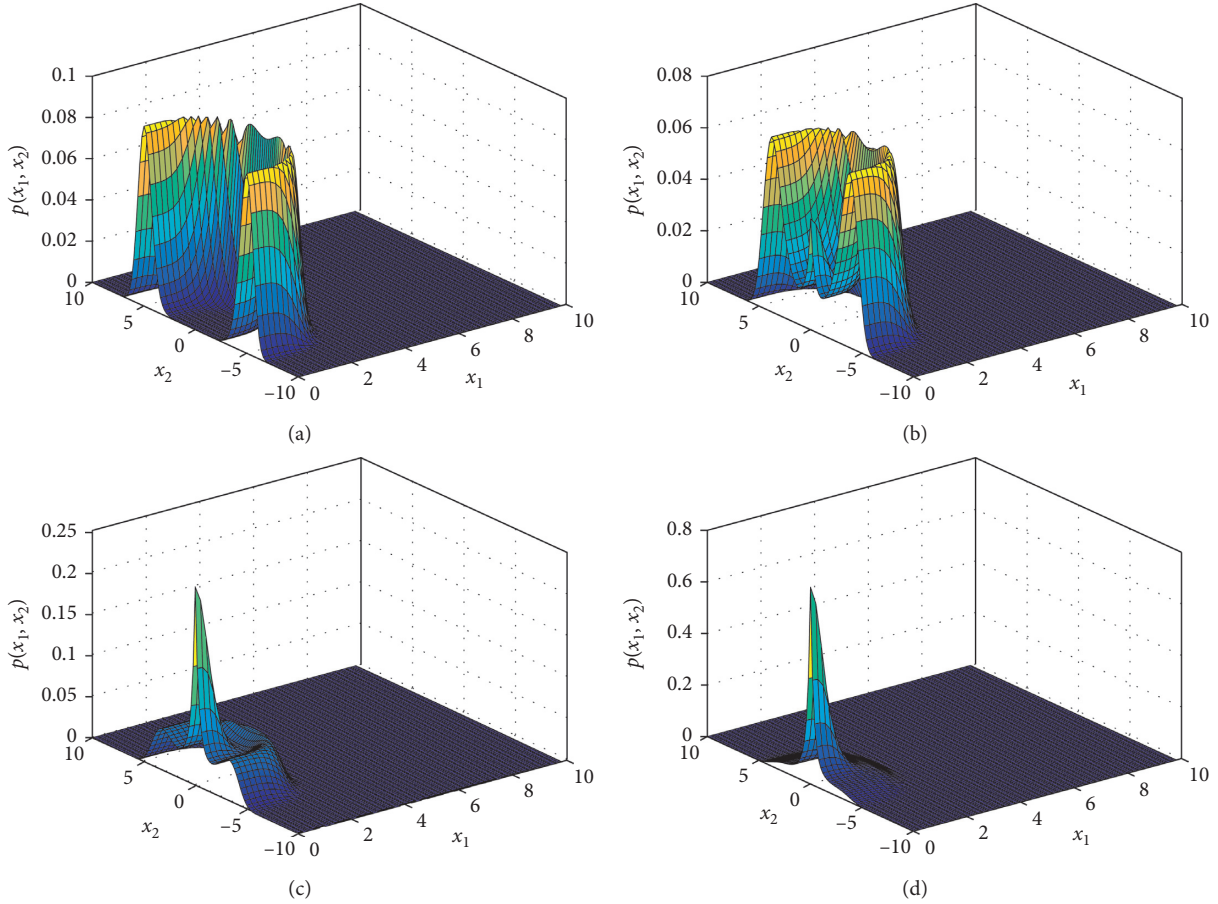


FIGURE 9: Analytical results of stationary joint PDFs for displacement x_1 and velocity x_2 for different amplitudes of friction: (a) $f_k = 0$, (b) $f_k = 2$, (c) $f_k = 2.5$, and (d) $f_k = 3$.

amplitudes of friction f_k are shown in Figure 10, which clearly present the changes of response PDFs in pace with the variation of f_k .

4.3. The Influence of Random Excitation. As is known to all, the random excitations are ubiquitous in practical mechanical systems. Their effects are usually not negligible and even play a crucial role. For the sake of understanding the random excitation's effect, the changes of the system's response are studied for different Gaussian white noise intensities. In Figures 11(a) and 11(b), the marginal PDFs for displacement x_1 and velocity x_2 are shown, respectively, when D varies; in the meantime, other system parameters are fixed as $c_1 = 3.0$, $c_2 = 1.0$, $f_k = 1.0$, and $r = 0.99$. The line denotes the analytical results and the bullet, circle, and asterisk mean the numerical results. It is easy to see that the peak values of marginal PDFs for displacement x_1 and velocity x_2 increase with the decrease of noise intensity. However, the shape of the PDFs has no substantial change. That is, there is no stochastic P-bifurcation occurring when the noise intensity changes. The results are similar as other parameters are given. For example, when $c_1 = 3.0$, $c_2 = 1.0$, $f_k = 1.0$, and $r = 0.97$, the marginal PDFs for displacement x_1 and velocity x_2 are

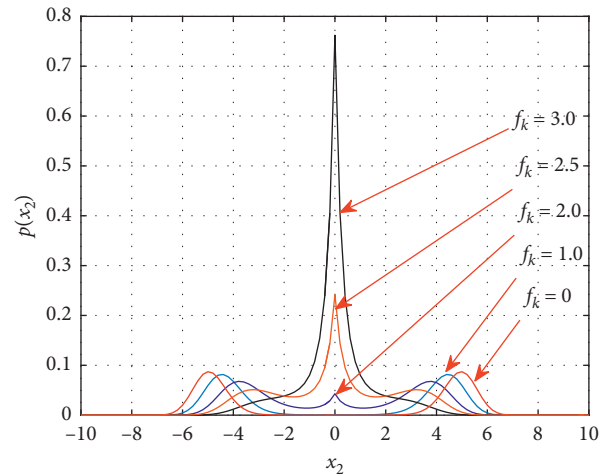


FIGURE 10: Section graphs of joint PDFs on the surface $x_1 = 0$ for different amplitudes of friction f_k .

shown in Figures 12(a) and 12(b). As can be observed from the figures, the peak values change with the variation of noise intensity, but the shape is little different, which indicates that the stochastic P-bifurcation does not appear.

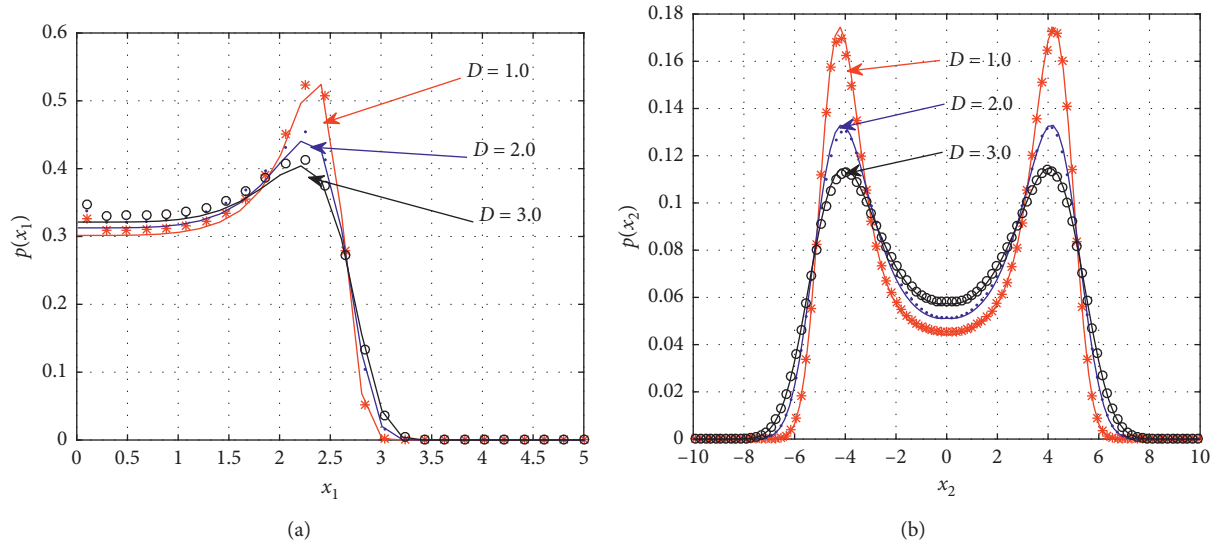


FIGURE 11: Stationary PDFs as $r = 0.99$: (a) displacement x_1 ; (b) velocity x_2 .

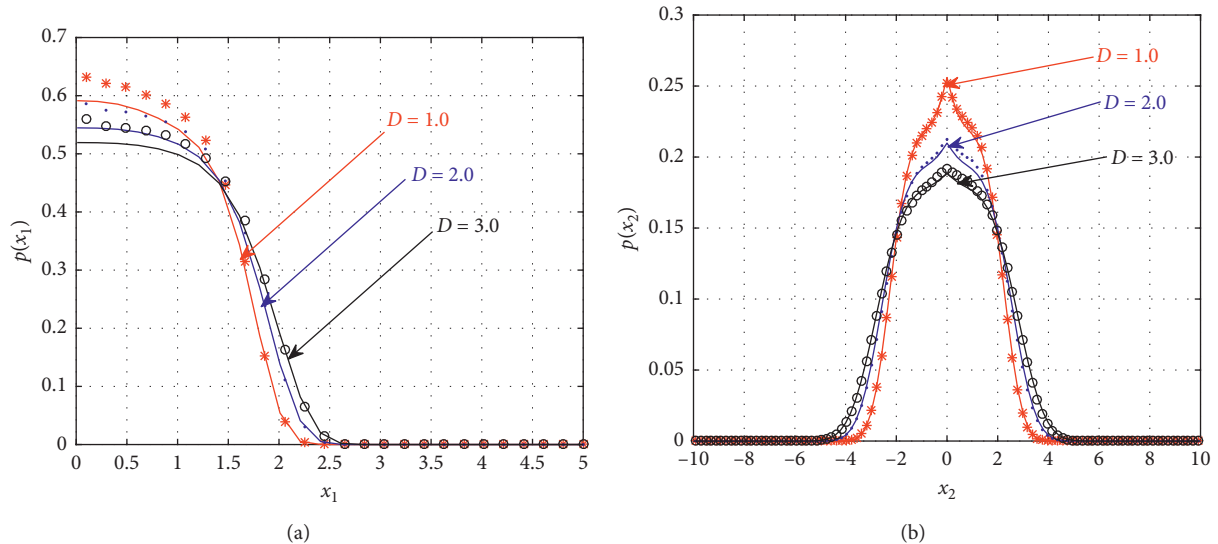


FIGURE 12: Stationary PDFs as $r = 0.97$: (a) displacement x_1 ; (b) velocity x_2 .

5. Conclusions

In this work, the combination of the nonsmooth transformation and the stochastic averaging method of energy envelope is extensively used to obtain the steady-state dynamical responses of a Van der Pol-Duffing vibro-impact system with Coulomb friction subjected to white noise excitation. The results obtained by the analytical procedure agree well with those from Monte Carlo simulation. What's more, effects of different restitution coefficients, amplitudes of friction, and Gaussian white noise intensities on the steady-state dynamical responses are discussed. Results show that the peak values change with the variation of Gaussian white noise intensity and different restitution coefficients and amplitudes of friction can lead to the stochastic P-bifurcation. Generally, the procedure in this paper

could be applied to study more complicated nonlinear systems with impact and dry friction.

Data Availability

The data used to support the findings of this study are included within the article.

Conflicts of Interest

The authors declare that they have no conflicts of interest.

Acknowledgments

This work was supported by the National Natural Science Foundation of China (Grant nos. 11702200 and 11702201), Natural Science Basic Research Plan in Shaanxi Province of

China (Grant no. 2018JQ1088), and Fundamental Research Funds for the Central Universities (Grant no. GHC1911).


References

- [1] W. Zhang and H. Y. Hu, *Advance in Nonlinear Dynamics Theory and Application*, Science Press, Beijing, China, 2009.
- [2] A. Ibrahim Raouf, *Vibro-impact Dynamics: Modeling, Mapping and Applications*, Springer, Berlin, Germany, 2009.
- [3] D. Huang, S. Zhou, and G. Litak, "Analytical analysis of the vibrational tristable energy harvester with a RL resonant circuit," *Nonlinear Dynamics*, vol. 97, no. 1, pp. 663–677, 2019.
- [4] D. Huang, S. Zhou, and G. Litak, "Theoretical analysis of multi-stable energy harvesters with high-order stiffness terms," *Communications in Nonlinear Science and Numerical Simulation*, vol. 69, pp. 270–286, 2019.
- [5] M. F. Dimentberg, *Statistical Dynamics of Nonlinear and Time-Varying Systems*, Wiley, London, UK, 1988.
- [6] D. P. Jin and H. Y. Hu, "Vibroimpacts and their typical behaviors of mechanical systems," *Advances in Mechanics*, vol. 25, no. 2, pp. 155–164, 1999.
- [7] K. Wang and X. B. Liu, "Stochastic resonance for a time-delayed metapopulation system driven by multiplicative and additive noise," *Chinese Physics Letters*, vol. 20, no. 7, p. 70504, 2013.
- [8] Y. Xu, Y. Li, and D. Liu, "A method to stochastic dynamical systems with strong nonlinearity and fractional damping," *Nonlinear Dynamics*, vol. 83, no. 4, pp. 1–11, 2015.
- [9] G. Q. Cai and Y. K. Lin, "Response distribution of non-linear systems excited by non-Gaussian impulsive noise," *International Journal of Non-linear Mechanics*, vol. 27, no. 6, pp. 955–967, 1992.
- [10] M. F. Dimentberg and D. V. Iourtchenko, "Random vibrations with impacts: a review," *Nonlinear Dynamics*, vol. 36, no. 2–4, pp. 229–254, 2004.
- [11] N. S. Namachchivaya and J. H. Park, "Stochastic dynamics of impact oscillators," *Journal of Applied Mechanics*, vol. 72, no. 6, pp. 862–870, 2005.
- [12] K. Kappaganthu and C. Nataraj, "Nonlinear modeling and analysis of a rolling element bearing with a clearance," *Communications in Nonlinear Science and Numerical Simulation*, vol. 16, no. 10, pp. 4134–4145, 2011.
- [13] Q. Ding and H. M. Zhai, "Progress in friction dynamics of mechanical systems," *Advance in Mechanics*, vol. 43, no. 1, pp. 112–131, 2013.
- [14] G. Luo, Y. Zhang, J. Xie, and J. Zhang, "Periodic-impact motions and bifurcations of vibro-impact systems near 1:4 strong resonance point," *Communications in Nonlinear Science and Numerical Simulation*, vol. 13, no. 5, pp. 1002–1014, 2008.
- [15] S. W. Shaw and P. J. Holmes, "A periodically forced piecewise linear oscillator," *Journal of Sound and Vibration*, vol. 90, no. 1, pp. 129–155, 1983.
- [16] G.-W. Luo and J.-H. Xie, "Hopf bifurcation of a two-degree-of-freedom vibro-impact system," *Journal of Sound and Vibration*, vol. 213, no. 3, pp. 391–408, 1998.
- [17] J. M. T. Thompson and R. Ghaffari, "Chaos after period-doubling bifurcations in the resonance of an impact oscillator," *Physics Letters A*, vol. 91, no. 1, pp. 5–8, 1982.
- [18] A. B. Nordmark, "Existence of periodic orbits in grazing bifurcations of impacting mechanical oscillators," *Nonlinearity*, vol. 14, no. 6, pp. 1517–1542, 2001.
- [19] A. B. Nordmark and P. T. Piiroinen, "Simulation and stability analysis of impacting systems with complete chattering," *Nonlinear Dynamics*, vol. 58, no. 1-2, pp. 85–106, 2009.
- [20] K. M. Cone and R. I. Zadoks, "A numerical study of an impact oscillator with the addition of dry friction," *Journal of Sound and Vibration*, vol. 188, no. 5, pp. 659–683, 1995.
- [21] Q. Feng and H. He, "Modeling of the mean Poincaré map on a class of random impact oscillators," *European Journal of Mechanics-A/Solids*, vol. 22, no. 2, pp. 267–281, 2003.
- [22] J. Q. Sun, "Random vibration analysis of a non-linear system with dry friction damping by the short-time Gaussian cell mapping method," *Journal of Sound and Vibration*, vol. 180, no. 5, pp. 785–795, 1995.
- [23] L. N. Virgin and C. J. Begley, "Grazing bifurcations and basins of attraction in an impact-friction oscillator," *Physica D*, vol. 132, pp. 43–57, 2001.
- [24] Y. Q. Zhang, W. C. Ding, and C. Sun, "Bifurcation and chaos of a vibration system with clearance and dry friction," *Vibration and Shock*, vol. 27, no. 7, pp. 102–105, 2008.
- [25] Y. Yue, P. Miao, and J. Xie, "Coexistence of strange non-chaotic attractors and a special mixed attractor caused by a new intermittency in a periodically driven vibro-impact system," *Nonlinear Dynamics*, vol. 87, no. 2, pp. 1187–1207, 2017.
- [26] H.-S. Jing and K.-C. Sheu, "Exact stationary solutions of the random response of a single-degree-of-freedom vibro-impact system," *Journal of Sound and Vibration*, vol. 141, no. 3, pp. 363–373, 1990.
- [27] Z. L. Huang, Z. H. Liu, and W. Q. Zhu, "Stationary response of multi-degree-of-freedom vibro-impact systems under white noise excitations," *Journal of Sound and Vibration*, vol. 275, no. 1-2, pp. 223–240, 2004.
- [28] M. Xu, Y. Wang, X. L. Jin, Z. L. Huang, and T. X. Yu, "Random response of vibro-impact systems with inelastic contact," *International Journal of Non-linear Mechanics*, vol. 52, pp. 26–31, 2013.
- [29] V. F. Zhuravlev, "A method for analyzing vibration-impact systems by means of special function," *Mechanical Solids*, vol. 11, pp. 23–27, 1976.
- [30] M. F. Dimentberg and D. V. Iourtchenko, "Towards incorporating impact losses into random vibration analyses: a model problem," *Probabilistic Engineering Mechanics*, vol. 14, no. 4, pp. 323–328, 1999.
- [31] M. F. Dimentberg and A. I. Menyailov, "Response of a single-mass vibroimpact system to white-noise random excitation," *ZAMM - Zeitschrift für Angewandte Mathematik und Mechanik*, vol. 59, no. 12, pp. 709–716, 1979.
- [32] D. V. Iourtchenko and L. L. Song, "Analytical analysis of stochastic vibroimpact systems," in *Proceedings of International Conference on Structural Safety and Reliability 2005*, pp. 1931–1937, Rome, Italy, June 2005.
- [33] H. T. Zhu, "Response of a vibro-impact Duffing system with a randomly varying damping term," *International Journal of Non-linear Mechanics*, vol. 65, pp. 53–62, 2014.
- [34] L. Chen, J. Qian, H. Zhu, and J.-Q. Sun, "The closed-form stationary probability distribution of the stochastically excited vibro-impact oscillators," *Journal of Sound and Vibration*, vol. 439, pp. 260–270, 2019.
- [35] X. Xie, J. Li, D. Liu, and R. Guo, "Transient response of nonlinear vibro-impact system under Gaussian white noise excitation through complex fractional moments," *Acta Mechanica*, vol. 228, no. 3, pp. 1153–1163, 2017.

- [36] W. J. Ding, *Damping Theory*, Tsinghua University Press, Beijing, China, 1988.
- [37] J. Sun, W. Xu, and Z. Lin, "Research on the reliability of friction system under combined additive and multiplicative random excitations," *Communications in Nonlinear Science and Numerical Simulation*, vol. 54, pp. 1–12, 2018.
- [38] M. Su, W. Xu, and G. Yang, "Response analysis of van der Pol vibro-impact system with Coulomb friction under Gaussian white noise," *International Journal of Bifurcation and Chaos*, vol. 28, no. 13, Article ID 1830043, 2018.
- [39] R. Z. Khasminskii, "On the averaging principle for stochastic differential Ito equation," *Kibernetika*, vol. 4, no. 3, pp. 260–279, 1968.
- [40] R. L. Stratonovich, *Topics in the Theory of Random Noise*, Gordon and Gordon, New York, NY, USA, 1967.
- [41] W. Zhu and Y. K. Lin, "Stochastic averaging of energy envelope," *Journal of Engineering Mechanics*, vol. 117, no. 8, pp. 1890–1905, 1991.

Research Article

A Time-Discontinuous Galerkin Finite Element Method for the Solution of Impact Problem of Gas-Saturated Coal

Jingfei Zhang,^{1,2} Deyong Guo,¹ Wenhua Wu,³ and Pan Guo ²

¹School of Emergency Management and Safety Engineering, China University of Mine and Technology, Beijing 100083, China

²School of Mechanics and Safety Engineering, Zhengzhou University, Zhouzhou 450001, China

³The State Key Laboratory for Structural Analysis of Industrial Equipment, Department of Engineering Mechanics, Faculty of Vehicle Engineering and Mechanics, Dalian University of Technology, Dalian 116024, China

Correspondence should be addressed to Pan Guo; panguo@zzu.edu.cn

Received 23 April 2020; Revised 31 July 2020; Accepted 4 August 2020; Published 29 August 2020

Academic Editor: Matteo Strozzi

Copyright © 2020 Jingfei Zhang et al. This is an open access article distributed under the Creative Commons Attribution License, which permits unrestricted use, distribution, and reproduction in any medium, provided the original work is properly cited.

Based on the general Biot theory of saturated porous media, a modified time-discontinuous Galerkin finite element method (MDGFEM) is presented to simulate the structural dynamics and wave propagation problems of gas-saturated coal subjected to impact loading. Numerical results of one dimension and two dimensions show that the present MDGFEM possesses better abilities and provides much more accurate solutions than the traditional Newmark method and previous DGFEM for the impact problem. It can effectively capture the discontinuities of the wave and filter out the effects of spurious numerical oscillation induced by high-frequency impulsive load. The results can provide a technological basis for the research of the prevention of coal and gas dynamic disasters under deep mining. And the method could be useful for the further numerical research of coal-rock-gas coupling problems and coal-gas-heat coupling problems subjected to impact loading.

1. Introduction

With the increase of coal mining depth, coal and gas outburst disasters are becoming more and more severe [1]. The mechanism of outburst accidents, which has been studied by many experts and scholars, demonstrates that the coupling scheme of gas pressure and coal structure plays a dominant role in the coal and gas outburst disasters, and the outburst accidents are always caused by different impact loading [1, 2]. However, understanding of the disaster caused by the impact load under complicated environment is far from enough and the risk of outburst accidents cannot be completely eliminated [1–4]. And one motivation of our research is to investigate the dynamic and wave propagation problem of gas-saturated coal subjected to impact loads.

In the past, efforts have been made to find a porous media model, such as Biot's theory, to discover the reflection and transmission of waves in a porous medium [5, 6]. Biot's theory derives the equations of motion of each phase based on energy considerations which include the inertial,

potential, and viscous coupling between the two phases. The equations governing the interaction of the solid and fluid media for dynamics phenomena were first established in 1956 by Biot [5]. Owing to its simplicity, many authors have followed Biot's approach to research the problem of wave propagation in gas-saturated coal [3, 4].

Developing a robust and efficient numerical method for the coupled problems subjected to the high-frequency impact loading is challenging, and the simulation of the problems is another motivation of our research. This is particularly the case for the problems of wave propagation in gas-saturated coal where discontinuities exist both in the time domain and the space domain. Despite the popularity, the traditional time integration method (such as Newmark method) [7–9] struggles to provide more accurate solutions and eliminate spurious numerical oscillations in numerical simulation of wave propagation involving sharp gradients and discontinuities in the time domain.

Li et al. presented a novel time-discontinuous Galerkin finite element method (DGFEM) for solving dynamics

and wave propagation in nonlinear solids and saturated porous media and heat wave propagation problem subjected to impact loading [10–12]. The remarkable characteristics of the DG method is that the basic unknown variables together with their temporal derivatives are assumed to be discontinuous at a defined time point and are assumed to be interpolated by third-order Hermite function and linear function in a time step, respectively. We then successfully applied the MDGFEM, based on an additional artificial damping scheme, to simulate heat wave propagation and generalized thermoelastic problems subjected to thermal shock [13, 14]. Numerical results demonstrate that the MDGFEM illustrates better performance in numerical simulation of wave propagation in eliminating spurious numerical oscillations and in providing more accurate solutions than that of the traditional time integration method and the DGFEM before being modified.

For the high-speed motion and high pressure of the gas-saturated coal problem under high-frequency loading, the acceleration of porous fluid should be considered [6]. In this article, an additional artificial damping discontinuous Galerkin numerical algorithm for gas-saturated coal problems is developed on the basis of elastic-plastic saturated porous medium model [6] and previous research studies [12]. An additional stiffness proportional damping scheme is brought into the final finite element discretized form to reduce the numerical oscillations appearing in the wave-front stage of the elastic-plastic stress wave and the pressure wave. Numerical results show clearly that the MDGFEM method is valid for filtering out spurious oscillations in both waves and for providing much more accurate solutions than those obtained using the previous DGFEM and the traditional time integration methods (e.g., the Newmark method). The present modeling method provides accurate numerical method for the prediction and early warning of coal and gas outburst and could also be extended to the study of coal-rock-gas coupling problems and coal-gas-heat coupling problems subjected to impact loading.

2. The Basic Dynamics Governing Equations and DGFEM Formulation for Coal and Rock Porous Media

This section summarizes the basic governing equations of gas-saturated coal porous media subjected to impact loading. As the porous fluid is compressible, the equations of motion for the coal skeleton can be expressed as [6]

$$\sigma_{ij,j} + \rho b_i - \rho \ddot{u}_i + \rho_f (\ddot{w}_i + \dot{w}_k \dot{w}_{i,k}) = 0. \quad (1)$$

For the pore fluid, the equation of motion can be written as

$$-p_{,i} + \rho_f b_i = \rho_f \left(\ddot{u}_i + \frac{1}{n} (\ddot{w}_i + \dot{w}_k \dot{w}_{i,k}) \right) + \frac{R_i}{n} = 0, \quad (2)$$

where $(R_i/n) = k_{w,i}^{-1} \dot{w}_i$; σ_{ij} is the total Cauchy stress; b_i is the body force acceleration; ρ , ρ_f , and ρ_s are the densities of the assembly, the fluid and the solid phases, respectively; w_k is the displacement of the fluid phase; u_i is the displacement of the solid phase; and n is the porosity.

Insertion of $U_i = u_i + (1/n)w_i$ into equations (1) and (2) and subtraction of equation (2) $\times n$ from equation (1) leads to the equation of solid skeleton equilibrium.

$$\sigma''_{ij,j} - (\alpha - n)p_{,i} + (1 - n)\rho_s b_i - (1 - n)\rho_s \ddot{u}_i - R_i = 0, \quad (3)$$

where $\sigma''_{ij} = \sigma_{ij} - \alpha p$ is the generalized Biot effective stress tensor and $R_i = n^2 k_{w,i}^{-1} (\dot{U}_j - \dot{u}_j)$. For an isotropic material, the Biot parameter $\alpha = 1 - (K_T/K_s)$, where $K_T = (E/3(1 - 2\nu))$.

Equation (2) can be written as

$$-np_{,i} + n\rho_f b_i - n\rho_f \ddot{U}_i - R_i = 0. \quad (4)$$

Then, the mass conservation equation of the fluid flow can be written as

$$-n\dot{U}_{i,i} = (\alpha - n)\dot{\epsilon}_{ii} + \frac{1}{Q}\dot{p}. \quad (5)$$

Using the definition of equation (5), equations (1) and (2) can be rewritten as

$$\sigma''_{ij,j} - (\alpha - n)Q \left[(\alpha - n)u_{k,k} + nU_{k,k} \right]_{,i} - (1 - n)\rho_s \ddot{u}_i - n^2 k_{w,i}^{-1} (\dot{U}_j - \dot{u}_j) = 0, \quad (6)$$

$$-nQ \left[(\alpha - n)u_{k,k} + nU_{k,k} \right]_{,i} - n\rho_f \ddot{U}_i - n^2 k_{w,i}^{-1} (\dot{U}_j - \dot{u}_j) = 0, \quad (7)$$

where $(1/Q) = (n/K_f) + (\alpha - n/K_s)$; K_f is the bulk modulus of the fluid; and K_s is the bulk modulus of the solid. The

linearized form of the semidiscretized systems of the motion equations (6) and (7) can be written as

$$\begin{bmatrix} \mathbf{M}_s & 0 \\ 0 & \mathbf{M}_f \end{bmatrix} \begin{bmatrix} \ddot{\mathbf{u}}(t) \\ \ddot{\mathbf{U}}(t) \end{bmatrix} + \begin{bmatrix} \mathbf{C}_{11} & \mathbf{C}_{12} \\ \mathbf{C}_{21} & \mathbf{C}_{22} \end{bmatrix} \begin{bmatrix} \dot{\mathbf{u}}(t) \\ \dot{\mathbf{U}}(t) \end{bmatrix} + \begin{bmatrix} \mathbf{K}_{11} & \mathbf{K}_{12} \\ \mathbf{K}_{21} & \mathbf{K}_{22} \end{bmatrix} \begin{bmatrix} \bar{\mathbf{u}}(t) \\ \bar{\mathbf{U}}(t) \end{bmatrix} = \begin{bmatrix} \mathbf{f}_u \\ \mathbf{f}_U \end{bmatrix}, t \in (0, T), \quad (8)$$

in which

$$\begin{aligned}
\mathbf{M}_s &= \int_{\Omega} N_K^u (1-n) \rho_s \delta_{ij} N_N^u d\Omega, \\
\mathbf{M}_f &= \int_{\Omega} N_K^U (1-n) \rho_f \delta_{ij} N_L^U d\Omega, \\
\mathbf{C}_{11} &= \int_{\Omega} N_K^u n^2 \delta_{ij} k_{w,ij}^{-1} N_L^u d\Omega, \\
\mathbf{C}_{12} &= \int_{\Omega} N_K^u n^2 \delta_{ij} k_{w,ij}^{-1} N_L^U d\Omega, \\
\mathbf{C}_{22} &= \int_{\Omega} N_K^U n^2 \delta_{ij} k_{w,ij}^{-1} N_L^U d\Omega, \\
\mathbf{K}_{11} &= \mathbf{K}_t + \mathbf{K}_{11}^*, \\
\mathbf{K}_t &= \int_{\Omega} N_{K,k}^u (\alpha - n)^2 Q N_{L,j}^u d\Omega, \\
\mathbf{K}_{11}^* &= \int_{\Omega} N_{K,k}^u D_{ijkl} Q N_{L,i}^u d\Omega, \\
\mathbf{K}_{12} &= \int_{\Omega} N_{K,k}^u n (\alpha - n) Q N_{L,j}^U d\Omega, \\
\mathbf{K}_{22} &= \int_{\Omega} N_{K,k}^U n^2 Q N_{L,j}^U d\Omega,
\end{aligned} \tag{9}$$

where $\bar{\mathbf{u}}(t)$ and $\bar{\mathbf{U}}(t)$ are the nodal displacements of the solid skeleton and the nodal intrinsic displacements of the pore fluid, respectively, D_{ijkl} is a fourth-order tensor defining a constitutive law for the solid skeleton, and $N_{K,i}^u$ and $N_{K,i}^U$ are the spatial derivatives of the shape functions of the K^{th} node with respect to the i coordinate axis for the spatial finite element discretization.

It should be noted that the appropriate boundary conditions associated with the governing equations (6) and (7) must be adopted. When the displacements are prescribed on the surfaces Γ_u and Γ_U , respectively, one has

$$\mathbf{u} = \mathbf{u}_0(t) \text{ on } \Gamma_u, \tag{10}$$

$$\mathbf{U} = \mathbf{U}_0(t) \text{ on } \Gamma_U, \tag{11}$$

where $\mathbf{U}_0(t)$ and $\mathbf{u}_0(t)$ are the prescribed values of fluid and solid displacement vector.

On the other hand, if surface loadings are applied to the corresponding surfaces Γ_u and Γ_U , the following boundary conditions should be satisfied:

$$\mathbf{f}_u = \mathbf{f}_{u0}(t) \text{ on } \Gamma_u, \tag{12}$$

$$\mathbf{f}_U = \mathbf{f}_{U0}(t) \text{ on } \Gamma_U, \tag{13}$$

where $\mathbf{f}_{u0}(t)$ and $\mathbf{f}_{U0}(t)$ are the given surface loadings, respectively.

In the present paper, surface impulse loading is applied with the form as

$$\mathbf{f}_{u0}(t) = \mathbf{f}_{U0}(t) = \begin{cases} P, & t \in [0, t_0], \\ 0, & t > t_0, \end{cases} \tag{14}$$

in which P and t_0 are the amplitude of loading and the constant time.

3. Temporal Discretization and Time-Discontinuous Galerkin Finite Element Method

3.1. Time-Discontinuous Galerkin Finite Element Method. The standard Galerkin discretized equation (8) can be re-written as follows:

$$\mathbf{M}\ddot{\mathbf{d}}(t) + \mathbf{C}\dot{\mathbf{d}}(t) + \mathbf{K}\mathbf{d}(t) = \mathbf{f}(t), t \in (0, T), \tag{15}$$

in which

$$\begin{aligned}
\mathbf{M} &= \begin{bmatrix} \mathbf{M}_s & 0 \\ 0 & \mathbf{M}_f \end{bmatrix}; \mathbf{C} = \begin{bmatrix} \mathbf{C}_{11} & \mathbf{C}_{12} \\ \mathbf{C}_{21} & \mathbf{C}_{22} \end{bmatrix}; \mathbf{K} = \begin{bmatrix} \mathbf{K}_{11} & \mathbf{K}_{12} \\ \mathbf{K}_{21} & \mathbf{K}_{22} \end{bmatrix}; \mathbf{f}(t) = \begin{bmatrix} \mathbf{f}_u \\ \mathbf{f}_U \end{bmatrix}; \\
\dot{\mathbf{d}}(t) &= \begin{bmatrix} \dot{\bar{\mathbf{u}}}(t) \\ \dot{\bar{\mathbf{U}}}(t) \end{bmatrix}; \ddot{\mathbf{d}}(t) = \begin{bmatrix} \ddot{\bar{\mathbf{u}}}(t) \\ \ddot{\bar{\mathbf{U}}}(t) \end{bmatrix}; \mathbf{d}(t) = \begin{bmatrix} \bar{\mathbf{u}}(t) \\ \bar{\mathbf{U}}(t) \end{bmatrix}.
\end{aligned} \tag{16}$$

The main features of the discontinuous Galerkin integration method in time domain have been described in our previous articles [13, 15]. Different from the continuous Galerkin method, the DGFEM permits the discontinuity of functions at discrete-time sequence, $0 \cdots < t_n < \cdots < t_N$. The temporal jump of the discontinuous function $\mathbf{d}(t_n)$ at t_n can be defined as

$$[[\mathbf{d}(t_n)]] = \mathbf{d}(t_n^+) - \mathbf{d}(t_n^-), \tag{17}$$

in which

$$\mathbf{d}(t_n^\pm) = \lim_{\varepsilon \rightarrow 0^\pm} \mathbf{d}(t_n + \varepsilon). \tag{18}$$

The global displacement vectors of solid and fluid at arbitrary time t in a time step $I_n = (t_n^+, t_{n+1}^-)$ are interpolated by using the third-order Hermite shape functions as

$$\mathbf{d}(t) = \mathbf{d}_n^+ N_1(t) + \mathbf{d}_{n+1}^- N_2(t) + \mathbf{v}_n^+ M_1(t) + \mathbf{v}_{n+1}^- M_2(t), \quad (19)$$

$$\begin{aligned} N_1(t) &= \lambda_1^2 (\lambda_1 + 3\lambda_2), N_2(t) = \lambda_2^2 (\lambda_2 + 3\lambda_1), \\ M_1(t) &= \lambda_1^2 \lambda_2 \Delta t, M_2(t) = -\lambda_2^2 \lambda_1 \Delta t, \\ \lambda_1 &= \frac{t_{n+1} - t_n}{\Delta t}, \\ \lambda_2 &= \frac{t_n - t_{n+1}}{\Delta t}, \end{aligned} \quad (20)$$

in which \mathbf{d}_n^+ and \mathbf{d}_{n+1}^- stand for the global nodal value of displacement vectors at times t_n and t_{n+1} and \mathbf{v}_n^+ and \mathbf{v}_{n+1}^- stand for the global nodal value of velocity vectors, respectively. We can rewrite equation (19) by dropping the superscripts of the displacement and velocity vectors and the time variable t as follows:

$$\mathbf{d}(t) = \mathbf{d}_n N_1(t) + \mathbf{d}_{n+1} N_2(t) + \mathbf{v}_n M_1(t) + \mathbf{v}_{n+1} M_2(t). \quad (21)$$

The global velocity vector of solid and fluid at arbitrary time t in a time step $I_n = (t_n^+, t_{n+1}^-)$ is interpolated as an independent variable by using the linear shape functions as follows:

$$\mathbf{v}(t) = \mathbf{v}_n^+ \lambda_1(t) + \mathbf{v}_{n+1}^- \lambda_2(t). \quad (22)$$

The weak forms of the semidiscretized equation (15) and the constraint condition $\dot{\mathbf{d}}(t) - \mathbf{v} = 0$ along with the discontinuity conditions \mathbf{d} and \mathbf{v} on a typical time subdomain can be expressed as

$$\int_{I_n} \delta \mathbf{v}^T (\mathbf{M} \ddot{\mathbf{d}}(t) + \mathbf{C} \dot{\mathbf{d}}(t) + \mathbf{K} \mathbf{d}(t) - \mathbf{f}(t)) dt + \int_{I_n} \delta \mathbf{d}^T \mathbf{K} (\dot{\mathbf{d}}(t) - \mathbf{v}) dt + \delta \mathbf{d}_n^T \mathbf{K} [[\mathbf{d}_n]] + \delta \mathbf{v}_n^T \mathbf{M} [[\mathbf{v}_n]] = 0. \quad (23)$$

Substituting equations (21) and (22) into (15), we obtain the following matrix equation of DGFEM for solving from independent variations:

$$\mathbf{d}_n^+ = \mathbf{d}_n^-, \quad (24)$$

$$\begin{bmatrix} \mathbf{M} + \frac{\Delta t}{6} \mathbf{C} - \frac{\Delta t^2}{12} \mathbf{K} & -\frac{\Delta t}{6} \mathbf{C} - \frac{\Delta t^2}{12} \mathbf{K} \\ \frac{\Delta t}{2} \mathbf{C} + \frac{\Delta t^2}{3} \mathbf{K} & \mathbf{M} + \frac{\Delta t}{2} \mathbf{C} + \frac{\Delta t^2}{6} \mathbf{K} \end{bmatrix} \begin{Bmatrix} \mathbf{v}_n \\ \mathbf{v}_{n+1} \end{Bmatrix} = \begin{Bmatrix} \mathbf{f}_1^e - \mathbf{f}_2^e + \mathbf{M} \mathbf{v}_n^- \\ \mathbf{f}_1^e + \mathbf{f}_2^e + \mathbf{M} \mathbf{v}_n^- - \Delta t \mathbf{K} \mathbf{d}_n^- \end{Bmatrix}, \quad (25)$$

$$\mathbf{d}_{n+1} = \mathbf{d}_n^- + \frac{1}{2} \Delta t (\mathbf{v}_n + \mathbf{v}_{n+1}), \quad (26)$$

in which $\mathbf{f}_1^e = (\Delta t/3) \mathbf{f}_n^e + (\Delta t/6) \mathbf{f}_{n+1}^e$ and $\mathbf{f}_2^e = (\Delta t/6) \mathbf{f}_n^e + (\Delta t/3) \mathbf{f}_{n+1}^e$.

It should be noted that the global nodal displacement vector of solid and fluid is continuous at any time level and the global nodal velocity vector is still discontinuous at any time level [10–15]. To demonstrate the advantage of the present DGFEM, we have to solve several problems in our previous work [10–15]. For the elastic-plastic dynamic problems, the Newton–Raphson process is used [10, 14].

3.2. Modified Time-Discontinuous Galerkin Finite Element Method. When simulating problems of structure dynamics and wave propagation under impulse load, the modified

time-continuous Galerkin finite element method shows better ability to filter out the effects of spurious numerical oscillations. Having demonstrated the applicability and advantage of the MDGFEM as indicated in our articles [13–15], we apply and discuss the method to solve the problem of gas-saturated coal based on Biot's model subjected to impulse load.

As we know that the selections of a stiffness proportional and mass proportional damping coefficient are effective for high-frequency oscillations and low-frequency oscillations, respectively, we modify the present DGFEM by using an artificial stiffness proportional Rayleigh-type damping scheme. The equations of the damping scheme can be written as follows:

$$\mathbf{C}_\lambda = \beta \mathbf{K}, \quad (27)$$

$$\beta = \frac{2\xi}{\omega_n}, \quad (28)$$

in which \mathbf{C}_λ is the stiffness proportional matrix, β is the damping constant, ξ is the damping ratio estimated from the

$$\begin{bmatrix} \mathbf{M} + \frac{\Delta t}{6}\mathbf{C}_w - \frac{\Delta t^2}{12}\mathbf{K} & -\frac{\Delta t}{6}\mathbf{C}_w - \frac{\Delta t^2}{12}\mathbf{K} \\ \frac{\Delta t}{2}\mathbf{C}_w + \frac{\Delta t^2}{3}\mathbf{K} & \mathbf{M} + \frac{\Delta t}{2}\mathbf{C}_w + \frac{\Delta t^2}{6}\mathbf{K} \end{bmatrix} \begin{Bmatrix} \mathbf{v}_n \\ \mathbf{v}_{n+1} \end{Bmatrix} = \begin{Bmatrix} \mathbf{f}_1^e - \mathbf{f}_2^e + \mathbf{M}\mathbf{v}_n^- \\ \mathbf{f}_1^e + \mathbf{f}_2^e + \mathbf{M}\mathbf{v}_n^- - \Delta t \mathbf{K} \mathbf{d}_n^- \end{Bmatrix}, \quad (29)$$

in which

$$\mathbf{C}_w = \mathbf{C} + \mathbf{C}_\lambda. \quad (30)$$

Equations (24), (26), and (29) form the final expressions of the MDGFEM to solve the problem of gas-saturated coal based on Biot's model.

4. Numerical Results and Discussion

In this section, three numerical examples of gas-saturated coal based on Biot's model subjected to impulse load are investigated. Various results in 1-D and 2-D are presented to demonstrate that the MDGFEM formulations are capable of producing reliable results in the problem [14]. Table 1 gives the basic parameters of gas-saturated coal.

4.1. 1-D Elastic Wave Propagation Problem of Gas-Saturated Coal Rock. We first consider a one-dimensional stress wave propagation problem in saturated gas-saturated coal. The length of the column is 200 m, and the area of the cross section is 1 m². The column, as shown in Figure 1, with one end fixed and one end loaded by an axial force impulse can be expressed by

$$F(t) = \begin{cases} 2000N, & (0 \leq t \leq 0.041s), \\ 0N, & (0.041s < t). \end{cases} \quad (31)$$

The column is meshed in elements of 0.4 m along the column axis. Figures 2 and 3 give the resulting stress wave and pore pressure wave propagation solutions at different time levels of 0.041 s and 0.08 s for the example using Newmark method, DGFEM, and the MDGFEM with time step size $\Delta t = 0.001$ s. It is noted that the results obtained by different methods are different from each other. As compared with the Newmark method, both DGFEMs filter out the serious numerical oscillation in the wave after. And the modified DGFEM shows better ability in filtering out the serious numerical oscillation in wave than DGFEM.

4.2. 1-D Elastic-Plastic Stress Wave Propagation Problem of Gas-Saturated Coal Rock. Secondly, we consider a column of

global behavior of the system, and ω_n is the basic frequency of the considered structure. From equation (27), we can see that the value of stiffness proportional damping constant β is complex to calculate. As discussed in our articles [13–15], the value should be less than or equal to the time step.

Using the stiffness proportional artificial damping matrix equation (27), (25) can be written in matrix form as

gas-saturated coal rock with the same geometry, boundary condition, load, and finite element mesh as the first example. The Drucker–Prager criterion and the linear strain hardening rule $c = c_0 + h_p^c \bar{\epsilon}^p$ for the cohesion are applied to simulate the elastic-plastic response of the gas-saturated coal rock. Here, c_0 , h_p^c , and $\bar{\epsilon}^p$ are the initial cohesion, strain hardening parameter, and the equivalent plastic strain, respectively. In the present example $c_0 = 5.0$ MPa, $h_p^c = 1$ MPa, the internal frictional angle $\phi = 22^\circ$, and the plastic potential angle $\psi = 5^\circ$ are used to account for the problem. Figures 4 and 5 give the resulting elastic-plastic effective stress wave and pore pressure wave propagation solutions at different time levels of 0.041 s and 0.08 s for the example using the Newmark method (blue lines) and the MDGFEM (red lines) with time step size $\Delta t = 0.001$ s. It is noted that the results obtained by different methods are different from each other. Serious spurious numerical oscillations could be observed both in effective stress and pressure profiles at different time levels by the Newmark method. By contrast, the smooth and continuous stress and pressure distributions are exhibited by using the MDGFEM. This indicates that artificial damping constant and discontinuous characteristic of basic unknown variables play significant roles in filtering out the spurious numerical oscillations and in providing much more accurate solutions for elastic-plastic wave propagation problem of gas-saturated coal rock subjected to a shock load.

4.3. 2-D Elastic-Plastic Wave Propagation Problem of Gas-Saturated Coal Rock. As the third example, we consider elastic-plastic wave propagation problem of gas-saturated coal rock in two dimensions. A square domain, which is 10 m deep, 10 m wide, and of infinite length in the horizontal direction, is subjected to an impulse inclined compression load at top left corner (0–1.4 m) as depicted in Figure 6. The left face of the domain is symmetry boundary. The domain, which is meshed with elements, is analyzed as a plane strain problem.

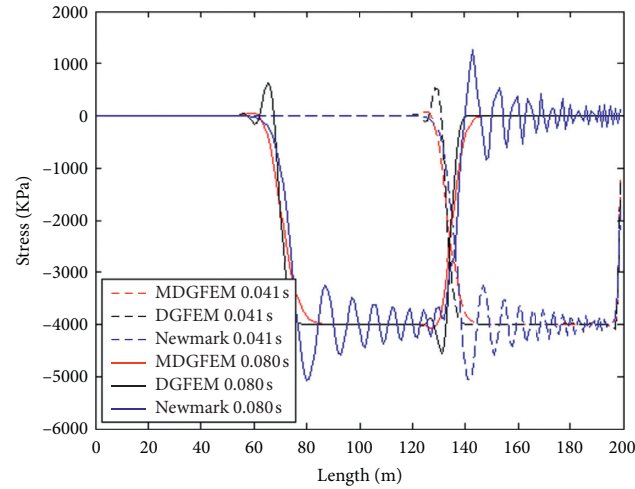
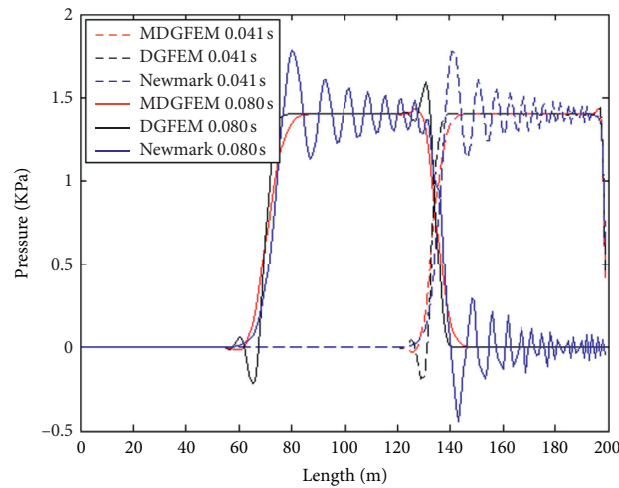
In the present example, the material property data are defined as follows: $c_0 = 5.0$ MPa, $h_p^c = 1$ MPa, $\phi = 22^\circ$, and $\psi = 0$. The impulse force can be expressed as

TABLE 1: Values of relevant parameters for calculations.

Parameters	Cortical bone
Hydraulic permeability k_w	1.0×10^{-6}
Biot parameter α	0.78
Porosity n	0.08
Young's modulus E (GPa)	3.0
Bulk modulus of the fluid K_f (GPa)	1.01×10^{-4}
Bulk modulus of the solid K_s (GPa)	3.33
Densities of the fluid ρ_f (kgm^{-3})	0.716
Densities of the solid ρ_s (kgm^{-3})	1500
Poisson's ratio	0.25



FIGURE 1: Model of example 1.

FIGURE 2: Stress profiles of different methods at $t = 0.041$ s and $t = 0.08$ s.FIGURE 3: Gas pressure profiles of different methods at $t = 0.041$ s and $t = 0.08$ s.

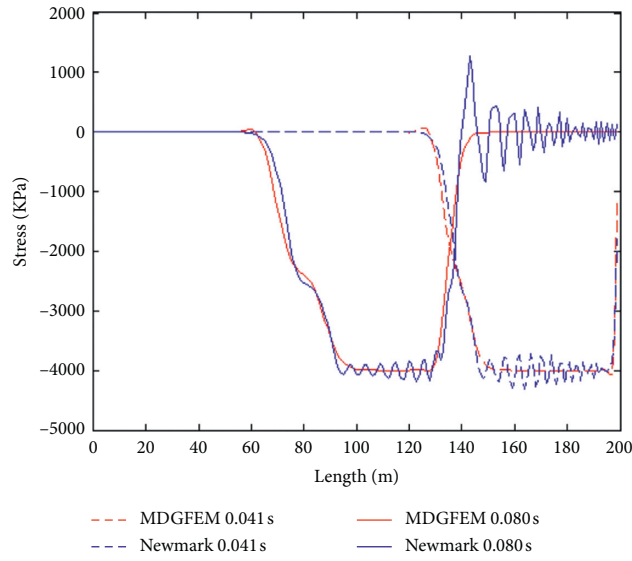


FIGURE 4: Elastic-plastic stress profiles of different methods at $t = 0.041$ s and $t = 0.08$ s.

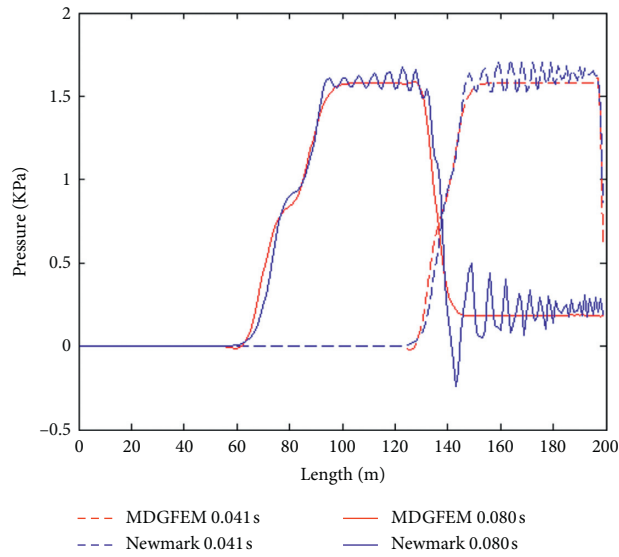


FIGURE 5: Pressure profiles of different methods at $t = 0.041$ s and $t = 0.08$ s.

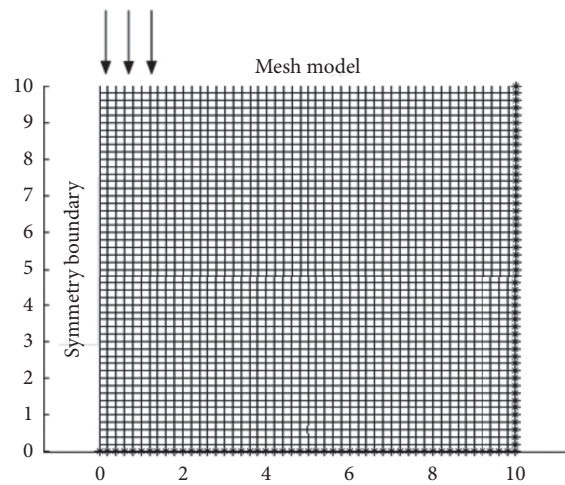


FIGURE 6: Modeling and mesh discretization for example 3.

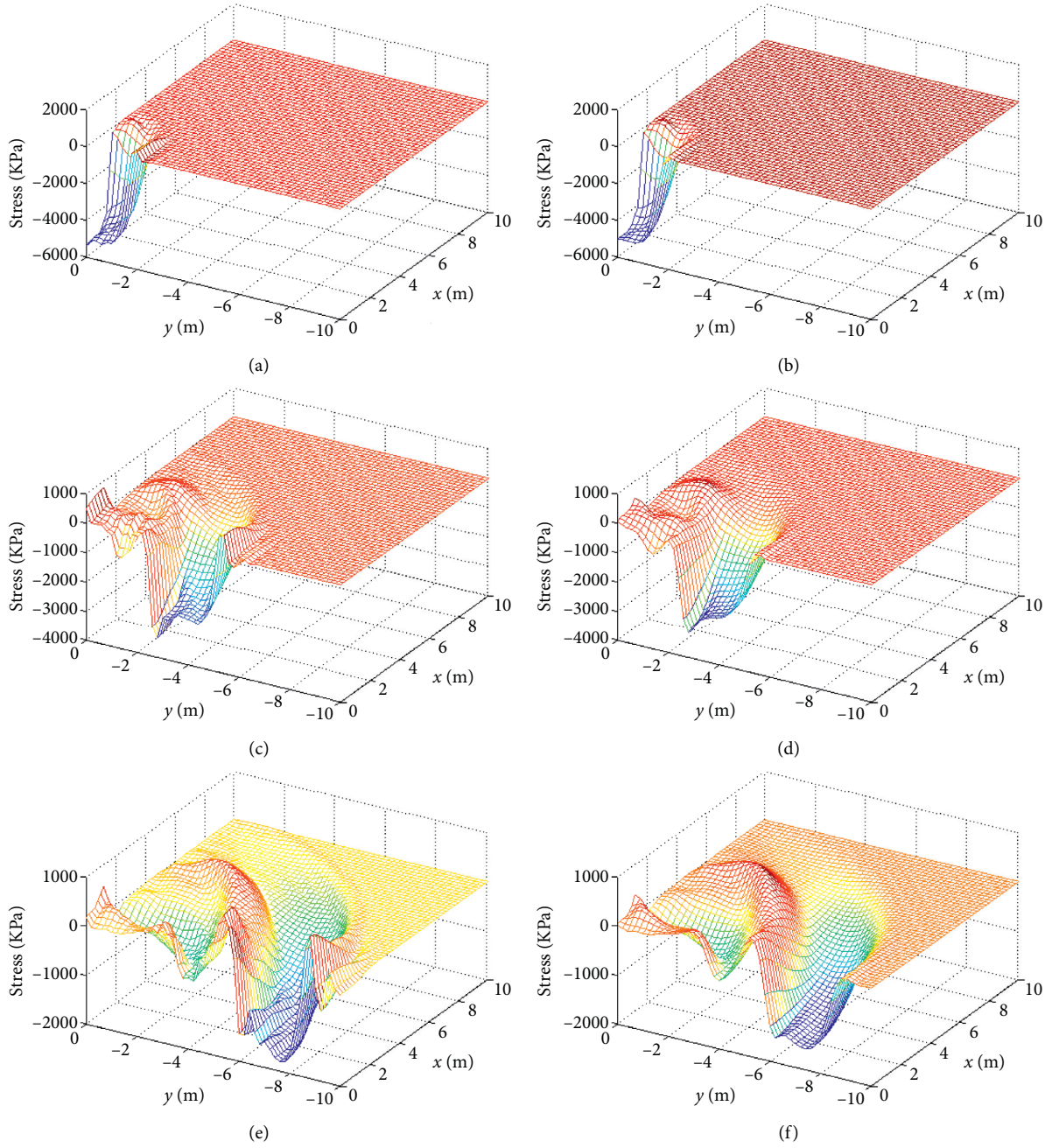


FIGURE 7: Comparison of the stress distributions between the Newmark method and the DGFEM. (a) Newmark method 0.001 s, (b) MDGFEM 0.001 s, (c) Newmark method 0.003 s, (d) MDGFEM 0.003 s, (e) Newmark method 0.005 s, and (f) MDGFEM 0.005 s.

$$F(t) = \begin{cases} 50\text{KN}, & (0 \leq t \leq 0.041\text{s}), \\ 0\text{N}, & (0.041\text{s} < t). \end{cases} \quad (32)$$

Figures 7 and 8 illustrate the numerical results for the mean stress distributions and the pore fluid pressure with the coal at time $t = 0.001$ s, 0.003 s, and 0.005 s, as obtained by the

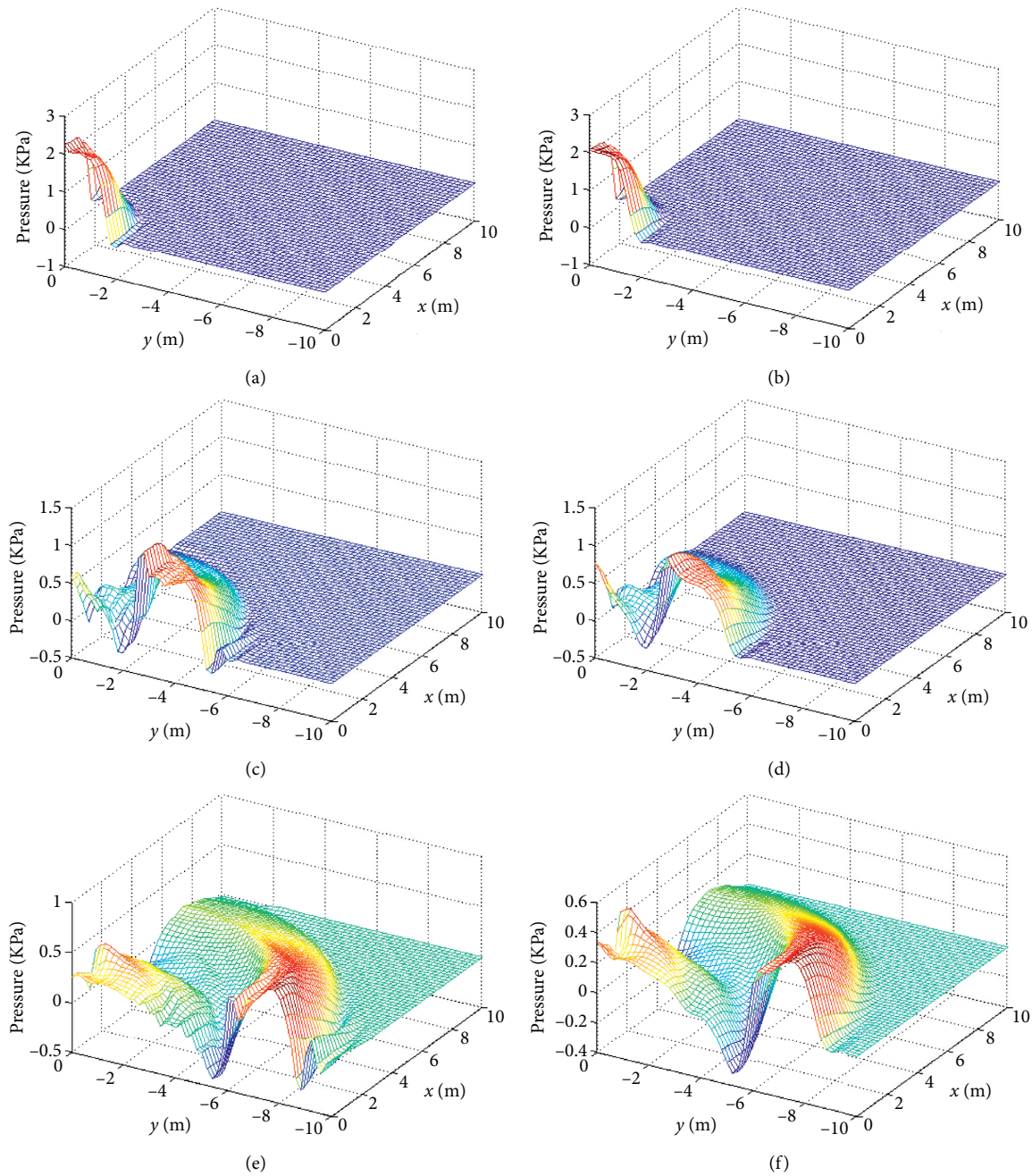


FIGURE 8: Comparison of the pressure distributions between the Newmark method and the MDGFEM. (a) Newmark method 0.001 s, (b) MDGFEM 0.001 s, (c) Newmark method 0.003 s, (d) MDGFEM 0.003 s, (e) Newmark method 0.005 s, and (f) MDGFEM 0.005 s.

MDGFEM method and the Newmark method using the time step. It should be remarked that due to incapability of filtering out the effect of the high modes, the spurious numerical oscillation occurring at the free end after the wave tail passes in the numerical solution by the Newmark method. Figures 7 and 8 demonstrate the good performance of the MDGFEM in reducing the numerical oscillations in the wave-front stage, while the Newmark method fails to do so.

5. Conclusions

The traditional Galerkin finite element method such as the Newmark method fails to capture the discontinuities or sharp gradients of the stress wave in solving the impact problem. An additional artificial damping discontinuous Galerkin numerical algorithm was incorporated into the final finite element discretised form to reduce the numerical

oscillations in the wave-front stage for the impact problem of gas-saturated coal. Based on the MDGFEM, series of numerical examples of dynamic problem of gas-saturated coal under impact loading show that the modified discontinuous Galerkin finite element method can effectively filter out the spurious numerical oscillations in the wave front of the elastic-plastic stress wave and the gas pressure wave. The study of the method in this paper demonstrates that it may also serve as a viable method for the coal-rock-gas coupling problem and coal-gas-heat coupling problems subjected to impact loading.

Data Availability

The data used to support the findings of this study are included within the article.

Conflicts of Interest

The authors declare that they have no conflicts of interest.

References

- [1] M. He, Y. Wang, J. Su, and D. Liu, "Analysis of fractal characteristics of fragment of sandstone impact rock burst under static and dynamic coupled loads," *Journal of China University of Mining & Technology*, vol. 47, no. 4, pp. 699–705, 2018.
- [2] Si Hu, X. Yong-Zhi, S. Zhang, S. Wu, and Z. Chen, "Numerical analysis for stress wave effects of rock broken under pulse jets," *Journal of Vibration and Shock*, vol. 35, no. 5, pp. 146–152, 2016.
- [3] Y. Zhao, Z. Jin, and J. Sun, "Mathematical model for coupled solid deformation and methane flow in coal seams," *Applied Mathematical Modelling*, vol. 18, no. 6, pp. 328–333, 1994.
- [4] T. Yang, B. Li, and Q. Ye, "Numerical simulation research on dynamical variation of permeability of coal around roadway based on gas-solid coupling model for gassy coal," *International Journal of Mining Science and Technology*, vol. 28, no. 6, pp. 925–932, 2018.
- [5] M. Biot, "The theory of propagation of elastic waves in fluid-saturated porous solid. I. higher frequency range," *The Journal of the Acoustical Society of America*, vol. 28, pp. 179–191, 1956.
- [6] O. C. Zienkiewicz and T. Shiomi, "Dynamic behavior of saturated porous media; the generalized Biot formulation and its numerical solution," *International Journal for Numerical Methods in Engineering*, vol. 8, no. 1, pp. 71–96, 1984.
- [7] X. D. Li and N. E. Wiberg, "Structural dynamic analysis by a time-discontinuous Galerkin finite element method," *International Journal for Numerical Methods in Engineering*, vol. 39, no. 12, pp. 2131–2152, 1996.
- [8] J. Freund, "The space-continuous-discontinuous Galerkin method," *Computer Methods in Applied Mechanics and Engineering*, vol. 190, no. 26–27, pp. 3461–3473, 2001.
- [9] K. K. Tamma and R. R. Namburu, "An effective finite element modeling analysis approach for dynamic thermoelasticity due to second sound effects," *Computational Mechanics*, vol. 9, no. 2, pp. 73–84, 1992.
- [10] X. K. Li, D. M. Yao, and R. W. Lewis, "A discontinuous Galerkin finite element method for dynamic and wave propagation problems in non-linear solids and saturated porous media," *International Journal for Numerical Methods in Engineering*, vol. 57, no. 12, pp. 1775–1800, 2003.
- [11] W. Wu and X. Li, "Application of the time discontinuous Galerkin finite element method to heat wave simulation," *International Journal of Heat and Mass Transfer*, vol. 49, no. 9–10, pp. 1679–1684, 2006.
- [12] X. Li and D. Yao, "Discontinuous Galerkin finite element method for wave propagation problems in elasto-plastic continua," *Acta Mechanica Solid Sinica*, vol. 24, no. 4, pp. 399–409, 2003.
- [13] P. Guo, W.-H. Wu, and Z. Wu, "A time discontinuous Galerkin finite element method for generalized thermo-elastic wave analysis, considering non-Fourier effects," *Acta Mechanica*, vol. 225, pp. 299–307, 2014.
- [14] P. Guo, W. Wu, and Z. Wu, "Application of the modified time discontinuous Galerkin finite element method to elasto-plastic wave propagation simulation," *Chinese Journal of Solid Mechanics*, vol. 34, no. 3, pp. 299–304, 2013.
- [15] P. Guo, W.-H. Wu, and J. Zhao, "Modeling of generalized thermoelastic wave propagation of multilayer material under thermal shock behavior," *Shock and Vibration*, vol. 2017, Article ID 8398673, 9 pages, 2017.

Research Article

Aeroelastic Flutter and Sliding Mode Control of Wind Turbine Blade

Lin Chang,¹ Yingjie Yu ,¹ and Tingrui Liu²

¹Department of Precision Mechanical Engineering, Shanghai University, Shanghai 200072, China

²College of Mechanical & Electronic Engineering, Shandong University of Science & Technology, Qingdao 266590, China

Correspondence should be addressed to Yingjie Yu; changlin@shu.edu.cn

Received 21 April 2020; Revised 16 June 2020; Accepted 4 July 2020; Published 26 July 2020

Academic Editor: Konstantin V. Avramov

Copyright © 2020 Lin Chang et al. This is an open access article distributed under the Creative Commons Attribution License, which permits unrestricted use, distribution, and reproduction in any medium, provided the original work is properly cited.

Flutter is an important form of wind turbine blade failure. Based on damping analysis, synthetically considering aeroelastic vibration instability of the blade and using the parameter fitting method, the aeroelastic flutter model of the pretwisted blade is built, with the simulation and emulation of flap and lead-lag directions flutter of the 2D dangerous cross section realized. Through the construction of two controllers, modular combinatorial sliding mode controller and sliding mode controller based on LMI for parameterized design suppress blade aeroelastic flutter. The results show that a better control effect can be achieved on the premise of the design of the precise parameters of the controller: the proposed sliding mode control algorithm based on LMI can effectively act on the aeroelastic system of the blade, significantly reduce the vibration frequency, and make the aeroelastic system converge to an acceptable static difference in a short time, which proves the effectiveness of sliding mode control in suppressing high-frequency vibration under high wind speed.

1. Introduction

Wind energy is a kind of clean energy with high commercial value, and wind turbine is an important part of capturing and converting wind energy into electric energy [1]. As the main part of wind turbine, the wind turbine blade has always been a significant research issue in the field because of its high-performance requirements, difficult size, and aerodynamic shape structure design. As a typical nonlinear aeroelastic unstable phenomenon, flutter is an important reason of fatigue damage for wind turbine [2]. How to effectively avoid flutter-induced aeroelastic instability has become an important research. The blade will be coupled by aerodynamic force, elastic force, inertial force, and other forces. Once the coupling result is divergent, the blade will show the instability of vibration and flutter, which is characterized by the fact that the amplitude cannot be automatically attenuated and gradually divergent. Flutter will bring fatal damage to the blade structure [3]. So, how to protect the blade from flutter becomes the focus point of wind turbine research.

In order to meet the analysis requirements of different wind turbine blades, it is necessary to select the appropriate simulation structure model. The commonly used structure analysis models include elastic hinge model [4], finite element model [5], and typical section model [6, 7]. The typical section model is widely used because it can reflect the aeroelastic vibration of blade easily, quickly, and accurately. The aeroelastic stability is a typical problem of whether the fluid solid coupling converges. That is to say, the blade, as an elastic body, is affected by the fluid in the fluid domain (air) to change its flexible shape, which in turn affects the fluid phenomenon; consequently, the research process is relatively complex. In [8], the method of passive control is used to suppress flutter by an adaptive design. In [9], the aeroelastic vibration response of the blade is improved by nonequilibrium aeroelastic cutting. In [10], the relationship between damping and aeroelastic instability is studied by modal analysis. In [11], two input and output controllers are designed based on the influence of nonlinear constraints on the flutter system. In [12], the coupling equations of motion of the system and the construction of the transonic aerosol

elastic model in the reduced order wing and control surface state space are considered, and the suboptimal control method output feedback based on genetic algorithm is constructed to design the flutter suppression law. Cheng et al. and Yang et al. [13, 14] analyzed the influence of blade structure and environmental variables on the blade system.

In this paper, the aeroelastic model expression and fitting aeroelastic factors considering structural damping are developed. Through the typical section analysis method, the aeroelastic vibration response of the blade in the case of high wind speed and high angle of attack is analyzed, and the active control process of sliding mode control of flutter is simulated. Sliding mode control is a simple and effective variable structure control method, which is flexible in physical realization, fast in response, and excellent in control effect. It has been applied in many industrial fields [15].

2. Modeling of Blade Vibration

2.1. Aeroelastic Model and Motion Equation. In the analysis of blade vibration, the damping phenomenon should be fully considered, including structural damping and aerodynamic damping. Composite material is often used in the blade manufacturing, and the structure damping can be detected through actual measurement. Aerodynamic damping is the action of air on the vibration of flexible body blades in reverse to the wind force. Before the occurrence of flutter, the aerodynamic damping is positive to suppress the vibration of blades and reduce the amplitude; otherwise, the vibration of blades will not be self-attenuated due to the strengthening of vibration. The typical section of large aspect ratio airfoil is considered in blade modeling, and the distance from the section to the blade root is $r = 3.75\text{m}$; y and z represent the displacement of leg and flap direction, respectively. α is attack angle; U is the wind speed value, which is 15m/s as to simulate the working conditions at high speed wind. c is chord length (chord direction t and normal direction n); V_0 is the relative wind speed after considering the blade rotation. The blade length L is 15m ; blade rotation speed $\Omega = \lambda \cdot U/L$, where λ is the tip speed ratio coefficient and the value is 2 .

In order to compensate for the power loss of aeroelastic deformation and increase the torsional rigidity, the blade pretorsional angle is as follows: $\theta = (r/L) \cdot \theta_0$, $\theta_0 = \pi/12$, ω_t and ω_n are chord and normal natural frequencies, respectively, which are chosen as 12rad/m and 8rad/m . ξ_t and ξ_n are chordal and normal damping ratios, respectively. In the aeroelastic flutter, the blade absorbs energy from the fluid so that the amplitude of the blade does not self-attenuate and shows negative aerodynamic damping, with absolute values of 0.03 and 0.06 , respectively. ρ_b is the section density, which is given in the form of parameter fitting. Air density

$\rho_a = 1.29\text{kg} \cdot \text{m}^{-3}$, and parameter distribution on the blade is shown in Figure 1.

The vibration equation model of two-dimensional typical dangerous section is selected, and the full damping behavior is fully considered [16, 17]. The relative reduction time is defined as $\tau = t \cdot V_0/c$. The section vibration flap angle is defined as $\varphi_z = z \cdot c/r$, and $\varphi_y = y \cdot c/r$ is section vibration leg angle. Then, the aeroelastic equations of the chosen section can be expressed as follows:

$$\varphi_i + \Omega^2 \varphi_i = \frac{c\rho_a V_0^2}{2\rho_b r \cdot [K_y \ K_z]^T}, \quad (1)$$

where $i = y, z$, and K_y and K_z are aerodynamic parameters of swing and swing directions, respectively. The set pretwist angle can provide complete damping for the blade, and the structural damping parameters are expressed as follows:

$$K_{CS} = C_{-\theta} K_{S0} C_{\theta}^T, \quad (2)$$

where K_{S0} is the reduced damping parameter matrix and C_{θ} is the pretwist effect coefficient, which are expressed as follows:

$$K_{S0} = \begin{bmatrix} \frac{2\xi_t \omega_t}{\Omega} & 0 \\ 0 & \frac{2\xi_n \omega_n}{\Omega} \end{bmatrix}, \quad (3)$$

$$C_{-\theta} = \begin{bmatrix} \cos \theta & -\sin \theta \\ \sin \theta & \cos \theta \end{bmatrix}. \quad (4)$$

So, the damping parameter matrix of complete structure can be expressed as ΩK_{CS} ; similarly, the structural stiffness parameters can be calculated:

$$K_s = C_{-\theta} K_{s1} C_{\theta}^T, \quad (5)$$

$$KS = C_{-\theta} \begin{bmatrix} \left(\frac{\omega_t}{\Omega}\right)^2 & 0 \\ 0 & \left(\frac{\omega_n}{\Omega}\right)^2 \end{bmatrix} C_{\theta}^T \quad (6)$$

The stiffness parameter matrix of complete structure can be obtained:

$$K_{sw} = K_s + I_{2 \times 2}. \quad (7)$$

Order $X = [\varphi_y \ \varphi_z]^T$, the aeroelastic equation of flap, and leg angle with full damping can be developed; $M\ddot{X} + C\dot{X} + KX = Q$ is considered; then, equation (8) can be derived:

$$\begin{bmatrix} 1 & 0 \\ 0 & 1 \end{bmatrix} \begin{bmatrix} \ddot{\varphi}_y \\ \ddot{\varphi}_z \end{bmatrix} + \Omega K_{CS} + \begin{bmatrix} \dot{\varphi}_y \\ \dot{\varphi}_z \end{bmatrix} \Omega^2 K_{sw} \begin{bmatrix} \varphi_y \\ \varphi_z \end{bmatrix} = \frac{c\rho_a V_0^2}{2\rho_a r} \begin{bmatrix} C_D \cos \Psi - C_L \sin \Psi \\ C_D \sin \Psi + C_L \cos \Psi \end{bmatrix}. \quad (8)$$

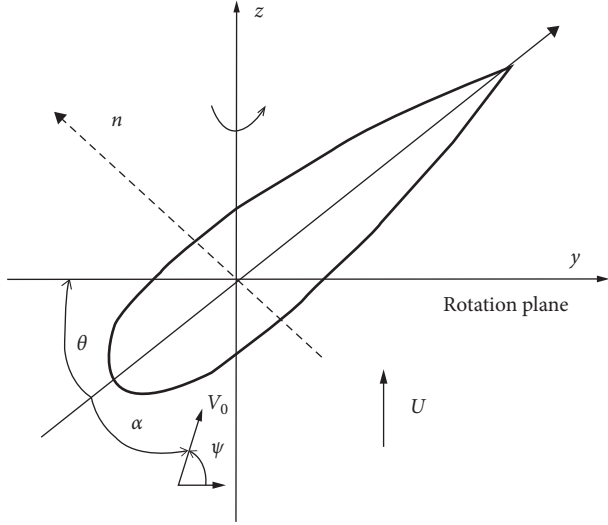


FIGURE 1: Displacement and parameters of two-dimensional typical section.

C_L and C_D are the aerodynamic lift and drag parameters, and ρ_b is the cross-section density. In order to be more practical, the fitting method is adopted to obtain the above parameters.

3. Parameter Fitting and Analysis

The blade is not a simple extension of the same section; the structural parameters at different sections are different and change with the analysis radius. In this paper, the section density ρ_b and chord length c are considered. The airfoil section based on NA63215 is considered. The chord length c and section density ρ_b are fitted to a sixth order sine sum curve:

$$F(n) = \sum_{i=1}^6 p_i \sin(q_i n + w_i), \quad (9)$$

where fitting variable $n = r/L$. When the aeroelastic stability of blades is analyzed, the accurate calculation of aerodynamic lift coefficient C_L and aerodynamic drag coefficient C_D are of practical significance. The curve fitting is also carried out for the attack angle with $-\pi/2 \sim \pi/2$; then, the fitting variable $n = \alpha$, and the results are shown in Table 1.

In order to carry out the subsequent analysis, the above expression is now converted into the state space form of the first-order equations: $Y = [\varphi_y \ \varphi_z \ \dot{\varphi}_y \ \dot{\varphi}_z]^T$, so we can obtain $\dot{Y}(t) = \Lambda Y(t) + B, Y_0(t) = CY(t)$, where

$$\Lambda = \begin{bmatrix} F_1 & F_2 \\ -M^{-1} \cdot K & -M^{-1} \cdot C \end{bmatrix}, \quad (10)$$

$$B = \begin{bmatrix} F_3 \\ -M^{-1} \cdot K \cdot Q \end{bmatrix}. \quad (11)$$

There are many methods to evaluate the stability of the system. For example, the eigenvalue determination, Bode diagram, and Lyapunov criterion. According to the

TABLE 1: Fitting parameters.

Type	c	ρ_b	C_L	C_D
P ₁	5.561	21.66	0.869	3.309
q ₁	3.943	4.656	2.073	0.351
w ₁	-0.382	0.260	0.041	1.488
P ₂	141.9	25.49	0.307	0.715
q ₂	8.576	8.564	4.013	2.037
w ₂	-0.396	-0.269	-0.058	-1.58
P ₃	139.1	12.50	0.199	2.658
q ₃	8.63	12.53	5.892	0.402
w ₃	2.71	0.794	-0.051	-1.663
P ₄	0.332	4.097	0.171	-0.018
q ₄	18.44	21.25	0.713	2.987
w ₄	-0.409	-1.891	0.847	-1.528
P ₅	0.258	2.297	0.138	0.020
q ₅	24.52	25.08	7.613	3.949
w ₅	-1.307	-1.400	-0.119	1.586
P ₆	0.140	0.370	0.086	0.0003
q ₆	30.59	36.38	9.298	4.816
w ₆	-1.185	-5.521	-0.193	-1.575

characteristics of the blade system, the stability of the blade in the two directions of the flap and leg is analyzed comprehensively. Even when the blade is stable, whether the amplitude and frequency are in line with the physical reality should be judged [15–17]. Therefore, time domain response analysis and limit cycle analysis are selected to observe the blade vibration response under aerodynamic force. Most of the dangerous sections appear at the blade root along the span of about 25% [17]. According to this standard, the section displacement is calculated by the fourth-order five level Runge–Kutta method, and the vibration of dangerous section is observed to represent the forced response of blade and the phase track distribution of blade in two directions, so as to comprehensively evaluate the aeroelastic vibration behavior of blade. The results are shown in Figure 2.

Based on the case of extreme wind speed, the uncontrolled vibration of the blade cross-section when the flutter occurs under the aerodynamic force is simulated with the medium-sized wind turbine parameters introduced into the aeroelastic model. From Figure 2, it can be found that the vibration divergence of the blade under the condition of high wind speed and high angle of attack, that is, the vibration in the two directions of flap and leg vibration does not decay with time, and the vibration frequency is high and the amplitude is increasing. It can be seen from the limit cycle distribution that the vibration range of the two directions is large and does not converge, and the vibration frequency is very high. It can be judged that, in this case, if the blade vibration is as shown in the simulation, the flutter failure will occur, so it must be suppressed.

4. Sliding Mode Flutter Control

4.1. Direct Sliding Mode Control Based on Module Building. Sliding mode control, originated from relay control and bang–bang control, is a branch of variable structure control. As a nonlinear control strategy, the basic feature is the discontinuity of the control process. The control system can

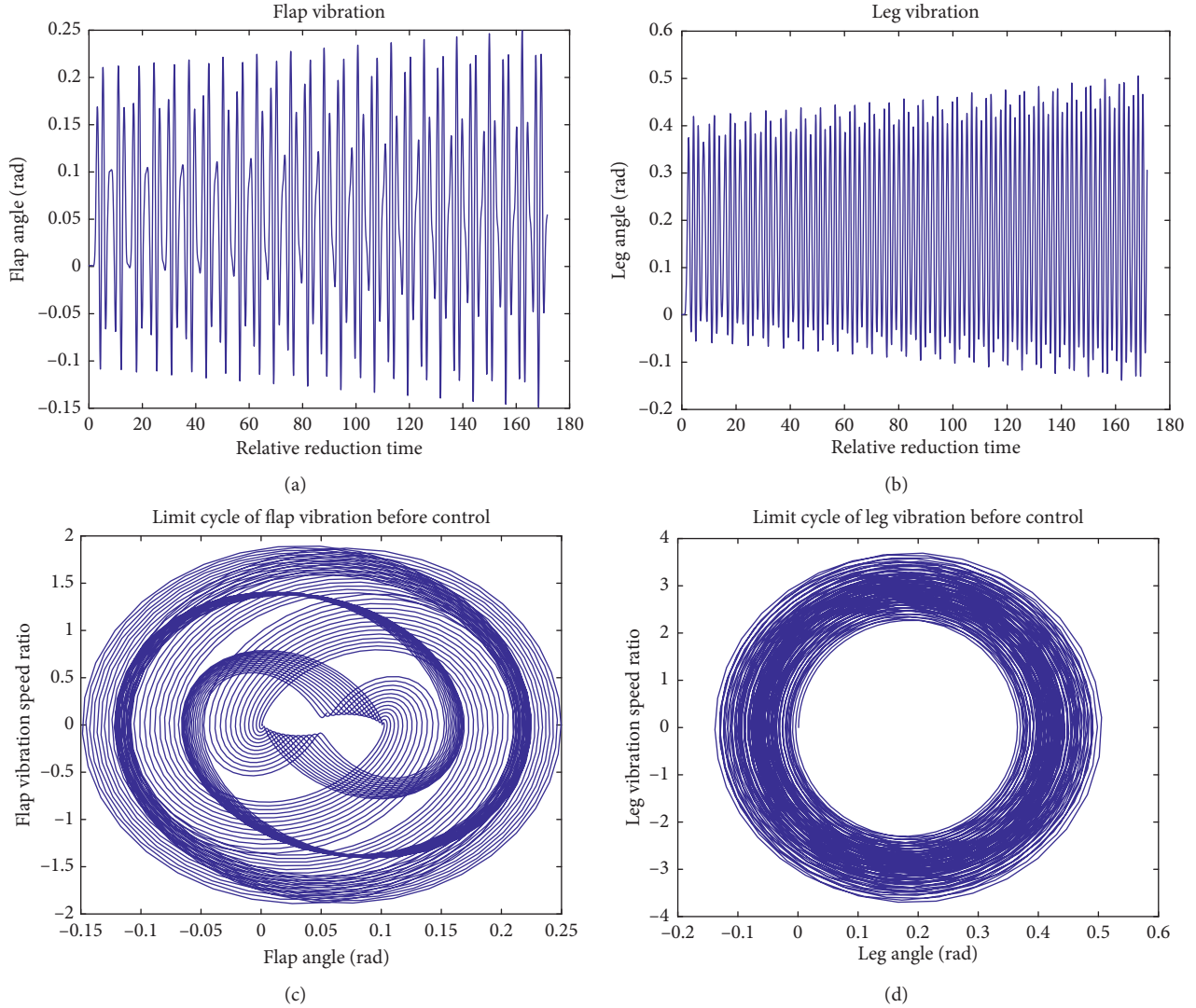


FIGURE 2: Uncontrolled vibration and limit cycles of the blade. (a) Uncontrolled flap vibration; (b) uncontrolled leg vibration; (c) limit cycle of uncontrolled flap vibration; (d) limit cycle of uncontrolled leg vibration.

change the control object purposefully and dynamically. The control structure can change the control structure and control law according to the degree of the system deviating from the preset “sliding mode” [18–20]. In this paper, the sliding mode-aeroelastic control system is constructed by two methods.

Simulink is an important part of MATLAB. It can be used in many kinds of simulation and experiments after being designed in the software environment. It can simulate the process of system control and data processing by building the modules of each part, constructing the relationship between modules, and assigning values within the modules. It is a simulation building form of the controller, which can be transformed into the design process of the actual controller. Firstly, a sliding mode control method based on Simulink is proposed. By adding an optimal control law, the control stability can be judged by observing the deviation index [19, 20]. The module construction is shown in Figure 3.

Take the deviation signal of the swing direction equivalent to the zero point as the feedback ($s = e$). Take the initial position before blade vibration as the standard point [21]. Select the proportional switching method, and set the sliding mode control function and control rate as follows:

$$S = K_3|s| + K_4\dot{s}, \quad (12)$$

$$u = K_5s + K_5\text{sgn}(s). \quad (13)$$

Set the feedback gain to K_4 as 0.5, K_i ($i = 1 \sim 5$) are set to 20, 20, 0.5, 2, and 0.5. Taking the relative reduction time as the abscissa to analyze the control performance, the control effect is as follows:

It is obvious that the amplitudes and frequencies of the flap and leg vibration can be greatly reduced under this sliding mode control. However, the disadvantages cannot be ignored; buffeting cannot be completely eliminated in this case. It can be clearly found in the controlled vibration

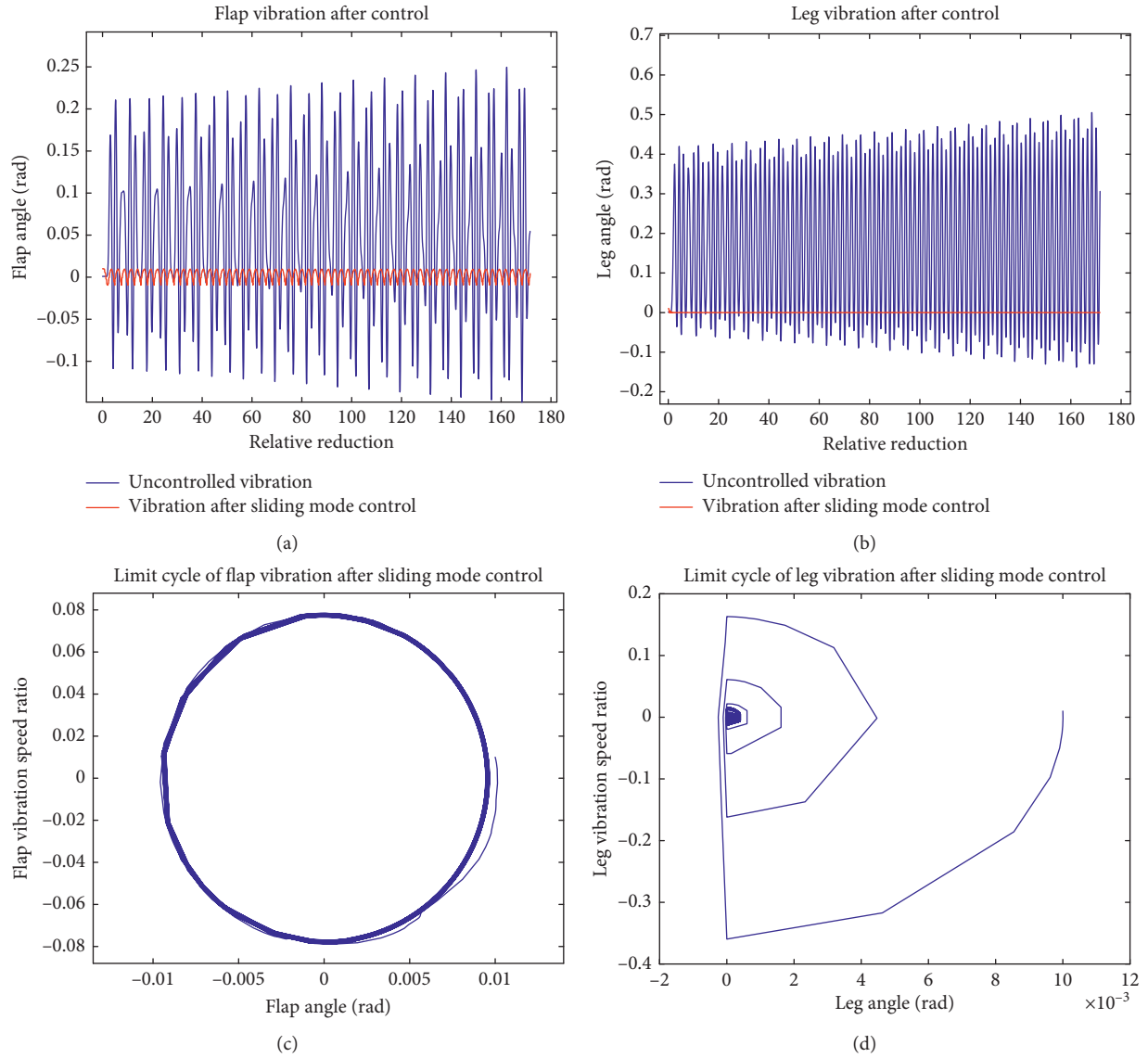


FIGURE 4: The results of direct sliding mode control based on module building. (a) Compared results before and after control of flap vibration; (b) compared results before and after control of leg vibration; (c) limit cycle of flap direction after sliding mode control; (d) limit cycle of leg direction after sliding mode control.

flap and leg after control can be observed by the model parameters mentioned above.

It can be observed from Figure 5 that when the aeroelastic system of the blade flutters, through the sliding mode control based on LMI, the flutter in both the flap and leg directions is well suppressed. Finally, the vibration in both directions converges to a stable value quickly, which means that, after the process of the proposed algorithm, the steady-state time of the system is short, reflecting the satisfactory steady-state control performance of the algorithm. Meanwhile, the vibration frequencies of the aeroelastic system are greatly reduced, which is able to avoid the hidden failure of the blade caused by high-frequency vibration. In the implementation of the algorithm, there is no need for complex iterative calculation; consequently, the processing speed is fast enough, which

can effectively suppress the errors that may be introduced in the implementation process. Compared with the modular sliding control algorithm, the stabilization time is shorter and the static error is smaller after stabilization. In engineering implementation, the control actuator has many options depending on different blade types and working conditions [22, 23]; it can be realized by connecting the pitch system and setting actuators in the blade skin, such as SMA electric heating, piezoelectric materials, and current control by electromagnetic rheological fluid. Besides, the sliding mode control based on LMI is mainly based on matrix operation, which can be implemented in statements with MATLAB or other programming languages. Through OPC technology [24], it can be easily realized in PLC controller hardware and has positive engineering practical application value.

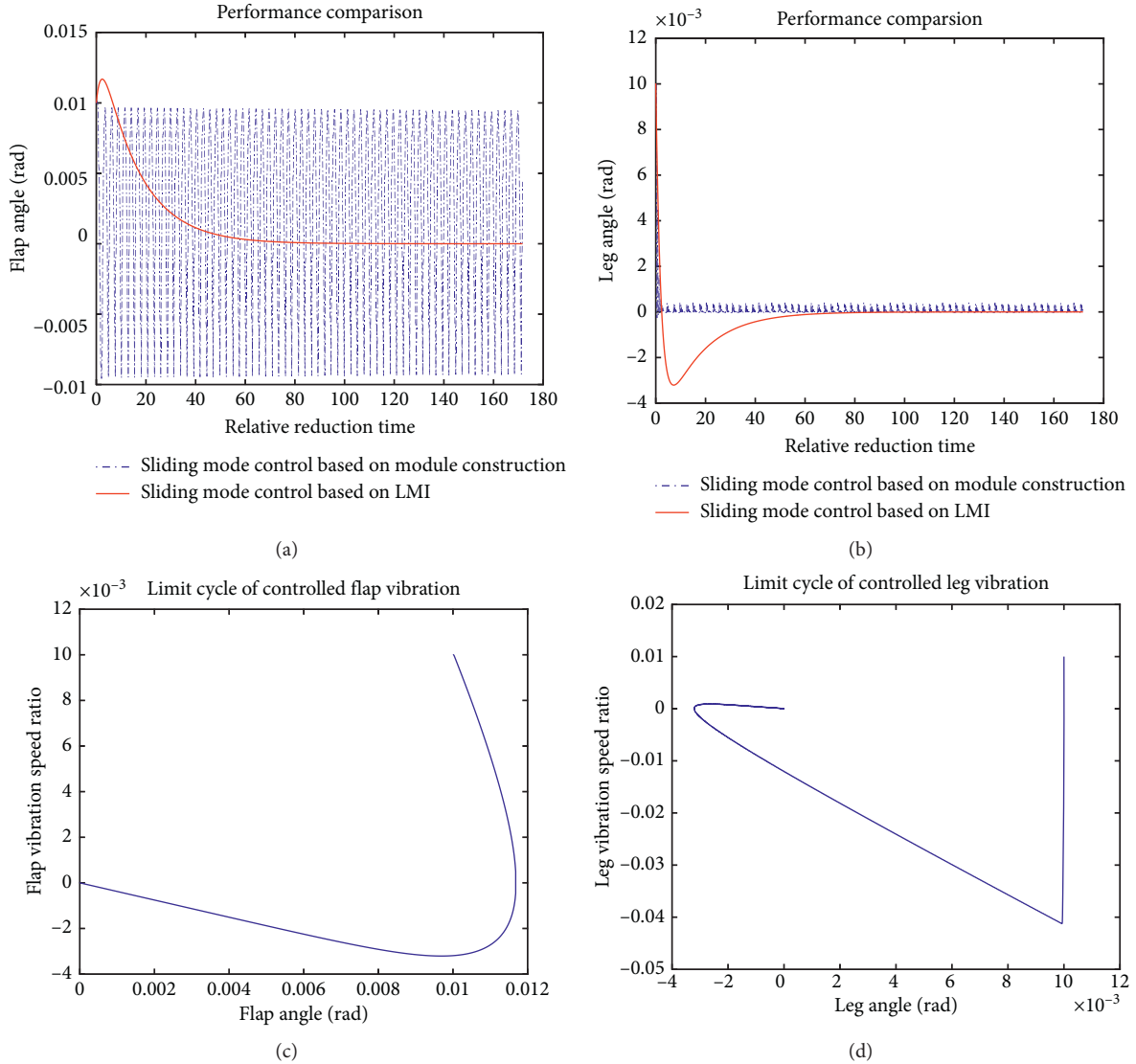


FIGURE 5: The results of sliding mode control based on LMI. (a) Compared results before and after control of flap vibration; (b) compared results before and after control of leg vibration; (c) limit cycle of flap direction after sliding mode control; (d) limit cycle of leg direction after sliding mode control.

5. Conclusion

- (1) In this paper, the aeroelastic response of the typical section of the blade under high wind speed and high angle of attack is modeled by fully considering the damping effect, which is used to analyze and simulate the vibration of the horizontal axis wind turbine blade under flutter.
- (2) A flexible sliding mode controller is built by the way of module building of Simulink, which can achieve the purpose of flutter suppression. Although there is local chattering, it is still a simple and economic controller design method. A new type of sliding mode controller is designed and constructed by parameters' LMI-based sliding mode controller. The results show that the final response converges, the amplitude and frequency are greatly reduced, the local chattering is weakened, the stability time is short, the static error is acceptable, and the control effect is satisfactory.
- (3) The advantages of the sliding mode algorithm are the accuracy of the model is not so essential and the algorithm is insensitive to parameter changes and external interference, with strong robustness. Through the switching of the sliding surface function, the tracking error is gradually reduced, and finally a better control performance is achieved. Especially for the flexible body of wind turbine blade, even if the small buffeting exists, the small static error can be accepted under the premise of response convergence, which can be well combined with the sliding mode controller. Through the analysis of vibration and limit cycle of LMI-based sliding mode control, we can conclude that the proposed

algorithm can suppress the flutter vibration of blades and make the aeroelastic system finally converge with short stability time, which can suppress the high-frequency vibration at high wind speed. Therefore, the effectiveness of the proposed algorithm is comprehensively verified. Sliding mode control has made great progress in many engineering fields, but the research on flutter suppression technology based on risk section analysis is still less, which has the research value.

Data Availability

The results of the analysis and the model building process have been completely presented, and even the values of the results are visualized. So, the result data used to support the findings of this study are included within the article.

Conflicts of Interest

The authors declare that there are no conflicts of interest regarding the publication of this article.

Acknowledgments

This work was supported by the National Natural Science Foundation of China (Grant no. 51675315).

References

- [1] M. Vahdati, N. Smith, and F. Zhao, "Influence of intake on fan blade flutter," *Journal of Turbomachinery*, vol. 137, no. 8, pp. 1–10, 2015.
- [2] T. Liu, "Aeroservoelastic pitch control of stall-induced flap/lag flutter of wind turbine blade section," *Shock and Vibration*, vol. 2015, Article ID 692567, 20 pages, 2015.
- [3] K. Hayat and S. K. Ha, "Flutter performance of large-scale wind turbine blade with shallow-angled skins," *Composite Structures*, vol. 132, pp. 575–583, 2015.
- [4] W. S. Nski and M. Gaunaa, "Wind turbine blade vibration at standstill conditions—the effect of imposing lag on the aerodynamic response of an elastically mounted airfoil," *Wind Energy*, vol. 18, no. 3, pp. 515–527, 2015.
- [5] D. Cárdenas, A. A. Escárpita, H. Elizalde et al., "Numerical validation of a finite element thin-walled beam model of a composite wind turbine blade," *Wind Energy*, vol. 15, no. 2, pp. 203–223, 2012.
- [6] T. Liu and L. Chang, "Vibration control of wind turbine blade based on data fitting and Pole placement with minimum-order observer," *Shock and Vibration*, vol. 2018, Article ID 5737359, 12 pages, 2018.
- [7] F. Bertagnolio, F. Rasmussen, N. N. Sørensen, J. Johansen, and H. A. Madsen, "A stochastic model for the simulation of wind turbine blades in static stall," *Wind Energy*, vol. 13, no. 4, pp. 323–338, 2010.
- [8] M. T. Herath, A. K. L. Lee, and B. Gangadhara Prusty, "Design of shape-adaptive wind turbine blades using Differential Stiffness Bend-Twist coupling," *Ocean Engineering*, vol. 95, pp. 157–165, 2015.
- [9] K. Hayat and S. K. Ha, "Load mitigation of wind turbine blade by aeroelastic tailoring via unbalanced laminates composites," *Composite Structures*, vol. 128, pp. 122–133, 2015.
- [10] Z. Chi, H. Xia, D. Li, and X. Zhang, "Study on modal aerodynamic damping analysis method for wind turbine blade," *Journal of Mechanical Engineering*, vol. 54, no. 2, pp. 176–183, 2018.
- [11] G. Dimitriadis and J. E. Cooper, "Characterization of the behaviour of a simple aeroservoelastic system with control nonlinearities," *Journal of Fluids and Structures*, vol. 14, no. 8, pp. 1173–1193, 2000.
- [12] W. Zhang and Z. Ye, "Control law design for transonic aeroservoelasticity," *Aerospace Science and Technology*, vol. 11, no. 2-3, pp. 136–145, 2007.
- [13] T. H. Cheng, M. Ren, Z. Z. Li, and Y. De Shen, "Vibration and damping analysis of composite fiber reinforced wind blade with viscoelastic damping control," *Advances in Materials Science and Engineering*, vol. 2015, Article ID 146949, 6 pages, 2015.
- [14] Y. Yang, C. Tan, D. Xie, Y. Xiong, Y. Shi, and W. Li, "Study on natural vibration characteristics of large scale composite wind turbine blades," *American Society of Mechanical Engineers, Power Division*, vol. 2, no. 1, pp. 569–573, 2011.
- [15] V. I. Utkin, "Sliding mode control design principles and applications to electric drives," *IEEE Transactions on Industrial Electronics*, vol. 40, no. 1, pp. 23–36, 1993.
- [16] C. Lin, L. Tingrui, X. Wei, and W. Hongcai, "Research and control of blade aeroelastic stability of large horizontal axis wind turbine," *Mechanical Design and Research*, vol. 34, pp. 199–204, 2018.
- [17] L. Tingrui, W. Jidai, and C. Guangqing, "Simulation and control of electronic expansion valve," in *Proceedings of 2008 pacific-asia Workshop on computational Intelligence and industrial application*, vol. 1, pp. 123–126, Wuhan, China, December 2008.
- [18] Y. Niu, D. W. C. Ho, and J. Lam, "Robust integral sliding mode control for uncertain stochastic systems with time-varying delay," *Automatica*, vol. 41, no. 5, pp. 873–880, 2005.
- [19] C.-T. Chen and S.-T. Peng, "A nonlinear control scheme for imprecisely known processes using the sliding mode and neural fuzzy techniques," *Journal of Process Control*, vol. 14, no. 5, pp. 501–515, 2004.
- [20] H. Alwi and C. Edwards, "Fault detection and fault tolerant control of a civil aircraft using a sliding mode based scheme," *IEEE Transactions on Control Systems Technology*, vol. 1, no. 11, pp. 2–12, 2007.
- [21] P. C.-P. Chao, C.-W. Chiu, and K.-T. Shih, "A novel low-torque ball re-positioning scheme based on a sliding-mode ball observer for an automatic balancer system," *Shock and Vibration*, vol. 15, no. 2, pp. 101–126, 2008.
- [22] L. Jinkun, *Matlab Simulation of Sliding Mode Variable Structure Control*, Tsinghua University Press, Beijing, China, Second Edition, 2015.
- [23] A. J. Kurdila, J. Li, T. Strganac, and G. Webb, "Nonlinear control methodologies for hysteresis in PZT actuated on-blade elevons," *Journal of Aerospace Engineering*, vol. 16, no. 4, pp. 167–176, 2003.
- [24] L. Tingrui, "Vibration control of blade section based on sliding mode PI tracking method and OPC technology," *Shock and Vibration*, vol. 2019, Article ID 8314898, 12 pages, 2019.

Research Article

A Novel Aerodynamic Force and Flutter of the High-Aspect-Ratio Cantilever Plate in Subsonic Flow

Li Ma,¹ Minghui Yao ,¹ Wei Zhang ,¹ Kai Lou,² Dongxing Cao ,¹ and Yan Niu ¹

¹College of Mechanical Engineering, Beijing University of Technology,
Beijing Key Laboratory of Nonlinear Vibrations and Strength of Mechanical Structures, Beijing 100124, China

²Water Transport Planning and Design Co., Ltd., Communications Construction Company Limited, Beijing 100007, China

Correspondence should be addressed to Minghui Yao; merry_mingming@163.com

Received 11 April 2020; Revised 13 May 2020; Accepted 27 May 2020; Published 19 June 2020

Academic Editor: Konstantin V. Avramov

Copyright © 2020 Li Ma et al. This is an open access article distributed under the Creative Commons Attribution License, which permits unrestricted use, distribution, and reproduction in any medium, provided the original work is properly cited.

This paper focuses on the derivation of the aerodynamic force for the cantilever plate in subsonic flow. For the first time, a new analytical expression of the quasi-steady aerodynamic force related to the velocity and the deformation for the high-aspect-ratio cantilever plate in subsonic flow is derived by utilizing the subsonic thin airfoil theory and Kutta-Joukowski theory. Results show that aerodynamic force distribution obtained theoretically is consistent with that calculated by ANSYS FLUENT. Based on the first-order shear deformation and von Karman nonlinear geometric relationship, nonlinear partial differential dynamical equations of the high-aspect-ratio plate subjected to the aerodynamic force are established by using Hamilton's principle. Galerkin approach is applied to discretize the governing equations to ordinary differential equations. Numerical simulation is utilized to investigate the relation between the critical flutter velocity and some parameters of the system. Results show that when the inflow velocity reaches the critical value, limit cycle oscillation occurs. The aspect ratio, the thickness, and the air damping have significant impact on the critical flutter velocity of the thin plate.

1. Introduction

With the development and popularization of unmanned aerial vehicles in fields of detection, disaster prevention, and disaster reduction, researchers paid more attention on aeroelastic problems of high-aspect ratio airfoils in subsonic airflow. Flutter is self-excited oscillation of a flight vehicle under the coupling effect of the aerodynamic pressure, the elastic force, and the inertia force. Cantilever plates in the axial flow may lose stability at sufficiently high flow velocity. Analysis of the linear theory indicates that there is a critical dynamic pressure. The motion of the panel becomes unstable when the dynamic pressure is higher than the critical value. Once the instability threshold is exceeded, flutter will take place. Under the condition of flutter in the system, the energy of the surrounding airflow will be continuously pumped into the plate to sustain the flutter motion. The lightweight and high performances of the modern aircraft make the aeroelastic problems of the aircraft more prominent.

One of the key issues of aeroelasticity is flutter, which usually leads to the disaster of the aircraft [1]. Thus, the aeroelasticity problem of the aircraft comes into our sight. Zhang et al. [2] applied the composite multilayer plate to supersonic aircraft under the aerodynamic pressure to investigate excessive nonlinear vibration suppression of the plate. Flutter is a fluid-structure coupling problem. Chernobryvko et al. [3] discussed nonlinear dynamic stability conical shells in a supersonic gas stream. Amabili and Pellicano [4] found that flutter is very sensible to small initial imperfections of the structure. Vedenev [5] studied flutter of an elastic thin plate and obtained the exact solution by solving the structural kinetic equation coupling with the hydrodynamic equation. When solving dynamic problems of the fluid-structure coupling system, researchers prefer adopting aerodynamic models to simulate the external flow field. Based on these aerodynamic models, aerodynamic characteristics related to motion state of the system, such as the displacement, velocity, and acceleration, are obtained.

Then, nonlinear dynamic equations of airfoils are derived, and aerodynamic characteristics of the system are investigated.

Aerodynamic force is a key factor in the analysis of the flutter phenomena, which directly determines the bucking form of the plate structure. So, it is necessary to select a proper aerodynamic force model in the study of flutter problem. Up to now, scholars have proposed abundant theories of the aerodynamic force. According to the dependence of aerodynamic forces on time and spatial, aerodynamic theories can be roughly divided into three types, such as the steady, quasi-steady, and unsteady aerodynamic theories. The first type is the steady aerodynamic model, namely, assuming the force acting on the lifting surface of the wing do not change with time. The steady aerodynamic model is mainly used for static aeroelastic analysis, such as the thin airfoil theory [6]. The second kind is the quasi-steady aerodynamic theory, in which we assume the aerodynamic force at any time is only related to the motion state of the wing at that time. By using this theory, the reduced frequency of motion is smaller, and vibration characteristics analysis of the airfoil subjected to the aerodynamic force can be simpler. Lin et al. [7] proposed a quasi-steady piston theory to calculate the flutter problem of a cantilever plate in supersonic flow. Hu et al. [8–10] investigated aeroelastic vibration of the plate subjected to the aerodynamic force obtained from the first order piston theory. Brouwer and McNamara [11] optimized the piston theory and verified it. Dowell and Ganji [12] extended the piston theory to higher order terms in several expansions and analyzed the flutter of single degree of freedom panel. Owing to the ignoring of the propagation effect of small perturbations in the subsonic airflow, the piston theory is not applicable in the subsonic airflow. Thus, scholars gave some new methods to compute aerodynamic. Grossman quasi-steady theory [13] can also be applied to calculate the total lift force and the total torque of high-aspect ratio wings, which can be simplified as an elastic beam without pretwist and the axial extension. Obviously, this theory is not suitable for plates with the small aspect ratio. The third one is the unsteady aerodynamic theory, which considers the influence of change of circulation and wake flow on the aerodynamic force of a moving airfoil. Xu et al. [14] deduced the solution of the unsteady aerodynamic force for a slender airfoil, which is modeled as a beam structure. However, this method can only be used to solve problems of 2D plate structures in the incompressible airflow. Based on the model constructed, by applying Theodorsen unsteady aerodynamic theory, researchers investigated stability of wings. However, Cordes et al. [15] pointed out Theodorsen function cannot capture the experimental transfer functions in frequency dependence when investigating the unsteady lift force of an airfoil.

Since exact solutions of unsteady potential equations are few, we can only acquire approximate analytical solutions through other methods. Peters [16] obtained a semiempirical, nonlinear, and unsteady ONERA model according to data of wind tunnel airfoils. Dunnp and Dugundjij [17] analyzed linear flutter of the composite wing using the harmonic balance method by adopting ONERA dynamic

stall model. Sadr et al. [18, 19] developed the ONERA model. However, the Theodorsen model and the ONERA model are not suitable for the aerodynamic analysis of plate structures. Zhang and Ye [20] established the integral aerodynamic reduced order model [21] based on the Volterra series theory. However, introduction of the integral form leads to the computational complexity. Zhang and Ye [22] developed the Volterra series theory and expressed the aerodynamic force as the sum of multiple convolutions. However, the aerodynamic force obtained is implicit, so it is hard to couple the implicit expression with kinetic equations of the plate. Guo et al. [23, 24] put forward the nonlinear harmonic balance method to analyze the unsteady flow in the turbomachinery and the airfoil. Based on proper orthogonal decomposition, Luo et al. [25] presented a hybrid modeling method for reconstructions of flow field and aerodynamic optimization. Nonlinear regression methods, instead of the linear regression widely used, are adopted to establish POD basis modes, which behave with good description performance in system space. Wang et al. [26] made a comprehensive review on the latest studies about the aeroelastic modeling. The CFD method is adopted in Refs. [27–29]; however, this method is not conducive to perform pneumatic elastic servo analysis. Munk et al. [30] studied the limit cycle of a two-dimensional cantilever plate under subsonic flow based on the vortex lattice method. Castells Marin and Poetsch [31] used the doublet lattice method to model the lifting surface, which is more accurate than the NLRI method. Xie et al. [32] obtained the aeroelasticity deformation of the geometrically nonlinear high-aspect ratio wing, which is in great agreement with the experimental result. Pashaei et al. [33] modeled the airflow by using the vortex lattice method and studied the effect of energy harvesting properties of the metal composite on the flutter margin and limit cycle oscillation amplitudes. Ramezani et al. [34, 35] established the aerodynamic model by adopting CFD/CSD coupling numerical computational method. Chen et al. [36–38] constructed reduced-order models of high speed vehicles based on CFD simulations. Results show that the ROM approach can significantly speedup unsteady aerodynamic calculations of a system.

Most of the results obtained from vibration of plates under subsonic airflow are related to flutter of panels. Flutter of the panel is similar to that of the wing. The main difference lies in that there is only one surface subjected to the aerodynamic force for the panel. However, for the plate, both surfaces are exposed to the airflow. Study of panel flutter began in the early 1970s. Tang et al. [39, 40] theoretically and experimentally researched the aeroelastic response of a wing and a cantilever plate under subsonic airflow. Dowell et al. [41, 42] proposed the linear potential flow theory, which can calculate the pressure distribution of any point on the surface of the panel. However, it is not suitable for plate or shell structures with airflow acting on both sides.

Generally, achievements have been made in the study of 2D infinite plate, panels, and beam structures in subsonic airflow. And aerodynamic models have already been applied in investigation of flutter. However, research works on

explicit expressions of aerodynamic forces of cantilever plates and shells under subsonic airflow are still few. In this paper, for the first time, an analytical expression of the quasi-steady aerodynamic force for the high-aspect ratio cantilever plate in subsonic flow is induced based on the subsonic thin-airfoil theory and Kutta–Joukowski lift theorem. Overall, aerodynamic force theoretically calculated by using the explicit expression we derived has a good agreement with that obtained by ANSYS FLUENT. In addition, the aerodynamic model constructed based on it could be applied to flutter analysis of cantilever plates and shells with the high-aspect ratio. Considering lateral vibration and deformation of the mean camber line of the cross section, nonlinear dynamic equations of transverse vibration of the high-aspect ratio cantilever plate are derived by utilizing the quasi-steady aerodynamic model. Influences of parameters of the system on the critical flutter velocity are investigated.

2. Aerodynamic Force Derivation for the High-Aspect-Ratio Cantilever Plate in Subsonic Flow

2.1. Analysis of the Aerodynamic Force for the High-Aspect-Ratio Cantilever Plate in Subsonic Flow Field. The schematic diagram of the cantilever plate considered is shown in Figure 1. The wing is simplified as a high-aspect ratio cantilever plate. The span length, chord length, and thickness of the plate are a , b , and h , respectively. The velocity of the subsonic airflow along the chordwise direction is denoted as U_∞ . Cross section of the cantilever plate is marked as A . (X, Y, Z) is the inertial coordinate system, and the origin of it is in point O . \vec{e}_x^0 is the spanwise direction, \vec{e}_y^0 is the chordwise direction, and \vec{e}_z^0 is the thickness direction, respectively. Based on the strip assumption, Kutta–Joukowski lift theorem, and linearized small perturbation theory, we induce an aerodynamic force model of a high-aspect ratio cantilever plate in subsonic airflow.

The strip assumption of the plate with high-aspect ratio can be briefly introduced as follows. Actually, the airflow on wings is a three-dimensional fluid. However, if then the geometric dimension of the cantilever plate does not change along the chordwise direction, the aspect ratio is high and the inflow velocity is not change along the spanwise. The velocity of the fluid can be considered as a component in 2D plane (YOZ plane) and the component in the spanwise axis (X -axis) is zero in the most part of the spanwise region. Thus, every chord section can be analyzed as a 2D airfoil with an infinite spanwise length. Diagrams of each section along the chordwise direction, such as section A , can be shown in Figure 1.

At the beginning of the 20th century, Joukowski proposed Kutta–Joukowski lift theorem, which established the relation of the lift and circular vector of moving objects in the air, as shown in equation (1). In the incompressible, low-velocity, inviscid, and straight uniform flow field, the force distribution on unit length of the spanwise of the closed 2D wing is perpendicular to the direction of the airflow. Its value can be expressed by product of the density of the fluid ρ , flow

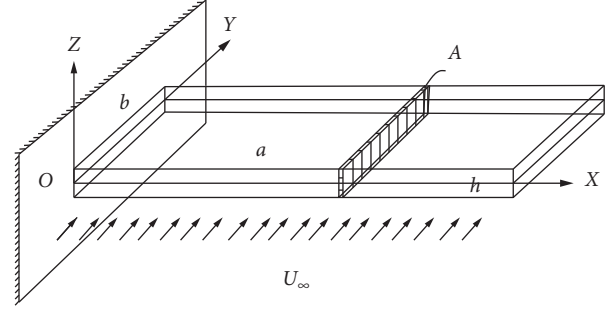


FIGURE 1: Model of the high-aspect-ratio cantilever plate.

velocity U_∞ , and the vortex strength $\gamma(Y)$ of unit arc length of the wing:

$$d_L = \rho U_\infty \gamma(Y) d_Y. \quad (1)$$

The vortex strength $\gamma(Y)$ on unit arc length is positive in a clockwise direction. When using Kutta–Joukowski lift theorem (inviscid potential flow theory) to solve the lift of the airfoil, the chief problem among the issues is how to obtain the local vortex strength $\gamma(Y)$.

The airfoil, whose ratio of the maximum thickness and the chord length is less than 12%, is defined as a thin airfoil. For a thin airfoil, we can use linearized small perturbation theory of the low speed flow around a thin airfoil in aerodynamics to calculate the local vortex strength $\gamma(Y)$. The problem about flow around a thin airfoil means the small attack angle and the small bending. In addition, a thin airfoil problem means the thin thickness. Thus, boundary conditions and pressure coefficient of the airfoil can be linearized. Therefore, based on principle of superposition, the attack angle, the bending, and the thickness can be considered separately and then superposed. The potential flow around a thin airfoil can be decomposed into three simple linear potential flows, which include the flow around a curved plate without an attack angle, a symmetrical airfoil without an attack angle, and a flat plate with a small attack angle. The flow around a symmetrical airfoil without an attack angle cannot generate the lift force, so we only need to consider the lift forces generated by the small attack angle and the bending of the airfoil. When the straight uniform airflow flows across the mean camber line of 2D airfoil with a small attack angle, we can use the surface vortex on the mean camber line to simulate the distribution of the local vortex strength $\gamma(Y)$, which has a trigonometric series solution. Lateral displacement of the mean camber line of the chordwise cross section is set up as W_Y . The chordwise position of an arbitrary point in the middle arc line can be written as

$$Y = \frac{b}{2} (1 - \cos \theta), \quad (0 \leq \theta \leq \pi). \quad (2)$$

When the plate vibrates slightly, a very small displacement d_{W_Y} appears. According to the mathematical definition of limit, the tangent value d_{W_Y}/d_Y is equal to the corresponding angle value. Thus, we express the attack angle as d_{W_Y}/d_Y , that is, the tangent value of the attack angle.

Substitute equation (2) into dW_Y/dY , then the expression of the attack angle is changed into function K_θ , which is related to W_Y and θ . Therefore, expression of W_Y is derived as after mentioned. If the attack angle K_θ is integrable, as given in equation (4), the local vortex strength $\gamma(Y)$ can be expressed as $\gamma(\theta)$:

$$\gamma(\theta) = 2U_\infty \left(A_0 \cot \frac{\theta}{2} + \sum_{n=1}^{\infty} A_n \sin(n\theta) \right), \quad (3)$$

where

$$A_0 = \alpha - \frac{1}{\pi} \int_0^\pi K_\theta d\theta, \quad (4a)$$

$$A_n = \frac{2}{\pi} \int_0^\pi K_\theta \cdot \cos(n\theta) d\theta, \quad (n = 1, 2, 3, 4, \dots). \quad (4b)$$

According to equation (3), when the analytic expressions of the attack angle and the mean camber line are given, there is a unique trigonometric series solution of the local vortex strength $\gamma(\theta)$. Coefficients of the solution can be confirmed by equations (4a) and (4b).

Linearized small perturbation theory of the flow around the thin airfoil is a steady theory, so it can only solve the steady local vortex strength of the thin airfoil without deformation and vibration. However, when a plate vibrates, additional attack angle caused by vibration velocity and trailing vortex caused by changing circular rector will impact local vortex strength, as shown in Figure 2. Lateral vibration velocity V_w and inflow velocity U_∞ will generate a new additional attack angle θ_2 , which is approximately V_w/U_∞ , as shown in Figure 3.

The additional attack angle of the thin plate θ_2 is defined as V_w/U_∞ , so flow theory of the thin airfoil can be used to calculate the local vortex strength caused by θ_2 . Substitute equation (2) into V_w/U_∞ , expression of the additional attack angle is marked as Q_θ , which is related to V_w and θ . Thus, expression of V_w is focused on. If the additional attack angle Q_θ is integrable, the local vortex strength caused by vibration velocity can be expressed as a function $\gamma'(\theta)$ as follows:

$$\gamma'(\theta) = 2U_\infty \left(A'_0 \cot \left(\frac{\theta}{2} \right) + \sum_{n=1}^{\infty} A'_n \sin(n\theta) \right), \quad (5)$$

where

$$A'_0 = \alpha - \frac{1}{\pi} \int_0^\pi Q_\theta d\theta, \quad (6a)$$

$$A'_n = \frac{2}{\pi} \int_0^\pi Q_\theta \cdot \cos(n\theta) d\theta, \quad (n = 1, 2, 3, 4, \dots). \quad (6b)$$

The total circular rector in the nonviscous flow field must be conserved. Thus, the integrable total circular rector of every point in that field must be zero. When a plate vibrates, equivalent wake vortex is generated by change of the circular rector. The wake vortex generated has a strong influence on the local vortex strength of airfoils. Therefore, the wake vortex will also affect deformation of the plate. Deformation will also generate new wake vortex. Both the

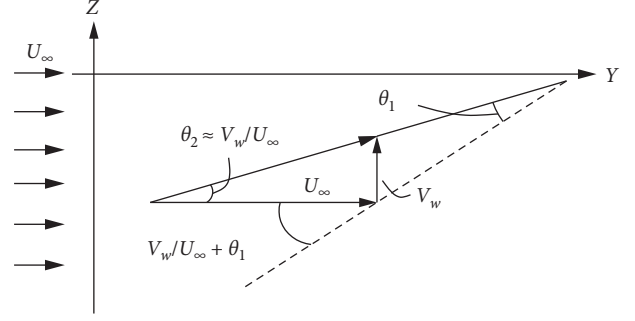


FIGURE 2: Additional attack angle of the plate.

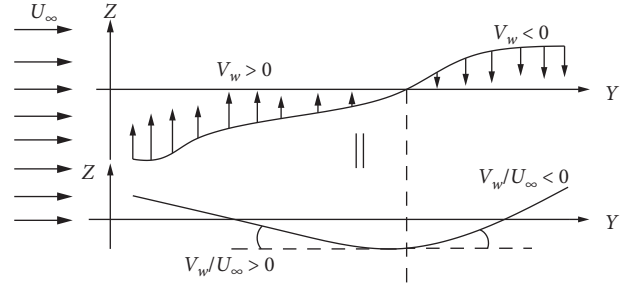


FIGURE 3: Equivalent diagram of the additional attack angle of the wing.

wake vortex and deformation of the plate have influence on the local vortex. Comparatively speaking, wake vortex has a smaller influence on the local vortex strength, so we introduce the quasi-steady hypothesis, in which the influences of the wake vortex on the local vortex strength are neglected. To sum up, under the quasi-steady hypothesis, we only need to consider the influence of the mean camber line's deformation and the additional angle of attack on local vortex strength.

2.2. Interpolation Functions of the Mean Camber Line's Deformation and Vibration Velocity. In order to use equations (3)–(6a) and (6b) to calculate the local vortex strength caused by the additional attack angle and deformation of the mean camber line, it is necessary to know analytic expressions of the mean camber line's deformation of the chord section W_Y and the vibration velocity distribution function V_w . Moreover, K_θ and Q_θ should be integrable on θ . However, when cantilever plate and shell structures vibrate, deformation and velocity are different at different time, which may not satisfy the condition mentioned above. Thus, a fitting method of the interpolation function is applied to express the deformation function W_Y and the vibration velocity distribution function V_w . Therefore, the sum of several interpolation functions can satisfy the condition. If these interpolation functions are integrable on θ after substituting Y into the deformation function W_Y and the distribution function V_w , W_Y and V_w of the vibration velocity can be approximately expressed as integrable functions about θ . Nonequidistant Lagrange interpolation method satisfies the condition abovementioned, so this

method is applied to fit W_Y and V_w . Interpolation functions are several polynomial functions of curves that pass through points given on the 2D plane.

Since the first mode of the cantilever plate vibration is the bending deformation, the first interpolation function WX_1 is set up as a constant, which is the average value of deformation of the mean camber line at $Y = 0$ and $Y = b$, as shown in Figure 4. WX_1 is expressed as

$$WX_1 = \frac{1}{2} (w(x, b, t) + w(x, 0, t)). \quad (7)$$

After the first fitting of the mean camber line's deformation, difference between the deformation curve CC_0 of the mean camber line and the first interpolation function WX_1 is CC_1 , as shown in Figure 5.

Since the second order mode of the cantilever plate vibration is the torsion deformation, the second interpolation function WX_2 is set up as a linear function, which is shown in Figure 6.

Let values of the interpolation function at $Y = 0$ and $Y = b$ be equal to values of residual CC_1 at $Y = 0$ and $Y = b$, respectively. Thus, slope of the first interpolation function can be calculated as follows:

$$\frac{1}{b} ((w(x, b, t) - WX_1) - (w(x, 0, t) - WX_1)). \quad (8)$$

The second interpolation function WX_2 can be written as follows:

$$WX_2 = \frac{1}{b} (w(x, b, t) - w(x, 0, t)) \cdot Y + w(x, 0, t) - WX_1. \quad (9)$$

Difference between residual CC_1 after the first fitting and the second interpolation function WX_2 is marked as CC_2 , which can be expressed as $CC_2 = W - WX_1 - WX_2$.

The third interpolation function WX_3 is set up as a quadratic function, as shown in Figure 7. Values of CC_2 at $Y = 0$ and $Y = b$ are 0. In order not to increase the residual at $Y = 0$ and $Y = b$ in the third fitting, the third interpolation function is taken as $K_2 \cdot Y(b - Y)$. The extreme point of the interpolation function appears at $Y = b/2$; thus, it is necessary to make $K_2 \times Y(b - Y)|_{Y=b/2} = CC_2|_{Y=b/2}$ in order to get a minimal difference between the third interpolation function and the residual CC_2 . According to the equation, unknown coefficient K_2 and the third interpolation function WX_3 can be calculated. WX_3 is written as follows:

$$WX_3 = \left(w\left(x, \frac{b}{2}, t\right) - W_{x1} \right) \frac{4}{b^2} \cdot Y(b - Y). \quad (10)$$

Difference between the residual CC_2 in the second fitting and the third interpolation function WX_3 is marked as CC_3 . The difference can be expressed as $CC_3 = W - WX_1 - WX_2 - WX_3$.

The fourth interpolation function WX_4 is chosen as a cubic function, which is shown in Figure 8. Values of CC_3 at

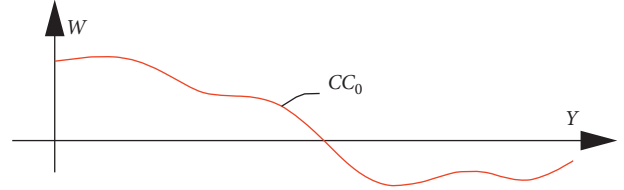


FIGURE 4: Deformation of the mean camber line.

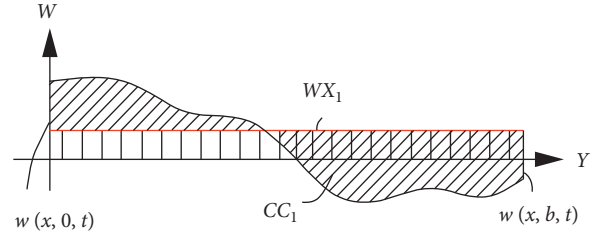


FIGURE 5: The first interpolation function on the plane (Y, Z).

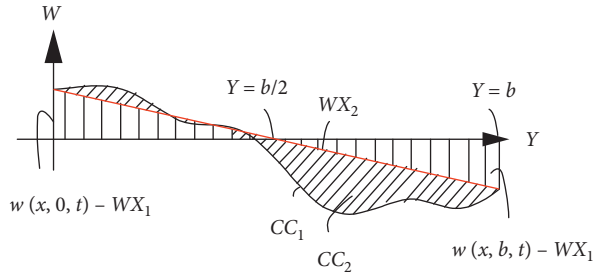


FIGURE 6: The second interpolation function on the plane (Y, Z).

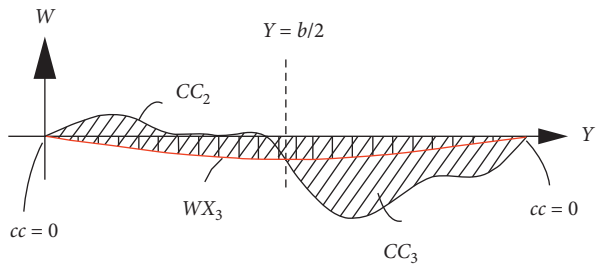


FIGURE 7: The third interpolation function on the plane (Y, Z).

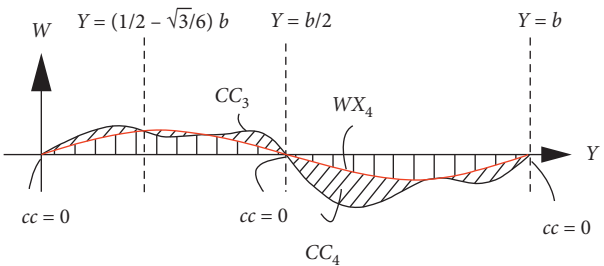


FIGURE 8: The fourth interpolation function on the plane (Y, Z).

$Y = 0$, $Y = b$, and $Y = b/2$ are 0. In order not to increase the residual at $Y = 0$, $Y = b$, and $Y = b/2$ in the fourth fitting, the fourth interpolation function is taken as $K_3 \times Y \times (b - Y) \times (b/2 - Y)$. Extreme points of the interpolation function occur at $Y = b/2 - \sqrt{3}b/6$ and $Y = b/2 + \sqrt{3}b/6$, so it is essential to establish the equation $[K_3 \times Y \times (b - Y) \times (b/2 - Y)]|_{Y=(b/2)-(\sqrt{3}b/6)} = CC_3|_{Y=(b/2)-(\sqrt{3}b/6)}$ in order to make the fourth interpolation function fit the residual CC_3 to the greatest extent. According to the equation, unknown coefficient K_3 and the expression of WX_4 can be calculated. WX_4 is shown as follows:

$$WX_4 = \frac{(w(x, y, t) - WX_1 - WX_2 - WX_3)|_{Y=(b/2)-(\sqrt{3}b/6)}}{((b/2) - (\sqrt{3}b/6))((b/2) + (\sqrt{3}b/6))(\sqrt{3}b/6)} \times Y(b - Y) \left(\frac{b}{2} - Y \right). \quad (11)$$

Similarly, difference between the residual CC_3 in the third fitting and the fourth interpolation function WX_4 is marked as CC_4 , which can be expressed as $CC_4 = W - WX_1 - WX_2 - WX_3 - WX_4$.

The fifth interpolation function WX_5 is set up as the form of a quartic function, as shown in Figure 9. Values of CC_4 at $Y = 0$, $Y = b$, $Y = b/2$, and $Y = (b/2) - (\sqrt{3}b/6)$ are zero. In order not to increase the residual at $Y = 0$, $Y = b$, and $Y = b/2$ in the fourth fitting, the fifth interpolation function is taken as $K_4 \times Y \times (b - Y) \times ((b/2) - Y) \times ((b/2) - (\sqrt{3}b/6) - Y)$. Difference at extreme points of the interpolation function

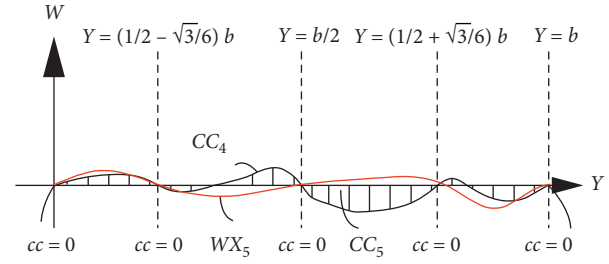


FIGURE 9: The fifth interpolation function on the plane (Y, Z) .

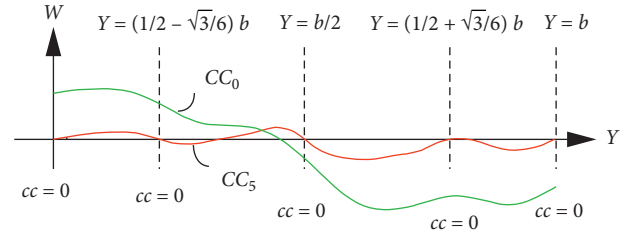


FIGURE 10: Residual error of the deformation in fitting.

$Y = (b/2) + (\sqrt{3}b/6)$ is still exist, so it is necessary to let $K_4 \times Y \times (b - Y) \times ((b/2) - Y) \times ((b/2) - (\sqrt{3}b/6) - Y)|_{Y=(b/2)-(\sqrt{3}b/6)} = CC_4|_{Y=(b/2)-(\sqrt{3}b/6)} = CC_4|_{Y=b/2+\sqrt{3}b/6}$ in order to make the fifth interpolation function fit the residual CC_4 to the greatest extent. According to the equation, unknown coefficient K_4 and the fifth interpolation function WX_5 can be calculated. WX_5 is shown as follows:

$$WX_5 = \frac{(w(x, y, t) - WX_1 - WX_2 - WX_3 - WX_4)|_{Y=(b/2)+(\sqrt{3}b/6)}}{((b/2) + (\sqrt{3}b/6))((b/2) - (\sqrt{3}b/6))(-(\sqrt{3}b/6))b} \times Y(b - Y) \left(\frac{b}{2} - Y \right) \left(\frac{b}{2} - \frac{\sqrt{3}}{6}b - Y \right). \quad (12)$$

Difference between the residual CC_4 in the fourth fitting and the fifth interpolation function WX_5 is marked as CC_5 . The difference can be expressed as $CC_5 = W - WX_1 - WX_2 - WX_3 - WX_4 - WX_5$. Values of CC_5 at $Y = 0$, $Y = b$, $Y = b/2$, $Y = (b/2) - (\sqrt{3}b/6)$, and $Y = (b/2) + (\sqrt{3}b/6)$ are 0.

After five times of deformation fitting abovementioned, the total residual CC_0 of five interpolation functions of the thin plate have the tendency to gradually converge to zero, as shown in Figure 10. If the mean camber line is more complicated, it is necessary to conduct more interpolation functions. For cantilever plates and shells with high-aspect ratio, chord deformation is relatively simple, so it is enough

to take top four interpolation functions to fit the deformation.

Velocity is the derivative of displacement, which is continuous while the plate is vibrating, so vibration velocity distribution of the plate is also continuous. If we represent the mean camber line's vibration velocity of the chord section as a curve, a method that is totally similar to the above can be used to fit the curve. Form of the interpolation function of velocity distribution is exactly the same as that of the interpolation function of deformation. Therefore, it only needs to replace items about deformation in equations (7) and (9)–(12) with a corresponding item about velocity. Then, five interpolation functions for fitting velocity distribution are obtained as follows:

$$\begin{aligned}
VX_1 &= \frac{(\partial w(x, b, t)/\partial t) + (\partial w(x, 0, t)/\partial t)}{2}, \\
VX_2 &= \frac{1}{b} \left(\frac{\partial w(x, b, t)}{\partial t} - \frac{\partial w(x, 0, t)}{\partial t} \right) Y + \frac{\partial w(x, 0, t)}{\partial t} - VX_1, \\
VX_3 &= \left(\frac{\partial w(x, (b/2), t)}{\partial t} - VX_1 \right) \frac{4}{b^2} (b - Y) Y, \\
VX_4 &= \left(\frac{((\partial w(x, b, t)/\partial t) - VX_1 - VX_2 - VX_3) \Big|_{Y=(b/2)-(\sqrt{3}b/6)}}{((b/2) - (\sqrt{3}b/6))((b/2) + (\sqrt{3}b/6))(\sqrt{3}b/6)} \right) \\
&\quad \times Y (b - Y) \left(\frac{b}{2} - Y \right), \\
VX_5 &= \left(\frac{((\partial w/\partial t) - VX_1 - VX_2 - VX_3 - VX_4) \Big|_{Y=(b/2)+(\sqrt{3}b/6)}}{((b/2) + (\sqrt{3}b/6))((b/2) - (\sqrt{3}b/6))(-(\sqrt{3}b/6))b} \right) \\
&\quad \times Y (b - Y) \left(\frac{b}{2} - Y \right) \left(\frac{b}{2} - \frac{\sqrt{3}}{6} b - Y \right).
\end{aligned} \tag{13}$$

2.3. Lift Force Calculation. Precondition of calculating lift force of the high-aspect-ratio cantilever plate is to obtain the local vortex strength, as shown in equation (1). Local vortex strength of the cantilever thin plate with high-aspect ratio is mainly caused by two factors, deformation of the mean camber line and the vibration velocity. Based on linearized small perturbation theory, the total local vortex strength caused by these two factors can be obtained by using linear superposition, as shown in equation (14). In the previous section, we give the interpolation functions of the two variables. In order to calculate the local vortex strength caused by deformation of the mean camber line, local vortex strength caused by every interpolation function can be calculated, respectively, and then the linear superposition can be carried out. Chordwise deformation of the plate structure is relatively simple, so top four interpolation functions are enough to fit the deformation of the cantilever plate accurately. WX_1 , WX_2 , WX_3 , and WX_4 are taken to calculate local vortex. First of all, attack angle caused by four interpolation functions d_{WX_1}/d_Y , d_{WX_2}/d_Y , d_{WX_3}/d_Y , and d_{WX_4}/d_Y are calculated, respectively. Substitute equation (2) into d_{WX_1}/d_Y , d_{WX_2}/d_Y , d_{WX_3}/d_Y , and d_{WX_4}/d_Y ; then, functions of the attack angle become related to θ . These four

functions are set up as K_1 , K_2 , K_3 , and K_4 , which are substituted into equations (4a) and (4b), respectively. A_0 and A calculated by equations (4a) and (4b) are substituted into equation (3) to solve the corresponding local vortex of top four interpolation functions: γWX_1 , γWX_2 , γWX_3 , and γWX_4 .

In order to calculate the local vortex caused by the vibration velocity, local vortex strength caused by each interpolation function of the velocity is calculated, respectively. Linear superposition is conducted to obtain total local vortex strength caused by the vibration velocity. Because vibration velocity of cantilever plate is relatively simple, it is accurate enough to take four interpolation functions to fit velocity distribution of the plate. Thus, top four interpolation functions VX_1 , VX_2 , VX_3 , and VX_4 are selected to calculate the local vortex. Firstly, angle of attack functions VX_1/U_∞ , VX_2/U_∞ , VX_3/U_∞ , and VX_4/U_∞ of four interpolation functions are calculated, respectively. And substitute equation (2) into VX_1/U_∞ , VX_2/U_∞ , VX_3/U_∞ , and VX_4/U_∞ . Then, angle of attack functions are translated into functions related to θ . These four functions are set up as Q_1 , Q_2 , Q_3 , and Q_4 , which are substituted into equations (6a) and (6b), respectively. A'_0 and A'_n calculated by equations (6a) and (6b) are substituted into equation (5) to solve the corresponding local vortex: γVX_1 , γVX_2 , γVX_3 , and γVX_4 of top four interpolation functions. To sum up, the total local vortex strength caused by the mean camber line's deformation and the lateral vibration velocity is γ_z , which can be expressed as linear superposition of the local vortex strength calculated by abovementioned eight interpolation functions. γ_z is written as follows:

$$\begin{aligned}
\gamma_z &= \gamma WX_1 + \gamma WX_2 + \gamma WX_3 + \gamma WX_4 + \gamma VX_1 + \gamma VX_2 \\
&\quad + \gamma VX_3 + \gamma VX_4 = pw_1 \cdot w(x, b, t) + pw_2 \cdot w(x, 0, t) \\
&\quad + pw_3 \cdot w\left(x, \frac{b}{2}, t\right) + pw_4 \cdot w\left(x, \frac{b}{2} - \frac{\sqrt{3}b}{6}, t\right) \\
&\quad + pv_1 \cdot \frac{\partial w(x, b, t)}{\partial t} + pv_2 \cdot \frac{\partial w(x, 0, t)}{\partial t} \\
&\quad + pv_3 \cdot \frac{\partial w(x, (b/2), t)}{\partial t} + pv_4 \cdot \frac{\partial w(x, (b/2) - (\sqrt{3}b/6), t)}{\partial t},
\end{aligned} \tag{14}$$

where

$$pw_1 = \left((12\sqrt{3} - 36) \frac{Y}{b} + (10 - 6\sqrt{3}) \right) \frac{U_\infty}{b} \times \sqrt{\frac{Y}{b} - \frac{Y^2}{b^2}} + \frac{\sqrt{3} - 7}{2} \frac{U_\infty}{b} \sqrt{\frac{b}{Y} - 1}, \tag{15a}$$

$$pw_2 = \left(-26 - 6\sqrt{3} + (12\sqrt{3} + 36) \frac{Y}{b} \right) \frac{U_\infty}{b} \sqrt{\frac{Y}{b} - \frac{Y^2}{b^2}} + \left(\frac{7 + \sqrt{3}}{2} \right) \frac{U_\infty}{b} \sqrt{\frac{b}{Y} - 1}, \tag{15b}$$

$$pw_3 = 48\sqrt{3} \frac{Y}{b} - 24\sqrt{3} \frac{U_\infty}{b} \sqrt{\frac{Y}{b} - \frac{Y^2}{b^2}} + 2\sqrt{3} \frac{U_\infty}{b} \sqrt{\frac{b}{Y} - 1}, \tag{15c}$$

$$pw_4 = \left(36\sqrt{3} - 72\sqrt{3} \frac{Y}{b} \right) \frac{U_\infty}{b} \sqrt{\frac{Y}{b} - \frac{Y^2}{b^2}} - 3\sqrt{3} \frac{U_\infty}{b} \sqrt{\frac{b}{Y} - 1}, \quad (15d)$$

$$pv_1 = (12 - 4\sqrt{3}) \left(\frac{Y}{b} - \frac{Y^2}{b^2} \right)^{3/2} + \left(\frac{\sqrt{3} - 3}{2} - \frac{4Y}{b} \right) \times \sqrt{\frac{Y}{b} - \frac{Y^2}{b^2}} - \frac{1}{2} \sqrt{\frac{b}{Y} - 1}, \quad (15e)$$

$$pv_2 = (-4\sqrt{3} - 12) \left(\frac{Y}{b} - \frac{Y^2}{b^2} \right)^{3/2} - \frac{1}{2} \sqrt{\frac{b}{Y} - 1} + \left(\frac{11 + \sqrt{3}}{2} - \frac{4Y}{b} \right) \sqrt{\frac{Y}{b} - \frac{Y^2}{b^2}}, \quad (15f)$$

$$pv_3 = -16\sqrt{3} \left(\frac{Y}{b} - \frac{Y^2}{b^2} \right)^{3/2} + \left(\frac{8Y}{b} + 2\sqrt{3} - 4 \right) \times \sqrt{\frac{Y}{b} - \frac{Y^2}{b^2}} - \sqrt{\frac{b}{Y} - 1}, \quad (15g)$$

$$pv_4 = 24 \left(\frac{Y}{b} - \frac{Y^2}{b^2} \right)^{3/2} \sqrt{3} - 3 \sqrt{\frac{Y}{b} - \frac{Y^2}{b^2}} \sqrt{3}. \quad (15h)$$

According to equations (1) and (14), the aerodynamic force Δp can be expressed as

$$\Delta p = \rho U_\infty \gamma_z. \quad (16)$$

Since the aerodynamic force expression is analytic, it is convenient to use analytic and semianalytic method to study the flutter problem of the cantilever plate.

2.4. Aerodynamic Correction and Error Analysis. Value of item $\sqrt{(b/Y) - 1}$ in equations (15a) and (15h) at $Y = 0$ is infinite, which leads to an infinite leading edge lift force. As a matter of fact, leading edge lift force of the wing cannot be infinite. Appearance of such a singularity at the leading edge of the wing which is attributed to the basic solution of the thin-wall theory gives no consideration to flow around the leading edge, namely, when air flows past the leading edge of the thin plate, part of air will pass through the upper panel from the lower panel. Neglecting thickness of the plate, the thin-airfoil theory leads to an infinite streaming velocity and an infinite lift force at the leading edge. As a result, it is necessary to correct this problem.

According to Ref. [43], although there is a singular point at the leading edge of the plate, the pressure distribution on 95% chord length range near the trailing edge has a good consistency with that of actual measurement. Thus, it is necessary to add a correlation coefficient in $\sqrt{(b/Y) - 1}$. The infinity value of this function at $Y = 0$ is corrected to be equal to the value of the original curve at $Y = 0.95b$. After trial, the item $\sqrt{(b/Y) - 1}$ in equation (15a) is corrected as $\sqrt{(b - Y)/(Y + 0.05b)}$. At the moment, the value of $\sqrt{(b - Y)/(Y + 0.05b)}$ at $Y = 0$ is equal to the value of $\sqrt{(b/Y) - 1}$ at $Y = 0.95b$. The value of these two functions at the trailing edge portion of the plate changes little, as shown in Figure 11. The corrected aerodynamic expression is denoted as $\Delta p'$.

If the air on the plate flows at a speed greater than 0.3 times the speed of sound, influences of the compressibility of air on aerodynamic force cannot be neglected. Thus, it is essential to modify the impact of compression. Von

Karman–Chandra Formula is used to estimate the influence of air compressibility on aerodynamic force, and equation (17) is the relationship between the two: aerodynamic pressure Δp_p on the plate surface in nonsticky, steady, and subsonic velocity and 2D compressible flow field and the corresponding pressure $\Delta p'$ in the incompressible flow. Ma_∞ is the ratio of the flow velocity U_∞ to the local velocity of sound.

To sum up, after correction and considering the compressibility of air, the aerodynamic force expression Δp_p is as follows:

$$\Delta p_p = \frac{\Delta p'}{\sqrt{1 - Ma_\infty^2} + (1/2)\Delta p' \cdot (1 - \sqrt{1 - Ma_\infty^2})}. \quad (17)$$

Aerodynamic force Δp_p is the linear superposition of aerodynamic forces calculated by several interpolation functions. Moreover, inflow air must satisfy hypotheses of irrotational and nonviscous. Thus, the aerodynamic force Δp_p calculated by equation (17) is an approximate result. There is an error between it and the real aerodynamic force. Effect of this approach is evaluated by estimating magnitude of the error between the two.

Mean camber line's deformation and the lateral vibration velocity are mainly considered in theoretical calculation of the aerodynamic force. The essential reason why the lift force can be generated is to change the attack angle of the wing, which indirectly affects the aerodynamic force. Thus, what is need is to make a comparison between the lift force generated by deformation of the mean camber line of the plate and that of the corresponding finite element model to illustrate effectiveness of the aerodynamic force theoretically calculated.

ANSYS FLUNT finite element software is applied to calculate the aerodynamic force distribution. A spline curve of definite shape whose chord length is 1 meter is drew in Computer Aided Design (CAD). Coordinates of control points of the spline are shown in Figure 12. A thin shell model of 0.01 meter thickness is constructed by stretching the spline curve we drew to 10 meters along the spanwise

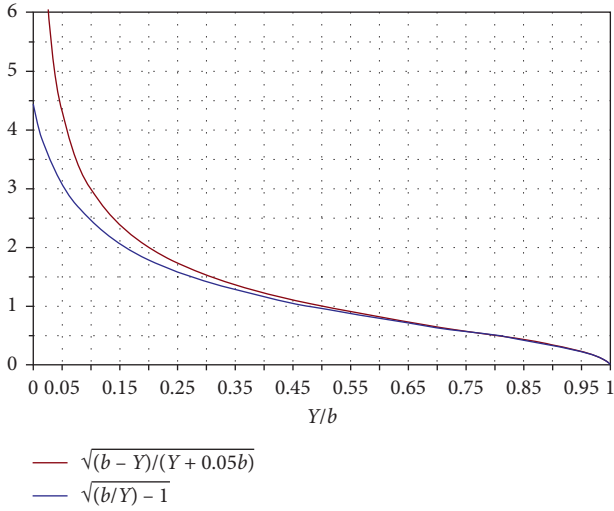


FIGURE 11: Correction of the coefficient of the aerodynamic force.

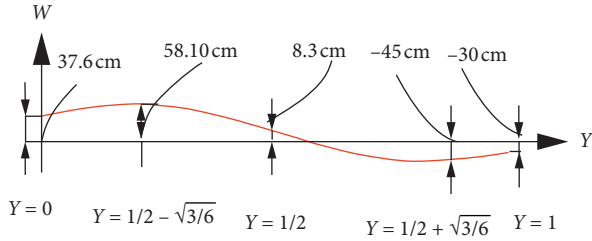


FIGURE 12: The coordinate graph of the spline curve.

direction. Assuming the elasticity modulus of the shell structure in subsonic, compressible, and nonsticky turbulence flow field is infinite. The velocity of the airflow is $U_\infty = 200$ m/s. After numerical simulation, pressure cloud pictures of the upper and lower surface can be obtained, as shown in Figures 13 and 14.

The lift force can be calculated by the pressure difference between the upper and lower surface of the airfoil, as shown in Figure 15.

If we take the spline curve in Figure 12 as a mean camber line of the cross section at a certain moment of the deformed high-aspect ratio cantilever plate structure, the aerodynamic force distribution on the section can be calculated according to equation (17). As shown in Figure 12, in calculation of the aerodynamic force, these items are introduced:

$$\begin{aligned}
 w(x, 0, t) &= 0.376, \\
 w\left(x, \frac{b}{2}, t\right) &= 0.083, \\
 w\left(x, \frac{b}{2} - \frac{\sqrt{3}b}{6}, t\right) &= 0.581, \\
 w(x, b, t) &= -0.3, \\
 w\left(x, \frac{b}{2} + \frac{\sqrt{3}b}{6}, t\right) &= -0.45.
 \end{aligned} \tag{18}$$

In calculation of the lift force generated only by deformation of the mean camber line, velocities in the aerodynamic force expression Δp_p are taken as zero, namely,

$$\begin{aligned}
 \frac{\partial w(x, 0, t)}{\partial t} &= 0, \\
 \frac{\partial w(x, (b/2), t)}{\partial t} &= 0, \\
 \frac{\partial w(x, (b/2) - (\sqrt{3}b/6), t)}{\partial t} &= 0, \\
 \frac{\partial w(x, b, t)}{\partial t} &= 0, \\
 \frac{\partial w(x, (b/2) + (\sqrt{3}b/6), t)}{\partial t} &= 0.
 \end{aligned} \tag{19}$$

Substituting abovementioned data into equation (17), aerodynamic force distribution calculated is shown in Figure 15. Trend of value theoretical calculated has a good agreement with that obtained by ANSYS FLUENT. In contrast with value obtained by ANSYS FLUENT, the result theoretical calculated is relatively small. In particular, the error is nearly about 20% at the trailing edge, as shown in Figure 15.

The comparison above indicates that the aerodynamic force fitted by utilizing interpolation functions can predict the influence of deformation on aerodynamic distribution approximately. Value of the aerodynamic force obtained by ANSYS is relatively large. Source of the error in the theoretical value is mainly due to the hypothesis of nonsticky and the neglecting of influence brought by the trailing vortex.

3. Establishment and Dispersion of Aerodynamic Equations for the Cantilever Plate

The schematic diagram of the wing is shown in Figure 1, which is simplified as a cantilever plate in subsonic flow. The rectangular plate is characterized by $a \times b \times h$, where a is the span length, b is the chord length, and h is the thickness. A is the cross section of the wing. (X, Y, Z) is the inertial coordinate system and the origin of it is located at the leading edge of the fixed end of the cantilever plate, which is marked by point O.

Considering the first-order shear deformation, Kirchhoff hypothesis [44], and scale effect, the displacement field of the plate is established. Displacement of any point along x , y , and z direction can be expressed by that of the neutral plane of the plate as follows:

$$u(x, y, z, t) = u_0(x, y, t) + z\varphi_x(x, y, t), \tag{20a}$$

$$v(x, y, z, t) = v_0(x, y, t) + z\varphi_y(x, y, t), \tag{20b}$$

$$w(x, y, z, t) = w_0(x, y, t), \tag{20c}$$

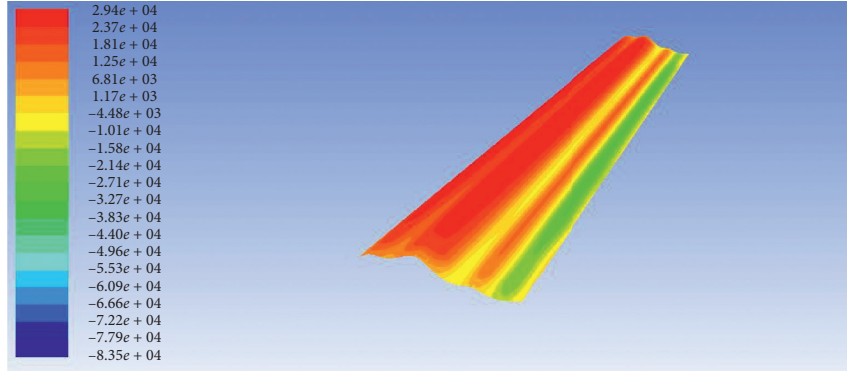


FIGURE 13: Pressure of the lower surface of the airfoil.

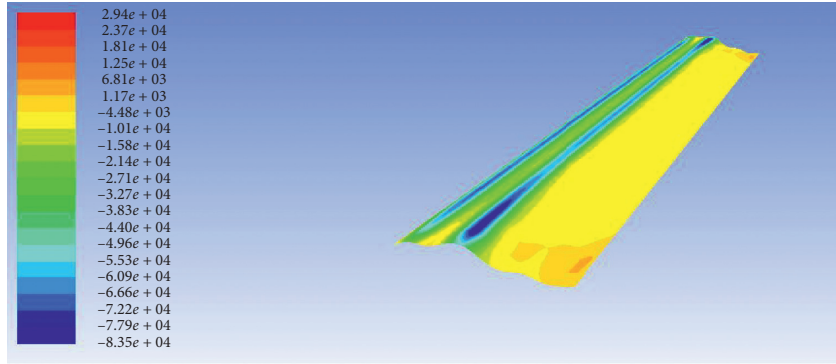


FIGURE 14: Pressure of the upper surface of the airfoil.

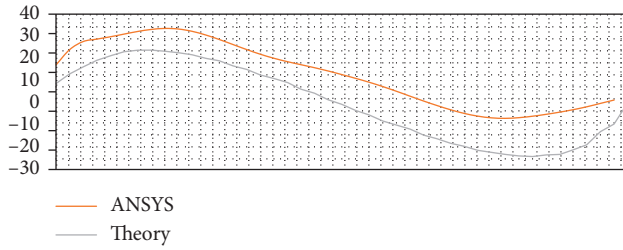


FIGURE 15: Comparison between the theoretical result and the ANSYS result.

where u_0 , v_0 , and w_0 are displacements along X , Y , and Z directions of points on the neutral plane of the blade, and φ_x and φ_y are rotation angles around y -axis and x -axis.

Strains of the von Karman plate, which are computed by using the nonlinear strain-displacement relation, are obtained as follows:

$$\varepsilon_{xx} = \frac{\partial u_0}{\partial x} + \frac{1}{2} \left(\frac{\partial w}{\partial x} \right)^2 + z \frac{\partial \varphi_x}{\partial x} = \varepsilon_{xx}^{(0)} + z \varepsilon_{xx}^{(1)}, \quad (21a)$$

$$\varepsilon_{yy} = \frac{\partial v_0}{\partial y} + \frac{1}{2} \left(\frac{\partial w}{\partial y} \right)^2 + z \frac{\partial \varphi_y}{\partial y} = \varepsilon_{yy}^{(0)} + z \varepsilon_{yy}^{(1)}, \quad (21b)$$

$$\begin{aligned} \gamma_{xy} &= \frac{\partial u_0}{\partial y} + \frac{\partial v_0}{\partial x} + \left(\frac{\partial w}{\partial x} \right) \left(\frac{\partial w}{\partial y} \right) + z \left(\frac{\partial \varphi_x}{\partial y} + \frac{\partial \varphi_y}{\partial x} \right) \\ &= \gamma_{xy}^{(0)} + z \gamma_{xy}^{(1)}, \end{aligned} \quad (21c)$$

$$\gamma_{xz} = \varphi_x + \frac{\partial w}{\partial x} \gamma_{yz} = \varphi_y + \frac{\partial w}{\partial y}. \quad (21d)$$

The constitutive relation of the isotropic material is expressed as follows:

$$\sigma_{xx} = \frac{E}{1-\nu^2} (\varepsilon_{xx} + \nu \varepsilon_{yy}), \quad (22a)$$

$$\sigma_{yy} = \frac{E}{1-\nu^2} (\varepsilon_{yy} + \nu \varepsilon_{xx}), \quad (22b)$$

$$\tau_{xy} = \frac{E}{2(1+\nu)} \gamma_{xy}, \quad (22c)$$

$$\tau_{xz} = \frac{E}{2(1+\nu)} \gamma_{xz}, \quad (22d)$$

$$\tau_{yz} = \frac{E}{2(1+\nu)} \gamma_{yz}, \quad (22e)$$

where E is the elasticity modulus of the material and ν is Poisson's ratio.

In order to simplify the calculation, relation between the internal forces and stresses is expressed as follows:

$$\begin{Bmatrix} Q_x \\ Q_y \end{Bmatrix} = \int_{-h/2}^{h/2} \begin{Bmatrix} \tau_{xz} \\ \tau_{yz} \end{Bmatrix} dz, \quad (23a)$$

$$\begin{Bmatrix} N_x \\ N_y \\ N_{xy} \end{Bmatrix} = \int_{-h/2}^{h/2} \begin{Bmatrix} \sigma_{xx} \\ \sigma_{yy} \\ \tau_{xy} \end{Bmatrix} dz, \quad (23b)$$

$$\begin{Bmatrix} M_x \\ M_y \\ M_{xy} \end{Bmatrix} = \int_{-h/2}^{h/2} \begin{Bmatrix} \sigma_{xx} \\ \sigma_{yy} \\ \tau_{xy} \end{Bmatrix} z dz. \quad (23c)$$

Substituting nonlinear strains of equations (21a)–(21d) obtained by von Karman nonlinear geometric relationship into equations (22a)–(22e) and combining the result with equations (23a)–(23c), the potential energy of the plate are obtained as follows:

$$U_d = \frac{1}{2} \int_{\Omega} (N_{xx}\varepsilon_{xx}^{(0)} + N_{yy}\varepsilon_{yy}^{(0)} + N_{xy}\gamma_{xy}^{(0)} + M_x\varepsilon_{xx}^{(1)} + M_y\varepsilon_{yy}^{(1)} + M_{xy}\varepsilon_{xy}^{(1)} + Q_{xz}\gamma_{xz} + Q_{yz}\gamma_{yz}) dx dy. \quad (24)$$

The kinetic energy and the virtual work done by external forces are as follows:

$$T = \frac{1}{2} \int_{\Omega} \int_{-h/2}^{h/2} \rho_c (\dot{u}^2 + \dot{v}^2 + \dot{w}^2) dx dy dz, \quad (25)$$

$$W_P = \int_{\Omega} \left(\Delta P \cdot w - c \cdot \frac{dW}{dt} \right) dx dy, \quad (26)$$

where ρ_c is material density and C is the air damping.

Nonlinear dynamic equations of motion for the rotating blade are established by using Hamilton's principle:

$$\int_{t_1}^{t_2} (\delta T - \delta U_d + \delta W_P) dt = 0. \quad (27)$$

The lateral displacement of the thin plate is more obvious compared with others. Thus, displacements u_0 and v_0 on the middle surface and rotation angle φ_x and φ_y are neglected. Substituting equations (24)–(26) into equation (27), nonlinear dynamic equation of the plate in the lateral direction is obtained as follows:

$$\begin{aligned} & \frac{1}{12} \frac{\pi^2 E ((\partial/\partial x)\phi x(x, y, t) + (\partial^2/\partial x^2)w(x, y, t))h}{2 + 2\nu} + \frac{1}{12} \frac{\pi^2 E ((\partial/\partial y)\phi y(x, y, t) + (\partial^2/\partial y^2)w(x, y, t))h}{2 + 2\nu} \\ & + \frac{(Ev h (\partial/\partial x)w(x, y, t) ((\partial/\partial y)w(x, y, t)) (\partial^2/\partial y \partial x)w(x, y, t))}{-v^2 + 1} + \frac{Eh (\partial/\partial x)w(x, y, t) ((\partial/\partial x)w(x, y, t)) (\partial^2/\partial x^2)w(x, y, t)}{-v^2 + 1} \\ & + \frac{((1/2\nu) ((\partial/\partial y)w(x, y, t))^2 h E (\partial^2/\partial x^2)w(x, y, t))}{-v^2 + 1} + \frac{(1/2) ((\partial/\partial x)w(x, y, t))^2 h E (\partial^2/\partial x^2)w(x, y, t)}{-v^2 + 1} \\ & + \frac{\pi^2 E ((\partial/\partial x)w(x, y, t))^2 ((\partial^2/\partial y^2)w(x, y, t))h}{12 \times (2 + 2\nu)} + \frac{(v ((\partial/\partial x)w(x, y, t)) (\partial^2/\partial y \partial x)w(x, y, t) Eh (\partial/\partial y)w(x, y, t))}{-v^2 + 1} \\ & + \frac{((\partial/\partial y)w(x, y, t)) (\partial^2/\partial y^2)w(x, y, t) Eh (\partial/\partial y)w(x, y, t)}{-v^2 + 1} + \frac{((1/2\nu) ((\partial/\partial x)w(x, y, t))^2 Eh (\partial^2/\partial y^2)w(x, y, t))}{-v^2 + 1} \\ & + (1/2) ((\partial/\partial y)w(x, y, t))^2 Eh (\partial^2/\partial y^2)w(x, y, t) - c (\partial/\partial t)w(x, y, t) + \Delta p = \rho_c h (\partial^2/\partial t^2)w(x, y, t). \end{aligned} \quad (28)$$

I_i is calculated by

$$\begin{Bmatrix} I_0 \\ I_1 \\ I_2 \end{Bmatrix} = \int_{-h/2}^{h/2} \rho_c \begin{Bmatrix} 1 \\ z \\ z^2 \end{Bmatrix} dz. \quad (29)$$

The boundary conditions of the fix end of the plate are

$$x = 0 \quad w = 0, \varphi_x = 0, \varphi_y = 0, \quad (30a)$$

$$y = 0 \quad w = 0, \varphi_x = 0, \varphi_y = 0. \quad (30b)$$

The boundary conditions of the free end of the plate are

$$x = a \quad w = 0, M_x = 0, M_{xy} = 0, Q_x = 0, \quad (31a)$$

$$y = b \quad w = 0, M_y = 0, M_{xy} = 0, Q_y = 0. \quad (31b)$$

Avramov and Mikhlin [45] have performed a lot of review of theoretical developments of nonlinear normal modes for continuum mechanical systems. Mode function that we choose must satisfy the first two order modes of lateral nonlinear vibration and the boundary conditions given in equations (30a), (30b), (31a), and (31b). According to mode approximation functions for the cantilever plate given in Ref. [46], the following mode functions are chosen

$$XM_1 = \cosh(k_1 \cdot x) - \cos(k_1 \cdot x) - \beta_1 (\sinh(k_1 \cdot x) - \sin(k_1 \cdot x)), \quad (32a)$$

$$XM_2 = \cosh(k_2 \cdot x) - \cos(k_2 \cdot x) - \beta_2 (\sinh(k_2 \cdot x) - \sin(k_2 \cdot x)), \quad (32b)$$

$$YM_1 = 1, \quad (32c)$$

$$YM_2 = \sqrt{3} \left(1 - 2 \frac{Y}{b} \right), \quad (32d)$$

where k_1 , k_2 , β_1 , and β_2 are calculated by

$$\begin{aligned} k_1 &= \frac{1.875}{a}, \\ k_2 &= \frac{4.694}{a}, \\ \beta_1 &= \frac{1.875}{a}, \\ \beta_2 &= \frac{\sinh(k_1 \cdot a) - \sin(k_1 \cdot a)}{\cosh(k_1 \cdot a) + \cos(k_1 \cdot a)}. \end{aligned} \quad (33)$$

TABLE 1: Value of parameters.

Physical quantity	Numerical value
a	5 m
b	1 m
h	0.02 m
ρ	1.28 kg/m ³
E	102 GPa
ρ_c	1750 kg/m ³
c	10 N·s/m
ν	0.3

The lateral displacement of the plate can be expressed as follows:

$$w = x_1 \cdot XM_1 \cdot YM_1 + x_3 \cdot XM_1 YM_2. \quad (34)$$

Substituting equations (33) and (34) and parameters in Table 1 into equation (28), ordinary differential equations of transverse vibration for the first two modes of the cantilever plate are obtained by using the Galerkin method [47] as follows:

$$\begin{aligned} \ddot{x}_1 &= -1470740.224x_1^3 + 575174.9082x_3^2 - 113819521.7x_3^2x_1 + 0.01384683053x_3^3 - 74.29541441x_1 + 0.3027136145U_\infty^2x_3 \\ &+ 0.001143287344x_1^2x_3 + 5383.891352x_1^2 + 0.04079 \cdot U_\infty \cdot \dot{x}_3 - 0.02857 \cdot 2 \cdot c \cdot \dot{x}_1, \end{aligned} \quad (35a)$$

$$\begin{aligned} \ddot{x}_3 &= 0.0005710592x_1^3 + 0.0004853467x_3^2 - 0.08089898x_3^2x_1 - 110064645x_3^3 - 11668.03765x_3 + 0.2032087116U_\infty^2x_3 \\ &- 113739904.7x_1^2x_3 + 1149545.143x_3x_1 - 0.02855 \cdot 2 \cdot c \cdot \dot{x}_3 + 0.04076 \cdot U_\infty \cdot \dot{x}_1. \end{aligned} \quad (35b)$$

In equations (35a) and (35b), x_1 and x_3 are generalized coordinates of the first-order and the second-order modals. The coefficient of $U_\infty \cdot \dot{x}_1$ is moved to the left end of the equation and is neglected, which shows that the aerodynamic force acts as a negative damping. Thus, amplitude of the vibrating structure increases continuously by absorbing energy from the airflow, which may lead to the occurrence of flutter.

4. Limit Cycle

Based on equations (35a) and (35b), Runge–Kutta algorithm is utilized to construct numerical simulation of flutter

phenomenon for the cantilever plate subjected to the aerodynamic force in subsonic air flow. Initial values of the ordinary differential equations (35a) and (35b) are given as $x_1 = 0.001$, $x_3 = 0.001$, $\dot{x}_1 = 0$, and $\dot{x}_3 = 0$.

When the inflow velocity U_∞ is chosen as 72 m/s, the system is in the stable state, as shown in Figure 16, in which vibration amplitude of the plate at $X = 5$ and $Y = 0.8$ decreases as time increases. Transverse displacement of the system is convergent when the inflow velocity fails to reach the critical flutter velocity. Figure 16(a) gives the waveform on the plane (t, w) , where w is the transverse vibration displacement. Figure 16(b) represents the phase portrait on

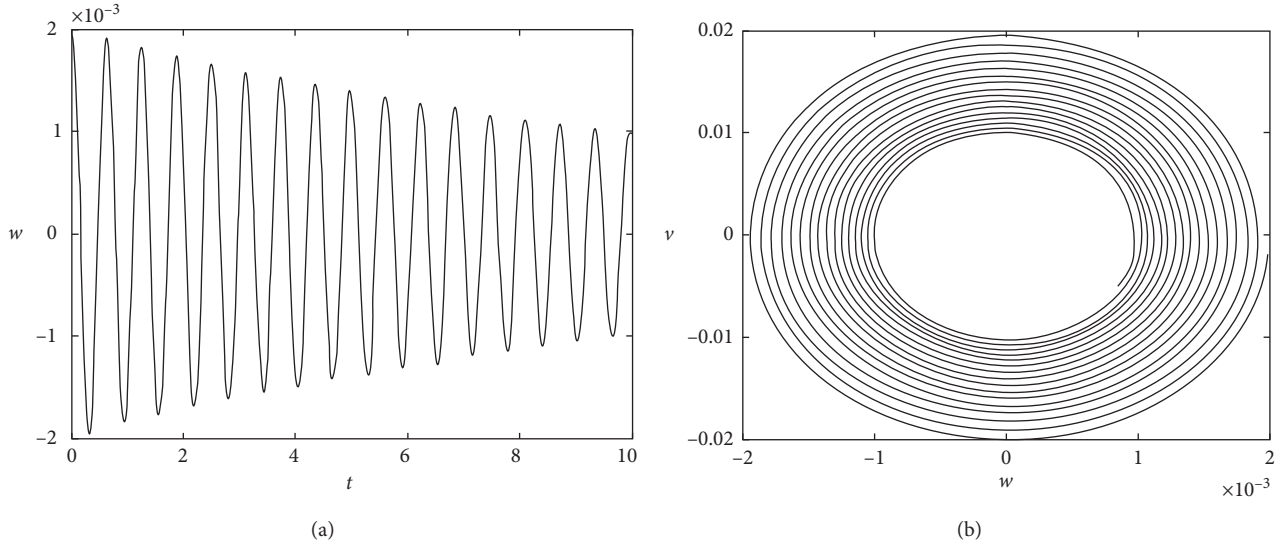


FIGURE 16: Stable state of the system when the inflow velocity U_∞ is chosen as 72 m/s: (a) time history diagram of vibration amplitude on plane (t, x_1) and (b) phase portrait on plane (w, v) .

the plane (w, v) , where v is the transverse vibration velocity. The adjacent trajectory gradually becomes a closed loop, as shown in Figure 16(b).

When the inflow speed U_∞ is set as 80.43 m/s, the system keeps in a critical state between stability and instability, as shown in Figure 17(a). The amplitude of the plate at $X = 5$ and $Y = 0.8$ converges to a constant. The phase portrait of the transverse displacement w and the transverse velocity v of the vibrating plate at $X = 5$ and $Y = 0.8$ is shown in Figure 17(b). The phase portrait is an isolated closed loop, which do not have closed rails nearby. This is called a limit cycle. At the moment, the critical flutter velocity is reached.

When the inflow velocity U_∞ is increased from 80.43 m/s to 89 m/s gradually, the system appears to diverge and becomes unstable, as shown in Figure 18(a). The phase portrait of transverse displacement w and transverse velocity v of the vibrating plate at $X = 5$ and $Y = 0.8$ is shown in Figure 18(b). The phase portrait is far from a closed loop.

In this paper, the high-aspect-ratio subsonic cantilever plate system is nonconservative, which means the system will perform steady periodic vibration under specific conditions. As shown in equations (35a) and (35b), the aerodynamic force play the role of negative damping in vibration of the plate. Thus, when the inflow velocity reaches a certain value, there will be periodic vibration of equal amplitudes, as shown in Figure 17. This indicates that energy supplied by the aerodynamic force and that dissipated by damping are in balance. In fact, since there is no periodic external force in the system, the system can only absorb energy from surroundings by the negative damping caused by the aerodynamic force.

Periodic motions in nonconservative system belong to self-excited vibrations, which corresponds to stable limit cycles of the autonomous system, that is, when the initial

conditions are disturbed, the original vibration state can still be restored. If the system subjects to some small disturbance, the original periodic motion will not be changed. For example, when the inflow velocity is chosen as 80.43 m/s, the system vibrates periodically with equal amplitudes. When the inflow velocity increases to a value smaller than 89 m/s, the system still keeps periodic motion with greater amplitude. Limit cycles of the linear system is often unstable and linear theory is not suitable for the system with large inflow velocity; thus, in this paper, nonlinear theory is more appropriate for limit cycles analysis of the cantilever plate.

Stability of the linear system can be judged by calculating eigenvalues, and the critical flutter velocity can be calculated. It is not easy to solve eigenvalues for nonlinear systems, so the critical flutter velocity cannot be solved by this method. We can assume the inflow velocity to be a certain value and substitute it into the ordinary differential equations of motion for the high-aspect-ratio cantilever plate. Based on the equations, phase portrait of the system are numerically obtained. When limit cycle appears in the phase space, the inflow velocity is exactly the critical flutter velocity.

In order to study the influence of system parameters on critical flutter velocity, different inflow velocity U_∞ is substituted into equations (35a) and (35b). When the phase portrait turns to be a limit cycle, the inflow velocity U_∞ reaches the critical flutter velocity. Parameters in Table 1 except thickness are brought into the equation. Corresponding critical flutter velocities of plates with different thickness are calculated, as shown in Figure 19(a). The critical flutter velocity increases as the thickness of the plate increases.

Change the length of the plate only to detect the influence of the aspect ratio on the critical flutter velocity. Other parameters are shown in Table 1. The critical flutter velocity is decreased with the increase of the aspect ratio, as shown in Figure 19(b).

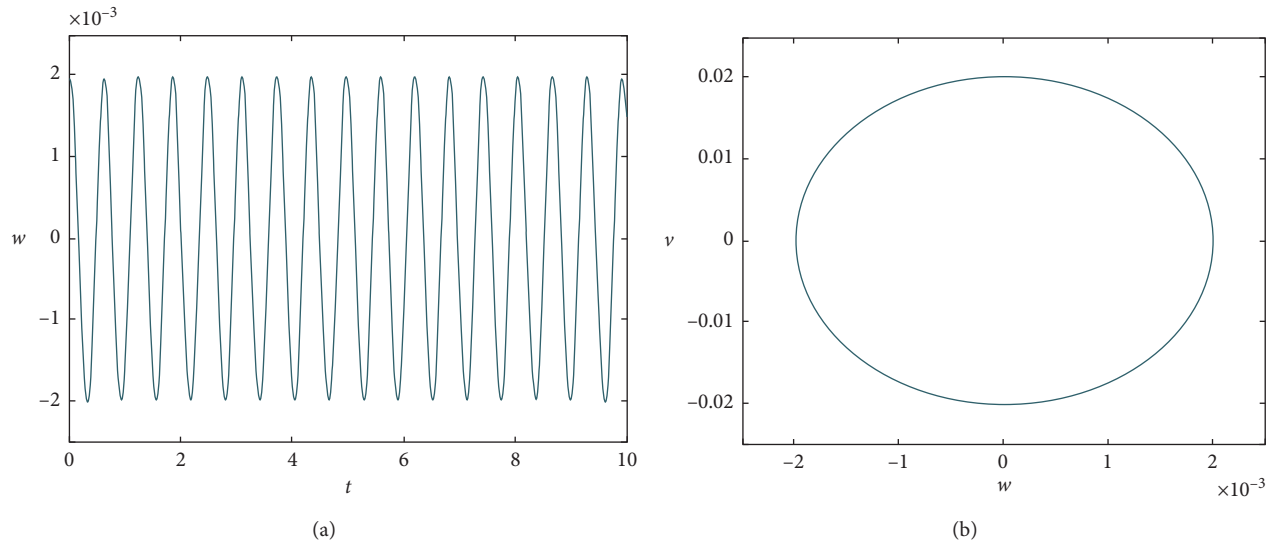


FIGURE 17: The system is kept in a critical state of stable and unstable when the inflow velocity U_∞ is chosen as 80.43 m/s: (a) time history diagram of vibration amplitude on plane (t, x_1) and (b) phase portrait on plane (w, v) .

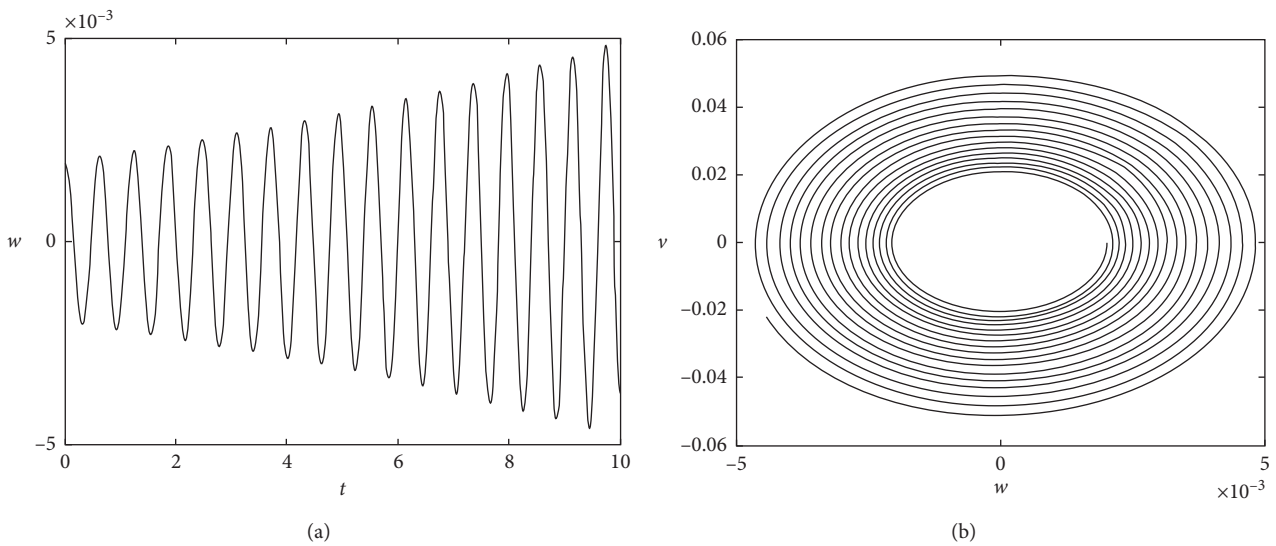


FIGURE 18: A divergent and unstable state of the system is kept in a critical state of stable and unstable when the inflow velocity U_∞ is chosen as 89 m/s: (a) time history diagram of vibration amplitude on plane (t, x_1) and (b) phase portrait on plane (w, v) .

Keep other parameters the same as that in Table 1, and only change the damping coefficient to calculate the corresponding critical flutter velocity. As shown in Figure 19(c), when the damping coefficient increases, the critical flutter velocity increases.

5. Conclusions

In order to use analytical or semianalytical method to analyze flutter of the high-aspect ratio cantilever plate, it is necessary to obtain an aerodynamic analytical expression of the plate under subsonic airflow. Giving the assumption of irrotationality, nonsticky, incompressibility, and strip theory

of high-aspect ratio and quasi-steady state, considering the skeleton line's deformation of airfoils' chord section and influences of lateral vibration velocity on quasi-steady aerodynamic force based on the thin-airfoil theory under subsonic flow and Kutta–Joukowski lift theorem, the authors induced a new quasi-steady aerodynamic analytical expression high-aspect ratio cantilever plate under subsonic airflow. It is confirmed that the analytical expression is consistent with the lift distribution tendency of finite element calculation. According to Reddy's first-order shearing plate theory and geometric equations of von Karman's large deformation, Hamilton principle was applied to establish nonlinear partial differential kinetic equation of cantilever

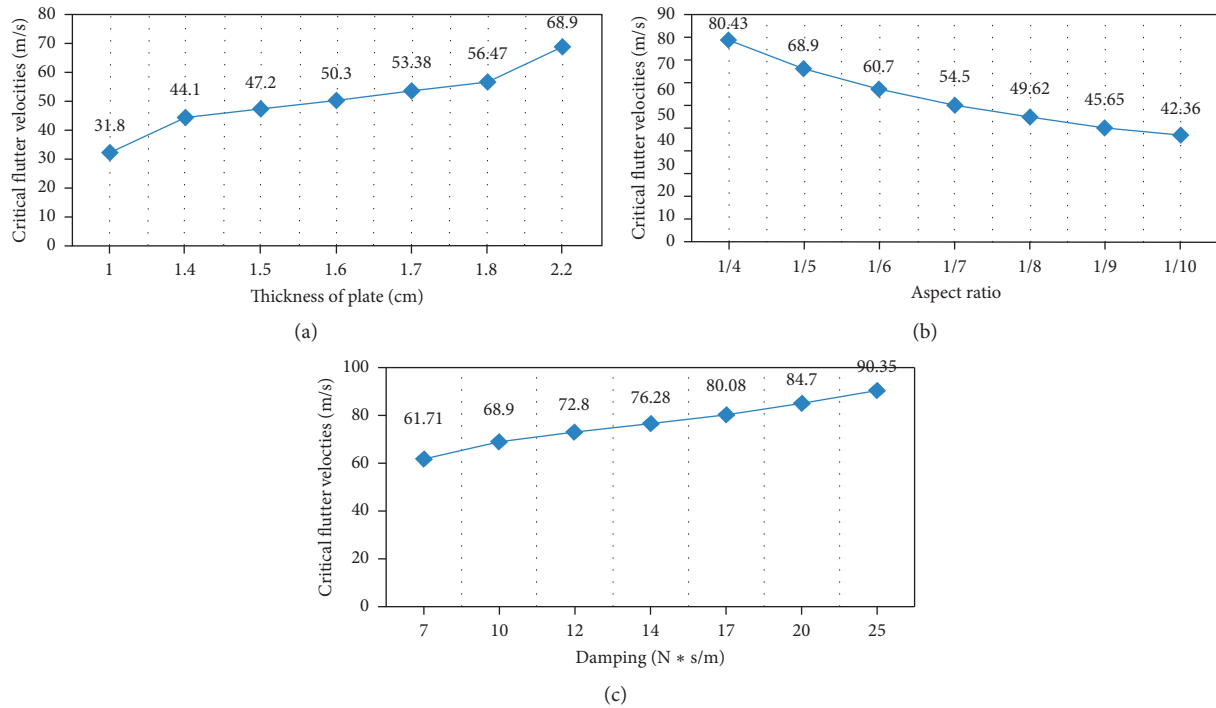


FIGURE 19: Influences of different factors on critical flutter velocities: (a) plate thickness; (b) aspect ratio; (c) damping.

plate, which suffers from aerodynamic force. The Galerkin method was used to obtain second-order ordinary differential governing equations of motion. Numerical simulation is carried out on the discrete nonlinear dynamic equations of ordinary differential equations to study the relation between critical flutter velocity and system parameters. The results showed that when inflow velocity reached the critical value, the limit cycle occurred. The increment of the aspect ratio or the thickness can both result in the decrement of the critical velocity of flutter. On the contrary, increment of air damping make the critical flutter velocity increase obviously.

Data Availability

The data used to support the findings of this study are available from the corresponding author upon request.

Conflicts of Interest

The authors declare that there are no conflicts of interest regarding the publication of this paper.

Authors' Contributions

Li Ma and Minghui Yao contributed equally to this work.

Acknowledgments

This work was supported by the National Natural Science Foundation of China (NNSFC) under Grant nos. 11972253, 11372015, 11832002, 11290152, 11427801, and 11972051.

References

- [1] S. Koksals, E. N. Yildiz, Y. Yazicioglu, and G. O. Ozgen, "Minimization of ground vibration test configurations for F-16 aircraft by subtractive modification," *Shock and Vibration*, vol. 2019, Article ID 9283125, 19 pages, 2019.
- [2] Y.-W. Zhang, H. Zhang, S. Hou, K.-F. Xu, and L.-Q. Chen, "Vibration suppression of composite laminated plate with nonlinear energy sink," *Acta Astronautica*, vol. 123, pp. 109–115, 2016.
- [3] M. V. Chernobryvko, K. V. Avramov, V. N. Romanenko, T. J. Batutina, and U. S. Suleimenov, "Dynamic instability of ring-stiffened conical thin-walled rocket fairing in supersonic gas stream," *Proceedings of the Institution of Mechanical Engineers, Part C: Journal of Mechanical Engineering Science*, vol. 230, no. 1, pp. 55–68, 2015.
- [4] M. Amabili and F. Pellicano, "Multimode approach to nonlinear supersonic flutter of imperfect circular cylindrical shells," *Journal of Applied Mechanics*, vol. 69, no. 2, pp. 117–129, 2002.
- [5] V. Vedenev, "Interaction of panel flutter with inviscid boundary layer instability in supersonic flow," *Journal of Fluid Mechanics*, vol. 736, pp. 216–249, 2013.
- [6] W. B. Zhu, M. McCrink, J. P. Bons, and J. W. Gregory, "Aerodynamic performance and trailing edge flow physics on an airfoil in an oscillating freestream," in *Proceedings of the AIAA Scitech Forum and Exposition 2020*, Orlando, FL, USA, January 2020.
- [7] H. Lin, D. Cao, and Y. Xu, "Vibration characteristics and flutter analysis of a composite laminated plate with a store," *Applied Mathematics and Mechanics*, vol. 39, no. 2, pp. 241–260, 2018.
- [8] Z. Hu and S. Mahadevan, "Reliability analysis of a hypersonic vehicle panel with spatio-temporal variability," *AIAA Journal*, vol. 57, no. 12, pp. 5403–5415, 2019.

- [9] K. Khorshidi and M. Karimi, "Flutter analysis of sandwich plates with functionally graded face sheets in thermal environment," *Aerospace Science and Technology*, vol. 95, Article ID 105461, 2019.
- [10] X. C. Wang, Z. C. Yang, Z. L. Chen et al., "Study on coupled modes panel flutter stability using an energy method," *Journal of Sound and Vibration*, vol. 468, Article ID 115051, 2020.
- [11] K. R. Brouwer and J. J. Mcnamara, "Enriched piston theory for expedient aeroelastic loads prediction in the presence of shock impingements," *AIAA Journal*, vol. 57, no. 3, pp. 1288–1302, 2019.
- [12] H. F. Ganji and E. H. Dowell, "Panel flutter prediction in two dimensional flow with enhanced piston theory," *Journal of Fluids and Structures*, vol. 63, pp. 97–102, 2016.
- [13] G. B. Chen, *Aeroelastic Design*, Beijing University of Aeronautics and Astronautics Press, Beijing, China, 2004.
- [14] Y. Q. Xu, D. Q. Cao, C. H. Shao, and H. G. Lin, "Nonlinear responses of a slender wing with a store," *Journal of Vibration and Acoustics*, vol. 141, no. 3, Article ID 031006, 2019.
- [15] U. Cordes, G. Kampes, T. Meissner, C. Tropea, J. Peinke, and M. Holling, "Note on the limitations of the theodorsen and sears functions," *Journal of Fluid Mechanics*, vol. 811, 2017.
- [16] D. A. Peters, "Toward a unified lift model for use in rotor blade stability analyses," *Journal of the American Helicopter Society*, vol. 30, no. 3, pp. 32–42, 1985.
- [17] P. Dunn and J. Dugundji, "Nonlinear stall flutter and divergence analysis of cantilevered graphite/epoxy wings," *AIAA Journal*, vol. 30, no. 1, pp. 153–162, 2012.
- [18] W. Wang, X. Zhu, Z. Zhou, and J. Duan, "A method for nonlinear aeroelasticity trim and stability analysis of very flexible aircraft based on co-rotational theory," *Journal of Fluids and Structures*, vol. 62, pp. 209–229, 2016.
- [19] M. H. Sadr, D. Badiei, and S. Shams, "Developments of a semiempirical dynamic stall model for unsteady airfoils," *Journal of the Brazilian Society of Mechanical Sciences and Engineering*, vol. 41, no. 10, Article ID 454, 2019.
- [20] W. W. Zhang and Z. Y. Ye, "On unsteady aerodynamic modeling based on CFD technique and its applications on aeroelastic analysis," *Advances in Mechanics*, vol. 38, no. 1, pp. 77–86, 2008.
- [21] X. Liu and Q. Sun, "Gust load alleviation with robust control for a flexible wing," *Shock and Vibration*, vol. 2016, p. 10, 2016.
- [22] W. W. Zhang and Z. Y. Ye, "Numerical simulation of aeroelasticity basing on Identification," *Chinese Journal of Aeronautics*, vol. 27, no. 4, pp. 579–584, 2006.
- [23] H.-L. Guo, Y.-S. Chen, and T.-Z. Yang, "Limit cycle oscillation suppression of 2-DOF airfoil using nonlinear energy sink," *Applied Mathematics and Mechanics*, vol. 34, no. 10, pp. 1277–1290, 2013.
- [24] T. Wu and A. Kareem, "A low-dimensional model for nonlinear bluff-body aerodynamics: a peeling-an-onion analogy," *Journal of Wind Engineering and Industrial Aerodynamics*, vol. 146, pp. 128–138, 2015.
- [25] J. Luo, Y. Zhu, X. Tang, and F. Liu, "Flow reconstructions and aerodynamic shape optimization of turbomachinery blades by POD-based hybrid models," *Science China Technological Sciences*, vol. 60, no. 11, pp. 1658–1673, 2017.
- [26] L. Wang, X. Liu, and A. Kolios, "State of the art in the aeroelasticity of wind turbine blades: aeroelastic modelling," *Renewable and Sustainable Energy Reviews*, vol. 64, pp. 195–210, 2016.
- [27] C. C. Xie, Y. Liu, C. Yang, and J. E. Cooper, "Geometrically nonlinear aeroelastic stability analysis and wind tunnel test validation of a very flexible wing," *Shock and Vibration*, vol. 2016, p. 17, 2016.
- [28] R. J. Higgins, A. Jimenez-garcia, G. N. Barakos, and N. Bown, "High-fidelity computational fluid dynamics methods for the simulation of propeller stall flutter," *AIAA Journal*, vol. 57, no. 12, pp. 5281–5292, 2019.
- [29] M. R. Chiarelli and S. Bonomo, "Numerical investigation into flutter and flutter-buffet phenomena for a swept wing and a curved planform wing," *International Journal of Aerospace Engineering*, vol. 2019, pp. 1–19, 2019.
- [30] D. J. Munk, D. Dooner, G. A. Vio, N. F. Giannelis, A. J. Murray, and G. Dimitriadis, "Limit cycle oscillations of cantilever rectangular designed using topology optimisation," *AIAA Journal*, 2020.
- [31] P. Castells marin and C. Poetsch, "Simulation of flexible aircraft response to gust and turbulence for flight dynamics investigations," in *Proceedings of the AIAA Scitech Forum and Exposition 2020*, Orlando, FL, USA, January 2020.
- [32] C. Xie, L. Wang, C. Yang, and Y. Liu, "Static aeroelastic analysis of very flexible wings based on non-planar vortex lattice method," *Chinese Journal of Aeronautics*, vol. 26, no. 3, pp. 514–521, 2013.
- [33] M. H. Pashaei, R. A. Alashti, S. Jamshidi, and M. Dardel, "Energy harvesting from limit cycle oscillation of a cantilever plate in low subsonic flow by ionic polymer metal composite," *Proceedings of the Institution of Mechanical Engineers Part G Journal of Aerospace Engineering*, vol. 229, no. 5, pp. 814–836, 2015.
- [34] H. Zhou, G. Wang, and Z. K. Liu, "Numerical analysis on flutter of Busemann-type supersonic biplane airfoil," *Journal of Fluids and Structures*, vol. 92, Article ID 102788, 2020.
- [35] C. D. Huang, J. Huang, X. Song, G. N. Zheng, and X. Y. Nie, "Aeroelastic simulation using CFD/CSD coupling based on precise integration method," *International Journal of Aeronautical and Space Sciences*, 2020.
- [36] Z. Chen, Y. Zhao, and R. Huang, "Parametric reduced-order modeling of unsteady aerodynamics for hypersonic vehicles," *Aerospace Science and Technology*, vol. 87, pp. 1–14, 2019.
- [37] D. F. Li, A. D. Ronch, G. Chen, and Y. M. Li, "Aeroelastic global structural optimization using an efficient CFD-based reduced order model," *Aerospace Science and Technology*, vol. 94, Article ID 105354, 2019.
- [38] H. J. Song, Y. Wang, and K. Pant, "Parametric fluid-structural interaction reduced order models in continuous time domain for aeroelastic analysis of high-speed vehicles," in *Proceedings of the AIAA Scitech Forum and Exposition 2020*, Orlando, FL, USA, January 2020.
- [39] D. Tang and E. H. Dowell, "Experimental and theoretical study on aeroelastic response of high-aspect-ratio wings," *AIAA Journal*, vol. 39, no. 8, pp. 1430–1441, 2001.
- [40] M. Ghalandari, S. Shamshirband, A. Mosavi, and K.-w. Chau, "Flutter speed estimation using presented differential quadrature method formulation," *Engineering Applications of Computational Fluid Mechanics*, vol. 13, no. 1, pp. 804–810, 2019.
- [41] E. H. Dowell, "Nonlinear aeroelasticity," *Solid Mechanics and Its Applications*, vol. 40, no. 5, pp. 857–874, 2012.
- [42] M. Amabili, F. Pellicano, and M. P. Paidoussis, "Non-linear dynamics and stability of circular cylindrical shells containing flowing fluid. part I: Stability," *Journal of Sound and Vibration*, vol. 225, no. 4, pp. 655–699, 1999.
- [43] C. Yang, *Aircraft Aeroelastic Principle*, pp. 36–172, Tsinghua University Press, Beijing, China, 2007.

- [44] Y. Du, L. P. Sun, X. H. Miao, F. Z. Pang, H. C. Li, and S. Y. Wang, "A unified formulation for free vibration of spherical cap based on the Ritz method," *Shock and Vibration*, vol. 2019, Article ID 7470460, 18 pages, 2019.
- [45] K. V. Avramov and Y. V. Mikhlin, "Review of applications of nonlinear normal modes for vibrating mechanical systems," *Applied Mechanics Reviews*, vol. 65, no. 2, 20 pages, 2013.
- [46] M. H. Zhao and W. Zhang, "Nonlinear dynamics of composite laminated cantilever rectangular plate subject to third-order piston aerodynamics," *Acta Mechanica*, vol. 225, no. 7, pp. 1985–2004, 2014.
- [47] M. Y. Shao, J. M. Wu, Y. Wang, and Q. M. Wu, "Nonlinear parametric vibration and chaotic behaviors of an axially accelerating moving membrane," *Shock and Vibration*, vol. 2019, Article ID 6294814, 11 pages, 2019.